A Biomechanical Model of the Human Head with Variable Material Properties for Intraoperative Image Correction

Alexander Hagemann

Dissertation zur Erlangung des akademischen Grades eines Doktors der Naturwissenschaften am Fachbereich Informatik der Universität Hamburg

Gutachter:	Prof. Dr. H. S. Stiehl Prof. Dr. K. Rohr Prof. Dr. D. P. F. Möller Dr. F. Kruggel
Tag der Disputation:	01. Februar 2001
Dekanin:	Prof. Dr. L. Dreschler-Fischer

Abstract

In order to improve the accuracy of image-guided neuronavigation systems, different *biomechanical models of the human head* have been developed to correct preoperative images with respect to intraoperative changes like brain shift or tumor resection. All existing approaches simulate different anatomical structures by using either appropriate boundary conditions or by spatially varying material parameter values, while assuming the same physical model for all anatomical structures. This generally leads to physically implausible deformation results, especially in the case of adjacent elastic and fluid structures.

In this thesis, we propose a new biomechanical model of the human head, which is based on the well-established physical theory of *continuum mechanics* to handle inhomogeneous materials. With our scheme, an inhomogeneous body is divided into a set of homogeneous regions, according to the underlying anatomical structure. To simulate different material properties, our approach uses the appropriate physical material description for each region, namely the *Navier equation* for rigid and elastic regions as well as the *Stokes equation* for fluid regions. To discretize and solve the resulting set of differential equations, we apply the *finite element method* (FEM) to each region, resulting in a corresponding set of sparse linear matrix systems. These matrix systems are then merged together by applying appropriate boundary conditions, which establish a physical link between the corresponding regions. As a result, a single linear matrix system which completely describes the physical behavior of an inhomogeneous body, comprising rigid, elastic, and fluid materials is obtained.

Instead of external forces, we use a set of given correspondences to drive the deformation. Our approach ensures, that these correspondences are exactly fulfilled by the calculated deformation. Reliable material parameter values for each region have been determined through a comprehensive literature study. Our approach has been experimentally compared with biomechanical models based entirely on either the Navier equation or the Stokes equation. It turns out, that the integrated treatment of rigid, elastic, and fluid materials significantly improves the deformation results compared to biomechanical models based on a single physical model only.

II

Acknowledgements

This thesis originates from a part of the IMAGINE project (IMage- and Atlas-Guided Interventions in NEurosurgery), carried out at the Department of Computer Science at the University of Hamburg.

First of all, I would like to thank Prof. Dr. K. Rohr and Prof. Dr. H. S. Stiehl for their outstanding support while supervising this thesis. Besides the numerous valuable discussions and remarks, the pleasing cooperation with both significantly contributed to this dissertation.

I would also like to thank Dr. F. Kruggel and Prof. Dr. D. P. F. Möller which kindly agreed to act as referees for this thesis.

Additionally, many thanks to the recent and former people and colleagues of the Cognitive Systems Research Group (KOGS): M. Fornefett, S. Frantz, J. Heers, T. Mantay, R. Franck, S. Utcke, J. Tellkamp, D. Jessen, and many other people for their support and help during all those critical periods which always occur while writing a dissertation.

I would also like to thank Philips Research Laboratories Hamburg for their financial support within the IMAGINE project. The medical image data used in this thesis were kindly provided by OA Dr. U. Spetzger and Prof. Dr. J. M. Gilsbach from the Neurosurgical Clinic, Aachen Institute of Technology (RWTH).

Finally, I would like to thank my family, my friends, and all those people who supported me during the last years.

Zusammenfassung der Dissertation

Die technologischen Fortschritte auf dem Gebiet der bildgebenden Verfahren für die Medizin – wie beispielsweise Magnetresonanz (MR), Computer Tomograpie (CT) oder Ultraschall (US) – haben die Möglichkeiten der medizinischen Diagnose und Behandlung von Erkrankungen innerhalb des menschlichen Kopfes signifikant verbessert. Insbesondere durch Erhöhung der Bildqualität sowie weite Verbreitung der bildgebenden Verfahren erfolgte eine starke Verbesserung auf dem Gebiet der Neurochirurgie, da eine Verbesserung der Genauigkeit bildgestützter Neuronavigationssysteme erreicht werden konnte. Derartige Systeme erleichtern dabei die präoperative Planung, d.h. sie ermöglichen eine präzise Bestimmung optimaler operativer Pfade, eine Identifizierung anatomischer Strukturen, eine Verringerung der Invasivität neurochirurgischer Eingriffe, eine Reduktion der intraoperativen bzw. postoperativen Mortabilitätsrate und können das postoperative Ergebnis verbessern.

Das prinzipielle Problem der bildgestützten Neurochirurgie ist das Auffinden einer Relation zwischen präoperativ gewonnenen Bilddaten und der aktuellen anatomischen Geometrie während der Operation, d.h. die Registrierung der Bilddaten mit der gegenwärtigen anatomischen Geometrie. Dieser Prozess erlaubt es dem Neurochirurgen die Positionen chirurgischer Instrumente in Relation zu wichtigen anatomischen Strukturen zu bestimmen und so die neurochirurgischen Eingriffe zu erleichtern. Die ersten Neuronavigationssysteme gingen von einem Starrkörperverhalten des menschlichen Kopfes aus, so daß die Registrierung auf Translationen und Rotationen des präoperativen Bildes beschränkt war. Da jedoch während einer Operation signifikante Bewegungen anatomischer Strukturen, welche auch als *brain shift* bekannt sind, auftreten, ist eine starre Registrierung der präoperativen Bilddaten nicht ausreichend. In der Folge wurden deshalb sogenannte *biomechanische Modelle* des menschlichen Kopfes entwickelt, die eine physikalisch basierte Anpassung der präoperativen Daten an die aktuelle anatomische Geometrie ermöglichen.

Fung [46] definiert Biomechanik als Mechanik, angewandt auf die Biologie, d.h. ein biomechanisches Modell umfaßt die physikalischen Eigenschaften des zu modellierenden Körpers und erlaubt es, Rückschlüsse auf die Mechanik der zugrundeliegenden biologischen Strukturen zu ziehen.

Aufgrund dieser Vorteile sind eine Reihe biomechanischer Modelle des menschlichen Kopfes entwickelt worden, welche eine physikalisch basierte, elastische Bildkorrektur erlauben. Als allgemein problematisch an diesen Ansätzen hat sich jedoch die Berücksichtigung von Materialinhomogenitäten herausgestellt, da diese einen signifikanten Einfluß auf die zu erwartende Deformation des Körpers haben. Derzeit simulieren alle existierenden Modelle solche Materialinhomogenitäten entweder mittels geeigneter Randbedingungen an den entsprechenden Organen oder durch lokale Variation der zugrundeliegenden Materialparameter, wobei hier für alle Materialien das gleiche physikalische Modell zugrunde gelegt wird. Diese Vereinfachungen führen generell zu ungenauen und zum Teil falschen Deformationsergebnissen, insbesondere in der Nähe von Strukturen mit unterschiedlichen physikalischen Eigenschaften wie beispielsweise in der Nähe von benachbarten flüssigen und elastischen Strukturen.

Um eine Verbesserung der Genauigkeit in der bildgestützten Neurochirurgie zu erreichen, wurde in dieser Arbeit ein neues biomechanisches Modell des menschlichen Kopfes entwickelt, welches eine physikalisch basierte Integration starrer, elastischer und flüssiger Materialien mittels geeigneter physikalischer Beschreibungen erlaubt. Als physikalische Grundlage unseres Ansatzes dient dabei die *Kontinuumsmechanik*, welche das Studium der Bewegung und des Gleichgewichts von Körpern sowie deren verursachende Kräfte erlaubt. Innerhalb der Kontinuumsmechanik werden dabei alle vorkommenden Funktionen wie beispielsweise Geschwindigkeiten, Dichten und Massenverteilungen als kontinuierlich im mathematischen Sinne betrachtet, so daß Ableitungen dieser Funktionen existieren.

Zur Simulation eines inhomogenen Körpers Ω teilen wir diesen entsprechend der zugrundeliegenden Anatomie in eine Menge homogener Regionen Ω_i auf. Den Materialeigenschaften der betrachteten Region entsprechend wird dann ein geeignetes *konstituierendes Gesetz* in die zugrundeliegende *Gleichgewichtsgleichung* eines allgemeinen Körpers,

$$\begin{cases} -\operatorname{div}[\boldsymbol{\sigma}] = \mathbf{f} & \text{in } \Omega_i, \\ \boldsymbol{\sigma}\mathbf{n} = \mathbf{g} & \text{auf } \Gamma_i, \end{cases} \tag{1}$$

substituiert. Hier bezeichnet $\boldsymbol{\sigma}$ den Spannungstensor, $\mathbf{n}$ die Oberflächennormale bezüglich des Randes Γ_i, sowie $\mathbf{f}$ und $\mathbf{g}$ die Vektoren der extern angreifenden Kräfte.

Als hinreichend genaues konstituierendes Gesetz für sowohl knöcherne Strukturen als auch für Gehirngewebe eignet sich das *Hookesche Gesetz*

$$\boldsymbol{\sigma} = \lambda\,(\mathrm{tr}\,\epsilon(\mathbf{u}))\,\mathbf{I} + 2\mu\epsilon(\mathbf{u}), \tag{2}$$

welches einen linearen Zusammenhang des Spannungstensors $\boldsymbol{\sigma}$ und des Verzerrungstensors $\boldsymbol{\epsilon}$ beschreibt. Mit $\mathbf{u}$ wird hier das zu bestimmende Verschiebungsvektorfeld benannt, während $\mathbf{I}$ die Einheitsmatrix und λ sowie μ die Laméschen Konstanten bezeichnen. Letztere nehmen unterschiedliche Werte für Knochen und Gehirngewebe an. Durch Substitution des Hookeschen Gesetzes in die Gleichgewichtsgleichung eines allgemeinen Körpers erhält man die *Naviergleichung*

$$(\lambda + \mu)\nabla\mathrm{div}[\mathbf{u}] + \mu\nabla^2\mathbf{u} + \mathbf{f} = \mathbf{0} \quad \text{in } \Omega_i, \tag{3}$$

welche den Gleichgewichtszustand eines elastischen Körpers bei angreifenden externen Kräften beschreibt.

Für flüssige Strukturen, wie die inkompressible *cerebrospinale Flüssigkeit*, wird stattdessen das *Navier-Poisson Gesetz*

$$\boldsymbol{\sigma} = -p\mathbf{I} + \lambda^\star(\mathrm{tr}\,\mathbf{D}(\mathbf{v}))\mathbf{I} + 2\mu^\star\mathbf{D}(\mathbf{v}) \tag{4}$$

verwendet. Dieses Gesetz beschreibt eine lineare Abhängigkeit des Spannungstensors $\boldsymbol{\sigma}$ vom Verzerrungsgeschwindigkeitstensor $\mathbf{D}$. Mit p wird an dieser Stelle der Druck, mit $\lambda^\star$ und $\mu^\star$ die Viskositätsparameter und mit $\mathbf{v}$ das Geschwindigkeitsvektorfeld bezeichnet. Man beachte, daß die Viskositätsparameter $\lambda^\star$ und $\mu^\star$ nicht den Laméschen Konstanten λ und μ des Hookeschen Gesetzes entsprechen. Durch Substitution des Navier-Poisson Gesetzes, unter gleichzeitiger Berücksichtigung der Inkompressibilität der cerebrospinalen Flüssigkeit mittels der *Kontinuitätsgleichung*

$$\mathrm{div}[\mathbf{v}] = 0 \quad \text{in } \Omega_i, \tag{5}$$

erhält man die *Stokesgleichung*

$$-\nabla p + \mu^\star\nabla^2\mathbf{v} + \mathbf{f} = \mathbf{0} \quad \text{in } \Omega_i \tag{6}$$

als physikalische Beschreibung des Gleichgewichtszustandes einer inkompressiblen Flüssigkeit. Unter der formalen Restriktion infinitesimaler Verschiebungsvektorfelder und Zeitintervalle dt kann anschließend die Deformation einer, eine Flüssigkeit enthaltende, Region aus dem Geschwindigkeitsvektorfeld durch

$$\mathbf{u} = \mathbf{v}dt \tag{7}$$

bestimmt werden.

Zur physikalischen Kopplung der einzelnen Regionen Ω_i haben wir geeignete Randbedingungen eingeführt, nämlich die *Gleichgewichtsbedingung*, die *Kompatibilitätsbedingung* und die *Haftbedingung* [145]. Erstere besagt, daß im Gleichgewichtszustand eines inhomogenen Körpers alle auf eine Oberfläche Γ_{ij} wirkenden Kräfte sich gegenseitig aufheben, so daß

$$\boldsymbol{\sigma}_i \mathbf{n} = \boldsymbol{\sigma}_j \mathbf{n}, \quad \forall \mathbf{x} \in \Gamma_{ij} \tag{8}$$

gilt, während die Kompatibilitätsbedingung die Gleichheit des Verschiebungsvektorfelds entlang der Grenze zweier Gebiete verlangt, d.h.

$$\mathbf{u}_i(\mathbf{x}) = \mathbf{u}_j(\mathbf{x}), \quad \forall \mathbf{x} \in \Gamma_{ij} \tag{9}$$

muß gelten. Mit der Haftbedingung wird ein Eindringen von Flüssigkeiten in umgebende Gebiete verhindert. Mathematisch wird dies durch die Forderung ausgedrückt, daß die Ableitung des Geschwindigkeitsvektorfeldes in Richtung der Oberflächennormalen verschwinden muß, d.h.

$$\mathbf{J}(\mathbf{v})\mathbf{n} = \mathbf{0}, \quad \forall \mathbf{x} \in \Gamma_{ij} \tag{10}$$

gelten muß. Hierbei bezeichnet $\mathbf{J}(\mathbf{v})$ die *Jakobimatrix* von $\mathbf{v}$.

Die Anwendung dieser drei Randbedingungen erlaubt dann die physikalische Beschreibung eines inhomogenen Körpers $\Omega = \Omega_i \cup \Omega_j$ bestehend aus elastischen und flüssigen Regionen Ω_i bzw. Ω_j, mittels des gekoppelten Systems von Differentialgleichungen

$$\begin{cases} (\lambda + \mu)\nabla \mathrm{div}[\mathbf{u}_i] + \mu \nabla^2 \mathbf{u}_i + \mathbf{f} = \mathbf{0} & \text{in } \Omega_i, \\ \boldsymbol{\sigma}_i \mathbf{n} = \boldsymbol{\sigma}_j \mathbf{n} & \text{auf } \Gamma_{ij}, \\ \mathbf{u}_i = \mathbf{u}_j & \text{auf } \Gamma_{ij}, \\ -\nabla p + \mu^\star dt^{-1} \nabla^2 \mathbf{u}_j + \mathbf{f} = \mathbf{0} & \text{in } \Omega_j \end{cases} \tag{11}$$

unter der formalen Annahme, daß die Kontinuitätsgleichung sowie infinitesimale Verschiebungen und Zeitintervalle gelten. Natürlich gelten für diese Beschreibung auch weiterhin Randbedingungen entlang der Teilränder von Ω_i und Ω_j, welche nicht dem gemeinsamen Rand Γ_{ij} entsprechen.

Zur numerischen Lösung dieses gekoppelten Systems von Differentialgleichungen wenden wir die *Methode der finiten Elemente* auf jede Region Ω_i an. Diese führt die entsprechenden Differentialgleichungen in eine Menge dünn besetzter, linearer Gleichungssysteme

$$\mathbf{A}^i \tilde{\mathbf{u}}^i = \mathbf{f} + \mathbf{g}^i \tag{12}$$

über, wobei der Vektor $\tilde{\mathbf{u}}^i$ die unbekannten Verschiebungsvektorkomponenten der entsprechenden Region Ω_i enthält. Die Matrix $\mathbf{A}^i$ wird in der Literatur auch als *Steifigkeitsmatrix* bezeichnet. Unter Berücksichtigung der Gleichgewichtsbedingung sowie der Kompatibilitätsbedingung läßt sich die Menge der linearen Gleichungssysteme in ein einziges lineares Gleichungssystem der Form

$$\begin{pmatrix} \mathbf{A}^i_{\Omega\Omega} & \mathbf{A}^i_{\Omega\Gamma} & \mathbf{0} \\ \mathbf{A}^i_{\Gamma\Omega} & \mathbf{A}^i_{\Gamma\Gamma} + \mathbf{A}^j_{\Gamma\Gamma} & \mathbf{A}^j_{\Gamma\Omega} \\ \mathbf{0} & \mathbf{A}^j_{\Omega\Gamma} & \mathbf{A}^j_{\Omega\Omega} \end{pmatrix} \begin{pmatrix} \tilde{\mathbf{u}}^i_\Omega \\ \tilde{\mathbf{u}}^{ij}_\Gamma \\ \tilde{\mathbf{u}}^j_\Omega \end{pmatrix} = \begin{pmatrix} \mathbf{f} + \mathbf{g}^i \\ \mathbf{f} \\ \mathbf{f} + \mathbf{g}^j \end{pmatrix} \tag{13}$$

überführen, welches vollständig den Gleichgewichtszustand eines inhomogenen Körpers bestehend aus starren, elastischen und flüssigen Materialien beschreibt. Mit $\tilde{\mathbf{u}}^i$ und $\tilde{\mathbf{u}}^j$ werden hier die Verschiebungen innerhalb jeder Region bezeichnet, während $\mathbf{A}^i_{\Omega\Omega}$ etc. die Submatrizen der Steifigkeitsmatrizen $\mathbf{A}^i$ und $\mathbf{A}^j$ jeder Region Ω_i und Ω_j benennen. Ein Index Γ, wie er beispielsweise in $\mathbf{A}^i_{\Omega\Gamma}$ vorkommt, bezeichnet diejenigen Submatrizen welche Komponenten enthalten, die sich auf den gemeinsamen Rand Γ_{ij} zwischen beiden Regionen beziehen.

Anstelle externer Kräfte, welche generell schwierig aus Bilddaten zu bestimmen sind, verwenden wir gegebene Korrespondenzen zwischen anatomischen Strukturen, um die Deformation unseres biomechanischen Modells zu steuern. Der Vorteil dieses Ansatzes ist, daß sich derartige Korrespondenzen einfach in das bestehende Gleichungssystem integrieren lassen und daß die berechnete Lösung des Gleichungssystems die gegebenenen Korrespondenzen exakt erfüllt. Unser Ansatz kann daher auch als ein landmarkenbasierter Registrierungsansatz angesehen werden. Als besonders vorteilhaft stellt sich dabei heraus, daß die vorgegebenen Korrespondenzen die notwendigen Kräfte automatisch justieren. Dies führt zu einer Entkoppelung der Materialparameter von expliziten physikalischen Einheiten, so daß nur noch die Verhältnisse zwischen den einzelnen Materialparametern eine Rolle spielen. Um diese zu bestimmen, haben wir eine umfangreiche Literaturstudie durchgeführt. Es stellte sich heraus, daß für die publizierten Werte nur eine geringe Anzahl unterschiedlicher Verhältnisse der Materialparameter von Schädelknochen und Gehirngewebe vorliegt. Wie experimentelle Untersuchungen mit diesen Werten ergaben, stellt der Mittelwert dieser Verhältnisse einen ersten zuverlässigen Wert für die Materialparameter dar. Aufgrund fehlender Angaben in der uns bekannten Literatur konnte ein entsprechender Wert für flüssige Materialien nur heuristisch bestimmt werden.

Abschließend haben wir einen Vergleich unseres neuen, gekoppelten Ansatzes mit biomechanischen Modellen durchgeführt, welche nur auf einem einzigen physikalischen Modell basieren. Zu diesem Zweck wurden in dieser Arbeit zwei weitere biomechanische Modelle entwickelt, von denen eins ausschließlich auf der Naviergleichung, das andere ausschließlich auf der Stokesgleichung zur Simulation aller Materialien basiert. Mittels räumlicher Variation der zugrundeliegenden Materialparameter wurden auch hier Inhomogenitäten simuliert.

Im Falle des ausschließlich auf der Stokesgleichung basierenden biomechanischen Modells hat sich dabei die Verwendung der sogenannten Q_2-P_1 *Crouzeix-Raviart* Elemente, welche die Lösbarkeit des resultierenden linearen Gleichungssystems sicherstellen, als problematisch erwiesen. Ursache ist hier zum einen die große Anzahl von resultierenden Freiheitsgraden, welche bereits für sehr kleine Bilddimensionen zu einem Speicherplatzbedarf von mehr als 1.5 GB führen, sowie zum anderen die numerischen Eigenschaften der resultierenden Steifigkeitsmatrix, welche eine Anwendung iterativer Lösungsverfahren verhindern. Zur Bewältigung dieser Probleme wurde in dieser Arbeit ein spezieller Typ finiter Elemente eingeführt, die sogenannten *divergenzfreien Elemente*. Diese Elemente reduzieren die Anzahl der Freiheitsgrade und somit den Speicherplatzbedarf der resultierenden Steifigkeitsmatrix derart, daß eine effiziente Anwendung dieses Ansatzes auf übliche Bildgrößen möglich ist. Außerdem werden die numerischen Eigenschaften der resultierenden Steifigkeitsmatrix dergestalt verändert, daß der Einsatz iterativer Lösungsmethoden erfolgen kann.

Der experimentelle Vergleich der genannten biomechnischen Modelle ergab, daß im Falle der auf nur einer einzigen Differentialgleichung basierenden biomechanischen Modelle, die geometrischen Strukturen starrer Körper generell erhalten geblieben sind. Jedoch resultierten bei diesen Modellen physikalisch implausible Deformationen in der Umgebung von Regionen mit verschiedenen Materialeigenschaften. Insbesondere in der Nähe flüssiger Strukturen, welche in diesen biomechanischen Modellen als starre Körper simuliert wurden um der Inkompressibilität der cerebrospinalen Flüssigkeit Rechnung zu tragen, können Verletzungen der zugrundeliegenden Topologie aufgrund großer Deformationen auftreten. Im Falle unseres neuen, gekoppelten Ansatzes wurden derartige Topologieverletzungen nicht beobachtet. Stattdessen liefert unser Ansatz hier physikalisch plausible Deformationen, bei denen die Inkompressibilität aller eine Flüssigkeit enthaltenden Gebiete gewahrt ist, wie ein Vergleich der Anzahl der das Flüssigkeitsgebiet umfassenden Bildpunkte ergab.

Ausgehend von den in dieser Arbeit erzielten Fortschritte auf dem Gebiet der biomechanischen Modellierung des menschlichen Kopfes zum Zwecke der intraoperativen Bildkorrektur, bleiben auch weiterhin viele Möglichkeiten der Weiterentwicklung. So stellt insbesondere die Berücksichtigung anisotroper

Materialien sowie nichtlinearen Materialverhaltens eine große Herausforderung an die biomechanische Modellierung dar. Eine erhebliche Verringerung der Rechenzeiten könnte durch den Einsatz verbesserter numerischer Verfahren sowie durch die Kombination der Methode der finiten Elemente mit der *Randelementemethode* zur Simulation von Flüssigkeitsgebieten erreicht werden. Die Konstruktion biomechanischer Modelle des menschlichen Kopfes bleibt also auch weiterhin eine interessante und spannende Herausforderung.

Contents

Abstract **I**

Zusammenfassung der Dissertation **V**

1 Introduction **1**
1.1 Biomechanical modeling in neurosurgery 1
1.2 Contributions of the dissertation 4
1.3 Structure of the dissertation 5

2 Modeling of biological tissues and fluids **7**
2.1 Mechanical properties of biological materials 7
2.2 Continuum mechanics 9
2.2.1 Some physical preliminaries 10
2.2.2 The equations of motion and equilibrium 15
2.2.3 The constitutive equations 17
2.2.4 The Navier equation 19
2.2.5 The Stokes equation 20
2.3 The finite element method 21
2.3.1 The method of weighted residuals 22
2.3.2 The Galerkin method 23
2.3.3 Uniqueness of the solution 24
2.4 Summary 26

3 Previous work **27**
3.1 Biomechanical models of the human head 28
3.1.1 Models for car crash impact analysis 28
3.1.2 Models for medical image correction 29
3.2 Biomechanical models of other organs 32
3.3 Tabular summary of the biomechanical models 34
3.4 Summary 34

4 A new biomechanical model **41**
4.1 Material descriptions . . . 42
4.1.1 Skull bone . . . 43
4.1.2 Cerebrospinal fluid . . . 43
4.1.3 Brain tissue . . . 43
4.2 Numerical solution using FEM . . . 47
4.2.1 FEM derivation of the Navier equation . . . 47
4.2.2 FEM derivation of the Stokes equation . . . 50
4.3 Finite elements . . . 55
4.3.1 Construction of a basis for the space $V^N(\Omega)$ . . . 55
4.3.2 Quadrilateral finite elements . . . 57
4.3.3 Computational complexity of fluid problems . . . 68
4.4 Inhomogeneous materials . . . 69
4.4.1 Physical theory . . . 69
4.4.2 Coupling of matrix systems . . . 72
4.4.3 Finite elements for coupled systems . . . 74
4.5 Specified displacements . . . 75
4.6 Material parameter values . . . 79
4.6.1 Material values for the Navier equation . . . 79
4.6.2 Material values for the Stokes equation . . . 83
4.6.3 Material values for the coupled system . . . 86
4.7 Summary . . . 86

5 Experimental results **89**
5.1 Experimental strategy . . . 89
5.2 The elastic model . . . 90
5.2.1 2D synthetic images . . . 91
5.2.2 3D synthetic images . . . 100
5.2.3 2D MR images . . . 102
5.3 The fluid model . . . 107
5.3.1 2D synthetic images . . . 109
5.3.2 2D MR images . . . 112
5.4 The coupled rigid/elastic/fluid model . . . 119
5.4.1 2D synthetic images . . . 120
5.4.2 2D MR images . . . 127
5.5 Summary . . . 131

6 Conclusion **133**

A Notation **137**

B Finite element mesh generation 141

Bibliography 144

Chapter 1

Introduction

1.1 Biomechanical modeling in neurosurgery

The technological developments of medical imaging devices like, e.g., *Magnetic Resonance* (MR), *Computed Tomography* (CT), *Positron Emission Tomography* (PET), and *Ultrasound* (US), radically changed the diagnosis and treatment of abnormalities within the human brain [117]. The advantages of these technological developments, especially the wide availability and the increased image quality of the tomographic scanners, remarkably changed the field of neurosurgery in the last decade since they improve the accuracy of image-guided neuronavigation systems. Such image-guided neuronavigation systems facilitate the preoperative planning stage through the accurate determination of access to lesions [13, 50], support the identification of anatomical structures, allow to minimize the invasiveness of neurosurgical procedures, reduce the surgical morbidity, and may enable to improve the postoperative outcome [13, 117, 143].

The principal problem of image-guided neuronavigation is to find a spatial correspondence between preoperatively acquired neuroradiological data and current anatomy, i.e. to register preoperative acquired patient data (usually given in form of, but not limited to, CT or MR images) with the actual intraoperative anatomical geometry of the patient. This process enables the surgeon to precisely relate positions of surgical instruments to anatomical or pathological structures of interest [70, 102, 143] and thus facilitates the neurosurgical intervention. For this registration process, the first image-guided neuronavigation systems monitored the positions of surgical instruments in the surgical field and generated appropriate orthogonal views of the human head[1] relative to the surgical instruments using the preoperatively acquired

[1] The expression head refers here to skull, brain, fluid, and skin.

MR/CT images [13]. For the necessary registration process, a rigid body behavior of the human head was commonly assumed, i.e. the preoperative image data was aligned to the actual anatomy by translation and rotation only [34]. However, the accuracy of these image-guided neuronavigation systems generally suffers from significant position and shape changes of the brain tissue occurring during neurosurgery [13, 50, 70]. According to [13, 50, 122, 70], this phenomenon results from a variety of surgical interventions like, e.g., cerebrospinal fluid drainage, tumor resection, use of diuretics, or hemorrhage and is usually known as *brain shift*. Thus, all systems assuming a rigid body behavior only are generally not suited for neuronavigation tasks like controlling the degree of tumor resection due to the continuously changing anatomical situation during neurosurgical interventions [143].

In order to increase the accuracy of image-guided neuronavigation systems, it is therefore necessary to correct the preoperatively acquired MR and/or CT images with respect to such intraoperative, non-rigid tissue movements. For this purpose, so-called *biomechanical models* of the human head have been introduced to further improve the registration accuracy in neuronavigation systems. Fung [46] defined *biomechanics* as mechanics applied to biological tissues and structures thus allowing to understand the mechanics of living systems. Consequently, a biomechanical model of the human head incorporates the physical properties of the human head. This is in contrast to registration schemes commonly used in medical image analysis [96, 123] like, e.g., thin-plate spline approaches, since these schemes do not model the physical behavior of the underlying anatomical structure. In other words, a biomechanical model allows a *physically-based* prediction of organ changes due to external alterations and proposes methods of interventions [46]. Thus biomechanical models directly support the tasks of diagnosis, simulation, and surgical intervention.

In the past, a variety of different biomechanical models for intraoperative image correction purposes have been proposed. Additionally, other biomechanical models have been developed in different contexts like car crash impact analysis or surgery simulation, but most of them are applicable for image correction purposes, too. Although the usage of such approaches increases the accuracy of image-guided neuronavigation systems [13, 107], problems still arise with biological material inhomogeneities. All existing biomechanical models simulate the physical behavior of different anatomical structures by either spatially varying the underlying material parameter values while assuming a single physical model for all anatomical structures, irrespective of their real physical properties, or by applying special mathematical boundary conditions. As an example of the latter case may serve rigid structures, e.g. bone, whose physical properties are usually simulated by preventing any

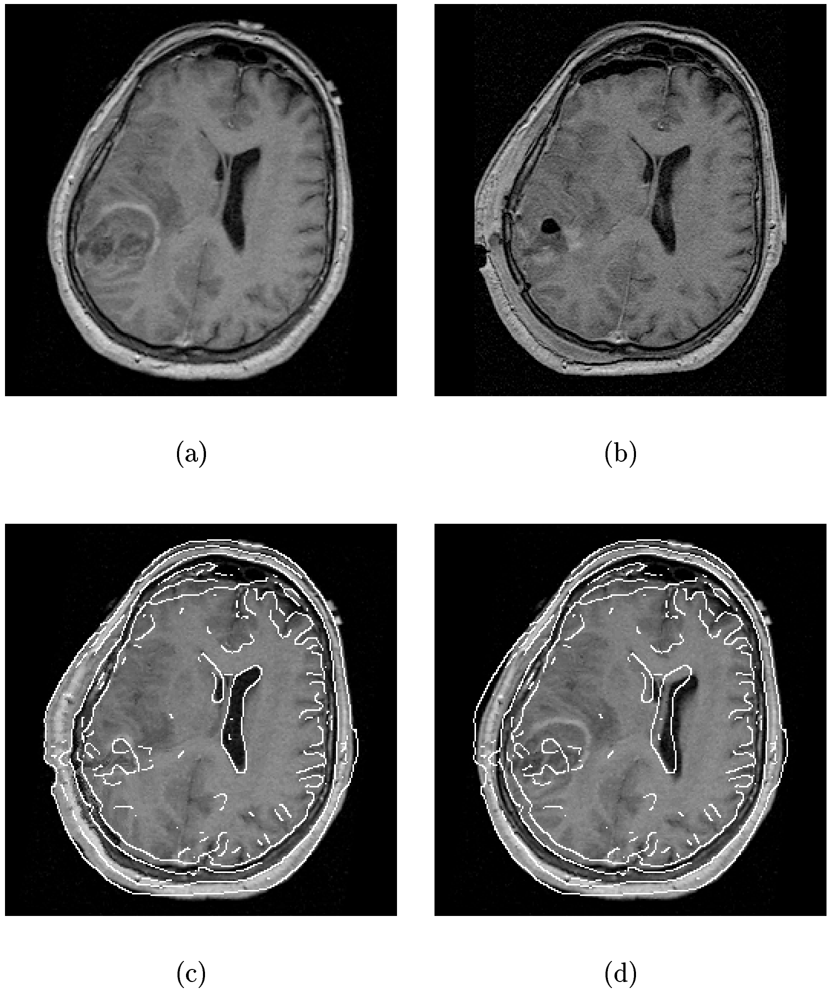

Figure 1.1: Simulation of fluids while treating them as rigid objects surrounded by elastic material: results of registration of (a) the preoperative image with (b) the postoperative image while (c) none of the prescribed displacements were given within the vicinity of the ventricular system (dark elongated region in the middle of the image) and (d) while using prescribed displacements directly at the ventricular system, leading to an unrealistic translation of the latter one. For a better visualization of the result, the computed edges of the postoperative image (b) have been overlaid on subfigures (c) and (d).

movement of such structures in this type of biomechanical models. However, such simplifications generally lead to physically inadequate simulations, particularly in case of combined elastic and fluid-filled structures, whose physical deformation behaviors differ significantly from each other. As a consequence, their physical properties cannot be described using a single physical model only. For example, the ventricular system in [64] was modeled as a rigid object, which was motivated by the reported incompressibility of cerebrospinal fluid [135, 146]. Using this assumption, good registration results were obtained if none of the prescribed displacements, which drive the deformation of the model, act in the vicinity of the ventricular system. Otherwise the model gives a poor registration result, leading to an unrealistic translation of the ventricular fluid structure as shown in Figure 1.1.

To enhance the accuracy of intraoperative image correction and finally of image-guided neuronavigation systems, we develop in this thesis a new biomechanical model of the human head that circumvents the limitations for combined elastic and fluid structures caused by the common usage of a single physical model only. The proposed algorithms are believed to pave the way for further developments in biomechanical modeling and thus will eventually support the neurosurgeon for the benefit of the patient.

1.2 Contributions of the dissertation

In this thesis, we propose a new biomechanical model of the human head which copes with anatomical structures consisting of *rigid*, *elastic*, and *fluid* materials while using the appropriate physical descriptions, namely the *Navier equation* and the *Stokes equation*. Our approach is based on the well-established physical theory of *continuum mechanics* to handle inhomogeneous materials. Within our approach, an inhomogeneous body is divided into a set of homogeneous regions, each simulating a different material according to the underlying anatomical structure. In contrast to other biomechanical models, our approach uses the appropriate physical model to describe the physical behavior of each region. For a discretization and solution of the problem, we apply the *finite element method* (FEM) to each region resulting in a corresponding set of sparse linear matrix systems. To merge these linear matrix systems together, we derive a set of boundary conditions, which establish a physical link between the corresponding regions. Application of these boundary conditions results in a single linear matrix system which completely describes the physical behavior of an inhomogeneous body comprising rigid, elastic, and fluid materials.

Instead of using external forces, which are generally difficult to determine from given corresponding images, we use a set of prescribed correspondences to drive the deformation of the biomechanical model. In our approach, it is ensured that these prescribed correspondences are exactly fulfilled by the computed deformation. Thus our approach can be seen as a landmark-based registration scheme [6, 130, 41]. Additionally, using such prescribed displacements it is guaranteed, that the values of the external forces that are necessary to lead to these desired displacements are automatically adjusted. This property of our approach decouples the material parameter values from explicit physical units such that only the ratios of the material parameter values with respect to each other remain important. To determine the latter mentioned ratios for the material parameter values, we carried out a comprehensive literature study, resulting in a set of reliable material parameter ratios. Thus, our approach successfully addresses the common problem of choosing appropriate material parameter values for biomechanical models.

Finally, we carry out experiments using different biomechanical models of the human head and compare the calculated deformations to assess the general efficiency of the different approaches as well as the influence of different physical models on the computed results. Besides a coupled rigid/elastic/fluid model, we develop two other biomechanical models, each of them based on a single physical model only. One represents a pure elastic model based on the Navier equation and the other a pure fluid model based on the Stokes equation. In case of the fluid model, a finite element discretization using the commonly applied types of finite elements leads to a huge number of degrees-of-freedom and thus to unacceptable computation times which generally prevent the application of such models. To circumvent these problems, we propose the usage of a non-common type of finite elements in this thesis which reduces the number of degrees-of-freedom while simultaneously enhancing the numerical properties of the approach, i.e. the condition number of the underlying linear matrix system, such that the memory requirements as well as the computation times are significantly reduced.

To simulate inhomogeneities within the purely elastic and the purely fluid model, we spatially vary the material parameter values using appropriate ratios of the latter one for different regions. The comparison of these two biomechanical models with the coupled rigid/elastic/fluid model reveals, that the integrated treatment of rigid, elastic, and fluid materials used in our new biomechanical model significantly improves the physical plausibility of the computed deformation results.

1.3 Structure of the dissertation

In order to develop a new biomechanical model of the human head, we start in **Chapter 2** with a brief overview of general properties of biological materials. The description focuses on those measurable physical entities of biological structures that are needed to simulate a deformation of a body in the underlying physical framework of continuum mechanics. A short introduction into the theory of continuum mechanics is given next, ending up with the derivation of the Navier equation and the Stokes equation as physical descriptions for elastic and fluid materials, respectively. For a solution of these differential equations, we apply the finite element method (FEM), the fundamentals of which are presented in the last part of Chapter 2.

Chapter 3 presents an overview of the existing literature dealing with biomechanical models. Besides a general description of these models, we also provide a compact summary of all approaches in tabular form.

Our new biomechanical model is developed in **Chapter 4**, starting with the determination and evaluation of appropriate material models for different biological structures. Following this, we present the complete FEM discretization of the differential equations used in our model, namely the Navier equation and the Stokes equation. Next, we give a short introduction into the underlying mathematical framework for constructing finite elements. Examples of appropriate finite elements which ensure the solvability of the final linear matrix system, especially in case of fluid-filled structures, are also presented.

So far, a set of linear matrix systems has been derived, each describing the physical behavior of a different homogeneous material. To merge these matrix systems into a single one, we then present the necessary boundary conditions to establish a physical link between neighboring regions. As a result, we end up with a single linear matrix system that completely describes the deformation behavior of an inhomogeneous anatomical structure like the human head, that comprises rigid, elastic, and fluid parts.

Following this, we discuss the integration of prescribed displacements into the final matrix systems. We also emphasize the problems associated with the assignment of prescribed displacements to finite elements belonging to fluid regions. The last part of Chapter 4 deals with the necessary determination of reliable material parameter values for the Navier equation and the Stokes equation, respectively.

In **Chapter 5**, we report on experiments which have been carried out to assess the general efficiency of the different approaches sketched above. We start with experiments using first a purely elastic model and second a purely fluid model to assess the validity and efficacy of biomechanical models based on a single physical model only. The chapter will end with a direct comparison of these two models with our new approach, allowing the coupling of different physical models.

Finally, **Chapter 6** gives a summary of this thesis and discusses objectives for future research.

Chapter 2

Modeling of biological tissues and fluids

In this chapter, we give a brief introduction into the physical theory and the mathematical methods used for the derivation of our biomechanical model of the human head. The term biomechanics refers here to the area of research that deals with the mechanics of biological tissues and structures. We begin with a short overview of properties of soft tissues reported in the literature, followed by an introduction into the theory of continuum mechanics, which serves as underlying physical theory. In this chapter we will also present the fundamentals of the finite element method (FEM), used for a numerical solution of those differential equations that describe the physical behavior of the modeled biological structures. Thus, a brief overview of the theories and methods necessary to develop a biomechanical model of the human head is presented in the following.

2.1 Mechanical properties of biological materials

Due to the large amount of existing literature concerning biomechanics and the measurable physical properties of soft tissues, we present mainly those important facts that are needed for the physical theory framework presented in the following section. More details and background knowledge about biomechanics research can be found in, e.g., [45, 46, 48, 101].

The physical properties of a biological structure depend mainly on i) the kind of material which builds up the structure and ii) the spatial arrangement of its components [46]. Common biological materials of which tissues and organs are composed of are, e.g., elastin, resilin, abducin, and collagen, where the latter one serves as basic structural element for a large variety of different tissues like, e.g., skin or the dura mater [46]. Apart from material types, the physical properties depend on the spatial organization of these materials into larger biological structures, i.e. on the organization of the material molecules into structures like fibers etc. As an example, observe bone, since its architecture is closely related to its mechanical function [46, 142]. But apart from the tissue specimen considered, the mechanical behavior of biological tissues is uniquely characterized by their *constitutive behavior*, i.e. the relationship between externally applied loads like, e.g., pressure forces, and the resulting deformation. This behavior can be diagrammed in form of so-called *load-deformation curves*, as depicted in Figure 2.1.

As found through different mechanical experiments regarding the stretch of tissue specimens, the load-deformation curves of most biological tissues typically share some common properties: at the beginning of the elongation (stretch) of a specimen, the load increases exponentially with the elongation, followed by a fairly linear relationship between elongation and load. Finally, the relationship becomes nonlinear again and ends up with a rupture of the specimen [46, 101], see Figure 2.1(a). Such a behavior can be found for a large variety of different tissues like, e.g., tendons, blood vessels, muscles, and skin [74, 48, 101]. Apart from these materials, others exist with load-deformation curves that deviate significantly from this behavior. Brain tissue serves as a prominent example since it shows a completely nonlinear load-deformation curve without any linear parts [36, 106, 160].

Some other important properties shared by most biological tissues are i) *stress relaxation*, which denotes the process of gradually decreasing load when a tissue specimen is suddenly stretched and maintained at its new length [101], and ii) *hysteresis*, for which the load-deformation curve of a tissue specimen shows different paths for the loading and the unloading cycle. This latter property of tissues is shown in Figure 2.1(b). Additionally, for multiple, subsequent loading/unloading cycles of a tissue specimen, the load-deformation curve is usually shifted to larger deformations. The difference between successive cycles decreases and even disappears if the test is repeated infinitely often. In this case, the tissue specimen is said to be *preconditioned* [46] and shows a well defined load-deformation curve, thus allowing a unique description of the mechanical tissue properties. A general mathematical formulation of these important load-deformation relationships is presented in the following section, while a specific treatment of brain tissue will be given in Section 4.1.

The properties of stress relaxation and hysteresis are features of *viscoelasticity*, where the load at a given time t depends on the complete history of the deformation [46, 32]. This is in contrast to *elastic* materials, where the

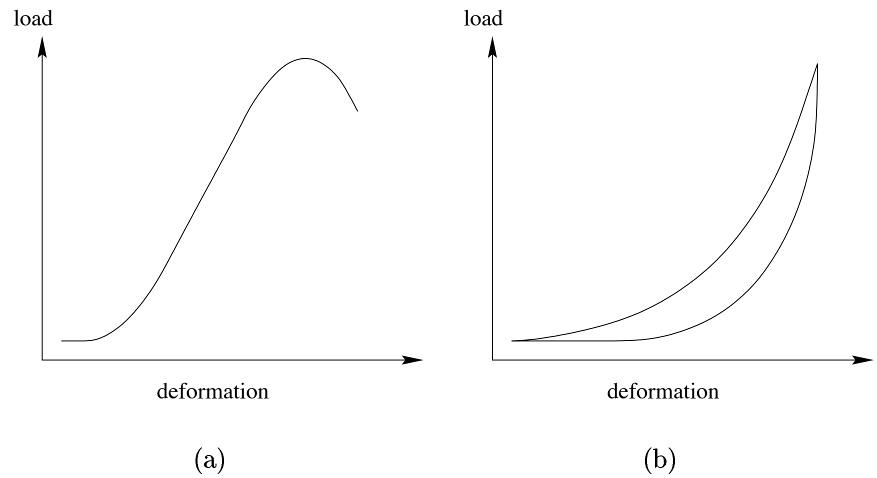

Figure 2.1: A typical load-deformation curve (a) for biological tissues. In case of cyclic loading, a hysteresis occurs (b). Both figures were adopted from [46].

load is always linearly proportional to the current deformation. However, an elastic mechanical behavior of tissues can be often assumed due to the linear part in the load-deformation curves of most biological tissues. Often, this assumption even holds for tissues with load-deformation curves deviating significantly from Figure 2.1(a) provided that the observation time, i.e. the time which an experiment lasts, is short compared to the stress relaxation times [161].

Besides the tissues which form an anatomical structure, biofluids play also an important role in organisms since their mechanical properties may significantly influence surrounding soft tissues. An important example is *cerebrospinal fluid* (CSF) which significantly interacts with brain tissue [78]. Most biofluids, like saliva and mucus, show a viscoelastic behavior [46], but others, like blood or cerebrospinal fluid, are considered as incompressible fluids [78, 135, 146] instead. The physical properties of fluids as well as the physical differences between fluids and elastic solids are described in the following.

2.2 Continuum mechanics

To develop a biomechanical model of the human head for the purpose of intraoperative image correction, *continuum mechanics* serves as physical basis.

Continuum mechanics allows for the study of motion or equilibrium of matter, as well as of the forces that cause such motions [47]. The term continuum indicates that all functions within the theory, like velocities, densities, and mass distributions, can be described mathematically as continuous functions.

Continuum mechanics can be divided into three parts [100]: The *general principles*, the *constitutive equations*, and the *specialized theories*. The general principles encompass the basic physical assumptions like conservation laws of mass, momentum, and energy, respectively, whereas the material properties of a specific body are described by the corresponding constitutive equations. The third part of continuum mechanics, the specialized theories, consists of an application of special cases of both, general principles and constitutive equations, given problem specific boundary conditions. Two famous instances of specialized theories of continuum mechanics are *elasticity theory* and *fluid mechanics*. Further details on continuum mechanics can be found in, e.g., [44, 100, 47].

In the sequel, we give a short summary of the main concepts of continuum mechanics, starting with some necessary definitions. Subsequently, we present the field equations which describe the physical behavior of a general body as well as the constitutive equations, which allow for individual material properties of the body. We finish this section with the basic equations of both, elasticity theory and fluid mechanics, which will be used for the development of our biomechanical model.

2.2.1 Some physical preliminaries

Deformation, displacement, and velocity

Here, a body Ω is defined as an open, bounded, and connected subset of $\mathbb{R}^3$ with Lipschitz-continuous[1] boundary Γ. The closure $\bar{\Omega}$ of Ω represents the volume of the body in the undeformed state, also known as the *reference configuration* [21]. If the reference configuration is chosen to be the initial configuration at time $t = 0$, then it is called *Lagrangian configuration* [100]. In case of applied forces, the body is exposed to a deformation. This deformation is defined as a smooth, injective, and orientation preserving mapping $\boldsymbol{\varphi} : \bar{\Omega} \times \mathbb{R}^+ \longrightarrow \mathbb{R}^3$ such that for every $\mathbf{x} \in \bar{\Omega}$

$$\boldsymbol{\varphi}(\mathbf{x}, t) = \hat{\mathbf{x}}(\mathbf{x}, t) = \mathbf{x} + \mathbf{u}(\mathbf{x}, t) \tag{2.1}$$

[1] A boundary Γ is called Lipschitz-continuous if $\forall \mathbf{x} \in \Gamma$ a neighbourhood exists, which can be represented as a Lipschitz-continuous function. A function f is denoted Lipschitz-continuous if $||f(\mathbf{x}_1) - f(\mathbf{x}_2)|| \leq \alpha ||\mathbf{x}_1 - \mathbf{x}_2||$ is valid for a constant $\alpha \in \mathbb{R}$ [12, 7].

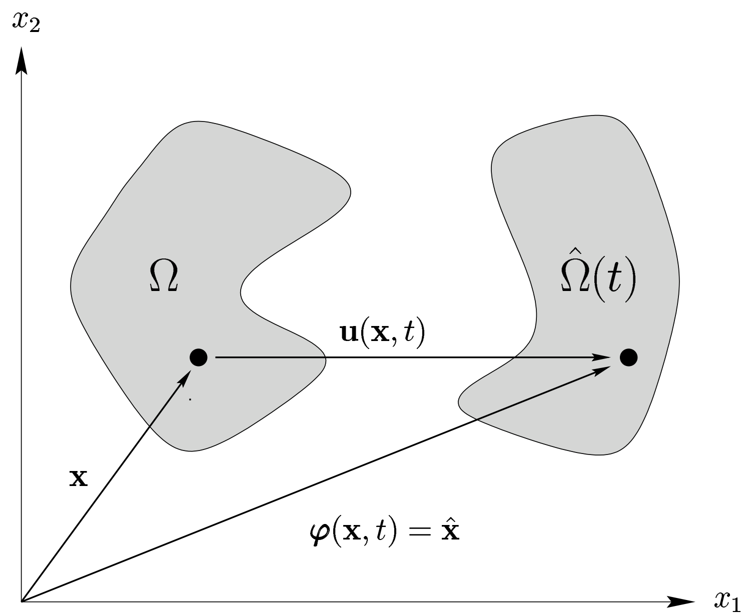

Figure 2.2: Transformation of a body Ω at $t = 0$ into a deformed configuration $\hat{\Omega}$ occupied at $t > 0$.

holds, where the vector field $\mathbf{u} : \bar{\Omega} \times \mathbb{R}^+ \longrightarrow \mathbb{R}^3$ is called the *displacement field* at time t [21]. The resulting configuration $\hat{\bar{\Omega}}(t) = \boldsymbol{\varphi}(\bar{\Omega}, t)$, adopted at a time $t > 0$, is called *Eulerian configuration.* The closure of Ω in the Eulerian configuration is denoted by $\hat{\bar{\Omega}}$, see also Figure 2.2.

To describe the local deformation of a body, the *deformation gradient* matrix [9]

$$\mathbf{J}(\boldsymbol{\varphi}) = (\nabla \boldsymbol{\varphi}^T)^T, \tag{2.2}$$

with $J(\boldsymbol{\varphi})_{ij} = \partial_j \varphi_i$, is introduced, which is also known as *Jacobian matrix* [38]. Here, ∇ denotes the *Nabla operator*, an upper T denotes the transpose, and ∂_i is the partial derivative with respect to the ith spatial component. Since the deformation $\boldsymbol{\varphi}$ is defined as an orientation preserving mapping,

$$\det\left[\mathbf{J}(\boldsymbol{\varphi})\right] > 0 \tag{2.3}$$

must hold for all $\mathbf{x} \in \bar{\Omega}$ [21, 38]. Analogously to (2.2), a *displacement gradient* $\mathbf{J}(\mathbf{u})$ can be defined, thus allowing a representation of $\mathbf{J}(\boldsymbol{\varphi})$ by

$$\mathbf{J}(\boldsymbol{\varphi}) = \mathbf{I} + \mathbf{J}(\mathbf{u}), \tag{2.4}$$

where $\mathbf{I}$ denotes the identity matrix.

So far, all definitions were made in the Lagrangian configuration $\bar{\Omega}$. An alternative formulation can be given in the Eulerian configuration $\hat{\bar{\Omega}}(t)$. Again, the deformation is a smooth, injective, and orientation preserving mapping $\hat{\boldsymbol{\varphi}} : \hat{\bar{\Omega}} \times \mathbb{R}^+ \longrightarrow \mathbb{R}^3$ such that for every $\hat{\mathbf{x}} \in \hat{\bar{\Omega}}$

$$\hat{\boldsymbol{\varphi}}(\hat{\mathbf{x}}, t) = \hat{\mathbf{x}} - \hat{\mathbf{u}}(\hat{\mathbf{x}}, t) \tag{2.5}$$

holds [43, 9], with $\hat{\mathbf{u}} : \hat{\bar{\Omega}} \times \mathbb{R}^+ \longrightarrow \mathbb{R}^3$ denoting the displacement vector field at time t. From (2.1) and (2.5) follows

$$\mathbf{u}(\mathbf{x}, t) = \hat{\mathbf{u}}(\hat{\mathbf{x}}, t), \tag{2.6}$$

according to the axiom of independence of physical entities from the underlying reference frame [21, 9].

Associated with the displacement field $\mathbf{u}$ is a velocity field $\mathbf{v} : \bar{\Omega} \times \mathbb{R}^+ \longrightarrow \mathbb{R}^3$ which describes the velocity of each particle $\mathbf{x} \in \bar{\Omega}$ in the Lagrangian configuration [100, 47]. As usual, the velocity is defined as [9]

$$\mathbf{v}(\mathbf{x}, t) = \frac{\partial \mathbf{u}(\mathbf{x}, t)}{\partial t} = \frac{\partial \varphi(\mathbf{x}, t)}{\partial t}. \tag{2.7}$$

Again, a formulation of the velocity field $\hat{\mathbf{v}} : \hat{\bar{\Omega}} \times \mathbb{R}^+ \longrightarrow \mathbb{R}^3$ in the Eulerian configuration can be given. Due to the time dependency of the deformed configuration $\hat{\bar{\Omega}}(t)$, the full time derivative has to be used instead [100, 9], yielding [16]

$$\hat{\mathbf{v}}(\hat{\mathbf{x}}, t) = \frac{d\hat{\mathbf{u}}(\hat{\mathbf{x}}, t)}{dt} = \frac{\partial \hat{\mathbf{u}}(\hat{\mathbf{x}}, t)}{\partial t} + \nabla \hat{\mathbf{u}}(\hat{\mathbf{x}}, t)\mathbf{v}(\mathbf{x}, t). \tag{2.8}$$

Equation (2.8) is also known as the *material derivative* of $\hat{\mathbf{u}}$.

Strain

Strain is a measure of deformation which is usually defined as rate of change of the initial length [47]. Considering an infinitesimal line element $d\hat{\mathbf{x}} \in \hat{\bar{\Omega}}$, which relates to the corresponding line element in the Lagrangian configuration through a Taylor series expansion [100, 47]

$$d\hat{\mathbf{x}} = \mathbf{J}(\boldsymbol{\varphi})d\mathbf{x}, \tag{2.9}$$

we can calculate the square of the length $d\hat{s} = |d\hat{\mathbf{x}}| = \sqrt{d\hat{\mathbf{x}}^T d\hat{\mathbf{x}}}$ of the line element in the Eulerian configuration by [100, 21, 47]

$$d\hat{s}^2 = d\mathbf{x}^T \mathbf{J}(\boldsymbol{\varphi})^T \mathbf{J}(\boldsymbol{\varphi}) d\mathbf{x} = d\mathbf{x}^T \mathbf{C} d\mathbf{x}. \tag{2.10}$$

The symmetric tensor $\mathbf{C}$ is called *right Cauchy-Green strain tensor* and can be understood as a measure of the quadratic length of a line element with respect to the Lagrangian configuration. According to (2.4) and (2.10), the equality

$$\mathbf{C}(\mathbf{u}) = \mathbf{J}(\varphi)^T\mathbf{J}(\varphi) = \mathbf{I} + \mathbf{J}(\mathbf{u})^T + \mathbf{J}(\mathbf{u}) + \mathbf{J}(\mathbf{u})^T\mathbf{J}(\mathbf{u}) \tag{2.11}$$

follows.

Equivalently, we can calculate the square of the length $ds = |d\mathbf{x}| = \sqrt{d\mathbf{x}^T d\mathbf{x}}$ of an infinitesimal line element $d\mathbf{x} \in \bar{\Omega}$ in the Lagrangian configuration by

$$ds^2 = d\hat{\mathbf{x}}^T\mathbf{J}(\hat{\varphi})^T\mathbf{J}(\hat{\varphi})d\hat{\mathbf{x}} = d\hat{\mathbf{x}}^T\hat{\mathbf{C}}d\hat{\mathbf{x}}. \tag{2.12}$$

In this case, the symmetric tensor

$$\hat{\mathbf{C}}(\hat{\mathbf{u}}) = \mathbf{J}(\hat{\varphi})^T\mathbf{J}(\hat{\varphi}) = \mathbf{I} - \mathbf{J}(\hat{\mathbf{u}})^T - \mathbf{J}(\hat{\mathbf{u}}) + \mathbf{J}(\hat{\mathbf{u}})^T\mathbf{J}(\hat{\mathbf{u}}) \tag{2.13}$$

is called *left Cauchy-Green strain tensor* and measures the quadratic length of a line element with respect to the Eulerian configuration [100]. If $\mathbf{C} = \hat{\mathbf{C}} = \mathbf{I}$, then $ds = d\hat{s}$ holds and the deformation is length-preserving, i.e. rigid.

To measure how close the deformation is to a rigid one in both different configurations, the *Green-St. Venant strain tensor*

$$\mathbf{E}(\mathbf{u}) = \frac{1}{2}(\mathbf{C} - \mathbf{I}) = \frac{1}{2}\left(\mathbf{J}(\mathbf{u})^T + \mathbf{J}(\mathbf{u}) + \mathbf{J}(\mathbf{u})^T\mathbf{J}(\mathbf{u})\right) \tag{2.14}$$

and, respectively, the *Almansi strain tensor*

$$\hat{\mathbf{E}}(\hat{\mathbf{u}}) = \frac{1}{2}(\mathbf{I} - \hat{\mathbf{C}}) = \frac{1}{2}\left(\mathbf{J}(\hat{\mathbf{u}})^T + \mathbf{J}(\hat{\mathbf{u}}) - \mathbf{J}(\hat{\mathbf{u}})^T\mathbf{J}(\hat{\mathbf{u}})\right) \tag{2.15}$$

have been introduced [100, 21, 99]. Both definitions allow a measurement of the change in the squared length of a line element [100]. In the Lagrangian configuration, this can be written as

$$\begin{aligned} d\hat{s}^2 - ds^2 &= d\mathbf{x}^T\mathbf{C}d\mathbf{x} - d\mathbf{x}^T d\mathbf{x} \\ &= d\mathbf{x}^T(\mathbf{C} - \mathbf{I})d\mathbf{x} \\ &= 2d\mathbf{x}^T\mathbf{E}d\mathbf{x}, \end{aligned} \tag{2.16}$$

whereas the formulation in the Eulerian configuration reads

$$\begin{aligned} d\hat{s}^2 - ds^2 &= d\hat{\mathbf{x}}^T d\hat{\mathbf{x}} - d\hat{\mathbf{x}}^T\hat{\mathbf{C}}d\hat{\mathbf{x}} \\ &= d\hat{\mathbf{x}}^T(\mathbf{I} - \hat{\mathbf{C}})d\hat{\mathbf{x}} \\ &= 2d\hat{\mathbf{x}}^T\hat{\mathbf{E}}d\hat{\mathbf{x}}. \end{aligned} \tag{2.17}$$

Rate-of-deformation

The *rate-of-deformation* of Ω can be analyzed in a similar way. Given an infinitesimal line segment $d\hat{\mathbf{x}} \in \hat{\bar{\Omega}}$, the difference of the velocities at the endpoints of $d\hat{\mathbf{x}}$ with respect to time t can be calculated through a Taylor series expansion [100, 47], giving

$$d\hat{\mathbf{v}} = \mathbf{J}(\hat{\mathbf{v}})d\hat{\mathbf{x}}. \tag{2.18}$$

Using only the symmetric part of $\mathbf{J}(\hat{\mathbf{v}})$, the symmetric *rate-of-deformation tensor* $\hat{\mathbf{D}}$ with

$$\hat{\mathbf{D}}(\hat{\mathbf{v}}) = \frac{1}{2}\left(\mathbf{J}(\hat{\mathbf{v}}) + \mathbf{J}(\hat{\mathbf{v}})^T\right) \tag{2.19}$$

can be introduced. This tensor allows a measurement of the rate-of-change of the squared length

$$\frac{\mathrm{d}}{\mathrm{d}t}d\hat{s}^2 = 2d\hat{\mathbf{x}}^T\hat{\mathbf{D}}d\hat{\mathbf{x}}, \tag{2.20}$$

as shown in [100]. Additionally, the skew-symmetric part of $\mathbf{J}(\hat{\mathbf{v}})$ is defined by

$$\hat{\mathbf{W}}(\hat{\mathbf{v}}) = \frac{1}{2}\left(\mathbf{J}(\hat{\mathbf{v}}) - \mathbf{J}(\hat{\mathbf{v}})^T\right), \tag{2.21}$$

which is called *spin tensor*.

Stress

In the deformed configuration $\hat{\bar{\Omega}}(t) = \boldsymbol{\varphi}(\bar{\Omega}, t)$, the body is subjected to externally applied forces which can be classified into *body forces* and *surface forces* [100, 21]. Applied body forces act on the interior of the body and are defined as a vector field

$$\hat{\mathbf{f}} : \hat{\Omega} \longrightarrow \mathbb{R}^3, \tag{2.22}$$

called *density of the applied body forces* per unit volume in the Eulerian configuration. Similarly, applied surface forces acting on a subset $\hat{\Gamma}_1 \subseteq \hat{\Gamma}$ of the boundary are defined by

$$\hat{\mathbf{g}} : \hat{\Gamma}_1 \longrightarrow \mathbb{R}^3, \tag{2.23}$$

called *density of the applied surface forces* per unit area in the Eulerian configuration. Examples of these types of forces are the gravity force as body force and contact forces acting on the boundary $\hat{\Gamma}_1$ as surface forces [21].

Aligned with the applied forces is a vector field $\hat{\mathbf{t}} : \hat{\bar{\Omega}} \times N \longrightarrow \mathbb{R}^3$, where $N = \{\mathbf{n} \in \mathbb{R}^3; |\mathbf{n}| = 1\}$, such that for any region $\hat{\Delta} \subset \hat{\bar{\Omega}}$ and for every point $\hat{\mathbf{x}} \in \hat{\Gamma}_1 \cap \partial\hat{\Delta}$ at which the outward unit vector $\hat{\mathbf{n}}$ exists,

$$\hat{\mathbf{t}}(\hat{\mathbf{x}}, \hat{\mathbf{n}}) = \hat{\mathbf{g}}(\hat{\mathbf{x}}) \tag{2.24}$$

holds. The vector $\hat{\mathbf{t}}(\hat{\mathbf{x}}, \hat{\mathbf{n}})$ is called *Cauchy stress vector* and represents the density of the surface force per unit area [100, 21, 47].

For an arbitrary plane through the body, the Cauchy stress vector $\hat{\mathbf{t}}$ is completely determined by three stress vectors $\hat{\mathbf{t}}_i$ each being coplanar with the planes perpendicular to the coordinate axes. Formally, we have

$$\hat{\mathbf{t}}(\hat{\mathbf{x}}, \hat{\mathbf{n}}) = \hat{\mathbf{T}}(\hat{\mathbf{x}})\hat{\mathbf{n}}, \tag{2.25}$$

also known as *Cauchy's formula.* The symmetric tensor $\hat{\mathbf{T}} : \hat{\bar{\Omega}} \longrightarrow \mathbb{R}^{3\times 3}$ is called *Cauchy stress tensor* and the elements of the ith row of $\hat{\mathbf{T}}$ contain the components of the Cauchy stress vector $\hat{\mathbf{t}}_i$.

With the aid of the *Piola transform* [21], the Cauchy stress tensor $\hat{\mathbf{T}}$ can be transformed into the Lagrangian configuration. The resulting non-symmetric tensor $\mathbf{T} : \bar{\Omega} \longrightarrow \mathbb{R}^{3\times 3}$

$$\mathbf{T}(\mathbf{x}) = (\det \mathbf{J}(\boldsymbol{\varphi}))\hat{\mathbf{T}}(\hat{\mathbf{x}})\mathbf{J}(\boldsymbol{\varphi})^{-T} \tag{2.26}$$

is called *first Piola-Kirchhoff stress tensor.* However, it is desirable to define a symmetric stress tensor in the Lagrangian configuration, essentially due to the important relation between the stress and symmetric strain tensors, see below in Section 2.2.3. Therefore, the symmetric *second Piola-Kirchhoff stress tensor* $\boldsymbol{\Sigma} : \bar{\Omega} \longrightarrow \mathbb{R}^{3\times 3}$

$$\boldsymbol{\Sigma}(\mathbf{x}) = \mathbf{J}(\boldsymbol{\varphi})^{-1}\mathbf{T}(\mathbf{x}) \tag{2.27}$$

is usually preferred.

2.2.2 The equations of motion and equilibrium

The deformation of a body Ω, subjected to applied body and surface forces $\hat{\mathbf{f}}$ and $\hat{\mathbf{g}}$, respectively, is governed by the *equation of motion.* This equation is based on Newton's second law of motion as well as on the conservation law of momentum and reads [44, 100]

$$\operatorname{div}[\hat{\mathbf{T}}] + \hat{\mathbf{f}} = \hat{\rho}\frac{d\hat{\mathbf{v}}}{dt} \quad \text{in } \hat{\Omega}, \tag{2.28}$$

where $\hat{\rho}$ denotes the density of $\hat{\Omega}$, i.e. the mass per volume of the body [44]. Note, that (2.28) is valid $\forall \hat{\mathbf{x}} \in \hat{\Omega}$ [21]. In the special case without acceleration, i.e. where $d\hat{\mathbf{v}}/dt = \mathbf{0}$ holds, the equation of motion reduces to the *equilibrium equation*

$$\operatorname{div}[\hat{\mathbf{T}}] + \hat{\mathbf{f}} = \mathbf{0} \quad \text{in } \hat{\Omega}, \tag{2.29}$$

which describes for a body the state of static equilibrium between internal and external forces.

Related to both partial differential equations are different types of *boundary conditions* such as to impose constraints on the spatial positions a body Ω can occupy in space [21]. Common types of boundary conditions are *Dirichlet boundary conditions*, where the value of the unknown variable is prescribed on a portion $\hat{\Gamma}_1 \subseteq \hat{\Gamma}$, *Neumann boundary conditions*, where the derivative $\partial/\partial\hat{\mathbf{n}}$ of the variable is prescribed on $\hat{\Gamma}_2 \subseteq \hat{\Gamma}$, or *Robbins boundary conditions*, where a combination of Dirichlet and Neumann boundary conditions is given on $\hat{\Gamma}_3 \subseteq \hat{\Gamma}$ [25]. Note, that for every $\hat{\mathbf{x}} \in \hat{\Gamma}$, a boundary condition must be specified and $\hat{\Gamma}_i \cap \hat{\Gamma}_j = \emptyset$ for $i \neq j$ must hold [141]. Normally, the equilibrium equation in the Eulerian configuration is combined with Cauchy's formula (2.25) as Neumann boundary condition,

$$\begin{cases} -\operatorname{div}[\hat{\mathbf{T}}] = \hat{\mathbf{f}} & \text{in } \hat{\Omega}, \\ \hat{\mathbf{T}}\hat{\mathbf{n}} = \hat{\mathbf{g}} & \text{on } \hat{\Gamma}, \end{cases} \tag{2.30}$$

where $\hat{\mathbf{T}}$ denotes Cauchy's stress vector and $\hat{\mathbf{n}}$ is the outward unit vector normal to $\hat{\Gamma}$.

A problem associated with (2.30) is its formulation in the Eulerian configuration, where $\hat{\mathbf{x}}$ is unknown. With the aid of the Piola transformation (see [21]), the problem can be rewritten in the Lagrangian configuration,

$$\begin{cases} -\operatorname{div}[\mathbf{T}] = \mathbf{f} & \text{in } \Omega, \\ \mathbf{T}\mathbf{n} = \mathbf{g} & \text{on } \Gamma, \end{cases} \tag{2.31}$$

where $\mathbf{T}$ is the first Piola-Kirchhoff stress tensor as defined in (2.26). Due to the properties of $\mathbf{T}$, being a non-symmetric tensor, the equilibrium equations are commonly formulated in terms of the second Piola-Kirchhoff stress tensor $\mathbf{\Sigma} = \mathbf{J}(\varphi)^{-1}\mathbf{T}$, yielding

$$\begin{cases} -\operatorname{div}[\mathbf{J}(\varphi)\mathbf{\Sigma}] = \mathbf{f} & \text{in } \Omega, \\ \mathbf{J}(\varphi)\mathbf{\Sigma}\,\mathbf{n} = \mathbf{g} & \text{on } \Gamma. \end{cases} \tag{2.32}$$

2.2.3 The constitutive equations

So far, the equilibrium equations in (2.29) do not take the nature of the underlying material into account. To incorporate specific material properties of Ω, appropriate *constitutive equations* have to be substituted into the equilibrium equations. Constitutive equations are specific expressions of the *response function*, which allows a representation of the stress tensor as a function of the deformation tensor [100].

For the sake of simplicity in this introduction, only *isotropic* and *homogeneous* materials will be considered here. A material is called isotropic, if no preferred direction in the material exists for a given point $\mathbf{x} \in \bar{\Omega}$, and it is called homogeneous, if the response function is independent of $\mathbf{x} \in \bar{\Omega}$ [77, 21]. Due to the variety of existing materials, many different constitutive equations exist. But, as pointed out in Section 2.1 above, an approximation of most materials by constitutive equations for either elastic solids or incompressible fluids is usually sufficient.

In case of elastic solids, the second Piola-Kirchhoff stress tensor (2.27) depends only on the Green-St. Venant strain tensor (2.14). If this relationship is linear, the response function of a *St. Venant-Kirchhoff* material is obtained [100, 47]:

$$\mathbf{\Sigma} = \lambda(\operatorname{tr}\mathbf{E})\mathbf{I} + 2\mu\mathbf{E}. \tag{2.33}$$

Equation (2.33) is commonly known as *Hooke's law.* The components of the second Piola-Kirchhoff stress tensor are determined as

$$\Sigma_{ij} = \left[\lambda\, \delta_{ij}\delta_{kl} + \mu\,(\delta_{ik}\delta_{jl} + \delta_{il}\delta_{jk})\right] E_{kl}, \tag{2.34}$$

where λ and μ denote the *Lamé constants*, $(\operatorname{tr}\,\cdot)$ is the trace operator, and δ_{ab} refers to the Kronecker delta symbol. For real materials, the Lamé constants take only positive values. With Hooke's law, the equilibrium equations (2.32) can be re-written in terms of the unknown displacement field $\mathbf{u}$, yielding

$$\begin{cases} -\operatorname{div}\left[(\mathbf{I} + \mathbf{J}(\mathbf{u}))\,(\lambda(\operatorname{tr}\mathbf{E}(\mathbf{u}))\mathbf{I} + 2\mu\mathbf{E}(\mathbf{u}))\right] = \mathbf{f} & \text{in } \Omega, \\ (\mathbf{I} + \mathbf{J}(\mathbf{u}))\,(\lambda(\operatorname{tr}\mathbf{E}(\mathbf{u}))\mathbf{I} + 2\mu\mathbf{E}(\mathbf{u}))\,\mathbf{n} = \mathbf{g} & \text{on } \Gamma. \end{cases} \tag{2.35}$$

So far, the nonlinear differential equations (2.35) describe the mechanical equilibrium of an elastic body subjected to *finite* deformations. To circumvent the difficulties associated with nonlinear differential equations, like, e.g., the approximation errors introduced by using iterative solution schemes [72], the deformation field is usually restricted to be *infinitesimal.* As a result, the distinction between the Lagrangian configuration and the Eulerian configuration becomes obsolete [46] and the displacements $\mathbf{u}$ as well as the displacement gradients $\mathbf{J}(\mathbf{u})$ assume small values such that the squares and products of $\mathbf{J}(\mathbf{u})$ are negligible compared to the first order terms [44, 100, 46]. Therefore, the quadratic components $\mathbf{J}(\mathbf{u})^T\mathbf{J}(\mathbf{u})$ of the Green-St. Venant strain tensor $\mathbf{E}$ (2.14) and $\mathbf{J}(\hat{\mathbf{u}})^T\mathbf{J}(\hat{\mathbf{u}})$ of the Almansi strain tensor $\hat{\mathbf{E}}$ (2.15) can be dropped. As a result, both tensors reduce to *Cauchy's infinitesimal strain tensor*

$$\boldsymbol{\epsilon}(\mathbf{u}) = \frac{1}{2}\left(\mathbf{J}(\mathbf{u})^T + \mathbf{J}(\mathbf{u})\right). \tag{2.36}$$

Also, the distinction between the Cauchy stress tensor $\hat{\mathbf{T}}$ and the first and second Piola-Kirchhoff stress tensors $\mathbf{T}$ and $\boldsymbol{\Sigma}$ vanishes, leading to the *Eulerian stress tensor* $\boldsymbol{\sigma}$ [44, 45].

In case of infinitesimal displacements, Hooke's law (2.33) reads

$$\boldsymbol{\sigma} = \lambda(\operatorname{tr}\boldsymbol{\epsilon})\mathbf{I} + 2\mu\boldsymbol{\epsilon} \tag{2.37}$$

instead and, consequently, the equilibrium equations can be written as

$$\begin{cases} -\operatorname{div}\left[\lambda(\operatorname{tr}\boldsymbol{\epsilon}(\mathbf{u}))\mathbf{I} + 2\mu\boldsymbol{\epsilon}(\mathbf{u})\right] = \mathbf{f} & \text{in } \Omega, \\ \left(\lambda(\operatorname{tr}\boldsymbol{\epsilon}(\mathbf{u}))\mathbf{I} + 2\mu\boldsymbol{\epsilon}(\mathbf{u})\right)\,\mathbf{n} = \mathbf{g} & \text{on } \Gamma. \end{cases} \tag{2.38}$$

Mathematically, this rather intuitive *linearization* can be obtained by writing (2.35) in terms of a nonlinear operator $\mathbf{A}(\mathbf{u})$ and by computing the derivative at $\mathbf{u} = \mathbf{0}$. Thus, the nonlinear operator $\mathbf{A}(\mathbf{u})$ is approximated through a Taylor series expansion,

$$\mathbf{A}(\mathbf{u}) = \mathbf{A}'(\mathbf{0})\mathbf{u} + \mathcal{O}(\mathbf{u}), \tag{2.39}$$

truncating the higher order terms $\mathcal{O}(\mathbf{u})$. The term $\mathbf{A}'(\mathbf{0})\mathbf{u}$ is then given as [21]

$$\mathbf{A}'(\mathbf{0})\mathbf{u} = -\operatorname{div}\left[\lambda(\operatorname{tr}\boldsymbol{\epsilon}(\mathbf{u}))\mathbf{I} + 2\mu\boldsymbol{\epsilon}(\mathbf{u})\right]. \tag{2.40}$$

In contrast to elastic solids, all fluids, being compressible or incompressible, neither sustain a shear stress at rest nor uniform flow and hence, the stress is a purely static pressure in this case [100]. This property allows fluids to fill out arbitrarily formed reservoirs [151]. Furthermore, fluids are divided into *non-viscous fluids* and *viscous fluids*. A non-viscous fluid, representing an idealized fluid [47], cannot sustain a shear stress even in motion, such that the constitutive equation simply reads [100, 47]

$$\hat{\mathbf{T}} = -\hat{p}\mathbf{I}. \tag{2.41}$$

For a viscous fluid instead, describing the behavior of real fluids like cerebrospinal fluid [47], the shear stress is a function of the rate-of-deformation tensor, as given by the *Navier-Poisson law* [100, 47]

$$\hat{\mathbf{T}} = -\hat{p}\mathbf{I} + \lambda^\star(\operatorname{tr}\hat{\mathbf{D}})\mathbf{I} + 2\mu^\star\hat{\mathbf{D}} \tag{2.42}$$

with coefficients

$$\hat{T}_{ij} = -\hat{p}\delta_{ij} + \left[\lambda^\star\delta_{ij}\delta_{kl} + \mu^\star(\delta_{ik}\delta_{jl} + \delta_{il}\delta_{jk})\right]\hat{D}_{kl}. \tag{2.43}$$

Here, $\hat{p}(\hat{\mathbf{x}})$ denotes the static pressure function whereas $\lambda^\star$ and $\mu^\star$ are the *viscosity parameters*. Note that, despite of the related notation, the viscosity parameters $\lambda^\star$ and $\mu^\star$ are *not* identical with the Lamé constants in Hooke's law in (2.33). Again, the term $-\hat{p}\mathbf{I}$ in (2.42) represents the static pressure if the fluid is at rest or, respectively, in uniform flow where $\hat{\mathbf{D}} = \mathbf{0}$ holds [47].

Substitution of the Navier-Poisson law into the equilibrium equations leads to an expression in terms of the unknown pressure function $\hat{p}$ and the unknown velocity field $\hat{\mathbf{v}}$,

$$\begin{cases} -\operatorname{div}[-\hat{p}\mathbf{I} + \lambda^\star(\operatorname{tr}\hat{\mathbf{D}}(\hat{\mathbf{v}}))\mathbf{I} + 2\mu^\star\hat{\mathbf{D}}(\hat{\mathbf{v}})] = \hat{\mathbf{f}} & \text{in } \hat{\Omega}, \\ (-\hat{p}\mathbf{I} + \lambda^\star(\operatorname{tr}\hat{\mathbf{D}}(\hat{\mathbf{v}}))\mathbf{I} + 2\mu^\star\hat{\mathbf{D}}(\hat{\mathbf{v}}))\hat{\mathbf{n}} = \hat{\mathbf{g}} & \text{on } \hat{\Gamma}. \end{cases} \tag{2.44}$$

To determine the associated displacement field $\hat{\mathbf{u}}$, the material derivative in (2.8) has to be used [15]. Again, this can be simplified if the displacement field is restricted to be infinitesimal. Thus, the displacement $\mathbf{u}$ can be approximated by multiplication of the velocity $\mathbf{v}$ with an infinitesimal time interval dt, i.e.

$$\mathbf{u} = \mathbf{v}dt \tag{2.45}$$

(see [47] for further details).

2.2.4 The Navier equation

Splitting the first part of the equilibrium equations for infinitesimal deformations (2.38) by means of the law $\operatorname{div}[\mathbf{A}+\mathbf{B}] = \operatorname{div}[\mathbf{A}] + \operatorname{div}[\mathbf{B}]$ into parts along with the use of the definition of the divergence of a tensor field $\mathbf{A}$, $\operatorname{div}[\mathbf{A}] := (\nabla^T\mathbf{A})^T$ [21, 9], yields the identities

$$\begin{aligned} \operatorname{div}[\lambda(\operatorname{tr}\mathbf{e}(\mathbf{u}))\mathbf{I}] &= \lambda(\partial_i^2 u_i + \partial_i\partial_j u_j) &&= \lambda\nabla\operatorname{div}[\mathbf{u}] \\ \operatorname{div}[2\mu\mathbf{e}(\mathbf{u})] &= \mu(2\partial_i^2 u_i + \partial_i\partial_j u_j + \partial_j^2 u_i) &&= \mu\nabla\operatorname{div}[\mathbf{u}] + \mu\nabla^2\mathbf{u}. \end{aligned} \tag{2.46}$$

By substituting (2.46) into the equilibrium equations, we get the well-known *Navier equation* [100]

$$(\lambda + \mu)\nabla \mathrm{div}[\mathbf{u}] + \mu \nabla^2 \mathbf{u} + \mathbf{f} = \mathbf{0} \quad \text{in } \Omega \tag{2.47}$$

as formal expression for the static equilibrium of a linear elastic solid.

Note, that a solution of (2.47) with given boundary conditions may not preserve the topology in case of *large* deformations due to the usage of Cauchy's infinitesimal strain tensor.

2.2.5 The Stokes equation

A formulation similar to the Navier equation can be derived for viscous fluids also. Again, the law $\mathrm{div}\,[\mathbf{A} + \mathbf{B}] = \mathrm{div}\,[\mathbf{A}] + \mathrm{div}\,[\mathbf{B}]$ can be used to split the first part of (2.44) into parts thus leading to the identities

$$\begin{aligned}
\mathrm{div}[-\hat{p}\mathbf{I}] &= & -\partial_i \hat{p} \qquad & = -\nabla \hat{p} \\
\mathrm{div}[\lambda^\star(\mathrm{tr}\,\hat{\mathbf{D}}(\hat{\mathbf{v}}))\mathbf{I}] &= & \lambda^\star(\partial_i^2 \hat{v}_i + \partial_i \partial_j \hat{v}_j) \qquad & = \lambda^\star \nabla \mathrm{div}[\hat{\mathbf{v}}] \\
\mathrm{div}[2\mu^\star \hat{\mathbf{D}}(\hat{\mathbf{v}})] &= & \mu^\star(2\partial_i^2 \hat{v}_i + \partial_i \partial_j \hat{v}_j + \partial_j^2 \hat{v}_i) & = \mu^\star \nabla \mathrm{div}[\hat{\mathbf{v}}] + \mu^\star \nabla^2 \hat{\mathbf{v}}.
\end{aligned} \tag{2.48}$$

A substitution of (2.48) into the equilibrium equations leads to the *Navier-Stokes equation*

$$-\nabla \hat{p} + (\lambda^\star + \mu^\star)\nabla \mathrm{div}\,[\hat{\mathbf{v}}] + \mu^\star \nabla^2 \hat{\mathbf{v}} + \hat{\mathbf{f}} = \mathbf{0} \quad \text{in } \hat{\Omega} \tag{2.49}$$

as formal physical expression for *compressible*, viscous fluids, here formulated for the case of the static equilibrium.

To take the incompressibility of cerebrospinal fluid into account [78, 135, 146], the Navier-Stokes equation has to be further modified. For *incompressible fluids*, the density $\hat{\rho}$ remains constant over $\hat{\Omega}$, resulting in

$$\mathrm{div}[\hat{\mathbf{v}}] = 0 \quad \text{in } \hat{\Omega} \tag{2.50}$$

as consequence of inserting $\hat{\rho} = \mathrm{const}$ into the *continuity equation*

$$\mathrm{div}[\hat{\mathbf{v}}] = -\frac{1}{\hat{\rho}}\frac{d\hat{\rho}}{dt} \quad \text{in } \hat{\Omega}, \tag{2.51}$$

the latter representing an alternative formulation to the law of the conservation of mass [100, 47], since a constant density $\hat{\rho}$ implies

$$\frac{d\hat{\rho}}{dt} = 0. \tag{2.52}$$

Now, the *Stokes equation*

$$-\nabla \hat{p} + \mu^\star \nabla^2 \hat{\mathbf{v}} + \hat{\mathbf{f}} = \mathbf{0} \quad \text{in } \hat{\Omega} \tag{2.53}$$

follows, which serves as formal notation for the static equilibrium of an incompressible, viscous fluid. Note, that the viscosity parameter $\lambda^\star$ does not appear in the Stokes equation due to (2.50).

2.3 The finite element method

Above, the necessary theoretical background for a physical model of biological tissues and fluids has been derived. In order to determine the deformation of a body Ω as a result of applied body and surface forces, the corresponding partial differential equations in conjunction with appropriate boundary conditions have to be solved for the unknown functions. Besides some specific classical problems for which analytical solutions exist [100], numerical methods must be applied in general. In our case, we use the *finite element method* (FEM) as numerical method to derive a linear matrix system which can be solved with common techniques from linear algebra, e.g., *Krylov subspace methods* or *splitting methods* [141, 7].

The finite element method divides a body Ω into a set of disjunct areas, called finite elements, and approximates the unknown function in a piecewise fashion by low order polynomials [72], i.e. the solution is approximated as a sum over low order polynomials multiplied with coefficients from a set of sampling points. In other words, the continuous problem is discretized using a set of finite elements, each equipped with a finite number of sampling points. Mathematically, the finite element method defines a bijective function L between the solution space of the problem and its corresponding dual space. Now, the solution $\mathbf{u}$ is simply determined by applying the inverse function L^{-1} to the dual space.

For the FEM derivation of a continuous problem, we start with an application of the *method of weighted residuals* due to the generality of this approach, i.e. its applicability to partial differential equations is admissible irrespectively of an existing equivalent extremal formulation [25]. With the method of weighted residuals, we require that the projection of the residuum (which results if an arbitrary function is substituted into a given partial differential equation) on the basis functions (which span the underlying solution space) vanishes over the body Ω in some average sense [72]. Thereafter, a matrix system can be derived by applying the *Galerkin method* which consists of approximating the solution space by a finite dimensional space only.

2.3.1 The method of weighted residuals

The mathematical framework described in the following is mainly presented on the basis of [25, 72, 12, 7]. Let a partial differential equation with mixed boundary conditions be given,

$$\begin{cases} \mathbf{A}(\mathbf{u}) = \mathbf{f} & \text{in } \Omega, \\ \mathbf{u} = \mathbf{g}_1 & \text{on } \Gamma_1, \\ \mathbf{J}(\mathbf{u})\, \mathbf{n}_2 = \mathbf{g}_2 & \text{on } \Gamma_2, \\ \mathbf{J}(\mathbf{u})\, \mathbf{n}_3 + \mathbf{u} = \mathbf{g}_3 & \text{on } \Gamma_3, \end{cases} \tag{2.54}$$

where $\mathbf{A}$ denotes a linear differential operator, $\mathbf{J}(\mathbf{u})$ is the Jacobian of the function $\mathbf{u}$, and $\mathbf{n}_i$ is the unit outward vector of Γ_i. Note, that $\Gamma_i \cap \Gamma_j = \emptyset$ for $i \neq j$ and $\Gamma_1 \cup \Gamma_2 \cup \Gamma_3 = \Gamma$ holds for the definition of the boundary conditions.

In order to solve problem (2.54), a normed vector space

$$V_{\mathbf{g}_1}(\Omega) = \{\mathbf{w} : \Omega \longrightarrow \mathbb{R}; \mathbf{w} = \mathbf{g}_1 \text{ on } \Gamma_1\}, \tag{2.55}$$

spanned by a countable basis

$$\operatorname{span}(\boldsymbol{\phi}_1, \boldsymbol{\phi}_2, \ldots) = V_{\mathbf{g}_1}(\Omega), \tag{2.56}$$

is introduced. Mathematically, $V_{\mathbf{g}_1}(\Omega)$ represents a subspace of the *Sobolev space*

$$H^m_{\mathbf{g}_1}(\Omega) = \{\mathbf{w} \in H^m(\Omega); \mathbf{w} = \mathbf{g}_1 \text{ on } \Gamma_1\} \tag{2.57}$$

of appropriate order $m \geq 0$ [25]. The Sobolev space $H^m(\Omega)$ is formally defined as the closure of $C^\infty(\Omega)$ with respect to the norm [20, 25, 7]

$$||\mathbf{w}||_{m,\Omega} = \sqrt{\sum_{|\alpha| \leq m} \int_\Omega |\partial^\alpha \mathbf{w}|^2 d\Omega}, \tag{2.58}$$

where $C^\infty(\Omega)$ denotes the space of all functions whose partial derivatives of arbitrary order exist over Ω [12]. In other words, a Sobolev space $H^m(\Omega)$ consists of those functions $\mathbf{w} \in L_2(\Omega)$, with $L_2(\Omega)$ defined as [25]

$$L_2(\Omega) = \{\mathbf{w} : \Omega \longrightarrow \mathbb{R}; \int_\Omega |\mathbf{w}|^2 d\Omega < \infty\}, \tag{2.59}$$

for which all partial derivatives $\partial^\alpha \mathbf{w}$, with $|\alpha| \leq m$, belong to the space $L_2(\Omega)$. The space $H^m(\Omega)$ is endowed with a *Hilbert structure*, i.e. the norm (2.58) and the scalar product

$$(\mathbf{u}, \mathbf{w})_{m,\Omega} = \sum_{|\alpha| \leq m} \int_\Omega \partial^\alpha \mathbf{u}\, \partial^\alpha \mathbf{w}\, d\Omega \tag{2.60}$$

exist [20, 25, 7]. To ensure the given Dirichlet boundary conditions of (2.54), they are explicitly introduced in the definition of the vector space $V_{\mathbf{g}_1}(\Omega)$, as indicated by the index $\mathbf{g}_1$ [12]. Therefore, the Dirichlet boundary conditions are also denoted as *essential boundary conditions*.

By substitution of an arbitrary function $\mathbf{v} \in V_{\mathbf{g}_1}(\Omega)$ into the partial differential equation (2.54),

$$\mathbf{A}(\mathbf{v}) - \mathbf{f} = \mathbf{r}, \tag{2.61}$$

a residual error $\mathbf{r}$ results. In order to find the solution, a function $\mathbf{u} \in V_{\mathbf{g}_1}(\Omega)$ is chosen such that the residual error is zero inside Ω [141, 25]. This can be accomplished by a projection of the residuum $\mathbf{r}$ on arbitrary weighting functions $\mathbf{w} \in V_{\mathbf{g}_1}(\Omega)$ along with the requirement that this projection must vanish, i.e.

$$\langle \mathbf{r}, \mathbf{w} \rangle = 0, \quad \forall \mathbf{w} \in V_{\mathbf{g}_1}(\Omega) \tag{2.62}$$

holds, where $\langle \cdot, \cdot \rangle$ denotes the inner product of $V_{\mathbf{g}_1}(\Omega)$. Substitution of (2.61) into this expression yields

$$\langle \mathbf{A}(\mathbf{u}) - \mathbf{f}, \mathbf{w} \rangle = 0, \quad \forall \mathbf{w} \in V_{\mathbf{g}_1}(\Omega) \tag{2.63}$$

(see, e.g., [141, 72] for details).

Note, that other solution methods can be derived, if $\mathbf{u}$ and $\mathbf{w}$ belong to different vector spaces. For example, the well known *boundary element method* (BEM) can be obtained by using the *Green's function* as weighting function $\mathbf{w}$ instead [72, 12].

2.3.2 The Galerkin method

In order to represent (2.63) as a linear matrix problem, the *Galerkin method* is applied [25, 72]. With this method, the solution space $V_{\mathbf{g}_1}(\Omega)$ is approximated by a finite dimensional space $V_{\mathbf{g}_1}^N(\Omega)$, spanned by N countable basis functions $\boldsymbol{\phi}_1, \ldots, \boldsymbol{\phi}_N$, such that the solution $\mathbf{u}$ and the weighting function $\mathbf{w}$ can be approximated as finite sums of basis functions multiplied with coefficients $\tilde{u}$ and $\tilde{w}$, respectively:

$$\tilde{\mathbf{u}} = \sum_{i=1}^{N} \tilde{u}_i \boldsymbol{\phi}_i \quad \text{and} \quad \tilde{\mathbf{w}} = \sum_{j=1}^{N} \tilde{w}_j \boldsymbol{\phi}_j. \tag{2.64}$$

Depending on the relationship between $V_{\mathbf{g}_1}^N(\Omega)$ and the solution space $V_{\mathbf{g}_1}(\Omega)$ of the problem considered, either the *conforming*, where the finite dimensional subspace $V_{\mathbf{g}_1}^N(\Omega)$ is a subset of the solution space $V_{\mathbf{g}_1}(\Omega)$ (i.e. $V_{\mathbf{g}_1}^N(\Omega) \subset$

$V_{\mathbf{g}_1}(\Omega)$ holds), or the *non-conforming finite element method*, where the finite dimensional subspace $V^N_{\mathbf{g}_1}(\Omega)$ is *not* a subset of the solution space $V_{\mathbf{g}_1}(\Omega)$ (i.e. $V^N_{\mathbf{g}_1}(\Omega) \not\subset V_{\mathbf{g}_1}(\Omega)$ holds), is derived [20, 12, 7]. With a substitution of (2.64) into (2.63), we obtain

$$\langle \sum_{i=1}^{N} \tilde{u}_i \mathbf{A}(\boldsymbol{\phi}_i) - \mathbf{f}, \sum_{j=1}^{N} \tilde{w}_j \boldsymbol{\phi}_j \rangle = 0, \tag{2.65}$$

which can be further transformed into

$$\sum_{i=1}^{N} \tilde{u}_i \langle \mathbf{A}(\boldsymbol{\phi}_i), \boldsymbol{\phi}_j \rangle = \langle \mathbf{f}, \boldsymbol{\phi}_j \rangle \quad j = 1 \dots N. \tag{2.66}$$

Equation (2.66) can be written in matrix notation as

$$\mathbf{A}\tilde{\mathbf{u}} = \mathbf{f} \tag{2.67}$$

and solved for the unknown coefficients $\tilde{u}_i$ by common numerical methods, e.g., Krylov subspace methods or splitting methods [7, 12]. In (2.67), $\mathbf{A}$ is commonly denoted as *stiffness matrix* while the righthand side vector $\mathbf{f}$ is known as *load vector* [25, 21].

The kind of basis functions and the number of unknowns has a significant influence on the accuracy of the final solution. There are many (non)linear problems for which it can be shown that $\tilde{\mathbf{u}} \longrightarrow \mathbf{u}$ holds for $N \longrightarrow \infty$ in (2.65) [72].

2.3.3 Uniqueness of the solution

An important topic related to the finite element method concerns the existence of a unique solution. To derive conditions for the uniqueness of the solution, (2.63) is written in terms of an *abstract variational problem* [20, 7]

$$a(\mathbf{u}, \mathbf{w}) = f(\mathbf{w}), \quad \forall \mathbf{w} \in V_{\mathbf{g}_1}(\Omega), \tag{2.68}$$

where $a(\cdot,\cdot) : V_{\mathbf{g}_1}(\Omega) \times V_{\mathbf{g}_1}(\Omega) \longrightarrow \mathbb{R}$ denotes a symmetric *bilinear form* and $f(\cdot) : V_{\mathbf{g}_1}(\Omega) \longrightarrow \mathbb{R}$ a *linear form*. This formulation is also known as *weak formulation* [12] and incorporates the given Neumann and Robbins boundary conditions. Associated with the abstract variational problem (2.68) is a linear function [7]

$$L : V_{\mathbf{g}_1}(\Omega) \longrightarrow V^*_{\mathbf{g}_1}(\Omega) \tag{2.69}$$

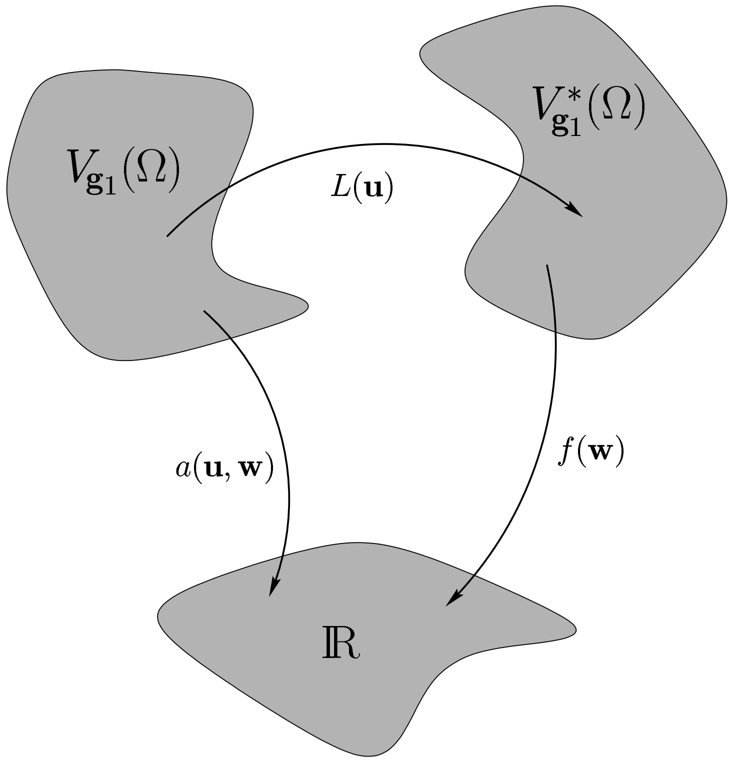

Figure 2.3: Sketch of the relationship between the finite dimensional vector space $V_{\mathbf{g}_1}(\Omega)$, its dual space $V^*_{\mathbf{g}_1}(\Omega)$, and $\mathbb{R}$. The finite element method defines an isomorphism $L(\cdot)$ between $V_{\mathbf{g}_1}(\Omega)$ and $V^*_{\mathbf{g}_1}(\Omega)$ such that the solution $\mathbf{u} \in V_{\mathbf{g}_1}(\Omega)$ is uniquely assigned to a linear function $f(\cdot)$ with the property $a(\mathbf{u}, \mathbf{w}) = f(\mathbf{w})$ for all $\mathbf{w} \in V_{\mathbf{g}_1}(\Omega)$.

through the relation

$$\langle L(\mathbf{u}), \mathbf{w} \rangle = a(\mathbf{u}, \mathbf{w}), \quad \forall \mathbf{w} \in V_{\mathbf{g}_1}(\Omega), \tag{2.70}$$

where $V^*_{\mathbf{g}_1}(\Omega)$ denotes the dual space to $V_{\mathbf{g}_1}(\Omega)$, i.e. the space of all homomorphisms over $V_{\mathbf{g}_1}(\Omega)$ [38]. Figure 2.3 shows a sketch of the relationships between the vector spaces involved.

In order to define a *well-posed problem* in the Hadamard sense [4], namely a problem where a solution exists, is unique, and depends continuously on the data, the function L must define an isomorphism, i.e. a continuous, bijective mapping [7, 38]. Then, the solution $\mathbf{u}$ is determined by $\mathbf{u} = L^{-1}(f)$, with $f \in V^*_{\mathbf{g}_1}(\Omega)$ [7]. It can be shown [20, 25], that L defines an isomorphism if the symmetric bilinear form $a(\cdot, \cdot)$ satisfies the following conditions:

- $a(\cdot,\cdot)$ is continuous, i.e. there exists an $\alpha \geq 0$ such that

$$|a(\mathbf{u},\mathbf{v})| \leq \alpha ||\mathbf{u}|| ||\mathbf{v}||, \quad \forall \mathbf{u},\mathbf{v} \in V_{\mathbf{g}_1}(\Omega) \tag{2.71}$$

  holds, where $||\cdot||$ denotes the norm over $V_{\mathbf{g}_1}(\Omega)$ and

- $a(\cdot,\cdot)$ is V-elliptic, i.e. there exists a constant $\beta > 0$ with

$$a(\mathbf{w},\mathbf{w}) \geq \beta ||\mathbf{w}||^2, \quad \forall \mathbf{w} \in V_{\mathbf{g}_1}(\Omega), \tag{2.72}$$

  or, in other words, the bilinear form $a(\cdot,\cdot)$ is positive definite [38].

For non-symmetric bilinear forms, the existence of the solution can be proven using the *Lax-Migram lemma* [20]. Thus, our biomechanical model must satisfy (2.71) and (2.72) to ensure the solvability of the approach, see Section 4.2 for details.

2.4 Summary

In this chapter, we presented the physical theory and mathematical methods necessary to develop our biomechanical model of the human head. First, we briefly summarized some important properties of biological materials, focusing on those measurable physical entities of biological structures that are necessary to model a deformation in the underlying physical framework of continuum mechanics. An introduction into this theory has been given, ending up with the Navier equation and the Stokes equation as physical models for elastic and fluid materials, respectively. Finally, we have given a short introduction into the finite element method which will be used as numerical solution method throughout this thesis.

Chapter 3

Previous work on biomechanical models

The development of biomechanical models of the human head has a relatively long tradition, as described in an early overview of biomechanical models by Khalil and Viano [82]. Already in 1943, Anzelius [2] contributed the first analytical model of a human head to investigate the response of a spherical mass to abrupt changes in velocity. In the following decades, only a few more analytical models [54, 35, 69] had been proposed in the field of car crash impact analysis. With the beginning of the seventies, however, the number of biomechanical head models developed for car crash impact analysis increased in a remarkable way. Extensive surveys on the broad spectrum of models proposed up to 1996 can be found in Sauren and Classens [136], King *et al.* [83], Voo *et al.* [155], as well as Hartmann [65]. Apart from the field of car crash impact analysis, a large number of biomechanical models have been developed in the field of medical image analysis during the last few years which are not covered by these reviews.

Owing to the existing, detailed reviews of biomechanical models for car crash impact analysis purposes [82, 136, 83, 155, 65], only a brief survey of these models will be given in the following. Instead, the main focus of our review will be on the analysis of biomechanical models used in the field of medical image analysis, which have not been completely covered by any other survey so far. For a quick comparison of all approaches, we summarize them in compact tabular form in Tables 3.1 and 3.2 at the end of this chapter.

3.1 Biomechanical models of the human head

3.1.1 Models for car crash impact analysis

Motivated by the huge amount of money annually spent for the treatment of head injuries caused by car crashes in the United States and Europe [86, 87, 168, 155, 65], a series of biomechanical models have been developed to investigate the relationship between *diffuse axonal injury*[1] (DAI) and impact-induced stress distributions throughout the human head. Beginning with a rather simplistic analytical model of a spherical human head [1] comprising the skull and the complete brain only, the finite element method (FEM) in conjunction with elasticity theory has been used soon to model the complicated geometry of the human head [163, 86, 92, 167] and thus to increase the reliability and accuracy of the calculated stress distributions. Later, different research groups investigated the influence of different types of boundary conditions[2] onto the predicted stress distributions computed for the human head [162, 90, 168, 91] to further improve the effectiveness of FEM based models in car crash impact analysis. These investigations led to the claim for an incorporation of additional anatomical structures like, e.g., the foramen magnum or the falx cerebri, due to their large influence on the response of the human head to externally applied frontal or occipital impacts. The incorporation of different anatomical structures was then commonly achieved through a spatial variation of the underlying material parameter values, namely the Lamé constants λ and μ appearing in the Navier equation (see also Section 2.2). Unfortunately, the parameter setting in terms of explicit values for the various anatomical structures had a paramount influence on the head response as shown by Ruan *et al.* [131, 132, 134, 133]. In a series of articles, these authors developed a complex FEM model of the human head to carry out a parametric study for various impact locations and different material parameter values as well to investigate the influence of choosing specific material parameter values on the resulting stress distribution.

Besides analyzing which mathematical boundary conditions and anatomical structures have to be included into a biomechanical model, other authors [30, 3, 134, 29, 90] assumed a viscoelastic material behavior instead of linear

[1] In case of angular accelerations of the human head, large shear forces occur at the central parts of the human head. These shear forces lead to small hemorrhages and disruptions of the axonal structures of the brain which are known as diffuse axonal injuries [65].

[2] The term boundary conditions comprises here the purely mathematical boundary conditions applied at the surfaces, e.g., different kinds of Dirichlet boundary conditions [90], as well as the kind of anatomical structures that were incorporated into the biomechanical model [168, 91].

elastic material properties to simulate the time-dependent material properties of brain tissue [49, 78, 137, 105, 156]. But a study carried out by Kuijpers *et al.* [90] regarding the stress distribution in case of the *coup-contrecoup phenomenon*[3], while using various versions of a FEM head model, revealed the fact that the assumption of viscoelastic brain properties did not significantly change the head's response to frontal impacts as compared to purely linear elastic material properties. Therefore, almost all biomechanical models used for car crash impact analysis still assume linear elastic material properties only.

An important feature of all these models concerns the number of finite elements used. The number of finite elements is crucial with respect to the accuracy of the computed stress distributions [72] and it can be shown, that the latter converges to the exact solution of the problem as the number of finite elements used is increased up to infinity in the ideal case. But since most biomechanical models consist of up to a few thousand finite elements only, see Table 3.1 for details, significant deviations from the exact solution must be expected [66]. Only the recent model developed by Hartmann [65] comprises a significantly larger number of finite elements such that a sufficient accuracy can be expected.

3.1.2 Models for medical image correction

About five years ago, the first biomechanical models in the field of medical image analysis have been proposed (e.g., the models of [146, 147]). Other approaches based on, e.g., mass-spring systems [13] were introduced for either surgical planning or intraoperative image correction purposes. Recent work in this field comprises a variety of models which simulate the biomechanical behavior of different anatomical structures by either spatially varying material parameter values while assuming the same physical model for all structures considered (e.g., an elastic or a fluid model) or by applying appropriate boundary conditions.

Some of these models are based on physical motivations[4] only, like the mass-spring model proposed by Bucholz *et al.* [13] which consists of an ar-

[3]The coup-contrecoup phenomenon occurs if an impact force affects the head thus causing a sprawling shock wave. This shock wave usually leads to additional serious injuries in the area opposite to the coup area [65].

[4]From a rather formal point of view, these models cannot be classified strictly as biomechanical models since they do not simulate the mechanics of biological tissues and structures [46, 47], i.e. they do not incorporate the physical properties of the human head. However, these models are enclosed in this review according to their importance for intraoperative image correction purposes.

ray of pre-compressed springs, interconnected in a grid-like fashion, and uses different spring constants to model variable material properties. Another approach proposed by Edwards *et al.* [33, 34] used a set of combined energy terms and minimized the spatial discrepancy between given landmark positions in the preoperative human head data and their current position while satisfying some prior given geometry constraints like, e.g., area preservation constraints. It has to be stressed, that all these models do not incorporate real physical material parameters and hence are only weakly related to the physical behavior of biological soft tissues [28]. In contrast to these rather *physically-motivated* models, other approaches based on a direct physical model of the biomechanical material behavior exist.

One *physically-based* approach is the brain model developed by Takizawa *et al.* [147] who investigated the distortion and stress distribution inside the head caused by putaminal hemorrhage. Although the model was mainly constructed for simulation purposes, the calculated deformation field could be used directly for image correction purposes. Using linear elasticity, the authors simulated different anatomical structures by varying the material parameter values entering the equilibrium equations describing the body. At the boundary, a so-called *homogeneous Dirichlet boundary condition* was assumed, i.e. the boundary of the simulated cerebral hemisphere was attached to the skull and therefore was assumed to be fixed to it. For the solution, the finite element method was applied.

Another approach is given through the model of Kyriacou and Davatzikos [93, 94] who used a variation of the Mooney-Rivlin strain energy function [113, 105] to simulate incompressible materials. This results in a so-called neo-Hookean material [164, 101] which can be derived from the Mooney-Rivlin strain energy function by setting the second Mooney-Rivlin parameter to zero, which is in contrast to the value that has been determined and compared against reported measurements [36], by Mendis *et al.* [105]. To solve the resulting differential equations, the finite element method is used. Instead of directly modeling different anatomical structures, the authors introduced appropriate boundary conditions, e.g., the dura mater obeys the homogeneous Dirichlet boundary condition and no movement between the dura mater and the brain at the contact surface is allowed, the latter condition is also known as *no-slip condition.*

To determine the deformation of the falx cerebri due to intracranial pressure differences, Schill *et al.* [139, 140] developed a finite element based model of this structure, using elasticity theory. The model assumed homogeneous Dirichlet boundary conditions at the skull interface and applied different values of the material parameter values in the horizontal and vertical directions to take the fiber structure of the falx cerebri into account. The resulting deformation field of the falx cerebri is then used to manipulate a complete MR data set through a free sampling process. Free sampling calculates the path a sampling beam follows in a ray-tracing process such that the deformation of the volume can be determined [139]. Different anatomical structures of the human head have been integrated in the free sampling process by using heuristic stiffness values for each region. However, while the free sampling process leads to visual appealing results, the physical validity of the calculated deformations remains questionable.

Škrinjar *et al.* [158, 157] used a set of mass nodes connected by Kelvin models to simulate the behavior of brain tissue. A Kelvin model is a simplified mechanical model of viscosity [116, 46] and consists of a parallel connection of a linear spring and a dashpot. Although it is known that external forces are difficult to determine directly from images, the deformation is driven by them, and they are calculated from the positions and velocities of the nodal points. To model different anatomical structures, again, appropriate boundary conditions have been used.

Paulsen *et al.* [117, 107] modified a previously proposed approach of Tada *et al.* [146] to deal with subsurface brain deformations. The approach is based on consolidation theory and the finite element method is used to solve the underlying differential equations. In consolidation theory, the brain is regarded as a biphasic system represented by a sponge-like elastic material and an interstitial fluid. Different material properties are introduced by spatially varying material parameter values as well as by applying appropriate boundary conditions. The deformation is driven by *inhomogeneous Dirichlet boundary conditions* only, i.e. the deformation at the brain surface is determined by a prescribed function $\mathbf{g} \neq \mathbf{0}$.

Ferrant *et al.* [37] applied the finite element method to solve the equilibrium equations of the assumed linear elastic body and used an additional image similarity term to constrain the calculated deformation. This similarity term has been derived from the image intensity values of two images and represents the forces, i.e. the external forces have been replaced by a similarity gauge of the image intensity functions. Thus, the approach is limited to images of the same modality. Different material properties are intended to be included through a spatial variation of the underlying material parameter values.

In contrast, Davatzikos [26] explicitly introduced two additional terms into the equilibrium description of the underlying linear elastic body thus describing the influence of material inhomogeneities on the state of equilibrium of a body. But the introduction of these additional terms, which have been derived by interpreting the Lamé constants as *mathematical functions* $a(\mathbf{x})$ such that $\operatorname{div}[a(\mathbf{x})\mathbf{A}] = a(\mathbf{x})\operatorname{div}[\mathbf{A}] + \mathbf{A}\nabla a(\mathbf{x})$ holds for the derivation of the Navier equation in Section 2.2.4, is mathematically motivated only, thus a physical motivation is lacking. Forces, derived from the curvatures of corresponding cortical sulci, have been used in this approach to drive the deformation of the body.

Despite the progress achieved, all these approaches generally lead to physically inadequate deformations in case of inhomogeneous materials since the fact that different anatomical structures such as soft tissues or fluids behave differently has not been taken into account. Particularly anatomical structures containing cerebrospinal fluid (CSF) cannot be simulated appropriately when simply assuming a linear elastic or viscoelastic behavior. One approach that directly simulates the physical properties of fluids on the basis of the Navier-Stokes equation has been developed by Lester *et al.* [97, 98]. Their model is motivated by the homogeneous fluid model of Christensen *et al.* [18, 16] and uses a modified version of the Navier-Stokes equation where the original pressure term has been dropped while two new terms have been added. This allows to cope with different anatomical structures through a spatial variation of the underlying viscosity parameter values. The deformation of the image is driven by weighted forces, computed from image intensity differences and image intensity gradients, such as to simulate a variable influence of different structures [98]. Additionally, homogeneous Dirichlet boundary conditions are applied to prevent the movement of so-called motionless structures. An apparent drawback of the models of Lester *et al.* as well as Christensen *et al.* is the assumption that all involved anatomical structures behave like a viscous fluid which is not the case for the human head.

3.2 Biomechanical models of other organs

Besides the numerous biomechanical models of the human head, a variety of models of other organs than the human head has been developed, mainly for surgery simulation purposes. For example, these models comprise the liver [22], muscle [14], or even different animal brains [163, 153]. Although some models are based on the finite element method [9, 14, 23, 81, 142, 164], the crucial requirement of real-time prediction of organ deformations for surgery simulation purposes in training systems still demands an effective speed-up of the original finite element algorithms. Therefore, Cotin *et al.* [24] pre-calculated the responses for each node of the finite element grid to infinitesimal forces and approximated the global deformation of their liver model as a superposition of these pre-calculated responses. Bro Nielsen [9] reduced the size of the linear equation system using a condensation technique [72, 11, 10] to convert a volume model of the lower leg into a surface model. A similar strategy was used by Kuhn *et al.* [89, 88] who applied a hierarchical mass-spring system [88] to simulate the deformation of a gall bladder. Within this hierarchical system, the movement of surface nodes is treated always relative to a previously specified internal node. Since all surface nodes are directly connected to a single internal node, this approach significantly reduces the number of internal nodes compared to common mass-spring systems.

Although mass-spring based models lead to visually appealing deformation results, see [148, 149, 80, 88] for example, the physical accuracy of deformations computed by these models remains questionable since the material is approximated by simplified mechanical models only and biomechanically relevant material parameters are not taken into consideration [80, 28]. Another physically-motivated approach has been developed by Gibson *et al.* [52, 51], where a ChainMail algorithm is used to propagate deformations through a soft tissue volume with real-time speed, but values for this real-time behavior have not been given so far. In a ChainMail algorithm, each node of the model propagates its displacements to all neighbors through variable connections, the variability of which depends on the material properties of the connected nodes. To simulate tissue elasticity for an arthroscopic knee surgery, the deformation process is followed by a distance adjustment between neighboring chain elements to minimize a not further specified local energy constraint. Although this results in a fast deformation algorithm, the physical accuracy of the predicted deformation result remains unclear [28]. Schiemann and Höhne [138] used a set of given correspondences at the surface of a kidney, to calculate a volume deformation based on the thin-plate spline interpolation scheme of Bookstein [6]. But within this scheme, it is impossible to distinguish between different materials due to the fact that biomechanically relevant tissue parameters cannot be incorporated into the thin-plate spline interpolation scheme.

In contrast to the hitherto mentioned schemes, Monserrat *et al.* [112, 111] used the boundary element method (BEM) [8] in conjunction with linear elasticity theory to develop a physically-based surface model of the liver that behaves like a volume model. The advantage of this technique is a significant reduction of the number of degrees-of-freedom as compared to the common finite element method, but problems arise with respect to the necessary accuracy of boundary approximations of organ contours, given the underlying regular image grid [53]. Additionally, the resulting stiffness matrices are dense such that efficient numerical solution techniques cannot be applied [5, 112, 53].

3.3 Tabular summary of the biomechanical models

To allow for a direct comparison of the existing biomechanical models discussed here, we give a compact summary of all human head models in Table 3.1 and of all models of other organs in Table 3.2, respectively. Besides a listing of all anatomical structures simulated by the models, we also included the underlying physical theory, the dimensionality of the model, the applied solution method, and the number of elements or nodes if provided by the authors. We use the abbreviations FEM (finite element method), CG (conjugate gradient), SOR (successive over-relaxation), RKn (nth order Runge-Kutta), IEA (implicit Eulerian approach), BEM (boundary element method), and TPS (thin-plate-splines) to characterize the solution method. For those models using a set of connected mass-nodes [13, 33, 157, 89, 84], the value given for the number of elements denotes the number of nodes instead. A hyphen in a column indicates the lack of available information, i.e. no information was given by the authors.

In the last two columns, the applications of each model is given as well as the data used for model validation. Note, that in most cases the measurements published by Nahum *et al.* [115] have been used for validation purposes. In their article, a series of human cadaver experiments were carried out to measure intracranial pressures at different locations. To this end, the human cadavers were seated and frontal impacts with rigid masses at constant velocities were investigated. The impactor masses were varied between 5.23 kg and 23.09 kg with velocities ranging from 8.41 m/s to 12.95 m/s resulting in peak input forces between 5200 N and 14840 N.

Due to these large input forces, the validation of biomechanical models developed for surgery simulation purposes on grounds of the values published in Nahum *et al.* [115] seems not appropriate. As a consequence, a validation of biomechanical models remains a crucial task [28]. However, although first steps towards a validation have been carried out by comparing the calculated deformations of a brain surface with the actual brain shift during neurosurgery [13, 107], the complete validation requires an additional measurement of stresses and applied forces on tissues as well as a comparison with those values calculated by the biomechanical model [28].

3.4 Summary

This chapter surveyed existing papers dealing with biomechanical models of the human head and other organs that are relevant for the simulation of

authors	anatomical structures considered	applied model	dimension	solution method	number of elements	simulation of	validation
Advani and Owings [1]	skull, brain	linear elasticity	2D	—	—	frontal and occipital impacts	Mc Elhaney *et al.* [103]
Hosey and Liu [71]	skull, brain, CSF, spinal cord, dura mater, jaw, falx cerebri, vertebra, cervical disks, tentorium cerebelli, region of corpus callosum third ventricle, diencephalon, superior portion of pons	linear elasticity	3D	FEM	875	frontal impacts	Nahum *et al.* [115]
Ward [162]	skull, brain, cerebrum, cerebellum, falx cerebri, tentorium cerebelli, cervival cord	linear elasticity	3D	FEM	362	impacts	cadaver and animal studies
Bandak and Eppinger [3]	skull, brain, dura mater, falx cerebri	linear elasticity, viscoelasticity	3D	FEM	—	rotational and translational accelerations	—
Chu *et al.* [19]	skull, brain	linear elasticity	2D	FEM	1261	frontal and occipital impacts	Nahum *et al.* [115]
Ruan *et al.* [133]	scalp, three layered skull, dura mater, CSF, interior sinuses, falx cerebri, tentorium cerebelli, brain, neck	linear elasticity, viscoelasticity	3D	FEM	1110	frontal, occipital and side impacts	Nahum *et al.* [115]
Tada *et al.* [146]	skull, CSF, gray matter, white matter, basal ganglia	linear consolidation	2D	FEM	822	CSF pressure and flow change in case of brain edema	pathological findings
Takizawa *et al.* [147]	cortex, white matter, caudate nucleus, lenticular nucleus, thalamus, falx cerebri, lateral ventricle	linear elasticity	2D	FEM	326	hematoma growth	Kanaya *et al.* [76]
Dimasi *et al.* [29]	skull, brain, longitudinal fissure, falx cerebri, dura mater	linear elasticity, viscoelasticity	3D	FEM	5900	A-pillar impacts	dummy crash test data

continued on next page

continued from previous page

authors	anatomical structures considered	applied model	dimension	solution method	number of elements	simulation of	validation
Kuijpers *et al.* [90]	skull, brain	linear elasticity, viscoelasticity	2D	FEM	228	frontal impacts	Nahum *et al.* [115]
Willinger *et al.* [167]	skull, CSF, cerebral hemispheres, cerebellum, cerebral trunk, membranes	linear elasticity	3D	FEM	—	impacts	modal analysis
Zhou *et al.* [168]	scalp, skull, dura mater, falx cerebri, tentorium cerebelli, pia mater, CSF, venous sinuses, ventricles, cerebrum, cerebellum, brain stem, parasagittal bridging veins	linear elasticity	3D	FEM	22995	frontal impacts	Nahum *et al.* [115]
Davatzikos [26]	brain, ventricular system	linear elasticity	3D	SOR	—	ventricular enlargement	—
Krabbel and Müller [85]	skull, brain	linear elasticity	3D	FEM	23235	frontal impacts	Kallieris *et al.* [75]
Kumaresan and Radhakrisnan [91]	skull, brain, CSF, falx cerebri, tentorium cerebelli, vertebrae C1-C7, invertebral discs, spinal cord	linear elasticity, viscoelasticity	3D	FEM	1265	occipital impacts	—
Bucholz *et al.* [13]	brain stem, components of the meninges, ventricles, choroid plexus, septum pellucidum, blood vessels, bordering areas of lesions, cortex	mass-spring model	2D	—	—	intraoperative brain shift	patient data
Christensen *et al.* [16]	brain	fluid mechanics	3D	SOR	—	—	—
Edwards *et al.* [34]	skull, CSF, brain	energy terms	2D	CG	16384	intraoperative brain shift	postoperative epilepsy data
Schill *et al.* [139]	falx cerebri	linear elasticity	3D	FEM	2543	pressure differences	—

continued on next page

continued from previous page

authors	anatomical structures considered	applied model	dimension	solution method	number of elements	simulation of	validation
Lester *et al.* [98]	scalp, brain	fluid mechanics	3D	SOR	—	image registration	—
Hartmann [65]	scalp, skull, white matter, gray matter, ventricular system, falx cerebri, tentorium cerebelli	linear elasticity	3D	FEM	140 000	frontal impacts, modal analysis	Nahum *et al.* [115]
Kyriacou *et al.* [94]	dura mater, falx cerebri, tentorium cerebelli, brain, tumor, ventricular system	neo-Hookean material	2D	FEM	—	simulation of tumor growth	—
Paulsen *et al.* [117]	brain	consolidation theory	3D	FEM	63411	brain swelling, brain shift [107]	patient data [107]
Škrinjar *et al.* [157]	brain, skull	mass nodes connected by Kelvin models	3D	RK4	2088	intraoperative brain shift	intraoperative brain surface data
Ferrant *et al.* [37]	brain	linear elasticity	3D	FEM	—	enlargement of the ventricular system	—

Table 3.1: Summary of the existing biomechanical models of the human head. Note, that the sequence of the models is given with respect to the time of their development. For all abbreviations used in this table as well as for further explanations, see text.

authors	anatomical structures considered	applied model	dimensions	solution method	number of elements	simulation of	validation
Chen and Zeltzer [14]	muscle	viscoelasticity	3D	FEM	4	gastrocnemius and biceps contraction	measured shape data
Terzopoulos and Waters [149]	cutaneous tissue, subcutaneous tissue, dermis, fascia, muscles	mass-spring model	3D	RK2	—	facial expressions	—
Kuhn [88]	gall bladder	mass-spring model	3D	IEA	443	surgical intervention	—
Bro-Nielsen [9]	lower leg	linear elasticity	3D	FEM	—	leg surface deformation	—
Cotin *el al.* [23]	liver	linear elasticity	3D	FEM	3902	hepatic surgery	—
Keeve *el al.* [81]	facial tissue	linear elasticity	3D	FEM	2583	craniofacial surgery	postoperative craniofacial data
Koch *el al.* [84]	facial surface	mass-spring model	3D	FEM	3100	craniofacial surgery	—
Smit [142]	vertebrae L3, L4 and L5, discs, spinal ligaments, facet joints, annulus	linear elasticity	3D	FEM	5696	basic lumbarspine loads	values found in literature (no further specification)
Weiss *el al.* [164]	knee	neo-Hookean material	3D	FEM	—	knee flexion	—
Monserrat *el al.* [112]	liver	linear elasticity	3D	BEM	—	endoscopic surgery	—
Schiemann and Höhne [138]	kidney	linear elasticity	3D	TPS	—	kidney surgery	—
Gibson *el al.* [51]	femur, tibia, fibula, patella, cartilage, lateral and medial menisci, anterior and posterior cruciate liagments	ChainMail	3D	—	125000	arthroscopic knee surgery	—

Table 3.2: Summary of the existing biomechanical models of other human organs. Note, that the sequence of the models is given with respect to the time of their development. For all abbreviations used in this table as well as for further explanations, see text.

tissue deformations. It turned out, that the existing models can be roughly classified in three groups depending on the motivation of their development: Models for car crash impact analysis, models for surgery simulation, and models for intraoperative image correction purposes.

Despite the anatomical complexity of biomechanical models developed for car crash impact analysis as compared to models belonging to the second and third groups, their application to image correction purposes remains problematic for reasons of unrealistic model assumptions. All models developed for car crash impact analysis investigate the *stress distribution* resulting from large impact forces (about 6000 N), but none determines the associated *deformations* which is the main aim of intraoperative image correction.

So far, all biomechanical models simulate different anatomical structures by using either appropriate boundary conditions, e.g., homogeneous Dirichlet boundary conditions to model rigid structures, or by spatially varying material parameter values, while assuming the same physical model for all anatomical structures (e.g., an elastic or a fluid model). In general, this leads to physically implausible results, especially in the case of adjacent elastic and fluid structures whose deformation behaviors differ significantly [59]. To increase the accuracy of the calculated deformation results, different physical models have to be included into a biomechanical model.

In conjunction with the large number of existing biomechanical models, the assumed material parameter values for the Lamé constants suffer from a great variability of up to two orders in magnitude. Consequently, the choice of the material parameter values remains crucial for the resulting deformation accuracy, see Section 4.6 below for further details. Additionally, since the determination of reliable external forces from given image data, as necessary for image correction purposes, remains difficult, a *landmark-based scheme* has advantages here. Within a landmark-based scheme, the correspondences between point, line, or surface landmarks are used as prescribed displacements to drive the deformation of the biomechanical model. The applied landmarks may be appropriate anatomical points [126, 127] or also fiducial markers.

Chapter 4

A new biomechanical model of the human head

In the previous chapters, we described the physical and mathematical background necessary for the deerivation of our new biomechanical model of the human head for the purpose of intraoperative image correction. From our literature study it follows, that different physical models should be included into the biomechanical model to further increase the accuracy of intraoperative image correction and finally of image-guided neuronavigation systems. This chapter deals with the derivation of a biomechanical model of the human head, allowing a coupling of elastic and fluid models.

As pointed out in Chapter 2, continuum mechanics serves as physical theory for our biomechanical model thus allowing for a physically-based simulation of organ deformations due to applied external forces. The accuracy of the predicted deformation depends mainly on the constitutive equations chosen to simulate the biomechanical behavior of the material. If the applied constitutive equations represent only a poor approximation of the load-deformation curves measured for these materials, then the calculated deformations will be physically inadequate [60, 63]. Therefore, it is necessary to determine appropriate constitutive equations for each material to be incorporated into the biomechanical model, as will be described in the following Section 4.1.

A substitution of these constitutive equations into the equilibrium equations leads to a set of differential equations, namely the Navier equation and the Stokes equation, each describing the state of equilibrium of a homogeneous body consisting of the specified material. For the numerical solution of these differential equations, we apply the finite element method (FEM). The complete FEM derivation for different materials is given in Section 4.2, followed by a construction scheme for the basis functions spanning the underlying solution space $V^N(\Omega)$ in Section 4.3.

In the first three sections of this chapter, only physical bodies consisting of homogeneous materials will be considered. To incorporate different anatomical structures, we divide the inhomogeneous body into a set of disjunct regions each describing a homogeneous material only. This division leads to a set of linear matrix systems that can be merged into a single linear matrix system by applying appropriate boundary conditions, as presented in Section 4.4. Instead of using forces, which are generally difficult to be determined from corresponding images, we use a set of given (landmark) correspondences in the sense of a sparse displacement vector field to drive the deformation of our model. As shown in Section 4.5, these correspondences can be easily integrated into the linear matrix system and the resulting deformation always satisfies these correspondences. Thus, our approach can also be considered as a landmark-based registration scheme [6, 130, 128, 129, 41]. Finally, Section 4.6 deals with the necessary determination of reliable values for the material parameters entering our biomechanical model, namely the Lamé constants and the viscosity parameter.

4.1 Material descriptions

Although the human head is composed of numerous different anatomical structures, we restrict our biomechanical model to skull bone, brain tissue, and cerebrospinal fluid only, since these are the most relevant structures in the human head for our purpose of image correction. Another argument in favor of this restriction is the lack of known mechanical properties for most biological tissues due to the difficulties associated with the measurement of tissue properties of living specimen [46]. Additionally, problems arise with the necessary segmentation of other anatomical structures than skull bone, brain tissue, and ventricular system in the preoperative image, see also Chapter 5 below.

In order to describe the biomechanical behavior of different anatomical structures, various investigations have been carried out, see for example [36, 106, 160, 137, 161]. Especially in the case of brain tissue, these investigations led to different descriptions of its mechanical properties, such that the validity of constitutive equations used in previously developed biomechanical models remains unclear (see Chapter 3 for a detailed description). So far, the choice of a specific constitutive equation, especially in conjunction with the reported properties of the material considered has not been critically discussed. In the following, we will discuss and compare therefore the reported tissue characterizations in terms of appropriate constitutive equations, ending up with an explicit choice of these equations for skull bone, brain tissue, and cerebrospinal fluid.

4.1.1 Skull bone

Skull bone is a rather rigid material which is brittle and cracks at low strain rates. The stress-strain relationship is similar to many engineering materials like steel or aluminum [46], i.e. the stress-strain relationship is a rather linear one thus suggesting that Hooke's law (2.33) is applicable [154, 46]. Since the range of strain is very small, it suffices to use Cauchy's infinitesimal strain tensor (2.36) here which allows a description of the physical behavior of skull bone through the Navier equation (2.47) [46].

4.1.2 Cerebrospinal fluid

The Cerebrospinal fluid (CSF), which is contained in the ventricular system and the subarachnoidal space, i.e. the space between brain tissue and the dura mater, can be considered as an incompressible fluid [135, 146]. Due to its biomechanical similarity to blood plasma [109, 108], it seems reasonable to assume equivalent physical properties for the cerebrospinal fluid. In [46] and [48], the mechanical properties of blood have been investigated. It was shown there, that blood can be considered as a viscous fluid and thus the Navier-Poisson law (2.42) serves as a sufficient approximation. Thus, the biomechanical properties of the cerebrospinal fluid can be simulated using the Stokes equation (2.53) which takes into account the incompressibility characteristic.

4.1.3 Brain tissue

Like most other soft tissues, e.g., skin or muscles [46, 101], brain tissue is usually characterized as a *linear viscoelastic material* [49, 78, 137, 105, 156], i.e. as a material for which the stress tensor depends on the entire history of the strain tensor. According to the *Boltzmann principle*, which claims that the Eulerian stress tensor $\boldsymbol{\sigma}(t)$ at the time t is a functional of the entire history of Cauchy's infinitesimal strain tensor $\boldsymbol{\epsilon}(t)$ [32], a constitutive equation for a linear viscoelastic solid can be derived, which reads [44, 46, 32]

$$\boldsymbol{\sigma}(t) = \int_{-\infty}^{t} \mathbf{G}(t-\tau)\frac{\partial \boldsymbol{\epsilon}(\tau)}{\partial \tau} d\tau. \tag{4.1}$$

The tensor $\mathbf{G}(t)$ denotes the *tensorial relaxation function* with components

$$G(t)_{ijkl} = \frac{g_2(t) - g_1(t)}{3}\,\delta_{ij}\delta_{kl} + \frac{g_1(t)}{2}\left(\delta_{ik}\delta_{jl} + \delta_{il}\delta_{jk}\right), \tag{4.2}$$

where $g_1(t)$ and $g_2(t)$ are scalar functions referring to the underlying material properties. Note, that the lower bound of the integral in (4.1) starts the integration before the beginning of the motion at $t = 0$. If $\boldsymbol{\sigma}(t) = \boldsymbol{\epsilon}(t) = \mathbf{0}$ holds for $t < 0$, then (4.1) reduces to

$$\boldsymbol{\sigma}(t) = \boldsymbol{\epsilon}(t_0^+)\mathbf{G}(t) + \int_0^t \mathbf{G}(t-\tau)\frac{\partial \boldsymbol{\epsilon}(\tau)}{\partial \tau}d\tau, \tag{4.3}$$

where $\boldsymbol{\epsilon}(t_0^+)$ denotes the value of the strain tensor for $t \to 0$ from the positive side.

However, the necessity for using a linear viscoelastic constitutive equation for brain tissue depends on the behavior of the tensorial relaxation function $\mathbf{G}(t)$ with respect to time [44]. Understanding the integral (4.1) in the Stieltjes' sense[1] [44], it is allowed to change the order of differentiation, leading to

$$\boldsymbol{\sigma}(t) = \int_{-\infty}^t \boldsymbol{\epsilon}(\tau)\frac{\partial \mathbf{G}(t-\tau)}{\partial \tau}d\tau. \tag{4.4}$$

The assumption that the tensorial relaxation function $\mathbf{G}(t)$ is a multiple step function in time, in other words, the time-dependent properties of the material change abruptly at discrete time instances only while remaining constant otherwise, yields [12]

$$\boldsymbol{\sigma}(t) = \sum_i \left[\mathbf{G}(t_i^+) - \mathbf{G}(t_i^-)\right]\boldsymbol{\epsilon}(t_i) \tag{4.5}$$

as constitutive equation, where t_i^- and t_i^+ represent the limits from the left and right side of the discrete time instance t_i, respectively. In case of a unit step behavior of $\mathbf{G}(t)$ at the time $t_i = 0$, (4.5) reduces to

$$\boldsymbol{\sigma}(t) = \left[\mathbf{G}(t_0^+) - \mathbf{G}(t_0^-)\right]\boldsymbol{\epsilon}(0) = \left[\alpha\,\delta_{ij}\delta_{kl} + \beta\,(\delta_{ik}\delta_{jl} + \delta_{il}\delta_{jk})\right]\boldsymbol{\epsilon}(0), \tag{4.6}$$

which is the constitutive equation of a linear elastic material, namely Hooke's law (2.37). Consequently, a linear elastic material can be characterized as a material without memory, i.e. as a material where the stress tensor depends on the instantaneous strain tensor only. It follows that the behavior of the tensorial relaxation function with respect to time completely determines the choice of the constitutive equation for brain tissue. The exact behavior of the tensorial relaxation function with respect to time is yet unknown to

[1] In probability theory, a Stieltjes' integral serves as a measure for the mass distribution of a continuously differentiable distribution function [12].

our current knowledge, but measurements indicate that brain tissue can be considered as a linear elastic material as long as the observation times are short compared to the stress relaxation time of brain tissue [161].

Besides the question of the appropriateness of Hooke's law, some authors characterized brain tissue as a *nonlinear viscoelastic material* [49, 137] instead. In this case, the strain $\boldsymbol{\epsilon}(t)$ in (4.1) or (4.3) has to be replaced by some nonlinear function $f(\boldsymbol{\epsilon}(t))$ [32]. Although the measured deviations from linear viscoelasticity are so small that the latter one still serves as a good approximation [49], efforts have been made to formulate such nonlinear functions for brain tissue [116, 105, 110]. Motivated by the idea of using such functions as constitutive equations for brain tissue instead, we summarize the common derivation scheme of such nonlinear functions in the following.

Starting point for all derivations is the assumption that brain tissue can be considered as a *hyperelastic material*, i.e. as a material whose response function is completely determined by an existing stored energy function $W : \bar{\Omega} \times \mathbb{R}^{3\times 3} \longrightarrow \mathbb{R}$ such that

$$\boldsymbol{\sigma}(\mathbf{x}) = \frac{\partial W}{\partial \boldsymbol{\epsilon}}(\mathbf{x}, \boldsymbol{\epsilon}) \tag{4.7}$$

holds [21, 32]. Assuming furthermore that brain tissue behaves as a homogeneous, isotropic, and incompressible material, the stored energy function W can be written in terms of the first two principal invariants $\iota_1(\boldsymbol{\epsilon})$ and $\iota_2(\boldsymbol{\epsilon})$ of the strain tensor $\boldsymbol{\epsilon}$ as [113, 32]

$$W = \alpha_1(\iota_1(\boldsymbol{\epsilon}) - 3) + \alpha_2(\iota_2(\boldsymbol{\epsilon}) - 3), \tag{4.8}$$

where the invariants are defined through [21, 105]

$$\begin{array}{lclcl} \iota_1(\boldsymbol{\epsilon}) & = & (\operatorname{tr}\boldsymbol{\epsilon}) & = & \lambda_1^2 + \lambda_2^2 + \lambda_3^2 \\ \iota_2(\boldsymbol{\epsilon}) & = & \frac{1}{2}\left((\operatorname{tr}\boldsymbol{\epsilon})^2 - (\operatorname{tr}\boldsymbol{\epsilon}^2)\right) & = & \lambda_1^2\lambda_2^2 + \lambda_2^2\lambda_3^2 + \lambda_3^2\lambda_1^2. \end{array} \tag{4.9}$$

With λ_1, λ_2, and λ_3, we denote the principal stretch ratios, i.e. the ratios between the final and initial length along the orthogonal x_1, x_2, and x_3 directions, respectively.

In case of pure tensile tests of a specimen in the x_1 direction, which serve as common experimental basis for the derivation of a nonlinear function $f(\boldsymbol{\epsilon})$ [116, 105, 110], the principal stretch ratios λ_2 and λ_3 are related to λ_1 through the simple relationship [105, 110, 32]

$$\lambda_2 = \lambda_3 = \frac{1}{\sqrt{\lambda_1}}. \tag{4.10}$$

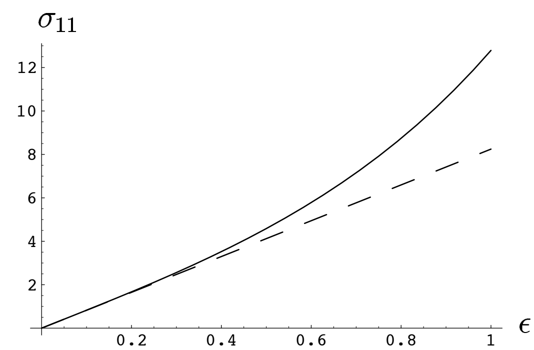

Figure 4.1: Comparison of the stress-strain relationship of different constitutive equations for brain tissue: Hooke's law to simulate a linear elastic material behavior (dashed line) and the nonlinear constitutive equation (4.11) (solid line) to simulate a nonlinear viscoelastic behavior. A significant deviation occurs for larger values of the natural strain ϵ only.

Based on (4.7), (4.8), and (4.10), while applying homogeneous Neumann boundary conditions at the lateral sides of the tissue specimen considered [32], a nonlinear relationship for the only non-zero stress component σ_{11} of the stress tensor $\boldsymbol{\sigma}$ [116, 21, 110] can be derived, leading to [116, 105]

$$\sigma_{11} = 2\alpha_1 \left(e^{2\epsilon} - \frac{1}{e^{\epsilon}} \right) + 2\alpha_2 \left(e^{\epsilon} - \frac{1}{e^{2\epsilon}} \right). \tag{4.11}$$

Note, that σ_{11} is expressed here in terms of the *natural strain* ϵ [100, 36],

$$\epsilon = \ln[\lambda_1], \tag{4.12}$$

which serves as the preferred measure of strain in case of pure tensile tests [36]. For small elongations of a tissue specimen, where $\lambda_1 \approx 1$ holds, the natural strain ϵ is approximately equal to the appropriate component ϵ_{11} of Cauchy's strain tensor $\boldsymbol{\epsilon}$ [100, 46].

A comparison of (4.11) with Hooke's law reveals a similar behavior for small strain rates while significant deviations occur for larger values, see Figure 4.1. But in the latter case, the linearized theory is no longer valid and the distinction between the Lagrangian and Eulerian configuration must be regarded, as pointed out in Chapter 2. To circumvent the problems associated with finite deformations (see Section 2.2.3 for details), we restrict the deformation field to be infinitesimal such that Hooke's law still serves as a good approximation for the constitutive equation of brain tissue. Consequently, this restriction allows the usage of Cauchy's infinitesimal strain tensor $\boldsymbol{\epsilon}$ such that the Navier equation (2.47) serves as a valid approximation to simulate the biomechanical behavior of brain tissue.

The formal limitation of the Navier equation to infinitesimal displacements and, consequently, deformations weakens in real applications, see Chapter 5 for details, but problems may arise in case of large deformations. To overcome such limitations, the *Lagrangian incremental method* [21, 118, 121, 120] should be used instead of a nonlinear constitutive equation which provides an approximate solution by successively solving linear problems.

4.2 Numerical solution using the finite element method

As pointed out in the last section, the Navier equation and the Stokes equation serve as valid physical models to simulate the deformation behavior of either skull bone and brain tissue or cerebrospinal fluid, respectively. For a numerical solution of the Navier equation and the Stokes equation, we will now apply the finite element method (FEM), ending up with a linear matrix system in both cases. In the following derivations, we consider only Dirichlet boundary conditions, where the value of the unknown is prescribed on the boundary (i.e. $\mathbf{u} = \mathbf{g}_1$ holds on Γ_1), and Neumann boundary conditions, where the derivative of the unknown is prescribed on the boundary (i.e. $\mathbf{J}(\mathbf{u})\mathbf{n} = \mathbf{g}_2$ holds on Γ_2). Robbins boundary conditions, which represent a combination of Dirichlet and Neumann boundary conditions (i.e. $\mathbf{J}(\mathbf{u})\mathbf{n} + \mathbf{u} = \mathbf{g}_3$ holds on Γ_3) are not considered here to keep the formulas readable, but note that the integration of this type of boundary conditions is a straightforward task [25].

4.2.1 FEM derivation of the Navier equation

To solve the Navier equation with specified homogeneous Dirichlet boundary conditions on Γ_1 as well as Neumann boundary conditions on Γ_2,

$$\begin{cases} -(\lambda + \mu)\nabla \mathrm{div}[\mathbf{u}] - \mu \nabla^2 \mathbf{u} = \mathbf{f} & \text{in } \Omega \\ \mathbf{u} = \mathbf{0} & \text{on } \Gamma_1 \\ \boldsymbol{\sigma}\mathbf{n} = \mathbf{g} & \text{on } \Gamma_2, \end{cases} \tag{4.13}$$

we apply the method of weighted residuals according to Section 2.3. The resulting expression, after substitution of the identities (2.46), can be written as

$$\int_\Omega (-\mathrm{div}[\lambda(\mathrm{tr}\,\boldsymbol{\epsilon}(\mathbf{u}))\mathbf{I} + 2\mu\boldsymbol{\epsilon}(\mathbf{u})], \mathbf{w})\, d\Omega = \int_\Omega (\mathbf{f}, \mathbf{w})\, d\Omega, \tag{4.14}$$

where $(\cdot, \cdot)$ denotes the common inner product and $\mathbf{w} \in V(\Omega)$ is an arbitrary weighting function of the underlying vector space $V(\Omega)$. Using Green's formula [21]

$$\int_\Omega (\mathrm{div}\mathbf{A}, \mathbf{w})\, d\Omega = \int_\Gamma (\mathbf{A}\mathbf{n}, \mathbf{w})\, d\Gamma - \int_\Omega (\mathbf{A}, \mathbf{J}(\mathbf{w}))\, d\Omega, \tag{4.15}$$

the order of differentiation can be reduced, leading to the expression

$$\int_\Omega (\lambda(\mathrm{tr}\,\boldsymbol{\epsilon}(\mathbf{u}))\mathbf{I} + 2\mu\boldsymbol{\epsilon}(\mathbf{u}), \mathbf{J}(\mathbf{w}))\, d\Omega = \int_\Omega (\mathbf{f}, \mathbf{w})\, d\Omega + \int_{\Gamma_2} (\mathbf{g}, \mathbf{w})\, d\Gamma_2. \tag{4.16}$$

For the derivation of (4.16), the identity $\boldsymbol{\sigma} = \lambda(\mathrm{tr}\,\boldsymbol{\epsilon}(\mathbf{u}))\mathbf{I} + 2\mu\boldsymbol{\epsilon}(\mathbf{u})$, i.e. Hooke's law, has been used to substitute the given Neumann boundary condition $\boldsymbol{\sigma}\mathbf{n} = \mathbf{g}$ on Γ_2. Note, that the boundary integral related to the portion Γ_1 of Γ

$$\int_{\Gamma_1} (\boldsymbol{\sigma}\mathbf{n}, \mathbf{w})\, d\Gamma_1 \tag{4.17}$$

vanishes in (4.16) since $\mathbf{w} = \mathbf{0}$ holds on Γ_1 due to the definition of the underlying solution space [25]

$$V(\Omega) = \{\mathbf{w} : \Omega \longrightarrow \mathbb{R}; \mathbf{w} = \mathbf{0} \text{ on } \Gamma_1\}. \tag{4.18}$$

Application of the law $(\mathbf{A}, \mathbf{B}) = (\mathrm{tr}\,\mathbf{A}^T\mathbf{B})$, and bearing the symmetry of Cauchy's infinitesimal strain tensor $\boldsymbol{\epsilon}(\mathbf{u})$ in mind, yields

$$\int_\Omega (\mathrm{tr}\,\lambda(\mathrm{tr}\,\boldsymbol{\epsilon}(\mathbf{u}))\mathbf{I}\,\mathbf{J}(\mathbf{w})) + (\mathrm{tr}\,2\mu\boldsymbol{\epsilon}(\mathbf{u})\mathbf{J}(\mathbf{w}))d\Omega = \int_\Omega (\mathbf{f}, \mathbf{w})\, d\Omega + \int_{\Gamma_2} (\mathbf{g}, \mathbf{w})\, d\Gamma_2, \tag{4.19}$$

which is equivalent to

$$\int_\Omega \lambda(\mathrm{tr}\,\boldsymbol{\epsilon}(\mathbf{u}))(\mathrm{tr}\,\mathbf{I}\,\mathbf{J}(\mathbf{w})) + 2\mu(\mathrm{tr}\,\boldsymbol{\epsilon}(\mathbf{u})\mathbf{J}(\mathbf{w}))d\Omega = \int_\Omega (\mathbf{f}, \mathbf{w})\, d\Omega + \int_{\Gamma_2} (\mathbf{g}, \mathbf{w})\, d\Gamma_2. \tag{4.20}$$

Due to the equality $(\operatorname{tr}\boldsymbol{\epsilon}(\mathbf{u})\mathbf{J}(\mathbf{w})) = (\boldsymbol{\epsilon}(\mathbf{u}), \mathbf{J}(\mathbf{w})) = (\boldsymbol{\epsilon}(\mathbf{u}), \boldsymbol{\epsilon}(\mathbf{w}))$ [21], this can be furthermore rewritten as

$$\int_\Omega \lambda(\operatorname{tr}\boldsymbol{\epsilon}(\mathbf{u}))(\operatorname{tr}\boldsymbol{\epsilon}(\mathbf{w})) + 2\mu\,(\boldsymbol{\epsilon}(\mathbf{u}), \boldsymbol{\epsilon}(\mathbf{w}))\,d\Omega = \int_\Omega (\mathbf{f}, \mathbf{w})\,d\Omega + \int_{\Gamma_2} (\mathbf{g}, \mathbf{w})\,d\Gamma_2. \quad (4.21)$$

Note, that for this derivation the relationship $(\operatorname{tr}\mathbf{J}(\mathbf{w})) = \partial_i w_i = (\operatorname{tr}\boldsymbol{\epsilon}(\mathbf{w}))$ has been applied.

Equation (4.21) can be expressed in terms of an abstract problem [20], leading to the following elliptic problem [20, 25]: Find $\mathbf{u} \in V(\Omega)$ such that

$$a(\mathbf{u}, \mathbf{w}) = f(\mathbf{w}), \quad \forall \mathbf{w} \in V(\Omega) \quad (4.22)$$

holds, where the bilinear form $a(\cdot,\cdot) : V(\Omega) \times V(\Omega) \longrightarrow \mathbb{R}$ and the linear form $f(\cdot) : V(\Omega) \longrightarrow \mathbb{R}$ are defined as [20]

$$a(\mathbf{u}, \mathbf{w}) = \int_\Omega \lambda(\operatorname{tr}\boldsymbol{\epsilon}(\mathbf{u}))(\operatorname{tr}\boldsymbol{\epsilon}(\mathbf{w})) + 2\mu\,(\boldsymbol{\epsilon}(\mathbf{u}), \boldsymbol{\epsilon}(\mathbf{w}))\,d\Omega \quad (4.23)$$

and

$$f(\mathbf{w}) = \int_\Omega (\mathbf{f}, \mathbf{w})\,d\Omega + \int_{\Gamma_2} (\mathbf{g}, \mathbf{w})\,d\Gamma_2, \quad (4.24)$$

respectively. The solution space $V(\Omega)$ of the Navier equation can be identified with the Sobolev space $H^1(\Omega)$, and it can be shown that the bilinear form $a(\cdot,\cdot)$ is continuous and V-elliptic [20, 25], i.e. the problem is well-posed in the Hadamard sense [4], see Section 2.3 for details.

For a numerical solution, the abstract problem (4.22) is converted into a linear matrix system through the Galerkin method, which results in a *conforming finite element method.* Therefore, the solution space $V(\Omega)$ is approximated by a finite dimensional subspace $V^N(\Omega)$, spanned by a finite number N of basis functions $\boldsymbol{\phi}_i$, thus allowing an approximation of $\mathbf{u}$ by

$$\tilde{\mathbf{u}} = \sum_{i=1}^{N} \sum_{k=1}^{3} \tilde{u}_{ki} \boldsymbol{\phi}_i = \sum_{i=1}^{N} \left(\tilde{u}_{1i}\boldsymbol{\phi}_{1i} + \tilde{u}_{2i}\boldsymbol{\phi}_{2i} + \tilde{u}_{3i}\boldsymbol{\phi}_{3i} \right), \quad (4.25)$$

where the basis functions read [25]

$$\boldsymbol{\phi}_{ki} = \begin{cases} (\phi_i, 0, 0)^T & \text{for } k = 1 \\ (0, \phi_i, 0)^T & \text{for } k = 2 \\ (0, 0, \phi_i)^T & \text{for } k = 3. \end{cases} \quad (4.26)$$

Substitution of (4.25) into (4.22) yields

$$\sum_{i=1}^{N} \tilde{u}_{ki} \int_{\Omega} \lambda(\operatorname{tr}\boldsymbol{\epsilon}(\boldsymbol{\phi}_i))(\operatorname{tr}\boldsymbol{\epsilon}(\boldsymbol{\phi}_j)) + 2\mu\,(\boldsymbol{\epsilon}(\boldsymbol{\phi}_i),\boldsymbol{\epsilon}(\boldsymbol{\phi}_j))\,d\Omega =$$
$$\int_{\Omega} (\mathbf{f},\boldsymbol{\phi}_j)\,d\Omega + \int_{\Gamma_2} (\mathbf{g},\boldsymbol{\phi}_j)\,d\Gamma_2 \quad k = 1\ldots 3,\;\; j = 1\ldots N, \tag{4.27}$$

which can be written in compact matrix notation as

$$\begin{pmatrix} \mathbf{A}_{11} & \mathbf{A}_{12} & \mathbf{A}_{13} \\ \mathbf{A}_{21} & \mathbf{A}_{22} & \mathbf{A}_{23} \\ \mathbf{A}_{31} & \mathbf{A}_{32} & \mathbf{A}_{33} \end{pmatrix} \begin{pmatrix} \tilde{\mathbf{u}}_1 \\ \tilde{\mathbf{u}}_2 \\ \tilde{\mathbf{u}}_3 \end{pmatrix} = \begin{pmatrix} \mathbf{f}_1 + \mathbf{g}_1 \\ \mathbf{f}_2 + \mathbf{g}_2 \\ \mathbf{f}_3 + \mathbf{g}_3 \end{pmatrix}. \tag{4.28}$$

Here, $\mathbf{A}_{11}, \ldots, \mathbf{A}_{33}$ denote the submatrices for the corresponding spatial dimensions x_1, x_2, and x_3. The $N \times N$ matrix entries of each diagonal submatrix $\mathbf{A}_{kk}$ are determined by

$$A_{kkij} = \int_{\Omega} \lambda \partial_k \boldsymbol{\phi}_{ki} \partial_k \boldsymbol{\phi}_{kj} + \mu\,(2\partial_k \boldsymbol{\phi}_{ki} \partial_k \boldsymbol{\phi}_{kj} + \partial_l \boldsymbol{\phi}_{ki} \partial_l \boldsymbol{\phi}_{kj} + \partial_m \boldsymbol{\phi}_{ki} \partial_m \boldsymbol{\phi}_{kj})\,d\Omega$$
$$k \neq l \neq m \in [1, \ldots, 3] \quad i, j = 1 \ldots N, \tag{4.29}$$

while the matrix entries for the other submatrices A_{kl} read

$$A_{klij} = \int_{\Omega} \lambda \partial_k \boldsymbol{\phi}_{ki} \partial_l \boldsymbol{\phi}_{lj} + \mu \partial_l \boldsymbol{\phi}_{ki} \partial_k \boldsymbol{\phi}_{lj}\,d\Omega$$
$$k \neq l \in [1, \ldots, 3] \quad i, j = 1 \ldots N \tag{4.30}$$

according to definition (4.26). For the spatial components $\mathbf{f}_1, \ldots, \mathbf{f}_3$ and $\mathbf{g}_1, \ldots, \mathbf{g}_3$ of the right-hand side of (4.28), the vector entries read

$$f_{kj} + g_{kj} = \int_{\Omega} f_{kj} \boldsymbol{\phi}_{kj}\,d\Omega + \int_{\Gamma_2} g_{kj} \boldsymbol{\phi}_{kj}\,d\Gamma_2$$
$$k \in [1, \ldots, 3] \quad j = 1 \ldots N. \tag{4.31}$$

4.2.2 FEM derivation of the Stokes equation

In contrast to the Navier equation, the Stokes equation defines a *constrained minimization problem* with an additional unknown pressure function $p \in W(\Omega)$ [12, 7]. Therefore, the incompressibility constraint (2.50) has to be solved simultaneously with the Stokes equation. The complete problem with specified homogeneous Dirichlet boundary conditions on Γ_1 as well as Neumann boundary conditions on Γ_2 reads now

$$\begin{cases} \nabla p - \mu^\star \nabla^2 \mathbf{v} = \mathbf{f} & \text{in } \Omega \\ \operatorname{div}[\mathbf{v}] = 0 & \text{in } \Omega \\ \mathbf{v} = \mathbf{0} & \text{on } \Gamma_1 \\ \boldsymbol{\sigma}\mathbf{n} = \mathbf{g} & \text{on } \Gamma_2. \end{cases} \tag{4.32}$$

An application of the method of weighted residuals with arbitrary weighting functions $\mathbf{w} \in V(\Omega)$ and $q \in W(\Omega)$ leads to the expressions

$$\begin{aligned} \int_\Omega \left(\nabla p - \mu^\star \nabla^2 \mathbf{v}, \mathbf{w}\right) d\Omega &= \int_\Omega (\mathbf{f}, \mathbf{w})\, d\Omega \\ \int_\Omega q \operatorname{div}[\mathbf{v}] d\Omega &= 0. \end{aligned} \tag{4.33}$$

With the identity $(\mathbf{A}, \mathbf{B} + \mathbf{C}) = (\mathbf{A}, \mathbf{B}) + (\mathbf{A}, \mathbf{C})$, the first part of (4.33) can be directly rewritten as

$$\int_\Omega (\nabla p, \mathbf{w}) - \mu^\star \left(\nabla^2 \mathbf{v}, \mathbf{w}\right) d\Omega = \int_\Omega (\mathbf{f}, \mathbf{w})\, d\Omega. \tag{4.34}$$

Using the law $(\nabla a, \mathbf{b}) = \operatorname{div}[a\mathbf{b}] - a \operatorname{div}[\mathbf{b}]$ [100, 12] gives

$$\int_\Omega \operatorname{div}[p\mathbf{w}] - p \operatorname{div}[\mathbf{w}] - \mu^\star \left(\nabla^2 \mathbf{v}, \mathbf{w}\right) d\Omega = \int_\Omega (\mathbf{f}, \mathbf{w})\, d\Omega, \tag{4.35}$$

which can be transformed through $(\nabla^2 \mathbf{a}, \mathbf{b}) = \operatorname{div}[\mathbf{J}(\mathbf{a})^T \mathbf{b}] - (\mathbf{J}(\mathbf{a}), \mathbf{J}(\mathbf{b}))$ into

$$\int_\Omega \operatorname{div}[p\mathbf{w}] - p \operatorname{div}[\mathbf{w}] - \mu^\star \operatorname{div}[\mathbf{J}(\mathbf{v})^T \mathbf{w}] + \mu^\star (\mathbf{J}(\mathbf{v}), \mathbf{J}(\mathbf{w}))\, d\Omega = \int_\Omega (\mathbf{f}, \mathbf{w})\, d\Omega. \tag{4.36}$$

An application of Green's formula [21]

$$\int_\Omega \operatorname{div}[\mathbf{a}] d\Omega = \int_\Gamma (\mathbf{a}, \mathbf{n})\, d\Gamma, \tag{4.37}$$

where $\mathbf{n}$ denotes the unit outward vector of the boundary Γ, to equation (4.36) yields

$$\int_\Omega -p \operatorname{div}[\mathbf{w}] + \mu^\star (\mathbf{J}(\mathbf{v}), \mathbf{J}(\mathbf{w}))\, d\Omega = \int_\Omega (\mathbf{f}, \mathbf{w})\, d\Omega - \int_{\Gamma_2} (p\mathbf{w}, \mathbf{n})\, d\Gamma_2 + \int_{\Gamma_2} \mu^\star \left(\mathbf{J}(\mathbf{v})^T \mathbf{w}, \mathbf{n}\right) d\Gamma_2. \tag{4.38}$$

Again, as shown in the previous section, the boundary integrals related to the homogeneous Dirichlet boundary condition vanish here, due to the definition of the underlying solution space $V(\Omega)$ [25]. The boundary integrals appearing on the right-hand side can be further simplified using the identities

$$\begin{aligned} (p\mathbf{w}, \mathbf{n}) &= p w_i n_i &&= (\mathbf{w}, p\mathbf{n}) \\ \mu^\star \left(\mathbf{J}(\mathbf{v})^T \mathbf{w}, \mathbf{n}\right) &= \mu^\star \partial_i v_j w_j n_i &&= \mu^\star \left(\mathbf{J}(\mathbf{v})\, \mathbf{n}, \mathbf{w}\right). \end{aligned} \tag{4.39}$$

A closer consideration of the first identity reveals, that the term $p\mathbf{n}$ represents a *pressure load* [21] on the surface Γ_2 such that $\mathbf{g} = p\mathbf{n}$ holds [21], which is directly related to Cauchy's stress vector $\mathbf{t}$ through equation (2.24). This observation is in accordance with the interpretation of the Cauchy stress vector $\mathbf{t}$ being a pressure [100, 21]. For the second identity, we simply assume for the moment that $\mathbf{J}(\mathbf{v})\,\mathbf{n}$ vanishes on Γ_2. The validity of this assumption will be discussed in detail in Section 4.4 below. Therefore, the final formula after application of the method of weighted residuals and substitution of the given Neumann boundary conditions reads

$$\begin{gathered} \int_\Omega -p\,\mathrm{div}[\mathbf{w}] + \mu^\star \left(\mathbf{J}(\mathbf{v}), \mathbf{J}(\mathbf{w})\right) d\Omega = \int_\Omega (\mathbf{f}, \mathbf{w})\, d\Omega - \int_{\Gamma_2} (\mathbf{g}, \mathbf{w})\, d\Gamma_2 \\ \int_\Omega q\,\mathrm{div}[\mathbf{v}] d\Omega = 0. \end{gathered} \tag{4.40}$$

Again, the finite element formulation of the Stokes equation can be written in terms of an abstract problem [152, 58]: find a pair $(\mathbf{v}, p) \in V(\Omega) \times W(\Omega)$ such that

$$a(\mathbf{v}, \mathbf{w}) + b(p, \mathbf{w}) + b(q, \mathbf{v}) = f(\mathbf{w}), \quad \forall (\mathbf{w}, q) \in V(\Omega) \times W(\Omega) \tag{4.41}$$

holds, where the bilinear forms $a(\cdot,\cdot) : V(\Omega) \times V(\Omega) \longrightarrow \mathbb{R}$ and $b(\cdot,\cdot) : W(\Omega) \times V(\Omega) \longrightarrow \mathbb{R}$ are defined as

$$a(\mathbf{v}, \mathbf{w}) = \int_\Omega \mu^\star \left(\mathbf{J}(\mathbf{v}), \mathbf{J}(\mathbf{w})\right) d\Omega \tag{4.42}$$

$$b(p, \mathbf{w}) = -\int_\Omega p\,\mathrm{div}[\mathbf{w}] d\Omega, \tag{4.43}$$

while the linear form $f(\cdot) : V(\Omega) \longrightarrow \mathbb{R}$ reads

$$f(\mathbf{w}) = \int_\Omega (\mathbf{f}, \mathbf{w})\, d\Omega - \int_{\Gamma_2} (\mathbf{g}, \mathbf{w})\, d\Gamma_2. \tag{4.44}$$

Appropriate solution spaces of $V(\Omega)$ and $W(\Omega)$ for the Stokes problem are the Sobolev space $H^1(\Omega)$ and the Hilbert space

$$L_{2,0}(\Omega) = \{q \in L_2(\Omega); \int_\Omega q\, d\Omega = 0\}, \tag{4.45}$$

respectively [58, 7]. With $L_2(\Omega)$, the space of all quadratic integrable functions over Ω is denoted, see also the definition (2.59). Note, that the pressure p appearing in the Stokes equation (4.32) is determined up to an additive constant only, so the commonly used standardization $\int_\Omega q \, d\Omega = 0$ is necessary here [58, 7].

In contrast to the Navier equation, the abstract Stokes problem (4.41) defines a *saddlepoint problem.* To ensure solvability in this case, the associated linear function

$$L : V(\Omega) \times W(\Omega) \longrightarrow V^*(\Omega) \times W^*(\Omega), \tag{4.46}$$

where $V^*(\Omega) \times W^*(\Omega)$ denotes the product space of the underlying dual spaces, must define an isomorphism, as pointed out in Section 2.3. Following [58, 7], it is therefore necessary and sufficient that the bilinear form $a(\cdot,\cdot)$ is continuous and V-elliptic, while the bilinear form $b(\cdot,\cdot)$ satisfies the *Babuška-Brezzi condition* [25, 58]: A continuous bilinear form $b(\cdot,\cdot) : W(\Omega) \times V(\Omega) \longrightarrow \mathbb{R}$ over the spaces $V(\Omega)$ and $W(\Omega)$, each equipped with a norm $||\cdot||_V$ and $||\cdot||_W$, respectively, satisfies the Babuška-Brezzi condition if there exists a constant $\alpha > 0$ with

$$\sup_{\mathbf{w} \in V} \frac{b(\mathbf{w}, q)}{||\mathbf{w}||_V} \geq \alpha ||q||_W, \qquad \forall q \in W(\Omega). \tag{4.47}$$

It can be shown that (4.42) and (4.43) satisfy the above mentioned conditions [7], i.e. the Stokes equation defines a well-posed problem in the Hadamard sense [4]. However, the abstract problem (4.41) leads to a *non-conforming finite element method* since the incompressibility constraint (2.50) is satisfied in a weak sense only [12, 58], i.e. the solution does not satisfy the incompressibility constraint pointwise but in the mean. It can be shown, however, that each classical solution of (4.41), i.e. a solution satisfying $\mathbf{u} \in C^2(\Omega) \cap C^0(\bar{\Omega})$ and $p \in C^1(\bar{\Omega})$, is still a classical solution of the Stokes problem (4.32) [7, 58]. As usual, the space $C^m(\Omega)$ denotes here the space of all functions $\mathbf{w} : \Omega \longrightarrow \mathbb{R}$ whose partial derivatives up to order m exist on Ω [12].

To derive a linear matrix system, the Galerkin method is applied again by choosing finite dimensional subspaces $V^N(\Omega)$ and $W^M(\Omega)$, each spanned by basis functions $\boldsymbol{\phi}_i$ and ψ_j, respectively. A substitution of the approximations

$$\tilde{\mathbf{v}} = \sum_{i=1}^{N} \sum_{k=1}^{3} \tilde{v}_{ki} \boldsymbol{\phi}_i = \sum_{i=1}^{N} (\tilde{v}_{1i} \boldsymbol{\phi}_{1i} + \tilde{v}_{2i} \boldsymbol{\phi}_{2i} + \tilde{v}_{3i} \boldsymbol{\phi}_{3i}) \tag{4.48}$$

and

$$\tilde{p} = \sum_{j=1}^{M} \tilde{p}_j \psi_j \tag{4.49}$$

into (4.41) yields for the Stokes equation

$$\sum_{i=1}^{N} \tilde{v}_{ki} \int_{\Omega} \mu^{\star} \left(\mathbf{J}(\boldsymbol{\phi}_i), \mathbf{J}(\boldsymbol{\phi}_j)\right) d\Omega - \sum_{i=1}^{M} \tilde{p}_i \int_{\Omega} \psi_i \mathrm{div}[\boldsymbol{\phi}_j] d\Omega = \int_{\Omega} \left(\mathbf{f}, \boldsymbol{\phi}_j\right) d\Omega - \int_{\Gamma_2} \left(\mathbf{g}, \boldsymbol{\phi}_j\right) d\Gamma_2 \quad k = 1 \ldots 3, \;\; j = 1 \ldots N \quad (4.50)$$

and for the incompressibility constraint

$$\sum_{i=1}^{N} \tilde{v}_{ki} \int_{\Omega} \psi_j \mathrm{div}[\boldsymbol{\phi}_i] d\Omega = 0 \quad k = 1 \ldots 3, \;\; j = 1 \ldots M. \quad (4.51)$$

Again, these equations can be written in matrix notation as

$$\begin{pmatrix} \mathbf{A}_{11} & \mathbf{A}_{12} & \mathbf{A}_{13} & \mathbf{P}_1 \\ \mathbf{A}_{21} & \mathbf{A}_{22} & \mathbf{A}_{23} & \mathbf{P}_2 \\ \mathbf{A}_{31} & \mathbf{A}_{32} & \mathbf{A}_{33} & \mathbf{P}_3 \\ \mathbf{P}_1^T & \mathbf{P}_2^T & \mathbf{P}_3^T & \mathbf{0} \end{pmatrix} \begin{pmatrix} \tilde{\mathbf{v}}_1 \\ \tilde{\mathbf{v}}_2 \\ \tilde{\mathbf{v}}_3 \\ \tilde{\mathbf{p}} \end{pmatrix} = \begin{pmatrix} \mathbf{f}_1 + \mathbf{g}_1 \\ \mathbf{f}_2 + \mathbf{g}_2 \\ \mathbf{f}_3 + \mathbf{g}_3 \\ \mathbf{0} \end{pmatrix}, \quad (4.52)$$

where $\mathbf{A}_{11}, \ldots, \mathbf{A}_{33}$ denote the $N \times N$ submatrices for the corresponding spatial dimensions x_1, x_2, and x_3 while $\mathbf{P}_1$, $\mathbf{P}_2$, and $\mathbf{P}_3$ denote the $N \times M$ submatrices for the terms which relate the pressure to the corresponding spatial dimensions [25].

Written in extenso, the matrix entries for the diagonal submatrices $\mathbf{A}_{kk}$ read

$$A_{kkij} = \int_{\Omega} \mu^{\star} \left(\partial_k \boldsymbol{\phi}_{ki} \partial_k \boldsymbol{\phi}_{kj} + \partial_l \boldsymbol{\phi}_{ki} \partial_l \boldsymbol{\phi}_{kj} + \partial_m \boldsymbol{\phi}_{ki} \partial_m \boldsymbol{\phi}_{kj}\right) d\Omega \quad k \neq l \neq m \in [1, \ldots, 3] \quad i, j = 1 \ldots N, \quad (4.53)$$

for the submatrices $\mathbf{A}_{kl}$ we have

$$A_{klij} = 0 \quad k \neq l \in [1, \ldots, 3] \quad i, j = 1 \ldots N, \quad (4.54)$$

and for the pressure submatrices $\mathbf{P}_k$ we have

$$P_{kij} = -\int_{\Omega} \psi_j \partial_k \boldsymbol{\phi}_{ki} d\Omega \quad k \in [1, \ldots, 3] \quad i = 1 \ldots N \quad j = 1 \ldots M. \quad (4.55)$$

For the right-hand side of (4.52), the vector entries read

$$f_{kj} + g_{kj} = \int_{\Omega} f_{kj}\boldsymbol{\phi}_{kj} d\Omega - \int_{\Gamma_2} g_{kj}\boldsymbol{\phi}_{kj} d\Gamma_2$$
$$k \in [1, \ldots, 3] \qquad j = 1 \ldots N. \quad (4.56)$$

4.3 Finite elements

So far, we simply assumed the existence of a finite dimensional vector space $V^N(\Omega)$ to approximate the corresponding solution space $V(\Omega)$ for the Navier equation and the Stokes equation, respectively. Remember, that each solution space $V(\Omega)$ is a subset of a Sobolev space $H^m(\Omega)$ of appropriate order m. An application of the Galerkin method demands now an explicit construction of the basis functions $\boldsymbol{\phi}_i$ and hence of the space $V^N(\Omega)$, as pointed out in Section 2.3. In order to construct such basis functions, the body Ω is divided into a finite set of N areas Ω_k, satisfying the properties [25, 7]

- $\bar{\Omega} = \cup_k \bar{\Omega}_k$, $1 \leq i \leq N$,
- $\Omega_k \cap \Omega_l = \emptyset$ if $k \neq l$, and
- $\bar{\Omega}_k$ and $\bar{\Omega}_l$, $k \neq l$, may only share a common surface, side, or vertex.

As usual, $\bar{\Omega}$ denotes the closure of the body Ω, while $\bar{\Omega}_k$ denotes the closure of the corresponding area Ω_k. The areas Ω_k are commonly known as *finite elements* and allow the introduction of basis functions $\boldsymbol{\phi}_i$ with compact support only. A direct consequence of the compactness is, that the resulting stiffness matrix $\mathbf{A}$ is sparse, i.e. $\mathbf{A}$ contains a large number of zeros, which is important for the application of efficient numerical solution methods [20]. Based on the finite elements, we will now present a construction scheme for the basis functions $\boldsymbol{\phi}_i$, following mainly [141, 72, 7].

4.3.1 Construction of a basis for the space $V^N(\Omega)$

For the explicit construction of a finite dimensional space $V^N(\Omega)$ over the body Ω, the following property of polynomial functions $\mathbf{w} : \bar{\Omega} \longrightarrow \mathbb{R}$ is exploited: $\mathbf{w} \in H^m(\Omega)$ holds if $\mathbf{w} \in C^{m-1}(\bar{\Omega})$ and the restrictions $\mathbf{w}|_{\Omega_k} \in C^m(\bar{\Omega}_k)$ are satisfied for all finite elements Ω_k [20, 58, 7]. Therefore, the unknown function $\mathbf{u}$ is usually approximated in each finite element Ω_k by polynomials of order m,

$$\tilde{\mathbf{u}}|_{\Omega_k} = \sum_{0 \leq i,j,k \leq m} \alpha_{ijk} x_1^i x_2^j x_3^k, \tag{4.57}$$

where $\tilde{\mathbf{u}}|_{\Omega_k}$ denotes the restriction of $\tilde{\mathbf{u}}$ on the finite element Ω_k. To ensure the invariance with respect to linear transformations of the representation of $\tilde{\mathbf{u}}|_{\Omega_k}$ within each finite element Ω_k, the polynomials (4.57) should possess the property of *geometric isotropy* [141, 72], i.e. they should be invariant with respect to linear transformations from one Cartesian coordinate system into another one. Therefore, either complete or incomplete polynomials of order m, where only pairs of symmetric terms with respect to the spatial coordinates x_1, x_2, and x_3 are dropped, are commonly used [141, 72].

The explicit choice of a polynomial function in (4.57) determines the type of finite elements and therefore the space $V^N(\Omega)$ through the number n of unknown coefficients α_{ijk}. These coefficients, usually denoted as *generalized coefficients*, are determined by choosing an appropriate number of nodal points $\mathbf{x}_i \in \bar{\Omega}_k$, $i = 1, \ldots, n$, thus allowing the construction of a linear matrix system for each finite element which can be solved for the generalized coefficients α_{ijk}. Substitution of these coefficients into (4.57), followed by a reordering of the components, leads to the representation

$$\tilde{\mathbf{u}}|_{\Omega_k} = \sum_{i}^{n} \tilde{u}_i \boldsymbol{\phi}_i|_{\Omega_k}, \tag{4.58}$$

where the function $\tilde{\mathbf{u}}|_{\Omega_k}$ is expressed in terms of a finite set of interpolation functions $\boldsymbol{\phi}_i|_{\Omega_k}$, which are polynomials themselves, multiplied with coefficients $\tilde{u}_i = \tilde{\mathbf{u}}|_{\Omega_k}(\mathbf{x}_i)$ [141].

All interpolation functions $\boldsymbol{\phi}_i|_{\Omega_k}$ satisfy the properties [25]

- $\boldsymbol{\phi}_i|_{\Omega_k} = \delta_{ij}$ at the nodal point $\mathbf{x}_j$,
- $\boldsymbol{\phi}_i|_{\Omega_k}$ has a prescribed behavior on $\bar{\Omega}_k$, e.g., linear or quadratic, and
- $\boldsymbol{\phi}_i|_{\Omega_k}$ is continuous on Ω_k.

The function spaces spanned by $\boldsymbol{\phi}_1|_{\Omega_k}, \ldots, \boldsymbol{\phi}_n|_{\Omega_k}$ over Ω_k are either the spaces[2] $P_m(\bar{\Omega}_k)$ or $P_m^+(\bar{\Omega}_k)$ for triangular types of finite elements or the space $Q_m(\bar{\Omega}_k)$

[2]The explicit function space spanned by the interpolation functions $\boldsymbol{\phi}_i|_{\Omega_k}$ for triangular types of finite elements depends on the actual number of nodal points used in the element Ω_k [25].

for quadrilateral types of finite elements. With $Q_m(\bar{\Omega}_k)$, the space of all polynomials of degree $\leq m$ in each variable is denoted, while $P_m(\bar{\Omega}_k) \subset Q_m(\bar{\Omega}_k)$ denotes the space of polynomials of order m and $P_m^+(\bar{\Omega}_k) \subset P_{m+1}(\bar{\Omega}_k)$ contains the space $P_m(\bar{\Omega}_k)$ [20, 25]. Note, that the inclusions $P_m(\bar{\Omega}_k) \subset P_m^+(\bar{\Omega}_k) \subset C^m(\bar{\Omega}_k)$ and $Q_m(\bar{\Omega}_k) \subset C^m(\bar{\Omega}_k)$ hold. Finally, the basis functions $\boldsymbol{\phi}_i$ are constructed by a unification of all interpolation functions $\boldsymbol{\phi}_j|_{\Omega_k}$ from adjacent finite elements Ω_k which share a common node $\mathbf{x}_i$ [141], i.e.

$$\boldsymbol{\phi}_i = \cup_k \boldsymbol{\phi}_j|_{\Omega_k} \quad \text{which satisfy} \quad \boldsymbol{\phi}_j|_{\Omega_k}(\mathbf{x}_i) = 1. \tag{4.59}$$

With this definition, the basis functions $\boldsymbol{\phi}_i$ have a compact support, they are continuous over the body Ω, and the space $V^N(\Omega)$ spanned by these basis functions is a subset of the Sobolev space $H^m(\Omega)$ [20, 58], according to the property of polynomial functions described at the beginning of this section. If homogeneous Dirichlet boundary conditions must be satisfied on Γ, all those basis functions $\boldsymbol{\phi}_i$ which belong to nodal points $\mathbf{x}_i \in \Gamma$ are dropped [12].

However, for the construction of a stiffness matrix $\mathbf{A}$, the scheme presented so far is seldomly applied due to the large amount of computation necessary to determine the generalized coefficients for each finite element Ω_k. Instead, a single finite element Ω_r, called *reference element*, is used to simplify the calculations. By definition, the reference element Ω_r has straight sides and the spatial coordinates x_1, x_2, and x_3 range between zero and one. For all finite elements Ω_k, the interpolation functions $\boldsymbol{\phi}|_{\Omega_k}$ are defined on the reference element Ω_r and are then transformed to match with the correct global position of the actual finite element Ω_k considered. This transformation is an affine mapping, which results in a fast and powerful computation of the stiffness matrix $\mathbf{A}$ [141, 25].

4.3.2 Quadrilateral finite elements

Since our biomechanical model will be applied to rectangular bodies Ω defined by the given image dimensions, the use of triangular finite elements is inapt [118]. Instead, quadrilateral finite elements in 2D, or hexahedral finite elements in 3D, are used such that the affine mapping from the reference finite element onto an actual finite element Ω_k is the identity mapping due to the underlying regular pixel grid, or voxel grid in 3D, of the image. The usage of quadrilateral finite elements increases the bandwidth of the stiffness matrix $\mathbf{A}$ in comparison to triangular finite elements, but, on the other hand, reduces the number of finite elements used. For simplicity, mainly 2D elements will be considered here, but also one hexahedral finite element for the 3D experiments described in Chapter 5 is presented.

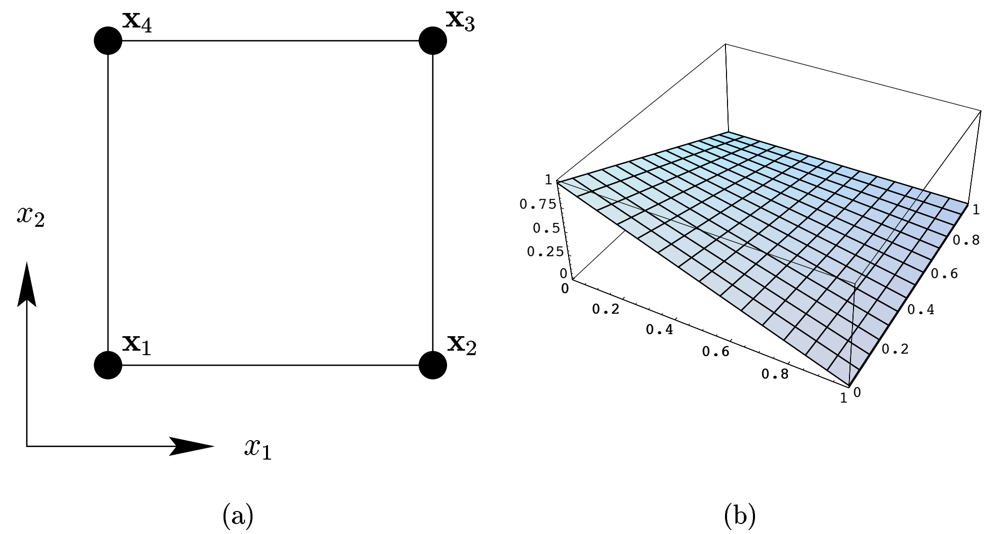

Figure 4.2: 2D bilinear reference finite element (a) and the interpolation function $\phi_{11}|_{\Omega_k}$ (b).

2D bilinear finite element

The simplest choice is the bilinear finite element shown in Figure 4.2(a) which consists of four nodal points $\mathbf{x}_i$, each located at a corner. For this type of finite element, the components $\phi_{1i}|_{\Omega_k}$ and $\phi_{2i}|_{\Omega_k}$ of the interpolation functions $\boldsymbol{\phi}_i|_{\Omega_k}$ with respect to these four nodal points read

$$
\begin{aligned}
\phi_{11}|_{\Omega_k} &= \phi_{21}|_{\Omega_k} = (1-x_1)(1-x_2) \\
\phi_{12}|_{\Omega_k} &= \phi_{22}|_{\Omega_k} = x_1(1-x_2) \\
\phi_{13}|_{\Omega_k} &= \phi_{23}|_{\Omega_k} = x_1 x_2 \\
\phi_{14}|_{\Omega_k} &= \phi_{24}|_{\Omega_k} = (1-x_1)x_2,
\end{aligned}
$$

thus resulting in interpolation functions $\boldsymbol{\phi}_i|_{\Omega_k}$ that are bilinear on Ω_k, which satisfy $\boldsymbol{\phi}_i|_{\Omega_k}(\mathbf{x}_j) = \delta_{ij}$, and span the space of all bilinear polynomials of order 1 over Ω_k, i.e. they obey $\text{span}(\boldsymbol{\phi}_1|_{\Omega_k}, \ldots, \boldsymbol{\phi}_4|_{\Omega_k}) = Q_1(\bar{\Omega}_k)$ [25]. The total number of degrees-of-freedom for a finite element grid consisting of $N \times N$ bilinear finite elements is $2(N+1)^2$.

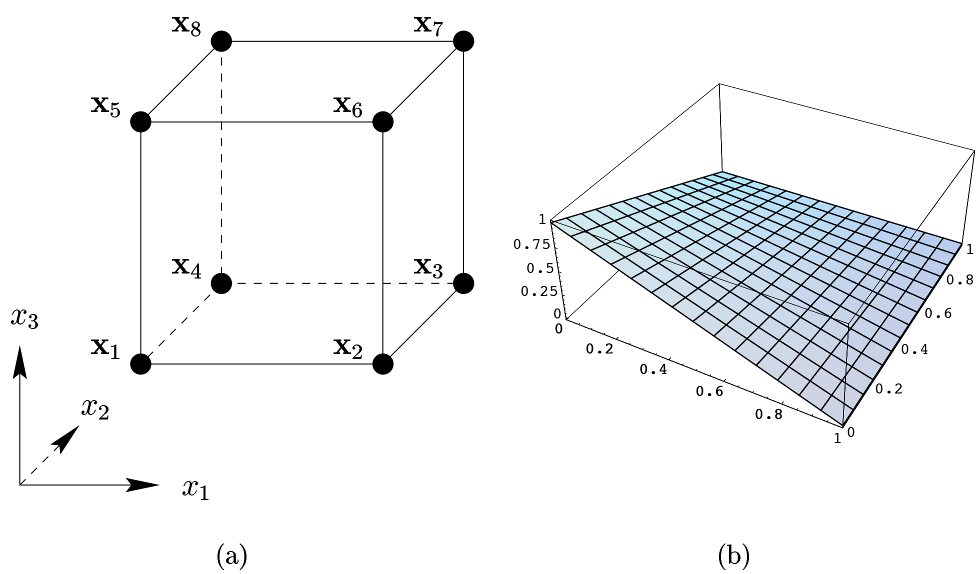

Figure 4.3: 3D trilinear reference finite element (a) and a projection of the interpolation function $\phi_{11}|_{\Omega_k}$ onto the x_1x_2-plane (b).

3D trilinear finite element

The simplest hexahedral finite element for three dimensions comprises eight nodal points, each located at a corner of the element cube as depicted in Figure 4.3(a). The interpolation functions $\boldsymbol{\phi}_i|_{\Omega_k}$, whose components $\phi_{1i}|_{\Omega_k}$, $\phi_{2i}|_{\Omega_k}$, and $\phi_{3i}|_{\Omega_k}$ read

$$
\begin{aligned}
\phi_{11}|_{\Omega_k} = \phi_{21}|_{\Omega_k} = \phi_{31}|_{\Omega_k} &= (1-x_1)(1-x_2)(1-x_3) \\
\phi_{12}|_{\Omega_k} = \phi_{22}|_{\Omega_k} = \phi_{32}|_{\Omega_k} &= x_1(1-x_2)(1-x_3) \\
\phi_{13}|_{\Omega_k} = \phi_{23}|_{\Omega_k} = \phi_{33}|_{\Omega_k} &= x_1x_2(1-x_3) \\
\phi_{14}|_{\Omega_k} = \phi_{24}|_{\Omega_k} = \phi_{34}|_{\Omega_k} &= (1-x_1)x_2(1-x_3) \\
\phi_{15}|_{\Omega_k} = \phi_{25}|_{\Omega_k} = \phi_{35}|_{\Omega_k} &= (1-x_1)(1-x_2)x_3 \\
\phi_{16}|_{\Omega_k} = \phi_{26}|_{\Omega_k} = \phi_{36}|_{\Omega_k} &= x_1(1-x_2)x_3 \\
\phi_{17}|_{\Omega_k} = \phi_{27}|_{\Omega_k} = \phi_{37}|_{\Omega_k} &= x_1x_2x_3 \\
\phi_{18}|_{\Omega_k} = \phi_{28}|_{\Omega_k} = \phi_{38}|_{\Omega_k} &= (1-x_1)x_2x_3,
\end{aligned}
$$

have a trilinear behavior on Ω_k, satisfy $\boldsymbol{\phi}_1|_{\Omega_k}(\mathbf{x}_j) = \delta_{ij}$, and span the space $Q_1(\bar{\Omega}_k)$ of all trilinear polynomials in x_1, x_2, and x_3 [25]. With this type of finite elements, $3(N+1)^3$ degrees-of-freedom result for a grid comprising $N \times N \times N$ finite elements.

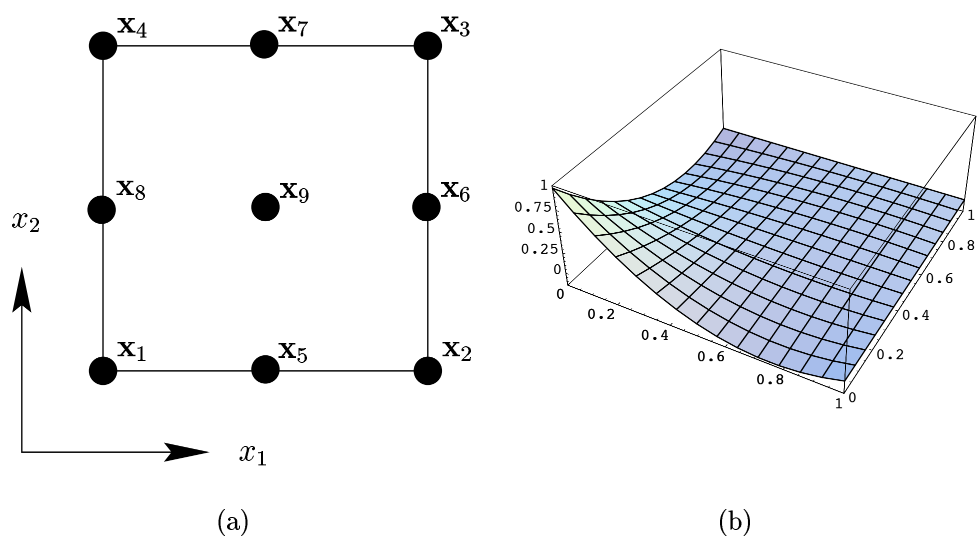

Figure 4.4: 2D biquadratic finite element (a) and the interpolation function $\phi_{11}|_{\Omega_k}$ (b).

2D biquadratic finite element

Another useful finite element is the biquadratic finite element shown in Figure 4.4(a). Here, the components of the interpolation functions $\boldsymbol{\phi}_i|_{\Omega_k}$ with respect to the nine nodal points are defined by

$$
\begin{aligned}
\phi_{11}|_{\Omega_k} = \phi_{21}|_{\Omega_k} &= (1-x_1)(1-2x_1)(1-x_2)(1-2x_2)\\
\phi_{12}|_{\Omega_k} = \phi_{22}|_{\Omega_k} &= x_1(2x_1-1)(1-x_2)(1-2x_2)\\
\phi_{13}|_{\Omega_k} = \phi_{23}|_{\Omega_k} &= x_1(2x_1-1)x_2(2x_2-1)\\
\phi_{14}|_{\Omega_k} = \phi_{24}|_{\Omega_k} &= (1-x_1)(1-2x_1)x_2(2x_2-1)\\
\phi_{15}|_{\Omega_k} = \phi_{25}|_{\Omega_k} &= 4x_1(1-x_1)(1-x_2)(1-2x_2)\\
\phi_{16}|_{\Omega_k} = \phi_{26}|_{\Omega_k} &= x_1(2x_1-1)4x_2(1-x_2)\\
\phi_{17}|_{\Omega_k} = \phi_{27}|_{\Omega_k} &= 4x_1(1-x_1)x_2(2x_2-1)\\
\phi_{18}|_{\Omega_k} = \phi_{28}|_{\Omega_k} &= (1-x_1)(1-2x_1)4x_2(1-x_2)\\
\phi_{19}|_{\Omega_k} = \phi_{29}|_{\Omega_k} &= 4x_1(1-x_1)4x_2(1-x_2),
\end{aligned}
$$

leading to interpolation functions $\boldsymbol{\phi}_i|_{\Omega_k}$ which have a biquadratic behavior on Ω_k and satisfy $\boldsymbol{\phi}_i|_{\Omega_k}(\mathbf{x}_j) = \delta_{ij}$. Figure 4.4(b) depicts the interpolation function $\boldsymbol{\phi}_{11}(\Omega_k)$. The space spanned by these functions is the space $Q_2(\bar{\Omega}_k)$

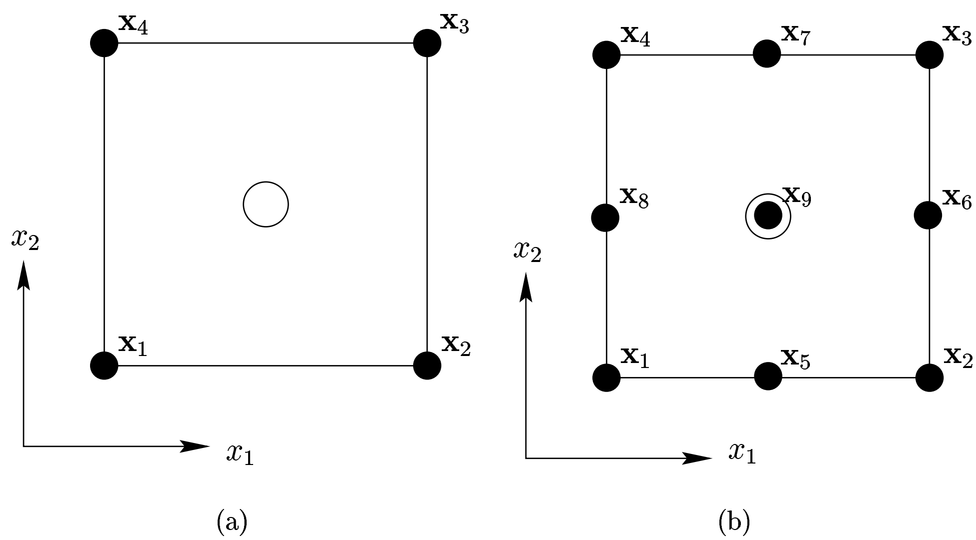

Figure 4.5: 2D Q_1-P_0 Crouzeix-Raviart element (a) with four nodal points (•) for a bilinear velocity approximation and one nodal point (◯) for a constant pressure approximation. In (b), the Q_2-P_1 Crouzeix-Raviart element with nine nodal points (•) for a biquadratic velocity approximation and one nodal point (◯), including two derivatives, for the linear pressure approximation is depicted.

[25]. The use of these finite elements results in $2(2N+1)^2$ degrees-of-freedom for a grid containing $N \times N$ elements.

2D Crouzeix-Raviart finite element

For a solution of the Stokes equation, *mixed finite elements* are commonly used [25, 58] which allow a simultaneous approximation of both underlying spaces $V(\Omega)$ and $W(\Omega)$, i.e. this type of finite elements allows to define multiple types of basis functions on the same area Ω_k. The simplest possible choice in this case is the so-called Q_1-P_0 *Crouzeix-Raviart* finite element depicted in Figure 4.5(a), with linear basis functions $\boldsymbol{\phi}_i|_{\Omega_k}$ for the velocity and constant basis functions $\psi_i|_{\Omega_k}$ for the pressure approximation, respectively. But for this element, it can be shown that the Babuška-Brezzi condition (4.47), necessary to ensure the solvability of the problem, is not satisfied thus numerically unstable results have to be expected [7].

To circumvent this problem, finite elements with higher order interpolation functions have to be used. One of the best known elements is the quadrilateral Q_2-P_1 *Crouzeix-Raviart* element shown in Figure 4.5(b). This element has the common biquadratic interpolation functions $\boldsymbol{\phi}_i|_{\Omega_k}$ for the velocity approximation and a linear, discontinuous pressure approximation, including two derivatives [25]. Therefore, the pressure p is approximated by a Taylor-series expansion up to order one at the midpoint $\mathbf{x}_9$ of the Crouzeix-Raviart element, i.e.

$$\tilde{p} = \tilde{p}(\mathbf{x}_9)\psi_1|_{\Omega_k} + \partial_1\tilde{p}(\mathbf{x}_9)\psi_2|_{\Omega_k} + \partial_2\tilde{p}(\mathbf{x}_9)\psi_3|_{\Omega_k}, \tag{4.60}$$

with interpolation functions

$$\begin{aligned} \psi_1|_{\Omega_k} &= 1 \\ \psi_2|_{\Omega_k} &= x_1 - \mathrm{x}_{19} \\ \psi_3|_{\Omega_k} &= x_2 - \mathrm{x}_{29}. \end{aligned} \tag{4.61}$$

Here, x_{i9} denotes the i-th component of the midpoint $\mathbf{x}_9$ of the Crouzeix-Raviart finite element.

In contrast to the velocity basis functions $\boldsymbol{\phi}_i$, whose support includes four neighboring finite elements, the support of the pressure basis functions ψ_i is limited to a single finite element only, i.e. $\psi_i = \psi_j|_{\Omega_k}$. The total number of degrees-of-freedom for this type of finite elements in a $N \times N$ grid is $2(2N+1)^2 + 3N^2$, with $2(2N+1)^2$ degrees-of-freedom for the velocity approximation and $3N^2$ degrees-of-freedom for the pressure approximation.

2D divergence-free finite element

A problem with the usage of Q_2-P_1 Crouzeix-Raviart finite elements while solving the Stokes equation is the large number of associated degrees-of-freedom which amount to 21 degrees-of-freedom per element in the 2D case. Additionally, the resulting global stiffness matrix $\mathbf{A}$ lacks the necessary positive definiteness [7, 95] and has a very large profile, i.e. the nonzero entries of the matrix in (4.52) are widely spreaded, such that iterative methods like the *conjugate gradient method* (CG) [25] cannot be applied. To improve the numerical properties of the Stokes problem, so called *solenoidal* or *divergence-free* finite elements can be used which allow a decoupling of pressure and velocity. As a result, the total number of degrees-of-freedom shrinks thus leading to smaller matrix systems with numerical properties such that iterative solution methods can be applied [25]. If necessary, the pressure can be calculated once the velocities have been determined.

The abstract Stokes problem (4.41) can be rewritten if the underlying Sobolev space $H^1(\Omega)$ is orthogonally decomposed into

$$H^1(\Omega) = S(\Omega) \oplus I(\Omega), \tag{4.62}$$

where the subspace $S(\Omega)$ contains all weakly solenoidal functions,

$$S(\Omega) = \{\mathbf{w} : \Omega \longrightarrow \mathbb{R}; \mathbf{w} \in H^1(\Omega), \int_\Omega q \,\mathrm{div}[\mathbf{w}] d\Omega = 0, \ \ \forall q \in W(\Omega)\}, \tag{4.63}$$

and the subspace $I(\Omega)$ is the complement of $S(\Omega)$ in $H^1(\Omega)$ [55, 56, 57, 58]. Note, that the functions $\mathbf{w} \in S(\Omega)$ are not pointwise divergence-free, but divergence-free in the mean. It follows from the definition, that $S(\Omega)$ represents the complete solution space of the abstract problem (4.41) [57], and consequently it is sufficient to use basis functions $\mathbf{\Phi}_i$ which span the solenoidal subspace $S(\Omega)$ only. With these modifications, the abstract problem reduces to [56, 152]: Find $\mathbf{v} \in S(\Omega)$ such that

$$a(\mathbf{v}, \mathbf{w}) = f(\mathbf{w}), \quad \ \forall \mathbf{w} \in S(\Omega). \tag{4.64}$$

Once the solution $\mathbf{v}$ has been calculated, the remaining subspace $I(\Omega)$ can be used to determine the corresponding pressure $p \in W(\Omega)$ [56, 25, 152]:

$$b(p, \mathbf{w}) = f(\mathbf{w}) - a(\mathbf{v}, \mathbf{w}), \quad \ \forall \mathbf{w} \in I(\Omega). \tag{4.65}$$

To construct a set of basis functions $\mathbf{\Phi}_i$ which approximate the solenoidal subspace $S(\Omega)$, the spatially limited support of the pressure basis functions is exploited thus allowing an elementwise analysis of the incompressibility constraint (4.43) [57, 25]. By taking the constant pressure interpolation function $\psi_1|_{\Omega_k}$ into account, the incompressibility constraint reduces to

$$\int_{\Omega_k} \mathrm{div}[\tilde{\mathbf{v}}] d\Omega_k = 0 \tag{4.66}$$

which can be written by virtue of (4.37) as

$$\sum_{i=1}^{4} \int_{\Gamma_{ki}} (\tilde{\mathbf{v}}, \mathbf{n}) d\Gamma_{ki} = 0, \tag{4.67}$$

if the boundary Γ_k has been splitted into four straight sides Γ_{ki} according to Figure 4.6.

From (4.67) it is clear that only interpolation functions $\boldsymbol{\phi}_{\mathbf{n}i}|_{\Omega_k}$ belonging to the normal components of each side Γ_{ki} have to be replaced while the tangential components $\boldsymbol{\phi}_{\mathbf{t}i}|_{\Omega_k}$ always satisfy (4.67). To that end, a *stream function* $\tilde{\boldsymbol{\psi}} = (0, 0, \tilde{\psi})^T$ satisfying

$$\tilde{\mathbf{v}} = \mathrm{curl}[\tilde{\boldsymbol{\psi}}] = \begin{pmatrix} \partial_2 \tilde{\psi} \\ -\partial_1 \tilde{\psi} \end{pmatrix}, \tag{4.68}$$

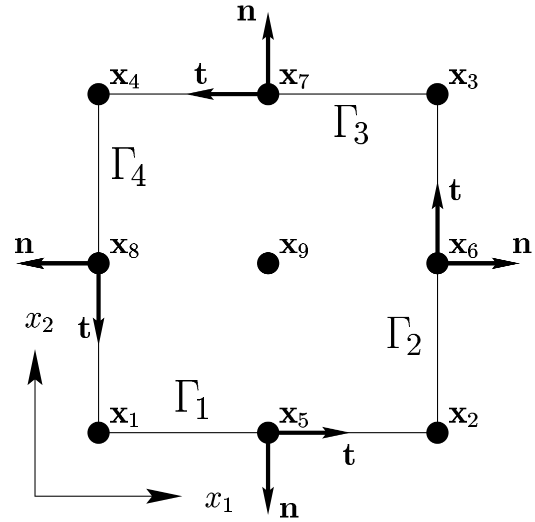

Figure 4.6: The complete notation of a nine node quadrilateral finite element, necessary to derive a divergence-free finite element.

is introduced which implies $\int_\Omega \operatorname{div}[\operatorname{curl}[\tilde{\boldsymbol{\psi}}]]d\Omega = 0$ [12]. It follows from (4.68), that $(\tilde{\mathbf{v}}, \mathbf{n}) = (\nabla\tilde{\psi}, \mathbf{t})$ holds, due to the relation between $\mathbf{n}$ and the unit tangential vector $\mathbf{t}$ of Γ_k. Then the integral (4.67) has for each side the general solution [56, 57, 25]

$$\int_{\Gamma_{ki}} (\tilde{\mathbf{v}}, \mathbf{n}) d\Gamma_{ki} = \tilde{\psi}_{i+1} - \tilde{\psi}_i, \tag{4.69}$$

where the $\tilde{\psi}_i$ denotes the value of the potential function $\tilde{\boldsymbol{\psi}}$ at the nodal points $\mathbf{x}_i$ belonging to the vertices of the side Γ_{ki}. Note, that $\tilde{\psi}_5 := \tilde{\psi}_1$ holds for $i = 4$ in equation (4.69).

The integral appearing on the left side of (4.69) can be further evaluated with the aid of *Simpson's rule* [144]

$$\int_{\Gamma_{ki}} \mathbf{a}\, d\Gamma_{ki} = \frac{||\Gamma_{ki}||}{6} \left(\mathbf{a}(\mathbf{x}_i) + \mathbf{a}(\mathbf{x}_{i+1}) + 4\mathbf{a}(\frac{\mathbf{x}_i + \mathbf{x}_{i+1}}{2}) \right), \tag{4.70}$$

thus allowing an elimination of the normal components at each mid-side node in favour of the potential function $\tilde{\boldsymbol{\psi}}$. Assuming a unit length $||\Gamma_{ki}||$ for all sides Γ_{ki} of element Ω_k gives

$$\tilde{v}_{\mathbf{n}5} = -\frac{1}{4}\left(\tilde{v}_{\mathbf{n}1} + \tilde{v}_{\mathbf{n}2}\right) + \frac{3}{2}\left(\tilde{\psi}_2 - \tilde{\psi}_1\right) \quad (4.71)$$

$$\tilde{v}_{\mathbf{n}6} = -\frac{1}{4}\left(\tilde{v}_{\mathbf{n}2} + \tilde{v}_{\mathbf{n}3}\right) + \frac{3}{2}\left(\tilde{\psi}_3 - \tilde{\psi}_2\right) \quad (4.72)$$

$$\tilde{v}_{\mathbf{n}7} = -\frac{1}{4}\left(\tilde{v}_{\mathbf{n}3} + \tilde{v}_{\mathbf{n}4}\right) + \frac{3}{2}\left(\tilde{\psi}_4 - \tilde{\psi}_3\right) \quad (4.73)$$

$$\tilde{v}_{\mathbf{n}8} = -\frac{1}{4}\left(\tilde{v}_{\mathbf{n}4} + \tilde{v}_{\mathbf{n}1}\right) + \frac{3}{2}\left(\tilde{\psi}_1 - \tilde{\psi}_4\right), \quad (4.74)$$

where the index of $\tilde{v}_{\mathbf{n}i}$ denotes the normal component of the ith node.

Furthermore, the center node $\mathbf{x}_9$ can be eliminated through the remaining pressure interpolation functions. Substitution of $\psi_2|_{\Omega_k}$ and $\psi_3|_{\Omega_k}$ into the incompressibility constraint,

$$\int_{\Omega_k} (x_1 - \mathrm{x}_{19})\mathrm{div}[\tilde{\mathbf{v}}]d\Omega_k = \int_{\Omega_k} (x_2 - \mathrm{x}_{29})\mathrm{div}[\tilde{\mathbf{v}}]d\Omega_k = 0, \quad (4.75)$$

followed by an integration by parts, yields for the x_1-direction [57, 25]

$$\sum_{i=1}^{4} \int_{\Gamma_{ki}} (x_1 - \mathrm{x}_{19})(\tilde{\mathbf{v}}, \mathbf{n})d\Gamma_{ki} - \int_{\Omega_k} \tilde{v}_1 d\Omega_k = 0 \quad (4.76)$$

and for the x_2-direction

$$\sum_{i=1}^{4} \int_{\Gamma_{ki}} (x_2 - \mathrm{x}_{29})(\tilde{\mathbf{v}}, \mathbf{n})d\Gamma_{ki} - \int_{\Omega_k} \tilde{v}_2 d\Omega_k = 0. \quad (4.77)$$

A repeated evaluation of all these integrals by Simpson's rule and substitution of (4.71)-(4.74) leads to the identities

$$4\tilde{v}_{19} = -\tilde{v}_{\mathbf{t}5} + \tilde{v}_{\mathbf{t}7} - \frac{3}{4}(\tilde{v}_{\mathbf{n}1} - \tilde{v}_{\mathbf{n}2} - \tilde{v}_{\mathbf{n}3} + \tilde{v}_{\mathbf{n}4}) - 3(\tilde{\psi}_1 + \tilde{\psi}_2 - \tilde{\psi}_3 - \tilde{\psi}_4) \quad (4.78)$$

and

$$4\tilde{v}_{29} = -\tilde{v}_{\mathbf{t}6} + \tilde{v}_{\mathbf{t}8} - \frac{3}{4}(\tilde{v}_{\mathbf{n}1} + \tilde{v}_{\mathbf{n}2} - \tilde{v}_{\mathbf{n}3} - \tilde{v}_{\mathbf{n}4}) + 3(\tilde{\psi}_1 - \tilde{\psi}_2 - \tilde{\psi}_3 + \tilde{\psi}_4). \quad (4.79)$$

After expressing all $\tilde{v}_{\mathbf{n}i}$ in terms of the usual coefficients $\tilde{v}_{ji}$, the divergence-free interpolation functions $\mathbf{\Phi}_i|_{\Omega_k}$ can be obtained by substitution of (4.71)-(4.74) and (4.78)-(4.79) into the approximation

$$\tilde{\mathbf{v}} = \sum_{i=1}^{9} \left(\tilde{v}_{1i}\boldsymbol{\phi}_{1i}|_{\Omega_k} + \tilde{v}_{2i}\boldsymbol{\phi}_{2i}|_{\Omega_k}\right), \quad (4.80)$$

where the components of the interpolation functions $\boldsymbol{\phi}_i|_{\Omega_k}$ are defined according to Section 4.3.2, which is then solved for the new coefficients $\tilde{v}_{ji}$, $\tilde{v}_{\mathbf{t}i}$ and $\tilde{\psi}_i$. The resulting approximation

$$\tilde{\mathbf{v}} = \sum_{i=1}^{4} \left(\tilde{v}_{1i} \boldsymbol{\Phi}_{1i}|_{\Omega_k} + \tilde{v}_{2i} \boldsymbol{\Phi}_{2i}|_{\Omega_k} + \tilde{v}_{\mathbf{t}i} \boldsymbol{\Phi}_{\mathbf{t}i}|_{\Omega_k} + \tilde{\psi}_i \boldsymbol{\Phi}_{\psi i}|_{\Omega_k} \right) \tag{4.81}$$

contains only divergence-free interpolation functions which read

$$\begin{aligned}
\boldsymbol{\Phi}_{11}|_{\Omega_k} &= \begin{pmatrix} \phi_{11}|_{\Omega_k} - \frac{1}{4}\phi_{18}|_{\Omega_k} \\ \frac{3}{16}\phi_{29}|_{\Omega_k} \end{pmatrix} &
\boldsymbol{\Phi}_{21}|_{\Omega_k} &= \begin{pmatrix} \frac{3}{16}\phi_{19}|_{\Omega_k} \\ \phi_{21}|_{\Omega_k} - \frac{1}{4}\phi_{25}|_{\Omega_k} \end{pmatrix} \\
\boldsymbol{\Phi}_{12}|_{\Omega_k} &= \begin{pmatrix} \phi_{12}|_{\Omega_k} - \frac{1}{4}\phi_{16}|_{\Omega_k} \\ -\frac{3}{16}\phi_{29}|_{\Omega_k} \end{pmatrix} &
\boldsymbol{\Phi}_{22}|_{\Omega_k} &= \begin{pmatrix} -\frac{3}{16}\phi_{19}|_{\Omega_k} \\ \phi_{22}|_{\Omega_k} - \frac{1}{4}\phi_{25}|_{\Omega_k} \end{pmatrix} \\
\boldsymbol{\Phi}_{13}|_{\Omega_k} &= \begin{pmatrix} \phi_{13}|_{\Omega_k} - \frac{1}{4}\phi_{16}|_{\Omega_k} \\ \frac{3}{16}\phi_{29}|_{\Omega_k} \end{pmatrix} &
\boldsymbol{\Phi}_{23}|_{\Omega_k} &= \begin{pmatrix} \frac{3}{16}\phi_{19}|_{\Omega_k} \\ \phi_{23}|_{\Omega_k} - \frac{1}{4}\phi_{27}|_{\Omega_k} \end{pmatrix} \\
\boldsymbol{\Phi}_{14}|_{\Omega_k} &= \begin{pmatrix} \phi_{14}|_{\Omega_k} - \frac{1}{4}\phi_{18}|_{\Omega_k} \\ -\frac{3}{16}\phi_{29}|_{\Omega_k} \end{pmatrix} &
\boldsymbol{\Phi}_{24}|_{\Omega_k} &= \begin{pmatrix} -\frac{3}{16}\phi_{19}|_{\Omega_k} \\ \phi_{24}|_{\Omega_k} - \frac{1}{4}\phi_{27}|_{\Omega_k} \end{pmatrix} \\
\boldsymbol{\Phi}_{\mathbf{t}1}|_{\Omega_k} &= \begin{pmatrix} \phi_{15}|_{\Omega_k} - \frac{1}{4}\phi_{19}|_{\Omega_k} \\ 0 \end{pmatrix} &
\boldsymbol{\Phi}_{\mathbf{t}2}|_{\Omega_k} &= \begin{pmatrix} 0 \\ \phi_{26}|_{\Omega_k} - \frac{1}{4}\phi_{29}|_{\Omega_k} \end{pmatrix} \\
\boldsymbol{\Phi}_{\mathbf{t}3}|_{\Omega_k} &= \begin{pmatrix} -\phi_{17}|_{\Omega_k} + \frac{1}{4}\phi_{19}|_{\Omega_k} \\ 0 \end{pmatrix} &
\boldsymbol{\Phi}_{\mathbf{t}4}|_{\Omega_k} &= \begin{pmatrix} 0 \\ -\phi_{28}|_{\Omega_k} + \frac{1}{4}\phi_{29}|_{\Omega_k} \end{pmatrix} \\
\boldsymbol{\Phi}_{\psi 1}|_{\Omega_k} &= \frac{3}{2}\begin{pmatrix} -\phi_{18}|_{\Omega_k} - \frac{1}{2}\phi_{19}|_{\Omega_k} \\ \phi_{25}|_{\Omega_k} + \frac{1}{2}\phi_{29}|_{\Omega_k} \end{pmatrix} &
\boldsymbol{\Phi}_{\psi 2}|_{\Omega_k} &= \frac{3}{2}\begin{pmatrix} -\phi_{16}|_{\Omega_k} - \frac{1}{2}\phi_{19}|_{\Omega_k} \\ -\phi_{25}|_{\Omega_k} - \frac{1}{2}\phi_{29}|_{\Omega_k} \end{pmatrix} \\
\boldsymbol{\Phi}_{\psi 3}|_{\Omega_k} &= \frac{3}{2}\begin{pmatrix} \phi_{16}|_{\Omega_k} + \frac{1}{2}\phi_{19}|_{\Omega_k} \\ -\phi_{27}|_{\Omega_k} - \frac{1}{2}\phi_{29}|_{\Omega_k} \end{pmatrix} &
\boldsymbol{\Phi}_{\psi 4}|_{\Omega_k} &= \frac{3}{2}\begin{pmatrix} \phi_{18}|_{\Omega_k} + \frac{1}{2}\phi_{19}|_{\Omega_k} \\ \phi_{27}|_{\Omega_k} + \frac{1}{2}\phi_{29}|_{\Omega_k} \end{pmatrix}.
\end{aligned}$$

The interpolation functions $\boldsymbol{\Phi}_{\mathbf{t}i}|_{\Omega_k}$ and $\boldsymbol{\Phi}_{\psi i}|_{\Omega_k}$ are characterized by the properties that [25]

- both have components that are linear in x_1 and x_2,
- $\boldsymbol{\Phi}_{\mathbf{t}i}|_{\Omega_k} = \mathbf{0}$ on all sides of the quadrilateral element not containing the node i,
- $\boldsymbol{\Phi}_{\mathbf{t}i}|_{\Omega_k} = \mathbf{t}_i$ at the midside node i,
- $\boldsymbol{\Phi}_{\psi i}|_{\Omega_k} = \mathbf{0}$ on the side opposite to vertex i, and
- $\boldsymbol{\Phi}_{\psi i}|_{\Omega_k} = \pm\mathbf{n}_i/||\Gamma_{ki}||$ at the two mid-side nodes of the sides containing the vertex i (the sign is such that it is opposite for these two nodes).

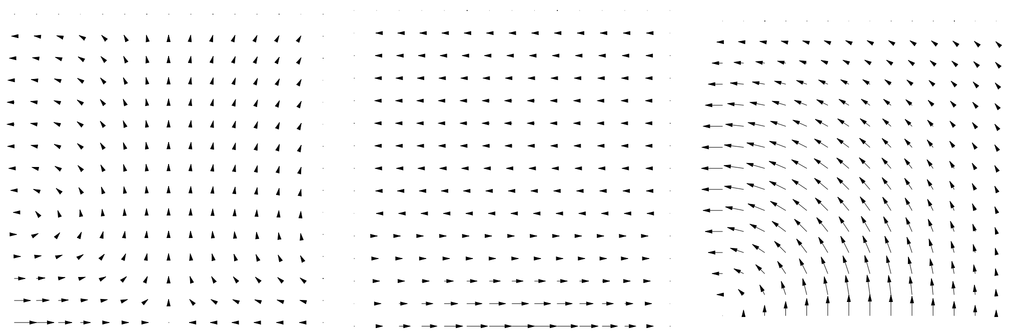

(a) (b) (c)

Figure 4.7: The vector-valued interpolation functions (a) $\mathbf{\Phi}_{11}|_{\Omega_k}$, (b) $\mathbf{\Phi}_{\mathbf{t}5}|_{\Omega_k}$ and (c) $\mathbf{\Phi}_{1\psi}|_{\Omega_k}$.

Figure 4.7 depicts sketches of some of the divergence-free interpolation functions. Note, that these functions are vector-valued functions and therefore have been represented by vectors in Figure 4.7.

To construct the divergence-free basis functions $\mathbf{\Phi}_{\mathbf{t}i}$, some caution is required since the interpolation functions $\mathbf{\Phi}_{\mathbf{t}i}|_{\Omega_k}$ are derived assuming outward normals at each finite element, as indicated in Figure 4.6. But the outward normal at a side Γ_{ki} of a finite element Ω_k corresponds to the inward normal of the adjacent finite element Ω_l that shares that side. There is no difficulty, however, if the tangential vector $\mathbf{t}_i$ is assigned in a unique sense, i.e. the interpolation function $\mathbf{\Phi}_{\mathbf{t}i}|_{\Omega_l}$ must be modified by a multiplication with -1 to ensure the continuity of the resulting basis functions $\mathbf{\Phi}_{\mathbf{t}i}$.

With these divergence-free basis functions, the linear matrix system

$$\mathbf{A}_d\tilde{\mathbf{v}}_d = \mathbf{f}_d + \mathbf{g}_d \tag{4.82}$$

can be directly computed from (4.64). But now, the solution vector $\tilde{\mathbf{v}}_d$ contains values for $\tilde{\psi}_i$ and $\tilde{v}_{\mathbf{t}i}$ instead of the original unknowns $\tilde{v}_{1i}$ and $\tilde{v}_{2i}$. Therefore, the stiffness matrix $\mathbf{A}_d$ is usually derived from the original system

$$\begin{aligned} \mathbf{A}\tilde{\mathbf{v}} + \mathbf{P}\tilde{\mathbf{p}} &= \mathbf{f} + \mathbf{g} \\ \mathbf{P}^T\tilde{\mathbf{v}} &= \mathbf{0}, \end{aligned} \tag{4.83}$$

where $\mathbf{A}$ and $\mathbf{P}$ denote the submatrices of (4.52) containing all matrices related to the displacement and pressure terms, respectively [56, 25, 152]. As pointed out, the construction of divergence-free finite elements implies the introduction of new unknowns $\tilde{\mathbf{v}}_d$ which are related to the original unknowns $\tilde{\mathbf{v}}$ through

$$\tilde{\mathbf{v}} = \mathbf{R}_d \tilde{\mathbf{v}}_d, \tag{4.84}$$

where the transformation matrix $\mathbf{R}_d$ can be constructed from the identities (4.71)-(4.74) and (4.78)-(4.79). For adjacent finite elements Ω_k and Ω_l, $\mathbf{R}_d$ must be manipulated such that the tangential vector $\mathbf{t}_j$ is uniquely assigned at the common boundary Γ_{kl}. Since the continuity equation

$$\mathbf{P}^T \tilde{\mathbf{v}} = \mathbf{P}^T \mathbf{R}_d \tilde{\mathbf{v}}_d = \mathbf{0} \tag{4.85}$$

must be valid for all $\tilde{v}_d$, it is necessary that

$$\mathbf{P}^T \mathbf{R}_d = \mathbf{0} \tag{4.86}$$

holds [56, 25]. Substitution of (4.84) into (4.83) and pre-multiplication by $\mathbf{R}_d^T$ gives

$$\mathbf{R}_d^T \mathbf{A} \mathbf{R}_d \tilde{\mathbf{v}}_d + \underbrace{\mathbf{R}_d^T \mathbf{P} \tilde{\mathbf{p}}}_{=\mathbf{0}^T} = \mathbf{R}_d^T \mathbf{f} + \mathbf{R}_d^T \mathbf{g}. \tag{4.87}$$

A comparison with (4.82) reveals that

$$\begin{aligned} \mathbf{A}_d &= \mathbf{R}_d^T \mathbf{A} \mathbf{R}_d \\ \mathbf{f}_d + \mathbf{g}_d &= \mathbf{R}_d^T \mathbf{f} + \mathbf{R}_d^T \mathbf{g} \end{aligned} \tag{4.88}$$

holds, i.e. a linear matrix system for divergence-free basis functions can be constructed if the transformation matrix $\mathbf{R}_d$ is known. Once the solution $\tilde{\mathbf{v}}_d$ has been calculated, it can be transformed into the original unknowns $\tilde{\mathbf{v}}$ by a simple pre-multiplication with $\mathbf{R}_d$.

The total number of degrees-of-freedom for a $N \times N$ grid of divergence-free finite elements is $2(N+1)(2N+1)+(N+1)^2$, with $2(N+1)(2N+1)$ degrees-of-freedom for the velocity components and $(N+1)^2$ degrees-of-freedom for the stream function.

4.3.3 Computational complexity of fluid problems

The solution of a fluid problem using divergence-free finite elements leads to a significant reduction of the space and time requirements compared to the Q_2-P_1 Crouzeix-Raviart finite elements. As summarized in Table 4.1, the divergence-free finite elements reduce the number of degrees-of-freedom

element type	elements	DOF	memory	time
Q_2-P_1 Crouzeix-Raviart finite elements	30×30	10142	792 MB	≈ 35 h
	40×40	17922	> 1.5 GB	—
	256×256	722946	—	—
divergence-free finite elements	30×30	4743	11 MB	≈ 1.5 min
	40×40	8323	12 MB	≈ 5.6 min
	256×256	329731	256 MB	≈ 28 h

Table 4.1: Comparison of the memory and time requirements for solving fluid problems with a different number of finite elements while using Q_2-P_1 Crouzeix-Raviart finite elements or divergence-free finite elements, respectively. With DOF, we denote the number of degrees-of-freedom of the finite element mesh. A hyphen indicates, that no value has been determined.

approximately by half, if the number of finite elements in each direction remains constant. The exact difference in degrees-of-freedom between Q_2-P_1 Crouzeix-Raviart finite elements and divergence-free finite elements counts to $2(2N+1)^2+3N^2-(2(N+1)(2N+1)+(N+1)^2) = 6N^2-1$. According to the improved numerical properties of the stiffness matrix $\mathbf{A}$ when using divergence-free finite elements, the amount of memory space drops also significantly such that 2D images of sizes 256×256 pixel can be handled since sparse matrix storage schemes may be applied. Also, the computation times using divergence-free finite elements are several orders of magnitude smaller compared to Q_2-P_1 Crouzeix-Raviart finite elements due to the possibility of applying iterative solution methods. In case of the latter type of finite elements, the huge amount of more than 1.5 GB storage space for the final linear matrix system usually prevents an application of fluid models to finite element mesh sizes larger than 40×40 elements.

4.4 Inhomogeneous materials

4.4.1 Physical theory

So far, we presented the physical theory necessary to determine the deformation of a *homogeneous* body Ω only, i.e. a body whose *response function* is independent of $\mathbf{x} \in \bar{\Omega}$. But based on the results of Section 4.1, it turns out that a reliable simulation of a composite anatomical structure consisting of skull bone, brain tissue, and cerebrospinal fluid demands the usage of different constitutive equations, namely Hooke's law (2.37) and the Navier-Poisson law (2.42), respectively. According to Section 2.2, a substitution of these constitutive equations into the equilibrium equation (2.29) leads either to the Navier equation as description of the physical deformation behavior of skull bone and brain tissue or to the Stokes equation simulating the physical deformation behavior of cerebrospinal fluid. To model such *inhomogeneous* structures, which refers to the case where the response function depends on the spatial coordinates of a particular point $\mathbf{x} \in \bar{\Omega}$, we decompose the inhomogeneous body Ω into a finite number M of homogeneous regions Ω_i. Note, that no relationship between the regions Ω_i and finite elements Ω_k exists since each of the former one corresponds to a specific anatomical structure of the modeled biological organ while the latter one simply divides an inhomogeneous body Ω (or even a homogeneous region Ω_i) into a set of areas, irrespectively of the underlying anatomical structure of Ω. Denoting with $\bar{\Omega}_i$ the closure of the region Ω_i, the decomposition of the inhomogeneous body Ω into a finite number M of homogeneous regions must satisfy the following properties

- $\cup_i \bar{\Omega}_i = \bar{\Omega}$, $1 \leq i \leq M$,
- $\Omega_i \cap \Omega_j = \emptyset$ if $i \neq j$, and
- $\bar{\Omega}_i \cap \bar{\Omega}_j = \Gamma_{ij}$ if Ω_i and Ω_j have a common boundary Γ_{ij}.

A physical interaction in the sense of a mutual deformation between two neighboring regions Ω_i and Ω_j takes place through their common surface Γ_{ij} only, or, in other words, the boundary conditions applied to Γ_{ij} completely determine the physical deformation behavior of the connected regions [47].

In the state of equilibrium between two adjacent regions Ω_i and Ω_j, the sum of applied surface forces $\mathbf{g}$ along Γ_{ij} must be zero as a consequence of Newtons third law [47]. With (2.24), this can be likewise expressed in terms of the Cauchy stress vector $\mathbf{t}$. Therefore, the stress vector $\mathbf{t}_i$ acting at an arbitrary point $\mathbf{x} \in \Gamma_{ij}$ on the surface of Ω_i must be equal to the stress vector $\mathbf{t}_j$ acting on the surface of Ω_j, hence

$$\mathbf{t}_i(\mathbf{x}, \mathbf{n}) = \mathbf{t}_j(\mathbf{x}, \mathbf{n}), \quad \forall \mathbf{x} \in \Gamma_{ij} \tag{4.89}$$

must hold. Equation (4.89) is also known as *equilibrium boundary condition* [8, 77, 47].

A rather similar boundary condition at Γ_{ij} exists for the displacement fields $\mathbf{u}_i(\mathbf{x})$ and $\mathbf{u}_j(\mathbf{x})$ at the common boundary between two solid regions Ω_i and Ω_j, known as *compatibility condition* [8, 77]. This condition simply states that the displacements at the common boundary should be equal:

$$\mathbf{u}_i(\mathbf{x}) = \mathbf{u}_j(\mathbf{x}), \quad \forall \mathbf{x} \in \Gamma_{ij}. \tag{4.90}$$

In contrast to the boundary between two solid regions, the validity of (4.90) at a boundary between a solid and a fluid depends on the physical properties of both materials. If the solid is impermeable for the fluid, the latter one must not penetrate the solid. Mathematically, this requires that the relative velocity component of the fluid normal to the surface Γ_{ij} must vanish, i.e.

$$\mathbf{J}(\mathbf{v})\mathbf{n} = \mathbf{0}, \quad \forall \mathbf{x} \in \Gamma_{ij} \tag{4.91}$$

must hold [100, 47]. Here, $\mathbf{J}(\mathbf{v})$ denotes the velocity gradient according to (2.2) and $\mathbf{n}$ the unit outward vector of the surface Γ_{ij}. This boundary condition is also known as *no-penetration condition*. Additionally, the *no-slip condition* [47] prevents from a tangential movement of viscous fluids at the common boundary Γ_{ij}, while non-viscous fluids[3] are permitted to slide along the surface, resulting in different tangential components of the velocity. In conjunction with (2.45), it becomes clear, that the compatibility condition (4.90) holds for non-penetrating, viscous fluids only, as in the case of the boundary between brain tissue and cerebrospinal fluid.

Collecting all conditions together, the physical deformation behavior of an inhomogeneous body $\Omega = \Omega_i \cup \Omega_j$ comprising an elastic solid Ω_i, which is modeled by the Navier equation

$$(\lambda + \mu)\nabla \mathrm{div}[\mathbf{u}_i] + \mu\nabla^2\mathbf{u}_i + \mathbf{f} = \mathbf{0} \quad \text{in } \Omega_i, \tag{4.92}$$

and an incompressible, no-penetrating, and viscous fluid Ω_j, modeled by the Stokes equation

$$-\nabla p + \mu^\star dt^{-1}\nabla^2\mathbf{u}_j + \mathbf{f} = \mathbf{0} \quad \text{in } \Omega_j, \tag{4.93}$$

can be completely described through the coupled system

$$\begin{cases} (\lambda + \mu)\nabla \mathrm{div}[\mathbf{u}_i] + \mu\nabla^2\mathbf{u}_i + \mathbf{f} = \mathbf{0} & \text{in } \Omega_i, \\ \mathbf{t}_i = \mathbf{t}_j & \text{on } \Gamma_{ij}, \\ \mathbf{u}_i = \mathbf{u}_j & \text{on } \Gamma_{ij}, \\ -\nabla p + \mu^\star dt^{-1}\nabla^2\mathbf{u}_j + \mathbf{f} = \mathbf{0} & \text{in } \Omega_j, \end{cases} \tag{4.94}$$

provided that infinitesimal displacement fields as well as time intervals dt are considered such that

$$\mathbf{u}_j = \mathbf{v}_j dt \tag{4.95}$$

[3] As shown in a large number of experiments, only viscous fluids exist, see [47] for more details.

holds. Note, that further Dirichlet, Neumann, or Robbins boundary conditions apply to the remaining parts $\Gamma_i \backslash \Gamma_{ij}$ and $\Gamma_j \backslash \Gamma_{ij}$ of the boundaries Γ_i and Γ_j of Ω_i and Ω_j, respectively, and that the continuity equation

$$\operatorname{div}[\mathbf{u}_j] = 0 \quad \text{in } \Omega_j \tag{4.96}$$

holds for Ω_j due to the incompressibility of the fluid. The combined parameter $\mu^\star dt^{-1}$ occurring in (4.93) has the physical unit of a pressure.

Besides the formal restrictions in terms of infinitesimal small displacement fields and time intervals dt, which allow to drop the distinction between the Lagrangian and the Eulerian configuration (see Section 2.2.3 for details), (4.94) leads to reasonable physical deformation results in case of finite small deformations, see Chapter 5 for an intensive treatment. In contrast, the simulation of large deformations requires the introduction of a so-called *arbitrary Lagrangian-Eulerian* (ALE) formulation which allows a description of all regions Ω_i in their preferred configurations [31, 73, 159].

4.4.2 Coupling of matrix systems

For a solution of the coupled problem (4.94), we apply the finite element method to each homogeneous region Ω_i, leading to a set of linear matrix systems due to the number of regions contained in the inhomogeneous body Ω. These matrix systems can be assembled together into a global matrix system using the equilibrium boundary condition (4.89), the compatibility boundary condition (4.90), and the no-penetration condition (4.91) [8, 77].

Considering, e.g., two regions Ω_i and Ω_j, connected through a common boundary Γ_{ij}, the matrix assembly process proceeds as follows [77]: First, all linear matrix systems $\mathbf{A}\tilde{\mathbf{u}} = \mathbf{f} + \mathbf{t}$ have to be reordered thus giving for the region Ω_i

$$\begin{pmatrix} \mathbf{A}^i_{\Omega\Omega} & \mathbf{A}^i_{\Omega\Gamma} \\ \mathbf{A}^i_{\Gamma\Omega} & \mathbf{A}^i_{\Gamma\Gamma} \end{pmatrix} \begin{pmatrix} \tilde{\mathbf{u}}^i_\Omega \\ \tilde{\mathbf{u}}^i_\Gamma \end{pmatrix} = \begin{pmatrix} \mathbf{f} + \mathbf{t}^i \\ \mathbf{f} + \mathbf{t}^i_\Gamma \end{pmatrix} \tag{4.97}$$

and for Ω_j

$$\begin{pmatrix} \mathbf{A}^j_{\Omega\Omega} & \mathbf{A}^j_{\Omega\Gamma} \\ \mathbf{A}^j_{\Gamma\Omega} & \mathbf{A}^j_{\Gamma\Gamma} \end{pmatrix} \begin{pmatrix} \tilde{\mathbf{u}}^j_\Omega \\ \tilde{\mathbf{u}}^j_\Gamma \end{pmatrix} = \begin{pmatrix} \mathbf{f} + \mathbf{t}^j \\ \mathbf{f} + \mathbf{t}^j_\Gamma \end{pmatrix}. \tag{4.98}$$

Here, $\mathbf{u}^i_\Omega$ and $\mathbf{u}^j_\Omega$ denote the displacements inside each region, $\mathbf{t}^i_\Gamma$ and $\mathbf{t}^j_\Gamma$ are the stress vectors acting on Γ_{ij}, while $\mathbf{A}^i_{\Omega\Omega}$ etc. denotes the submatrices of the corresponding stiffness matrices $\mathbf{A}^i$ and $\mathbf{A}^j$ for the regions Ω_i and Ω_j, respectively. An index Γ, as appearing in $\mathbf{A}^i_{\Omega\Gamma}$ etc., indicates those submatrices which comprise degrees-of-freedom belonging to the common surface Γ_{ij} between the regions Ω_i and Ω_j. Second, using the boundary conditions (4.89) and (4.90) and bearing the definition of Cauchy's stress vector (2.24) in mind, all matrix systems can be coupled together into the single system

$$\underbrace{\begin{pmatrix} \mathbf{A}^i_{\Omega\Omega} & \mathbf{A}^i_{\Omega\Gamma} & \mathbf{0} \\ \mathbf{A}^i_{\Gamma\Omega} & \mathbf{A}^i_{\Gamma\Gamma} + \mathbf{A}^j_{\Gamma\Gamma} & \mathbf{A}^j_{\Gamma\Omega} \\ \mathbf{0} & \mathbf{A}^j_{\Omega\Gamma} & \mathbf{A}^j_{\Omega\Omega} \end{pmatrix}}_{\mathbf{A}} \underbrace{\begin{pmatrix} \tilde{\mathbf{u}}^i_{\Omega} \\ \tilde{\mathbf{u}}^{ij}_{\Gamma} \\ \tilde{\mathbf{u}}^j_{\Omega} \end{pmatrix}}_{\tilde{\mathbf{u}}} = \underbrace{\begin{pmatrix} \mathbf{f} + \mathbf{t}^i \\ \mathbf{f} \\ \mathbf{f} + \mathbf{t}^j \end{pmatrix}}_{\mathbf{b}}, \tag{4.99}$$

where $\tilde{\mathbf{u}}^{ij}_{\Gamma}$ denotes the displacements at the common boundary Γ_{ij}. The global matrix $\mathbf{A}$ is commonly denoted as *stiffness matrix* while the right-hand side vector $\mathbf{b} = \mathbf{f} + \mathbf{t}$ is known as *load vector* [20, 25]. Note, that this construction scheme holds for an arbitrary number of regions Ω_i, provided that all linear matrix systems are properly reordered, as indicated in (4.97) and (4.98). The linear matrix system (4.99) completely describes the equilibrium of an inhomogeneous body subjected to externally applied forces.

In order to apply this construction scheme to our coupled problem (4.94), we have to identify the appropriate mathematical terms in our finite element formulations of the Navier equation

$$\int_{\Omega_i} \lambda(\operatorname{tr}\boldsymbol{\epsilon}(\mathbf{u}_i))(\operatorname{tr}\boldsymbol{\epsilon}(\mathbf{w})) + 2\mu\,(\boldsymbol{\epsilon}(\mathbf{u}_i), \boldsymbol{\epsilon}(\mathbf{w}))\,d\Omega_i = \int_{\Omega_i} (\mathbf{f}, \mathbf{w})\,d\Omega_i + \int_{\Gamma_{ij}} (\mathbf{g}_i, \mathbf{w})\,d\Gamma_{ij} \tag{4.100}$$

and of the Stokes equation

$$\int_{\Omega_j} -p\,\mathrm{div}[\mathbf{w}] + \mu^\star dt^{-1}\,(\mathbf{J}(\mathbf{u}_j), \mathbf{J}(\mathbf{w}))\,d\Omega_j = \int_{\Omega_j} (\mathbf{f}, \mathbf{w})\,d\Omega_j - \int_{\Gamma_{ij}} (\mathbf{g}_j, \mathbf{w})\,d\Gamma_{ij} + \int_{\Gamma_{ij}} \mu^\star \left(dt^{-1}\mathbf{J}(\mathbf{u}_j)\mathbf{n}_j, \mathbf{w}\right) d\Gamma_{ij}, \tag{4.101}$$

thus allowing an application of the equilibrium and compatibility boundary conditions. Considering the boundary integral appearing on the righthand side of (4.100) reveals that the stress vector $\mathbf{t}_i$ acting on the common boundary Γ_{ij} is identical to the density of the surface force $\mathbf{g}_i$ according to (2.24). A similar statement holds for the stress vector $\mathbf{t}_j$ and the density of the surface force $\mathbf{g}_j$ appearing on the righthand side of (4.101). From the no-penetration boundary condition (4.91) follows, that

$$dt^{-1}\mathbf{J}(\mathbf{u}_j)\mathbf{n}_j = \mathbf{J}(\mathbf{v}_j)\mathbf{n}_j = \mathbf{0}, \quad \forall \mathbf{x} \in \Gamma_{ij} \tag{4.102}$$

holds and the last boundary integral appearing on the right-hand side of (4.101) therefore vanishes. Thus, we can directly merge the linear matrix systems derived for the Navier equation (4.28) and the Stokes equation (4.52) using the equilibrium boundary condition and the compatibility boundary condition, ending up with a single, linear matrix system that completely describes the deformation behavior of an inhomogeneous body comprising rigid, elastic, and fluid materials.

4.4.3 Finite elements for coupled systems

In order to solve the linear matrix system (4.99), we have to choose appropriate types of finite elements for the rigid or elastic regions Ω_i and the fluid regions Ω_j. Optimal choices from the point of minimizing the number of degrees-of-freedom and thus the computation times are bilinear finite elements for elastic regions Ω_i and divergence-free finite elements for fluid regions Ω_j (see also Section 4.3). However, such finite elements cannot be directly linked at the common boundary Γ_{ij} since the stream function $\tilde{\boldsymbol{\psi}}$, which has to be introduced for fluid regions Ω_j if divergence-free finite elements were used, is not defined for elastic regions Ω_i. Instead, new types of finite elements have to be derived for this case ensuring a transition between bilinear finite elements and divergence-free finite elements. But to our knowledge, no such transition elements exist. For this reason, we still use Q_2-P_1 Crouzeix-Raviart finite elements for all fluid regions Ω_j. To ensure furthermore the continuity of the resulting displacement vector field as well as the solvability of the final linear matrix system (4.99), we use biquadratic finite elements for all rigid and elastic regions Ω_i since a direct coupling between Q_2-P_1 Crouzeix-Raviart finite elements and bilinear finite elements is impossible. This prohibition is justified by the fact that two neighboring finite elements may only share a common surface, side, or node, which is violated in case of neighboring bilinear finite elements and Q_2-P_1 Crouzeix-Raviart finite elements, see Section 4.3 for details. Note, that a coupling between finite elements used for rigid as well as elastic regions Ω_i and fluid regions Ω_j is limited to mixed finite elements with pressure functions defined with respect to internal nodes only. Otherwise, similar to the stream function, the pressure function prevents a coupling of mixed finite elements with common quadrilateral finite elements.

4.5 Specified displacements

For the solution of a linear equation system $\mathbf{A}\tilde{\mathbf{u}} = \mathbf{b}$, with $\mathbf{b} = \mathbf{f} + \mathbf{g}$, like, e.g., (4.28), (4.52), or (4.99), values specified by given Dirichlet, Neumann, or Robbins boundary conditions have to be introduced. Otherwise, the linear matrix system cannot be solved according to the singularity of the stiffness matrix $\mathbf{A}$ [72]. In the following, we concentrate on *pure displacement problems* with given Dirichlet boundary conditions only. Note, that for all regions modeled by the Stokes equation, the assumption that the displacement vector field $\tilde{\mathbf{u}}$ is related to the velocity vector field $\tilde{\mathbf{v}}$ by (4.95), leads to a linear matrix system $\mathbf{A}\tilde{\mathbf{u}} = \mathbf{b}$ which is directly expressed in terms of the displacement vector field $\tilde{\mathbf{u}}$. The entries of the stiffness matrix $\mathbf{A}$ are determined in this case through (4.101) instead of (4.40). Thus, our approach can actually be considered as a landmark-based registration scheme like, e.g., [6, 125, 40, 124, 42], where the specified displacements represent the landmark correspondences. The handling of *pure traction problems* with given Neumann boundary conditions instead, is a straightforward task which will be not considered here due to the difficulties associated with a reliable determination of *forces* directly from corresponding image data [27].

For the incorporation of specified displacements, the procedure described in [72, 119, 120] is applied: Given a value for the unknown $\tilde{u}_j$, it can be incorporated into the linear equation system by a subtraction of the product $\tilde{u}_j\mathbf{A}_j$, where $\mathbf{A}_j$ denotes the jth column of the stiffness matrix $\mathbf{A}$, from the right-hand side vector $\mathbf{b} = \mathbf{f} + \mathbf{g}$,

$$\tilde{\mathbf{b}} = \mathbf{b} - \tilde{u}_j\mathbf{A}_j, \tag{4.103}$$

followed by a substitution of the given value $\tilde{u}_j$ into the jth row of $\tilde{\mathbf{b}}$. Thereafter, the jth row and column of $\mathbf{A}$ are set to zero and, respectively, the diagonal element A_{jj} to one. By repeating this procedure for a set of displacements, e.g., to be given at the surface of an anatomical structure, a direct mapping from the undeformed to the deformed state of the anatomical structure results. It follows from the construction scheme, that the specified displacements are always exactly satisfied, independently of the material parameter values used, or, in other words, the model automatically adjusts the necessary forces $\mathbf{f}$ and $\mathbf{g}$ [21, 118]. Figure 4.8 shows the difference between a pure displacement and a pure traction problem if the material parameter values of the body Ω were changed. In case of a pure traction problem, the significant influence of the underlying material parameter values on the applied force field is clearly visible. Additionally, the applied force fields do not have equal magnitudes compared to the given correspondences of a pure displacement problem. Note, that all specified displacements were integrated in

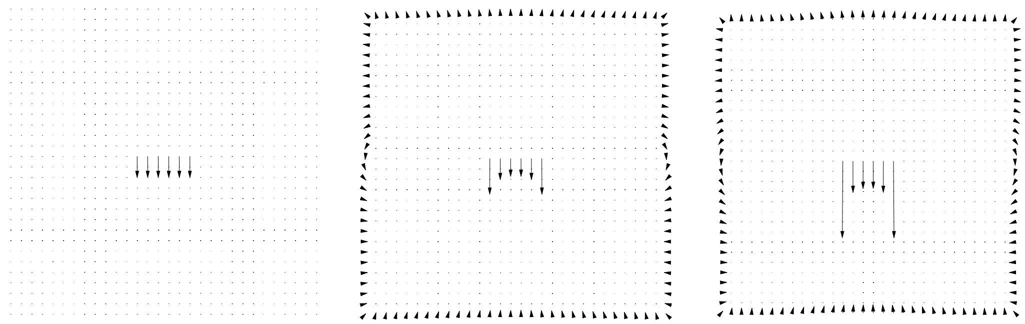

(a) (b) (c)

Figure 4.8: Differences between a pure displacement and a pure traction problem for different material parameter values. In the former case, the specified displacements in (a) are always satisfied, independent of the assumed material parameter values. For a pure traction problem, the force field in (b) must be applied to ensure that the solution satisfies these displacements. If the underlying material parameter values are changed, the force field (c) must be applied instead to satisfy the given displacements.

a way that the original number of equations remains unchanged, thus avoiding a time-consuming restructuring of the internal matrix storage scheme. A proof concerning the invertibility of the modified matrix system can be found in [118].

For the specification of prescribed displacements for biomechanical models based entirely on the Stokes equation, i.e. models where all regions are simulated as fluids, special attention is required if divergence-free finite elements are used, since given values for $\tilde{\mathbf{u}}$ must be transformed with respect to the new unknowns $\tilde{u}_{\mathbf{t}i}$ and $\tilde{\psi}_i$, as pointed out in Section 4.3. This transformation is straightforward for all $\tilde{u}_{\mathbf{t}i}$, if the direction of the corresponding tangential vector $\mathbf{t}$ is taken into account. But for the stream function $\tilde{\boldsymbol{\psi}}$, the boundary conditions have to be computed from line integrals

$$\tilde{\psi}_{i+1} = \tilde{\psi}_i + \int_{\Gamma_{ki}} (\tilde{\mathbf{u}}, \mathbf{n}) d\Gamma_{ki} \tag{4.104}$$

according to (4.69). Setting an arbitrary $\tilde{\psi}_i$ to zero allows for a direct computation of all values for $\tilde{\psi}$ along the boundary [25]. For the final integration of these values into the linear matrix system, we use the procedure described above.

However, the usage of divergence-free finite elements for image correction purposes leads to some problems if each image pixel is directly mapped onto the center of a divergence-free finite element, see also Appendix B. Due to the elimination process of the center node $\mathbf{x}_9$ of the divergence-free element described above, the prescribed displacement value has to be mapped onto the remaining nodes of the element such that the final transformation $\tilde{\mathbf{u}} = \mathbf{R}_d\tilde{\mathbf{u}}_d$ gives the desired value at the center node $\mathbf{x}_9$. This can be directly achieved by assuming a constant displacement vector field $\tilde{\mathbf{u}} = (\tilde{u}_1, \tilde{u}_2)^T$ within the divergence-free element, thus giving

$$\begin{aligned}\tilde{\psi}_1 &= 0\\ \tilde{\psi}_2 &= -\tilde{u}_2\\ \tilde{\psi}_3 &= \tilde{u}_1 - \tilde{u}_2\\ \tilde{\psi}_4 &= \tilde{u}_1\end{aligned}$$

as necessary boundary conditions for the stream function $\tilde{\boldsymbol{\psi}}$. Here, the value of $\tilde{\psi}_1$ was arbitrarily set to zero. But the choice which $\tilde{\psi}_i$ has been set to zero has a significant influence on the resulting stream function and, as a consequence, on the calculated displacement vector field, as demonstrated by the following example shown in Figure 4.9.

The left column of Figure 4.9 displays the stream function (top), the displacement vector field (middle), and the corresponding grid deformation (bottom) resulting from using $\tilde{\mathbf{u}} = (5.0, 0.0)^T$ as prescribed displacement. Setting $\tilde{\psi}_1 = 0$ leads to larger magnitudes of the displacement vector field in the lower part of the image (left column of Figure 4.9), i.e. the resulting deformation is non-symmetric with regard to the prescribed displacements. Assuming that $\tilde{\psi}_4 = 0$ holds instead, leads to the results shown on the right column of Figure 4.9. Again, a non-symmetric behavior is observable, but now the displacement vector field has larger magnitudes in the upper part of the image. Comparing the corresponding subfigures of the second and third row in Figure 4.9 with each other shows the significant influence on the resulting deformation of setting an individual $\tilde{\psi}_i$ to zero. As a consequence, the specification of boundary conditions for the stream function, i.e. the assignment of explicit values to any $\tilde{\psi}_i$, should generally be avoided. Instead, a mapping of image pixels on the corner nodes of the divergence-free finite elements should be preferred such that each pixel is mapped onto a node where four neighboring elements of the underlying finite element mesh meet. A disadvantage in this case is, that the boundaries between different anatomical structures must follow exactly the boundaries of the underlying finite element mesh, as shown in Appendix B.

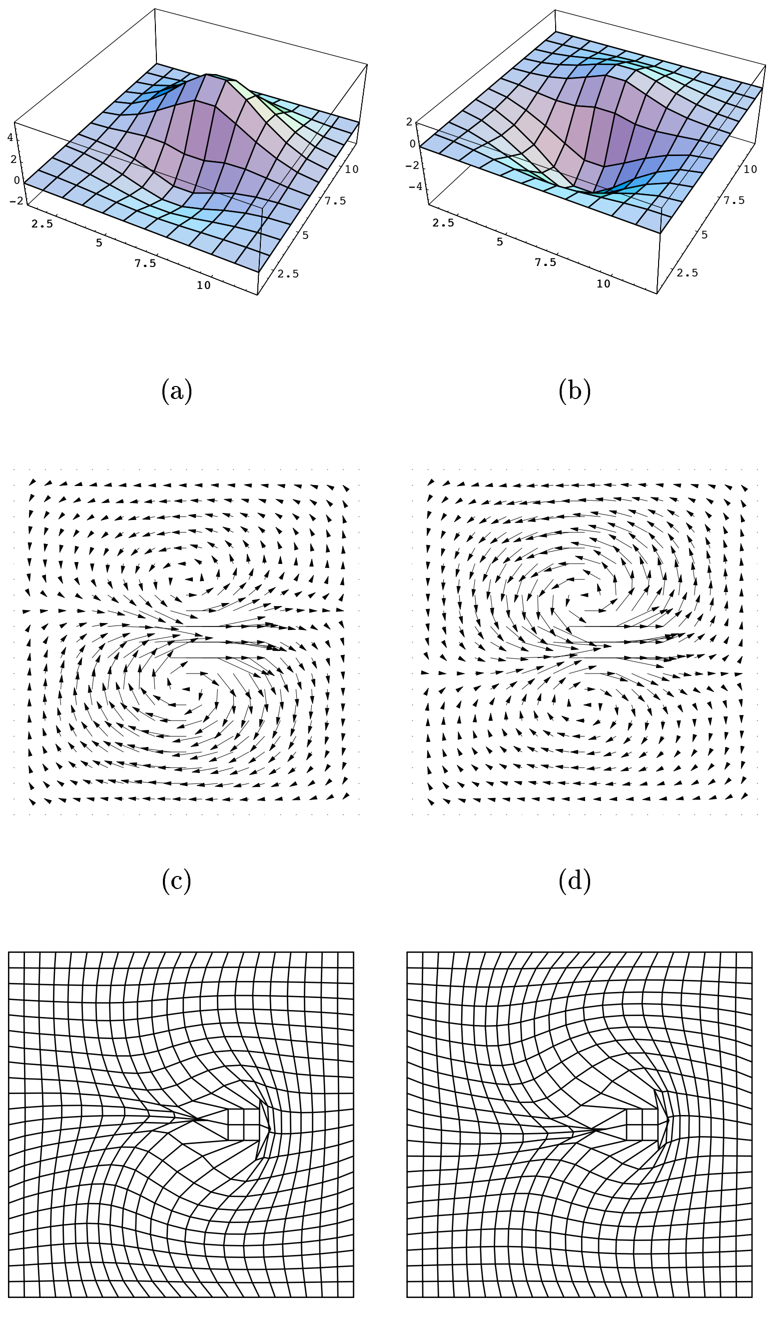

Figure 4.9: Comparison of the stream function (top row), the displacement vector field (middle row), and the grid deformation (bottom row) while setting $\tilde{\psi}_1 = 0$ (left column) and $\tilde{\psi}_4 = 0$ (right column).

4.6 Material parameter values

The application of biomechanical models for image correction purposes requires a specification of the material parameter values entering the corresponding stiffness matrices **A**. Depending on the assumed biomechanical model, which is either a pure elastic model based entirely on the Navier equation, a pure fluid model based entirely on the Stokes equation, or a coupled model based on both equations, values for the Lamé constants λ and μ and/or the combined parameter $\mu^\star dt^{-1}$ have to be specified in (4.28), (4.52), or (4.99), respectively.

4.6.1 Material values for the Navier equation

In order to determine appropriate values of the Lamé constants for a biomechanical model based entirely on the Navier equation, we carried out a comprehensive literature study about reported values on skull bone and brain tissue. It turns out, that a variety of different values can be found for the Lamé constants for both materials, as summarized in Tables 4.2 and 4.3. In the original papers nearly all values were given in terms of *Poisson's ratio* ν, measuring the ratio between the relative transversal contraction and the relative longitudinal dilation, and *Young's modulus* E, which relates the tension to the relative stretch in the longitudinal direction [21]. These values can be directly converted into values for the Lamé constants λ and μ through the well-known relationships [44, 100]

$$\lambda = \frac{E\nu}{(1+\nu)(1-2\nu)} \tag{4.105}$$

and

$$\mu = \frac{E}{2(1+\nu)}. \tag{4.106}$$

Some of the values given in Tables 4.2 and 4.3, i.e. those used by [146, 90, 91, 67], were taken from other work, mainly the works of Sauren and Classens [136] as well as Nagashima *et al.* [114]. Other authors like [71, 162, 131, 166, 19, 165] incorporated measured in vitro data, reported by, e.g., McElhaney *et al.* [103] or Nahum *et al.* [115]. In our approach, where the deformations are driven by given correspondences, the Navier equation (2.47) can be transformed into

$$(\frac{\lambda}{\mu}+1)\nabla \mathrm{div}[\mathbf{u}] + \nabla^2\mathbf{u} + \frac{\mathbf{f}}{\mu} = \mathbf{0}, \tag{4.107}$$

material parameter values for brain tissue		
article	λ_{br} $[kPa]$	μ_{br} $[kPa]$
Hosey and Liu 1982 [71]	11101.8	22.2482
Ward 1982 [162]	5270.27	219.595
Ruan *et al.* 1991 [131]	540.811	22.5338
Willinger *et al.* 1992 [166]	5472.97	228.041
Chu *et al.* 1994 [19]	4110.74	83.8926
Tada *et al.* 1994 [146]	8060.27	164.495
Takizawa *et al.* 1994 [147]	41.7945	2.66773
Kuijpers *et al.* 1995 [90]	8108.11	337.838
Kumaresan and Radhakrisnan 1996 [91]	540.811	22.5338
Hartmann and Kruggel 1998 [67]	12483.3	25.0167

Table 4.2: Reported values of the Lamé constants λ and μ for brain tissue. Tada *et al.*, Takizawa *et al.*, as well as Hartmann and Kruggel distinguished originally between grey matter and white matter, but here, only the values for grey matter are given.

material parameter values for skull bone		
article	λ_{sk} $[kPa]$	μ_{sk} $[kPa]$
Hosey and Liu 1982 [71]	1334570	1842980
Ward 1982 [162]	1334570	1842980
Ruan *et al.* 1991 [131]	2093090	2663930
Willinger *et al.* 1992 [166]	1388890	2083330
Chu *et al.* 1994 [19]	1805560	2708330
Tada *et al.* 1994 [146]	1466820	2025600
Kuijpers *et al.* 1995 [90]	1805560	2708330
Kumaresan and Radhakrisnan 1996 [91]	1945000	2685950
Whitman *et al.* 1996 [165]	180556	270833
Hartmann and Kruggel 1998 [67]	2093090	2663930

Table 4.3: Reported values of the Lamé constants λ and μ for skull bone.

such that only the ratio

$$\frac{\lambda}{\mu} = \frac{2\nu}{(1-2\nu)} \tag{4.108}$$

of the Lamé constants is important since the external forces $\mathbf{f}/\mu$ are automatically adjusted in this case, see Section 4.5 for a detailed treatment. In Table 4.4, the calculated ratios for the values given in Tables 4.2 and 4.3 are summarized. Analyzing Table 4.4 reveals the interesting fact that only

ratios of the material parameter values			
article	λ_{br}/μ_{br}	λ_{sk}/μ_{sk}	$\lambda_{sk}/\lambda_{br}$
Hosey and Liu 1982 [71]	498.998	0.724137	120.212
Ward 1982 [162]	24.0	0.724137	253.226
Ruan *et al.* 1991 [131]	24.0	0.785715	3870.28
Willinger *et al.* 1992 [166]	23.9999	0.666668	253.773
Chu *et al.* 1994 [19]	49.0	0.666669	439.23
Tada *et al.* 1994 [146]	49.0001	0.724141	181.981
Kuijpers *et al.* 1995 [90]	24.0	0.666669	222.686
Kumaresan and Radhakrisnan 1996 [91]	24.0	0.724139	3596.45
Hartmann and Kruggel 1998 [67]	498.999	0.785715	167.671

Table 4.4: Calculated ratios for the Lamé constants for brain and skull tissue. Only those articles have been listed where material parameter values have been reported for both, brain tissue and skull bone.

a small number of different Lamé constant ratios for brain tissue and skull bone exists. The highly different ratios for brain tissue result from a small variation of the underlying Poisson's ratio ν (between $\nu = 0.48, \ldots, 0.499$) according to (4.108).

To analyze the influence of the variations of the Lamé constant ratios on the deformation result, we carried out several experiments using a 30×30 grid to visualize the resulting deformation. In Figure 4.10, four parallel correspondences were given while taking the calculated ratios $\lambda/\mu = 24.0$, $\lambda/\mu = 49.0$, and $\lambda/\mu = 498.999$ in Table 4.4 into account, respectively. The applied correspondences in all cases point in the direction of the lower right corner of the grid. As can be seen from Figure 4.10, only relatively slight differences in the deformations result. Thus, we conclude that the mean values of the ratios, namely $\lambda_{br}/\mu_{br} = 135.111$ and $\lambda_{sk}/\mu_{sk} = 0.718666$, serve as valid estimates for the corresponding Lamé constant ratios [64].

For the simulation of different anatomical structures, we also have to determine appropriate ratios for the Lamé constants between those structures. Following our previous practice for homogeneous materials, we calculated the ratios for the λ-values of skull bone and brain tissue and listed them in the last column of Table 4.4. Here, a larger variability of the calculated ratios can be observed. However, it seems reasonable to choose again the mean value as ratio between the λ-values, namely $\lambda_{sk}/\lambda_{br} = 1011.72$, while keeping the internal Lamé constant ratios of each material constant. To demonstrate the

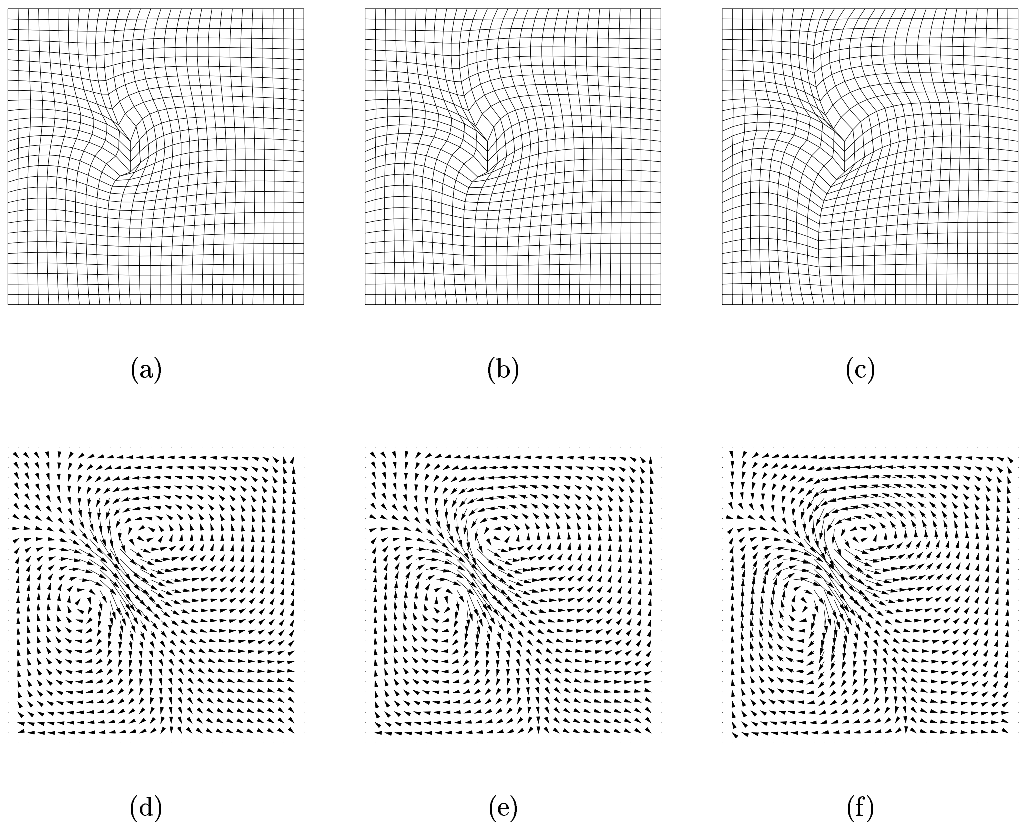

Figure 4.10: To investigate the influence of different Lamé constant ratios, we compared the deformations of homogeneous brain tissue. Four parallel correspondences, given in the upper left part of a 30×30 grid, were applied. The calculated grid deformations (top row) and displacement vector fields (bottom row) for values of $\lambda/\mu = 24.0$, $\lambda/\mu = 49.0$, and $\lambda/\mu = 498.999$ (from left to right) show only relatively small differences.

influence of the determined Lamé constant values on the deformation result, four parallel correspondences were applied again while taking the calculated mean ratios into account. As indicated by the resulting grid deformations as well as calculated displacement vector fields shown in Figure 4.11, the material parameter values for homogeneous skull bone result in a significant stiffer behavior compared to homogeneous brain tissue. By dividing the whole grid into two regions Ω_1 and Ω_2, we obtain the result shown in Figure 4.11(c). In this case, the applied correspondences lead to a pure translation of the simulated bony rectangle, surrounded by soft brain material. The corresponding displacement vector field reveals, that the behavior of the surrounding soft

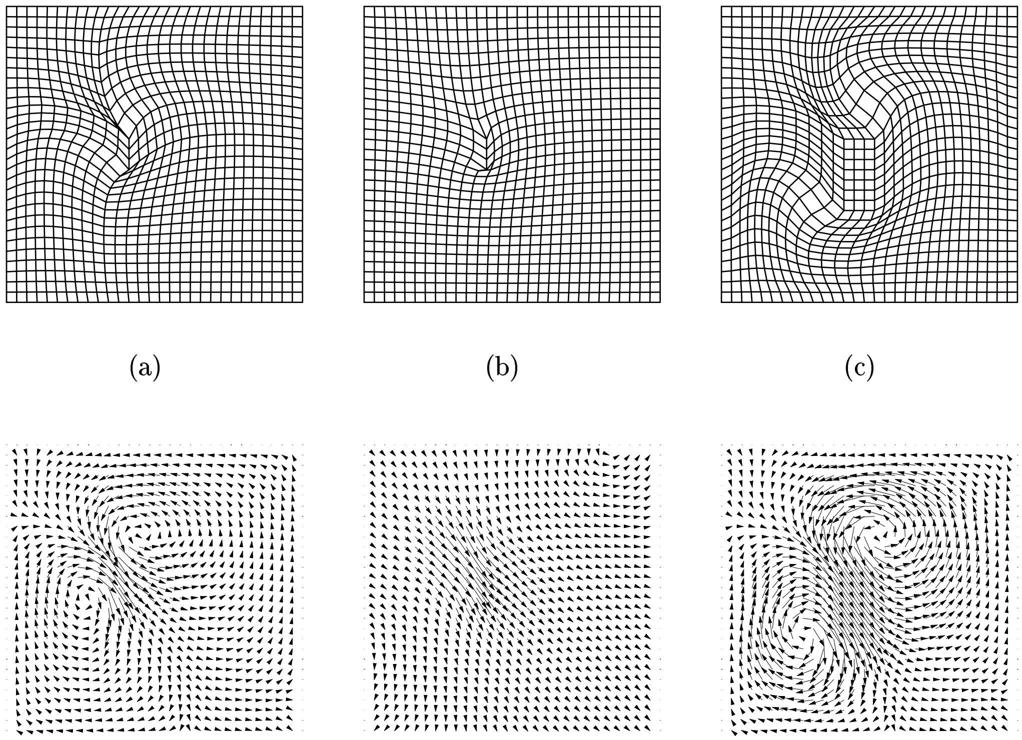

(a) (b) (c)

(d) (e) (f)

Figure 4.11: Resulting grid deformations (top row) and displacement vector fields (bottom row) while simulating different elastic materials. In (a) and (b), homogeneous areas of type brain tissue and skull bone were assumed, respectively. As expected, the assumed skull material results in a much stiffer behavior. By spatially different Lamé constant ratios, we can combine different materials as shown in (c). Here, a (simulated bony) rectangle embedded in simulated brain tissue results in a pure translation of the rectangle.

material is physically plausible: Along the path of translation, a stretching of the soft material occurs, while two vortices can be observed due to the lateral inflow of soft material.

4.6.2 Material values for the Stokes equation

For a biomechanical model based entirely on the Stokes equation (2.53), we also launched a literature study to determine appropriate values for the combined parameter $\mu^\star dt^{-1}$. This study revealed that, in contrast to the material

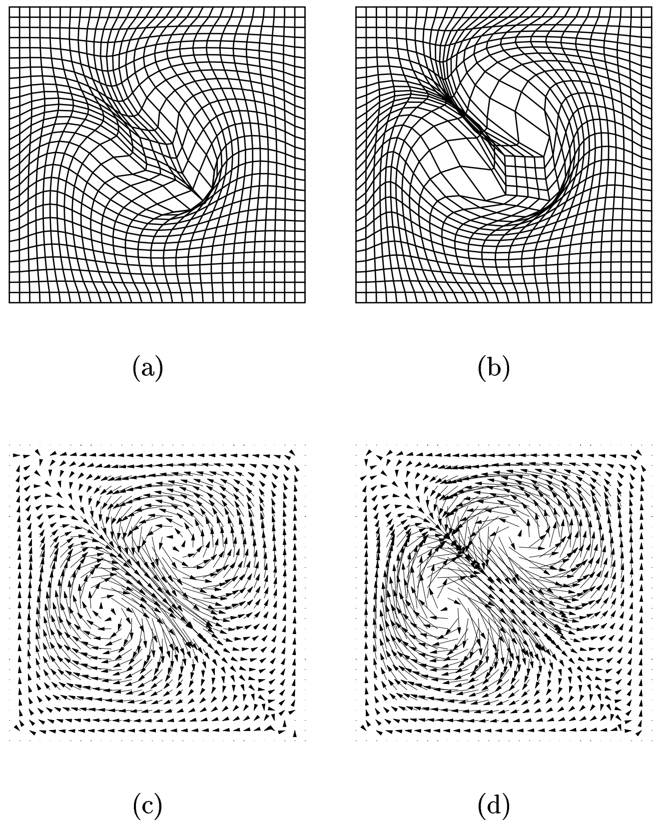

Figure 4.12: Resulting grid deformation (top row) and displacement vector field (bottom row) for different combined parameter ratios while using a fluid model. The ratio $\mu_{br}^{\star} dt^{-1} / \mu_{sk}^{\star} dt^{-1}$ varies between 0.1 (left column) and 0.01 (right column), see also the continuation of these experiments in Figure 4.13.

parameters for the Navier equation, no reliable values for the viscosity parameter exist. Also those approaches entirely based on the Navier-Stokes equation (2.49) [17, 97] use heuristically determined values in the range of $0.1 \leq \mu \leq 1.0$. To study the influence of different ratios between $\mu_{br}^{\star} dt^{-1}$ and $\mu_{sk}^{\star} dt^{-1}$ on the deformation, we calculated the deformation of a rigid structure, modeled as a thick liquid, embedded into soft material, modeled as a thin liquid[4]. Note, that all regions were simulated using the Stokes equation, i.e. only the viscosity of the fluid is spatially changed. Figure 4.12

[4]In German, the term *thick liquid* denotes a *zähflüssige Flüssigkeit* while the term *thin liquid* can be translated into *dünnflüssige Flüssigkeit*, according to [145].

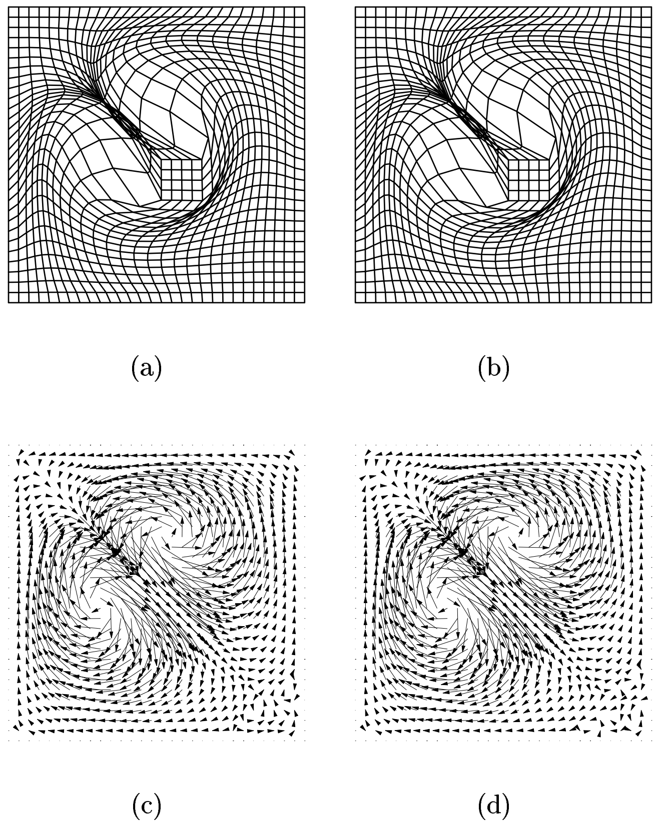

Figure 4.13: Same as Figure 4.12, but the ratio $\mu^{\star}_{br}dt^{-1}/\mu^{\star}_{sk}dt^{-1}$ varies between 0.001 (top row) and 0.0001 (bottom row).

shows the deformation of the 30×30 grid in case of the single prescribed displacement $\mathbf{u} = (5.0, 5.0)^T$ acting on the lower right corner of a thick liquid structure of rectangular shape. It can be easily seen from Figures 4.12(a) and (c), that a ratio of $\mu^{\star}_{br}dt^{-1}/\mu^{\star}_{sk}dt^{-1} = 0.1$ between the combined parameters for thin liquids and thick liquids, results in a significant deformation of the thick liquid structure. Since the time interval dt remains constant over the inhomogeneous body Ω, this experiment equals those carried out by Lester *et al.* [97, 98] while assuming a ratio of $\mu^{\star}_{br}/\mu^{\star}_{sk} = 0.1$ between the viscosity parameters of soft and rigid regions. Thus it seems that the shape of rigid structures in [97, 98] is mainly maintained through the additional weighting function applied to the assumed forces.

By increasing the ratio between the combined parameters, for the ratios $\mu^{\star}_{br}dt^{-1}/\mu^{\star}_{sk}dt^{-1} = 0.001$ and $\mu^{\star}_{br}dt^{-1}/\mu^{\star}_{sk}dt^{-1} = 0.0001$ see Figure 4.13, the shape of the thick liquid region is more and more preserved, until a ratio of 0.0001 leads to a well translation of the thick liquid structure, see Figure 4.13. Based on these experiments, we will use the ratio $\mu^\star_{br} dt^{-1}/\mu^\star_{sk} dt^{-1} = 0.0001$ for the experiments carried out in Chapter 5.

4.6.3 Material values for the coupled system

After having estimated appropriate material parameter ratios for our biomechanical models based entirely on the Navier equation or the Stokes equation, respectively, we will now determine appropriate material parameter ratios for our new coupled approach.

Since our previously determined ratios for skull bone and brain tissue are based on reported and measured values, we will use these ratios, namely $\lambda_{sk}/\mu_{sk} = 0.718666$, $\lambda_{br}/\mu_{br} = 135.111$, and $\lambda_{sk}/\lambda_{br} = 1011.72$, for the corresponding rigid and elastic regions of our coupled approach (4.99). However, we still have to determine a ratio for the combined parameter $\mu^\star dt^{-1}$ with respect to the material parameter values of skull bone and brain tissue. In the absence of reliable parameter values for cerebrospinal fluid, we use as a first step an experimentally determined ratio, in our case $\mu^\star dt^{-1}/\mu_{br} = 0.01$, leading to visually appealing deformation results, see Figure 4.14. Since no real measurements concerning the viscosity of cerebrospinal fluids have been carried out, the choice of a reliable parameter value remains an open problem.

4.7 Summary

In this chapter, we presented the derivation of a new biomechanical model of the human head. Our model copes with rigid, elastic, and fluid structures whose deformation behaviors are simulated using the appropriate physical model, namely the Navier equation for rigid and elastic structures as well as the Stokes equation for fluid structures. We decompose an inhomogeneous body comprising different anatomical structures into a set of homogeneous regions and apply the appropriate physical model to each structure seperately. For the solution of these differential equations, we apply the finite element method, leading to a set of linear matrix systems, depending on the number of homogeneous regions. This set of linear matrix systems can be further merged together using appropriate boundary conditions. These physical conditions are the equilibrium and compatibility boundary conditions between regions of different elastic solids as well as the equilibrium, no-slip, and no-penetration boundary conditions between regions simulating elastic solids and incompressible fluids. The result is a single linear matrix

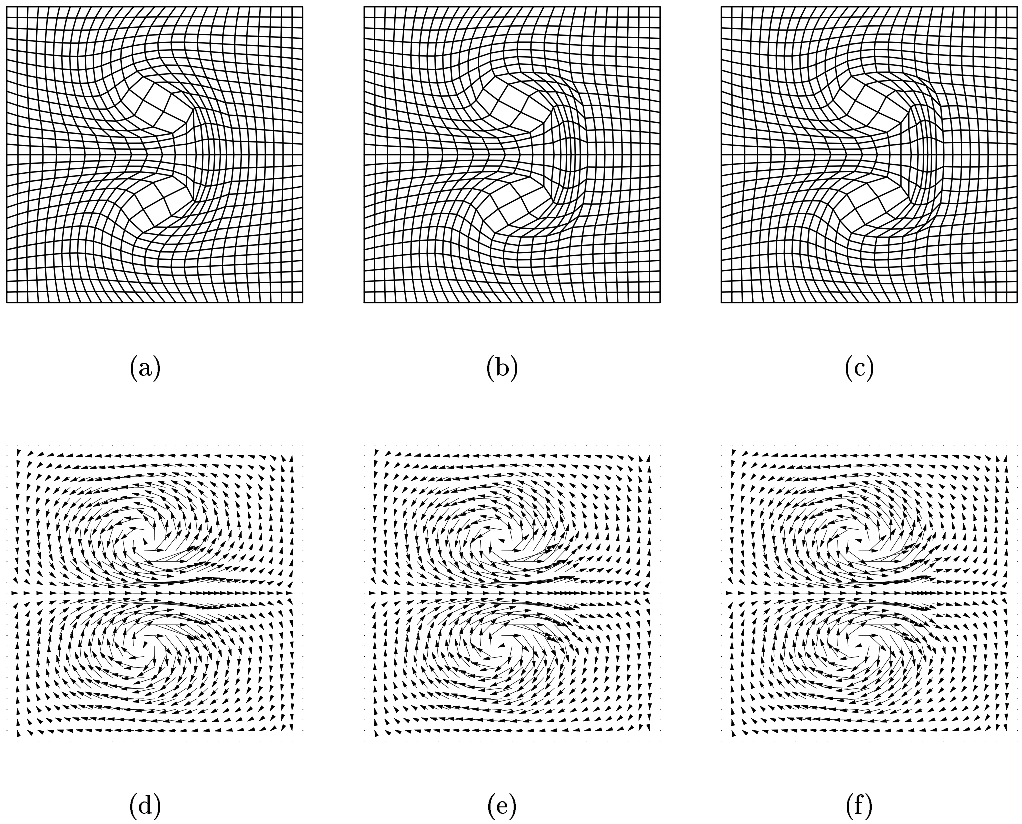

Figure 4.14: Resulting grid deformations (top) and displacement vector fields (bottom) of a rectangular fluid region embedded into an elastic region for different ratios between the combined parameter $\mu^{\star} dt^{-1}$ and the Lamé constant μ_{br}. The ratio $\mu^{\star} dt^{-1}/\mu_{br}$ varies between 1.0 (left), 0.1 (middle), and 0.01 (right).

system completely describing the deformation behavior of an inhomogeneous body comprising rigid, elastic, and fluid regions.

Note, that an application of the Navier equation and of the boundary conditions (namely the compatibility and the no-penetration boundary conditions in case of adjacent elastic solid and fluid regions) restricts the resulting deformation field to small deformations only. For large deformations, the linearization of the Navier equation with respect to the strain tensor is not valid and the full time derivative has to be used instead to determine the deformation field of the fluid regions. Additionally, Hooke's law will no longer serve as a sufficient approximation to model the biomechanical behavior of brain tissue in this case hence a more apt constitutive equation has to be used instead.

Using the finite element method, the underlying solution space of each differential equation is approximated by a finite dimensional space, spanned by a finite number of basis functions. These basis functions serve as interpolation functions for the solution and must be chosen carefully to ensure the solvability of each resulting linear matrix system. While biomechanical models based entirely on either the Navier equation or the Stokes equation may use bilinear finite elements or divergence-free finite elements, respectively, for our coupled approach one may not apply these types of finite elements. Instead, we use biquadratic finite elements for rigid and elastic regions, and Q_2-P_1 Crouzeix-Raviart finite elements for fluid regions. Otherwise, problems arise at the boundary between regions modeled through the Navier equation and the Stokes equation.

To apply our biomechanical model for image correction purposes, we use specified displacements instead of forces since a reliable determination of the latter one from given corresponding image data remains problematic, as demonstrated in Section 4.5 above. The prescribed displacements can be easily integrated into the linear matrix system and they are always satisfied by the resulting deformation. Thus, our approach can actually be regarded as a landmark-based registration scheme. Additionally, it is not necessary to specify explicit values for the material parameters, instead it suffices to use ratios between the material parameters. Such ratios for the Lamé constants λ and μ have been determined through a comprehensive literature study while appropriate ratios for the combined parameter $\mu^\star dt^{-1}$ have been determined through experimental parameter studies due to the lack of reported values.

It has to mentioned, that the validity of the chosen values for the combined parameter $\mu^\star dt^{-1}$ remains unclear, although visual appealing deformations result using these values. In contrast to the Lamé constant values determined for skull bone and brain tissue, respectively, no real physical measurements have been used as basis for choosing appropriate values for the combined parameter $\mu^\star dt^{-1}$. Thus, further research is necessary in this case to determine more reliable material parameter values.

Chapter 5

Experimental results

Based on the investigations of Chapter 4, we apply in the following different biomechanical models of the human head to simulate brain deformations given prior specified displacements. In Section 5.1, we start with an outline of our experimental strategy. In Sections 5.2 and 5.3, we describe experiments using different biomechanical models based on either the Navier equation (called the *elastic model*) [62, 64, 61] or the Stokes equation (called the *fluid model*) to assess the general validity of the deformation results using these approaches. Section 5.4 then reports results using our new approach, which allows for a physically adequate simulation of the effect of forces acting upon rigid, elastic, and fluid regions by coupling the Navier equation and the Stokes equation (called *coupled rigid/elastic/fluid model*) [63, 59]. We compare the results with the elastic model as well as the fluid model.

All biomechanical models have been developed and implemented within the finite element programming environment DIFFPACK [95]. For the final transformation of the original image into the deformed image, we used a bilinear interpolation for both, the calculated displacement vector field and the image intensity function.

5.1 Experimental strategy

In the following Sections 5.2 and 5.3, we carry out experiments using a pure elastic model and a pure fluid model. To simulate inhomogeneous anatomical structures, we use spatial variations of the underlying material parameter values. In both cases, we start with experiments based on synthetic images, comprising translation, scaling, shear, and rotation of a rigid structure, to assess the general properties of the approaches. In particular, we are interested in the physical plausibility of the calculated deformations which has been assessed through visual inspection of the computed results. Therefore, we investigated whether the shape of rigid structures has been preserved while the deformation of the surrounding soft material matches the physical perception of the observer. Note, that a ground truth in form of intraoperative image data combined with reliable stress and strain measurements of living tissues for validation purposes of biomechanical models [28] has not been given so far, since medical (as well as legal) problems arise in conjunction with the accurate measurement of such data from patients. Additionally, less is known on the effects of additional surgical parameters like, e.g., specific narcotics, which influence the deformation behavior of living brain tissue [70].

After the experiments with synthetic images, we carry out registration experiments using real MR datasets and investigate the potential of our approach with respect to intraoperative image correction applications. Due to the lack of intraoperative MR images, we use a set of corresponding pre- and postoperative MR images to verify the accuracy of the calculated deformation. For comparison purposes, we always compute the deformation of a pure homogeneous model first, thus allowing us to analyze the influence of different simulated material properties on the final deformation.

In Section 5.4, we finally compare the pure elastic model and the pure fluid model with our coupled rigid/elastic/fluid model to assess the effect of different physical models on the calculated deformation. Again, we will start with some experiments using synthetic images. Following this, we carry out experiments using a section of a real preoperative MR image. In the experiments, we simulate the growth of a tumor compressing a nearby fluid structure. Due to the lack of ground truth or of at least a real MR image showing the final deformation caused by such a tumor growth, we are only able to compare the calculated deformation results on the basis of a visually observable physical plausibility of the resulting deformation.

5.2 The elastic model

Our elastic model described in Section 4.2 above, which is completely based on the Navier equation as underlying physical model, has been tested using 2D synthetic and tomographic datasets, as well as using 3D synthetic images. As ratios for the Lamé constants λ and μ, we took the values determined in Section 4.6, namely the ratios $\lambda_{br}/\mu_{br} = 135.111$ for soft materials, $\lambda_{sk}/\mu_{sk} = 0.718666$ for rigid materials, and $\lambda_{sk}/\lambda_{br} = 1011.72$ as ratio between rigid and soft materials.

For the assignment of individual material parameter values to the underlying finite element mesh, a direct mapping of each pixel (voxel) to the center

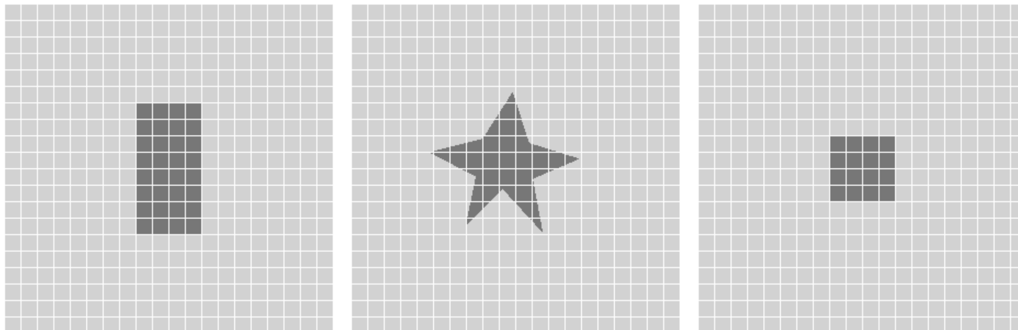

(a) (b) (c)

Figure 5.1: Synthetic images used in our experiments. The dark regions represent the rigid structures, while the bright ones represent the soft material. For better visualization purposes of the deformation process in the experiments, a white grid is overlaid in all cases.

of a four node (eight node) quadrilateral finite element in 2D (3D) has been used. This results in $2(N+1)^2$ degrees-of-freedom for a 2D image with $N \times N$ pixels. In the concrete case of a 256×256 image, the final matrix system contains 132098 degrees-of-freedom which can be solved with the current, non-optimized implementation in about 45 minutes on a Sun ultra 2/1300 workstation with 300 MHz.

5.2.1 2D synthetic images

Our synthetic experiments comprise different types of movements (translation, rotation) and affine transformations (scaling, shearing) of a simulated rigid object, embedded into simulated soft material. Figure 5.1 depicts the synthetic source images which have been used in the experiments. The size of these images are 301×301 pixels. As usual, it is assumed that the origin of the image coordinate system is in the upper left corner of the respective image.

Translation of a rigid structure

In our first experiments, we systematically investigated the translation of a simulated rigid structure of size 61×121 pixels, given a sparse set of prescribed displacements (or landmark correspondences). Figure 5.2 depicts the

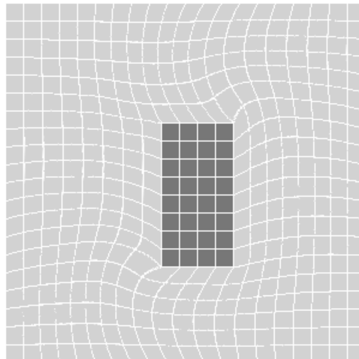

(a)

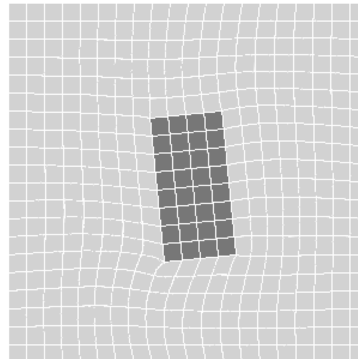

(b)

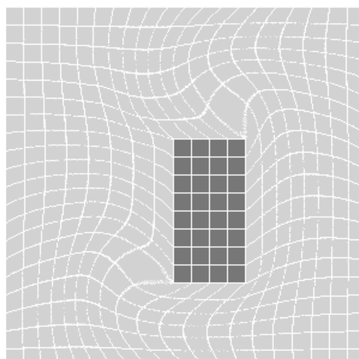

(c)

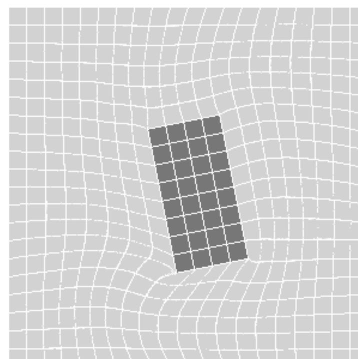

(d)

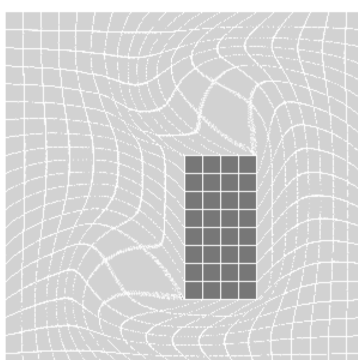

(e)

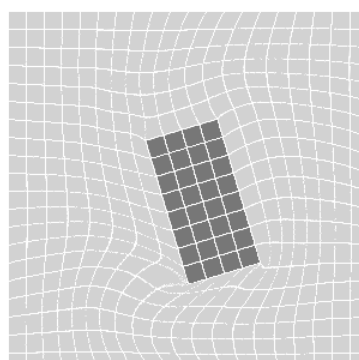

(f)

Figure 5.2: Usage of two prescribed displacements (left column) vs. one (right column) in order to enforce a translation of the simulated rigid rectangle, see text for details.

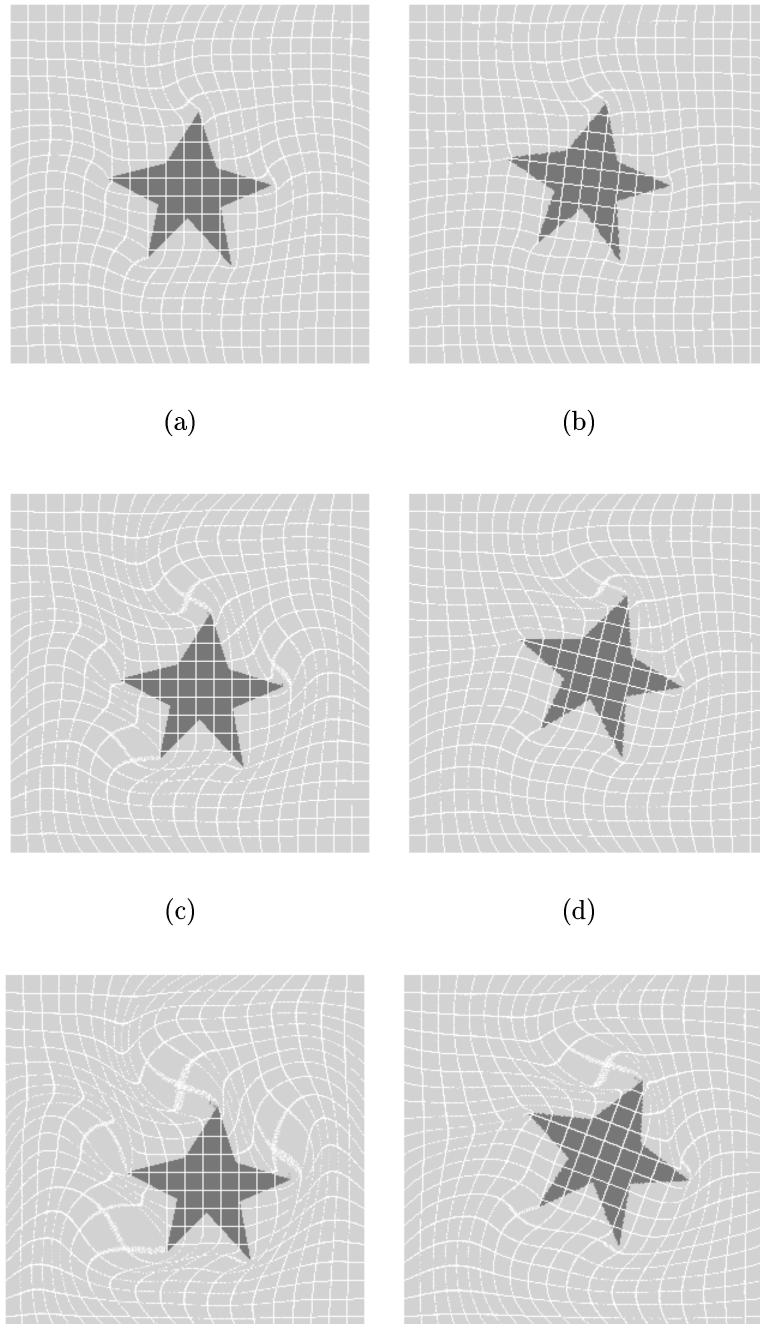

(a) (b)

(c) (d)

(e) (f)

Figure 5.3: Usage of two prescribed displacements (left column) vs. one (right column) in order to enforce a translation of the simulated rigid star-shaped structure.

deformation results while using a different number of prescribed displacements to enforce such a translation of the rectangular structure. For the results shown at the left column of Figure 5.2, two displacements were applied at the lower corners of the rectangle. As prescribed displacements, we used the vectors (a) $\mathbf{u} = (10.0, 10.0)^T$, (c) $\mathbf{u} = (20.0, 20.0)^T$, and (e) $\mathbf{u} = (30.0, 30.0)^T$, respectively, serving as different scales of translation from top to bottom in Figure 5.2. At the right column of Figure 5.2, only a single prescribed displacement with identical translation magnitudes as before was used instead, acting on the lower right corner of the rectangle.

A visual inspection of the deformation results reveals that the shape of the rigid structure is well-preserved in all cases. The grid lines inside the rectangle remain parallel and the whole deformation is limited to the surrounding soft material. The application of two prescribed displacements forces the rectangle into a pure translation, leading to large deformations in the surrounding soft material. In contrast, if only a single prescribed displacement is used, the surrounding material forces the rectangle into a combined motion of translation and rotation.

Figure 5.3 depicts the results for the star-shaped rigid structure of Figure 5.1(b), using the same prescribed displacements as in the previous examples. For the left column of Figure 5.3, a prescribed displacement acts on each, the right tip and the lower right tip of the star-shaped structure, respectively, while the single prescribed displacement used at the right column of Figure 5.3 acts on the right tip only. The results are still remarkably good, because the shape of the rigid structure remains preserved in all cases, even at the convex tips of the star.

An interesting point is the apparent broadening of the grid lines, as clearly visible in, e.g., Figures 5.3(e) and (f). Considering the section of the computed displacement vector field in Figure 5.4, taken from the lower left tip of the star, reveals the source of this behavior: The deformation process significantly spreads the regular pixel positions, each originally located at the back ends of the corresponding displacement vectors shown in Figure 5.4(a), such that a non-regular pixel structure results after the deformation. This leads to areas in the regular pixel structure of the deformed image which have not been assigned to any intensity values. To fill these gaps in the intensity function of the deformed image, appropriate intensity values have to be interpolated (using here a bilinear interpolation based on the four nearest neighbors) thus leading to the apparent blurring of the grid lines.

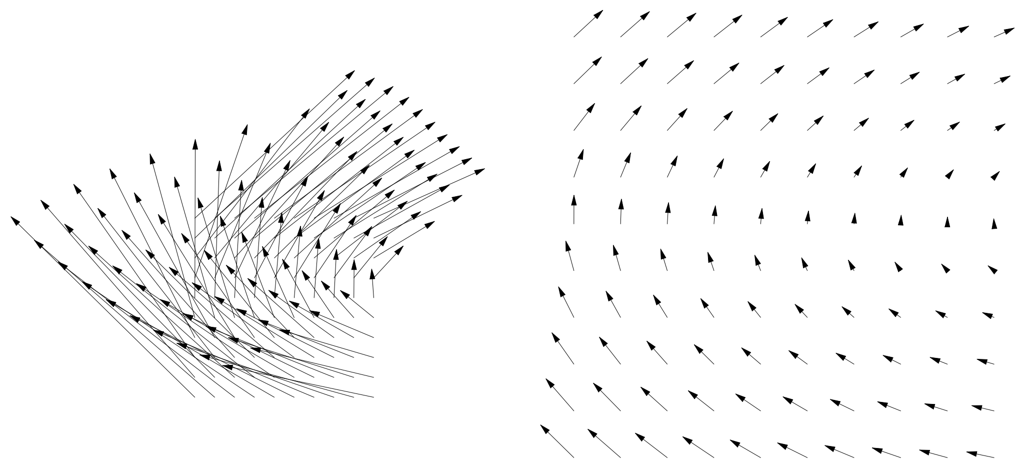

(a) (b)

Figure 5.4: A 10×10 section of the computed displacement vector field which transforms the star-shaped structure of Figure 5.1(b) into Figure 5.3(f). At the left side, a part of the original computed displacement vector field near the lower left tip of the star-shaped structure is shown. To obtain a better impression of the vector field, the right side depicts the same section, but in an enlarged and normalized vector representation, i.e. all displacements were appropriately scaled with respect to the largest displacement magnitude.

Scaling of a rigid structure

We also investigated the scaling of a rectangular structure. Looking at the results shown in Figures 5.5(a) and (c), where four prescribed displacement vectors $\mathbf{u} = (\pm 20.0, \pm 20.0)^T$ or $\mathbf{u} = (\pm 30.0, \pm 30.0)^T$ were placed at each corner of the rectangle such that a magnification of the structure results, reveals an interesting property: While the rectangular structure is stretched in longitudinal direction, it simultaneously shrinks in the lateral direction. This deformation behavior is in contrast to a shape-preserving growth of biological structures like, e.g., some lesions, but it is physically plausible for real materials that are stretched without additional mass supply, since the Poisson ratio ν, which measures the ratio between the relative transversal contraction and the relative longitudinal dilation, is greater than zero for all real materials [21, 68].

To simulate a shape-preserving growth of a biological structure, we en-

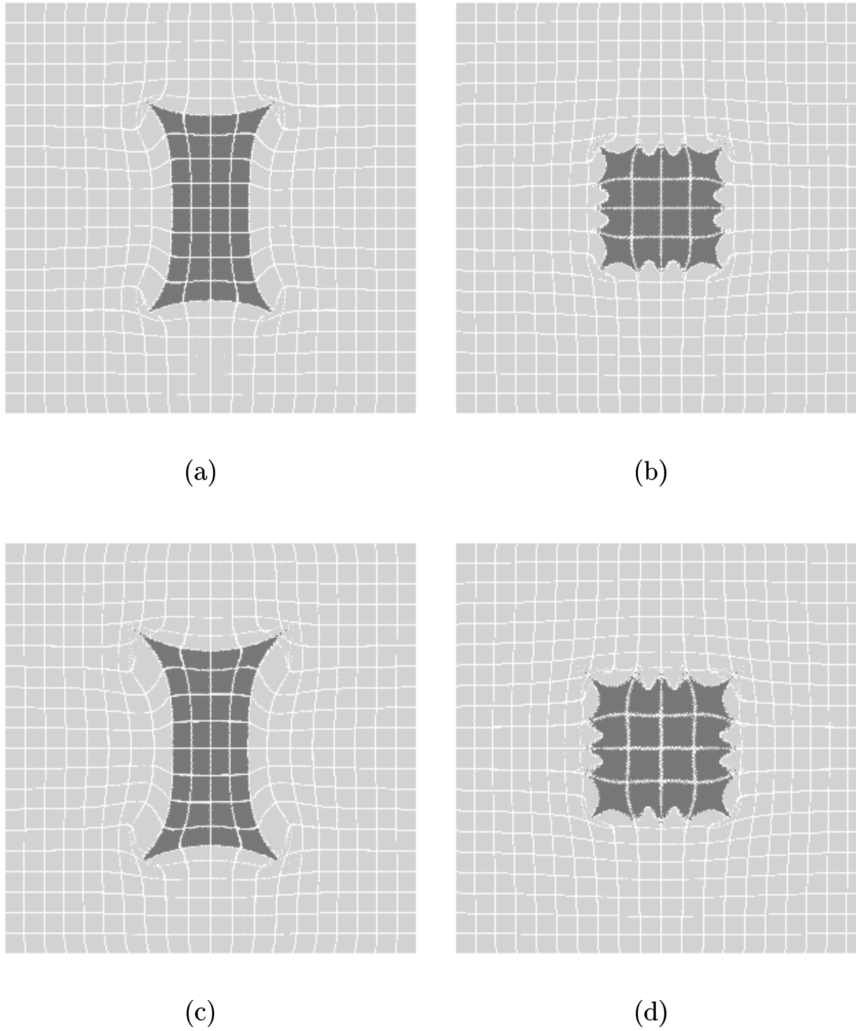

Figure 5.5: Left column: Magnification of a rectangle using a sparse set of prescribed displacements. Right column: Magnification of a rigid block using five equidistant prescribed displacements on each side. The components of the prescribed vectors are $\mathbf{u} = (\pm 20.0, \pm 20.0)^T$ in the top row and $\mathbf{u} = (\pm 30.0, \pm 30.0)^T$ in the bottom row, respectively.

larged the rigid block in Figures 5.5(b) and (d) using an increased number of 5 prescribed displacements at each side. Again, a shrinking is visible between the loci where the prescribed displacements act. It follows, that a relatively large number of prescribed displacements would be necessary to simulate an ideal shape-preserving magnification of a rigid object.

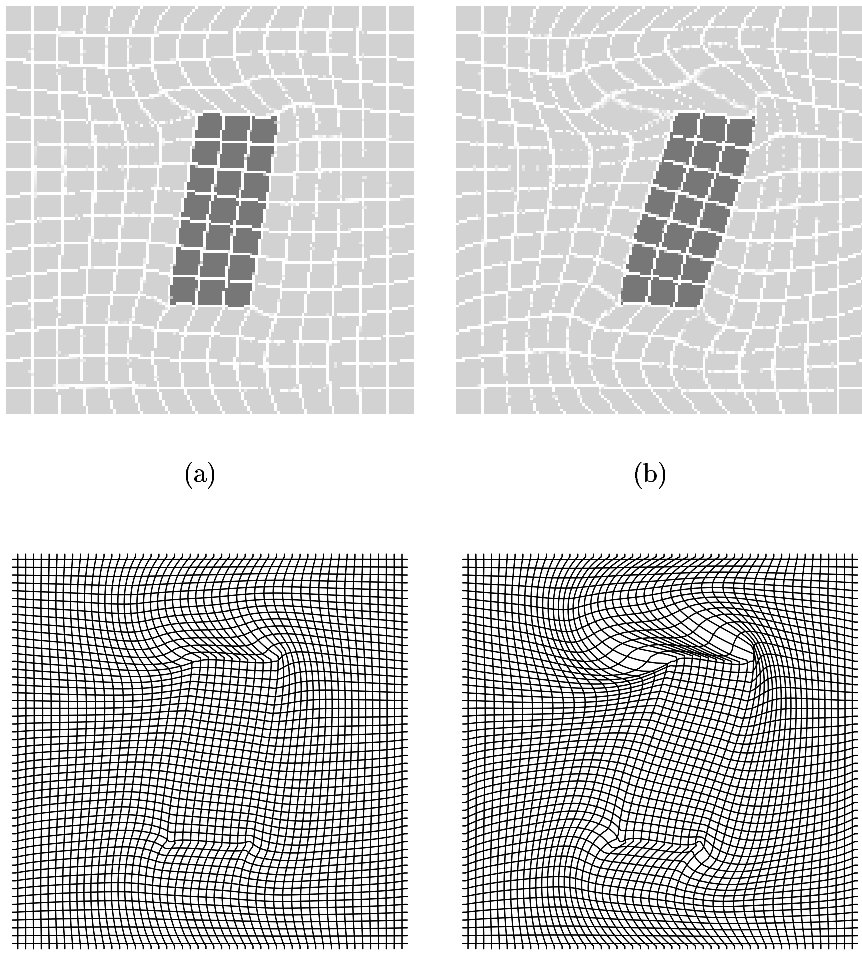

(a) (b) (c) (d)

Figure 5.6: Shearing of a rectangular structure. The magnitude of the prescribed displacements used for the shear is either $\mathbf{u} = (10.0, 0.0)^T$ (left column) or $\mathbf{u} = (20.0, 0.0)^T$ (right column).

Shear of a rigid structure

Next, we carried out experiments with a rigid object undergoing a shear. For the purpose of comparing the deformations with the results of our fluid model presented below, we reduced the image size in these experiments to 151×151 pixels.

To enforce a shear of a rectangular structure, we applied two identical displacements at both upper corners of the rectangle while using two vectors with components $\mathbf{u} = (0.0, 0.0)^T$ at the lower corners of the structure. The left column of Figure 5.6 shows the result and corresponding grid deformation, if the vector components of both prescribed displacements read $\mathbf{u} = (10.0, 0.0)^T$. For the right column of Figure 5.6, prescribed displacements with components $\mathbf{u} = (20.0, 0.0)^T$ have been used instead.

Especially the grid deformations in the bottom row of Figure 5.6 indicate, that deformations occur within the rigid structure. Furthermore, the amount of bending significantly increases with the magnitude of the shear. The physical reason of this deformation behavior lies in the fact, that an elastic body, which is simulated using the Navier equation, can sustain a shear stress at rest. In other words, $\sigma_{ij} \neq 0$ for $i \neq j$ holds for the components of the Eulerian stress tensor $\boldsymbol{\sigma}$ and with Hooke's law (2.37) also for the corresponding components ϵ_{ij} of Cauchy's infinitesimal strain tensor $\boldsymbol{\epsilon}$. It follows from

$$\epsilon_{ij} = \frac{1}{2} \left(\partial_j u_i + \partial_i u_j \right) \tag{5.1}$$

due to definition (2.36), that changes of the ith component of the displacement field $\mathbf{u}$ in the jth direction occur, i.e. a bending of the rigid structure occurs as a result of the shear stress.

Rotation of a Rigid Structure

Our final experiments with 2D synthetic images comprise the rotation of the rigid square shown in Figure 5.1(c) around its center in a clockwise direction. To enforce the rotation, we used two prescribed displacements, one acting at the upper right corner and one acting at the lower left corner of the square. Appropriate components for the applied displacement vectors have been calculated through the relations [39]

$$\mathrm{x}_1' = \mathrm{x}_1 \cos\vartheta + \mathrm{x}_2 \sin\vartheta \tag{5.2}$$

and

$$\mathrm{x}_2' = \mathrm{x}_2 \cos\vartheta - \mathrm{x}_1 \sin\vartheta, \tag{5.3}$$

where x_1' and x_2' denote the components of the new position $\mathbf{x}'$ of the corner point $\mathbf{x} = (\mathrm{x}_1, \mathrm{x}_2)^T$ and ϑ the rotation angle. Figure 5.7 depicts the results for a rotation of 10°, 20°, 45°, and 90° degree, respectively.

Interestingly, our approach works well for rotation angles up to about 45°, but fails otherwise. Especially in case of a rotation about 90° degree,

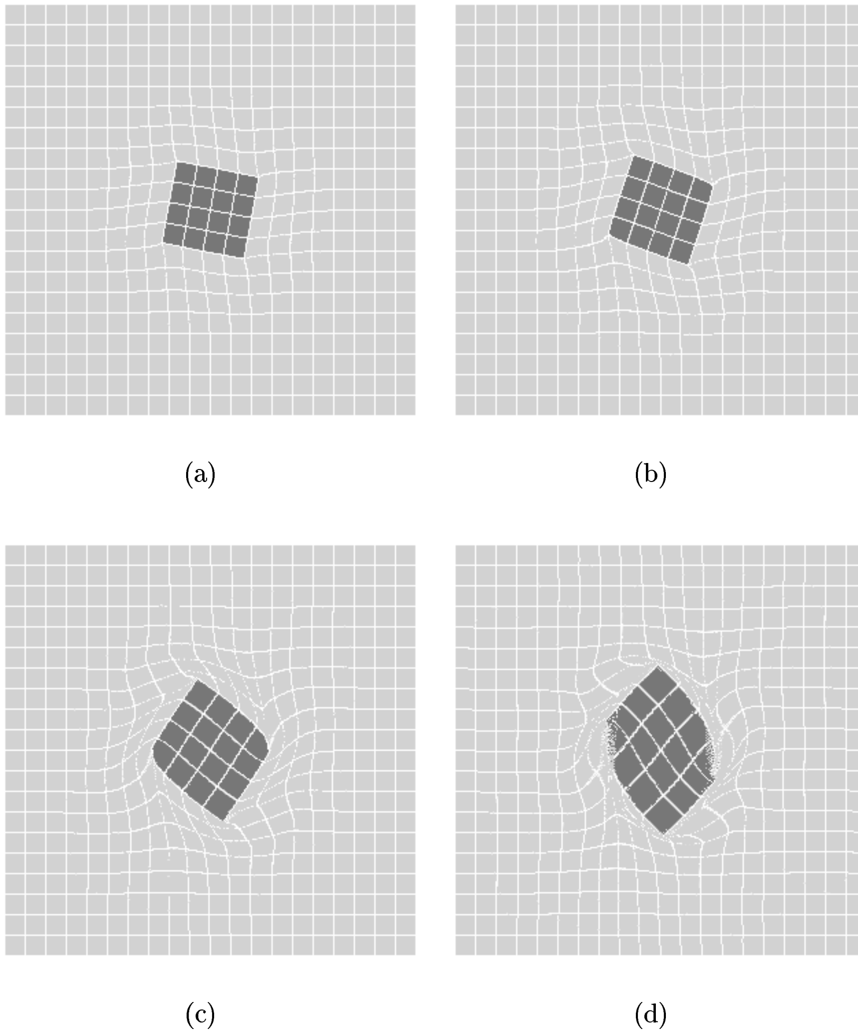

Figure 5.7: Clockwise rotation of a rigid square around its center. The necessary prescribed correspondences were calculated using equations (5.2) and (5.3). The applied angles ϑ were (a) $10°$, (b) $20°$, (c) $45°$ and (d) $90°$ degree.

the whole square is strongly deformed, as indicated by the curved grid-lines inside the square shown in Figure 5.7(d). Since the assumption of *small* deformations is violated here, the *linear* elasticity theory, assuming infinitesimal displacements (see Section 2.2.3 for details) cannot be used. Instead, large deformations occur such that the second Piola-Kirchhoff stress tensor $\mathbf{\Sigma}$ as well as the Green-St. Venant strain tensor $\mathbf{E}$ have to be used. An al-

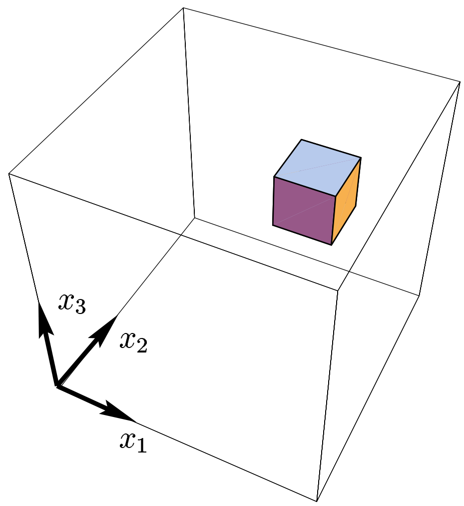

(a)

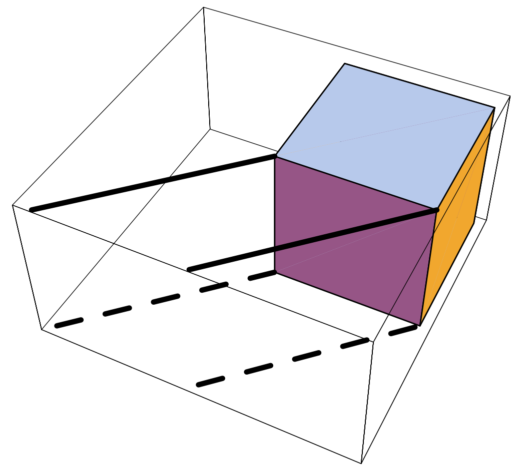

(b)

Figure 5.8: Left side: Synthetic 3D image used in our experiments. The coordinates of the lower left corner of the embedded rigid cube read $(40, 40, 40)^T$. Right side: Enlarged section of the synthetic 3D image with four prescribed displacements (shown as solid and dashed lines) whose components read $\mathbf{u} = (-15.0, -15.0, 0.0)^T$, each acting on a corner of the rigid cube. For our second experiment, we used the two prescribed displacements denoted by solid lines only.

ternative formulation for the simulation of large deformations represents the Lagrangian incremental approach [21, 118] which allows an approximation of the solution by successively solving linear problems.

5.2.2 3D synthetic images

After the experimental analysis of the behavior of the elastic model in 2D, we will now carry out some 3D experiments. The used synthetic 3D image showing a rigid cube embedded into soft material, has the dimensions of $71 \times 71 \times 71$ voxels, while the size of the embedded cube is $15 \times 15 \times 15$ voxels, see Figure 5.8(a). For the material parameter values, we took the same ratios as in the previous section.

Our first experiment simulates the translation of the rigid cube using four parallel prescribed displacements with components $\mathbf{u} = (-15.0, -15.0, 0.0)^T$ thus forcing the cube into a pure translation within a xy-plane of the image.

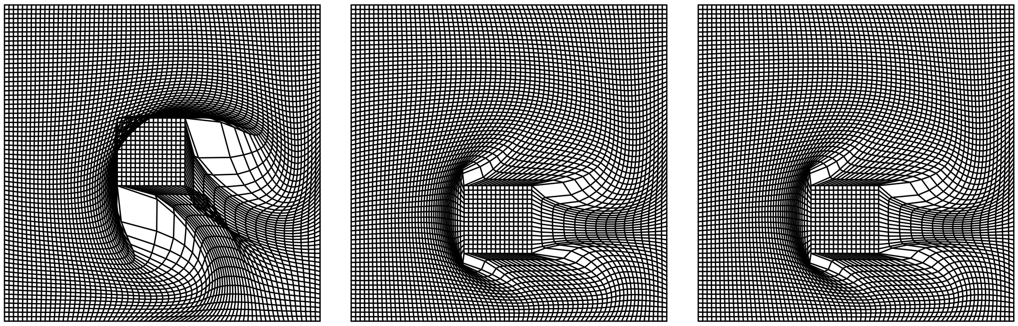

(a) (b) (c)

Figure 5.9: Translation of a rigid cube in the xy-plane: projections of the displacement vector field in three orthogonal planes, namely (a) slice 40 of the xy-plane, (b) slice 40 of the xz-plane, and (c) slice 40 of the yz-plane.

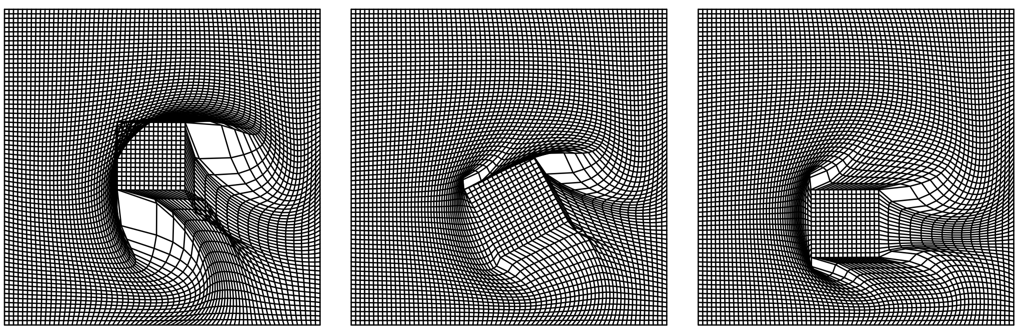

(a) (b) (c)

Figure 5.10: Translation of a rigid cube using two displacements in the xy-plane: projections of the displacement vector field in three orthogonal planes, namely (a) slice 40 of the xy-plane, (b) slice 40 of the xz-plane, and (c) slice 40 of the yz-plane.

Figure 5.8(b) depicts the cube with the four prescribed displacements acting at the corners of the cube.

The resulting deformation is shown in Figure 5.9. Here, three orthogonal views are presented, namely the projections of the displacement vector field onto (a) the xy-plane, (b) the xz-plane, and (c) the yz-plane, respectively. At first glance, it seems that a violation of the underlying grid topology occurs within the xy-plane, but Figures 5.9(b) and (c) reveal, that this apparent violation is merely a consequence of the projection of the displacement vector field onto the xy-plane. In fact, the soft material is mainly deformed in the z-direction, as indicated by the significant compression of the grid in Figures 5.9(b) and (c). The shape of the rigid cube is still well-preserved here thus leading to a physically plausible 3D deformation result of our biomechanical model.

In a second experiment, we applied two prescribed displacements with components $\mathbf{u} = (-15.0, -15.0, 0.0)^T$ at the upper corners of the cube, i.e. we used only a subset of the prescribed displacements as shown in Figure 5.8(b). The lack of given displacements at the lower corners of the cube leads to a significantly different deformation result compared to the previous experiment. Figures 5.10(a) and (c) reveal, that the deformations with respect to the xy-plane and the yz-plane are identical to the previous translation experiment. This is in accordance with the application of two parallel correspondences, spanning a single plane in the space, which forces the cube to a pure translation along this plane. But within the xz-plane, which is depicted in Figure 5.10(b), the influence of the soft material on the calculated deformation is clearly visible. The lack of prescribed displacements given outside the plane defined by the first two correspondences leads to a rotation of the rigid cube due to the influence of the surrounding soft material.

Based on these first experiments with a 3D synthetic image, it can be summarized that our elastic model leads to physically plausible deformation results in the 3D case. Nevertheless, further experiments should be carried out to assess the behavior of the approach in 3D under different conditions.

5.2.3 2D MR images

For the experiments with real data, we used pre- and postoperative 3D MR images which were routinely acquired in conjunction with the planning and radiological control of a tumor resection. Although our elastic model is valid in 3D, we carried out 2D experiments only since the necessary region segmentation as well as the finding of correspondences in 3D is generally more difficult and costly than in the case of 2D images.

The used 2D images, as shown in Figure 5.11, are corresponding slices of the 3D datasets which were aligned prior to our experiments by a rigid registration using 34 manually determined landmarks. Due to the lack of intraoperative image data, a postoperative image was used to simulate an intraoperative one.

To determine correspondences which can be used as input data for our

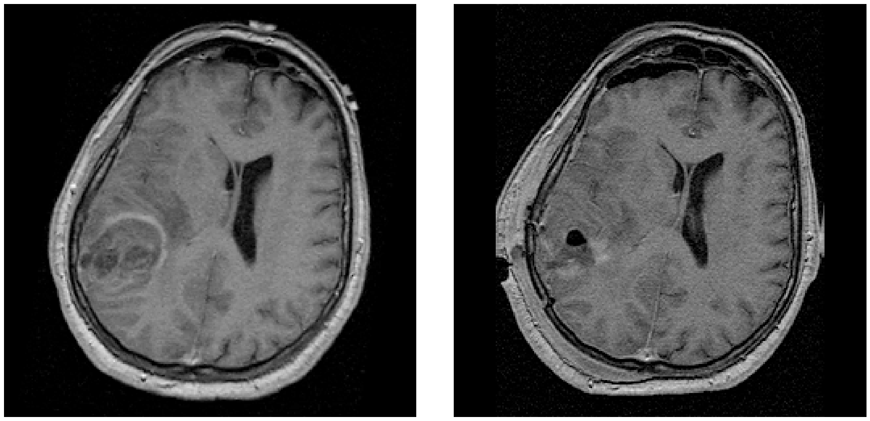

(a) (b)

Figure 5.11: Slices 34 of pre- (left side) and postoperative (right side) MR datasets (Courtesy of Neurosurgical Clinic, Aachen Institute of Technology (RWTH Aachen).

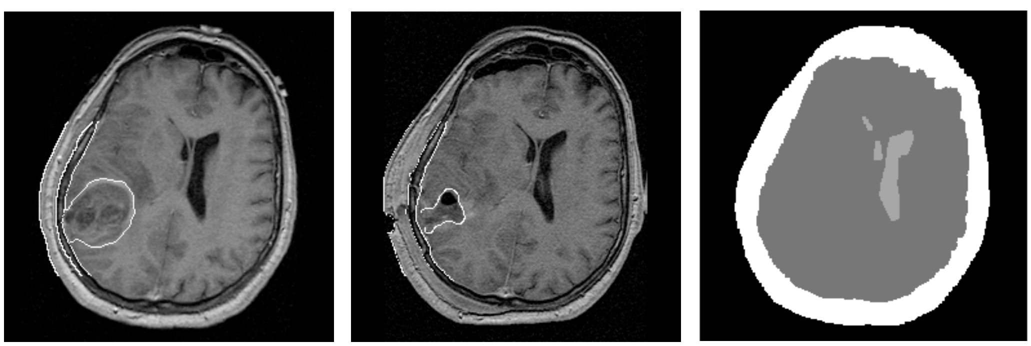

(a) (b) (c)

Figure 5.12: Manually determined outlines in (a) the pre- and (b) the post-operative image. In (c), the regions as segmented with an interactive 2D watershed algorithm are depicted.

model to match the pre- with the postoperative image, the corresponding tumor and resection area outlines in both images were manually determined by a medical expert as indicated in Figures 5.12(a) and (b) by the white outlines. Thereafter, a snake algorithm [79] has been applied to each image, which resulted in 618 correspondences between the contours of Figures 5.12(a) and (b) [118]. For this purpose, the two snakes were represented as two sets of points whose evolution over time have been tracked and finally used for correspondence finding [118]. To determine correspondences for a 3D application of the elastic model, it seems most promising to use deformable models [104] instead. In clinical applications, other input data like the insertion depth of surgical instruments could be used to determine correspondences.

According to our experimental strategy, which allows to assess the influence of different material properties in subsequent experiments, Figure 5.13(a) shows a locally erroneous registration result since homogeneous soft material for the whole image was only assumed. Note that local errors are clearly visible, especially in the vicinity of the ventricular system (see also the enlarged part of the ventricular system depicted in Figure 5.15(a)).

In order to improve this registration result, different materials were incorporated by assigning spatially different Lamé constants λ and μ in accordance with the underlying anatomical structures. To this end, the preoperative image was segmented with a 2D interactive watershed algorithm [150] into four different regions, shown in Figure 5.12(c): Combined skin/skull region (white), brain (dark grey), cerebrospinal fluid (light grey), and surrounding air, i.e. image background (black). The air in the frontal sinus of the skull bone was assigned to the skull bone region since Hooke's law does not describe the physical behavior of air. Intracranial air and subarachnoidal CSF spaces between skull and brain were assigned to the brain tissue region, resulting in a rather simplified border between brain tissue and skull bone. But due to the viscosity of fluids like cerebrospinal fluid, the applied compatibility boundary condition seems to be valid [47]. For brain tissue and skull bone, the previously determined ratios for the material parameter values were used, while the cerebrospinal fluid, motivated by its reported incompressibility [135, 146], was roughly approximated as rigid material using the same ratios as for skull bone. The air of the image background was modeled as a highly soft material, i.e. we arbitrarily assumed the ratios $\lambda_{air}/\mu_{air} = 100.0$ and $\lambda_{br}/\lambda_{air} = 1490.0$, respectively.

The registration result is shown in Figure 5.13(d). Here, a global movement of the head, forced by the given correspondences, can be observed which leads to a surprisingly poor registration result. Nevertheless, the assumption of inhomogeneous material properties leads to a completely different deformation behavior as shown in the section of the displacement vector field in Figure 5.13(f). According to the rigid material assumption, the ventricular system cannot deform here thus leading to a small rotation of the whole ventricular system with respect to the postoperative image, best seen in the

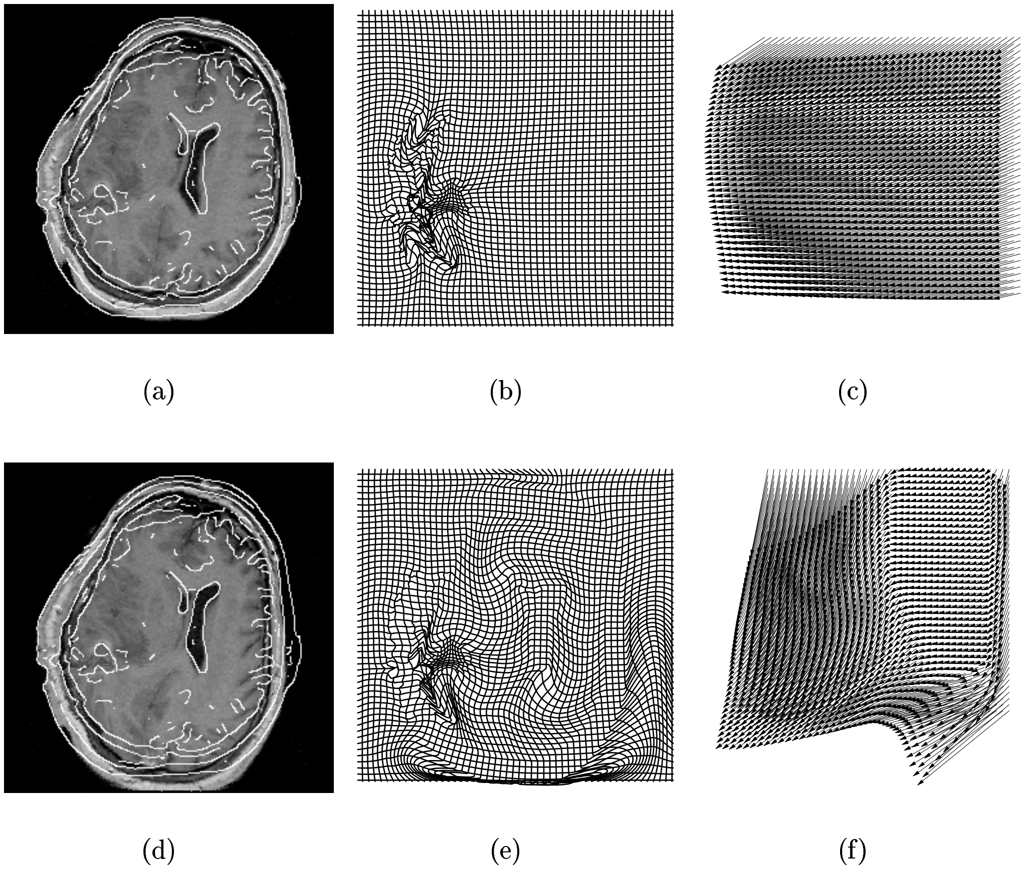

Figure 5.13: Top row: (a) Registration result assuming homogeneous soft material properties for the whole image (with overlaid Canny edges of the original postoperative image), (b) resulting grid deformation after application of the calculated displacement vector field, and (c) section of the displacement vector field from the bottom part of the ventricular system. Bottom row: Based on the segmentation given in Figure 5.12(c), inhomogeneous material properties in conjunction with a soft image background have been assumed instead.

enlarged section depicted in Figure 5.15(b). As indicated by the corresponding grid deformation in Figure 5.13(e), there is a global movement of the head. This movement can be suppressed by preventing a deformation of the image background, i.e. by using the Lamé constant ratio of a rigid body for the image background, see Figures 5.14(a)-(c). In this case, an overall good registration result can be achieved, even in the vicinity of the ventricular

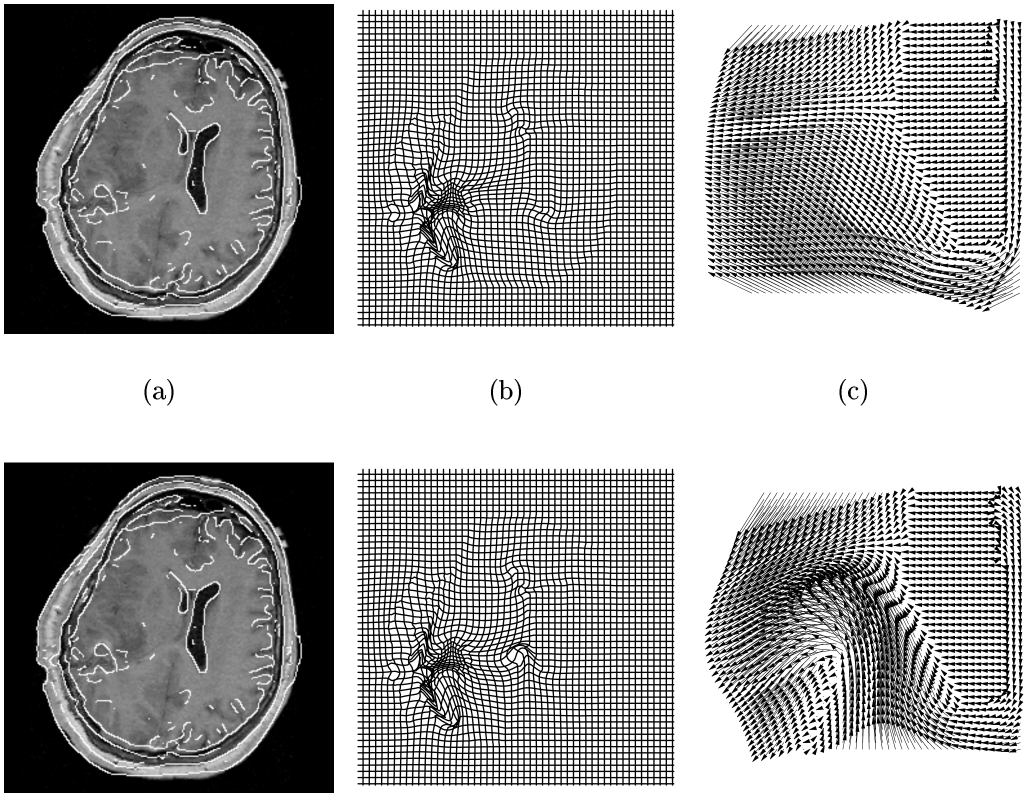

(a) (b) (c)

(d) (e) (f)

Figure 5.14: Same as Figure 5.13(d)-(f) but assuming a rigid image background (top row) plus additionally 68 correspondences given at the midline in the posterior half of the brain (bottom row).

system, as clearly depicted in Figure 5.15(c). Note, that no correspondences were given at the ventricular system, only the assumed inhomogeneous material properties suppress a deformation of the ventricular system with respect to the postoperative image.

However, a closer consideration of the results shown in Figures 5.13(a), 5.13(d), and 5.14(a) reveals a significant shift of the midline in the posterior half of the brain which is in contrast to the postoperative image in Figure 5.11(b) (see also [102]). This shift can be suppressed by using additional correspondences at the posterior midline (in this case, we used 68 manually determined correspondences) thus giving the result shown in Figure 5.14(d). Here, an overall good registration result is achieved and no shift of the poste-

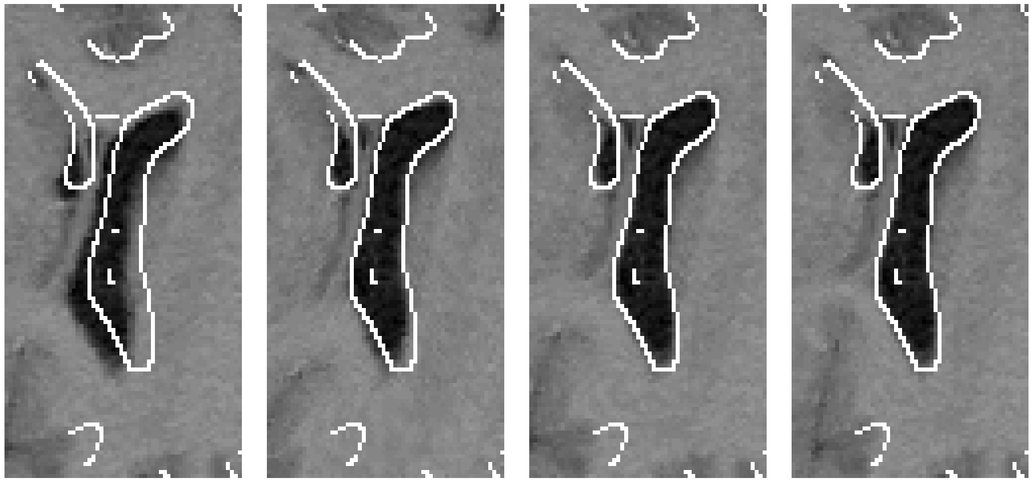

(a) (b) (c) (d)

Figure 5.15: Enlarged parts of the ventricular systems of Figures 5.13(a), 5.13(d), 5.14(a), and 5.14(d) with overlaid Canny edges of the original post-operative image. Subfigure (a) shows the result for homogeneous soft material, (b) for the inhomogeneous case, (c) for the inhomogeneous case with rigid image background, and (d) for the case with additional 68 correspondences.

rior midline occurs, see the enlarged sections in Figure 5.16 for a comparison of the posterior midlines. As indicated by the corresponding grid deformations in Figures 5.14(b) and (e), the additionally applied correspondences significantly suppress the deformations in the left hemisphere. Deformations occur only between the top end of the posterior midline and the ventricular system due to the deformation of the soft brain tissue, see Figure 5.14(f). Since real measurements indicate that deviations of the posterior midline seldom occur as intraoperative deformations during surgical interventions [102], a movement of the latter one should be generally suppressed using appropriate correspondences at the posterior midline.

5.3 The fluid model

Our fluid model derived in Section 4.2 above, which is completely based on the Stokes equation as underlying physical model, has been tested using synthetic and tomographic datasets. As material parameter values for the

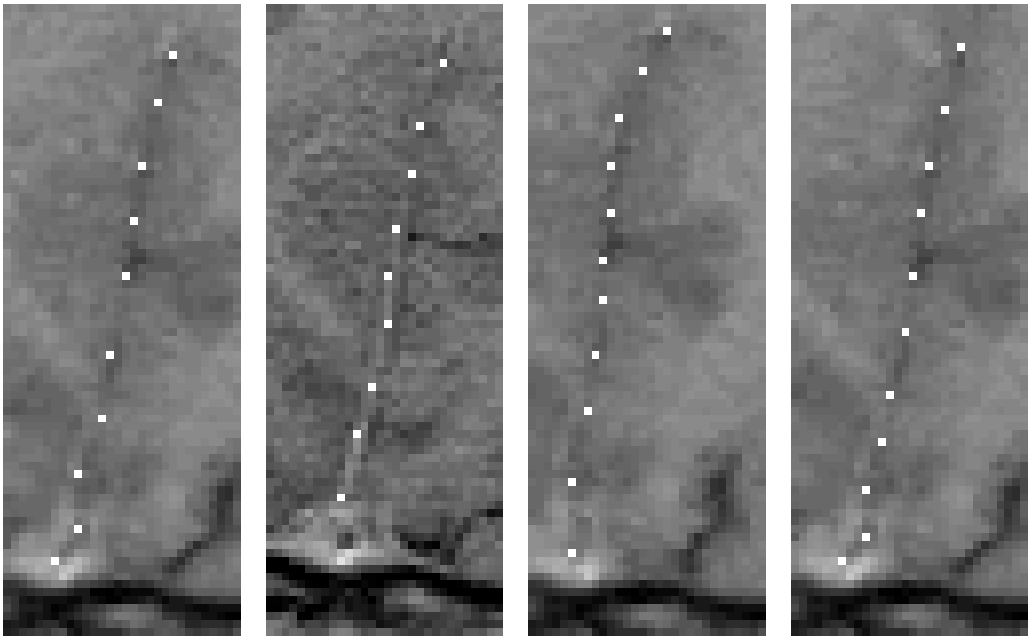

(a) (b) (c) (d)

Figure 5.16: Enlarged parts of the posterior midline from (a) the preoperative image, (b) the postoperative image, (c) the image in Figure 5.14(a) with inhomogeneous material properties, and (d) the image in Figure 5.14(d) with inhomogeneous materials and additional correspondences given at the posterior midline. For visualization purposes, we manually marked the posterior line with white squares. A comparison with the pre- and postoperative images reveals, that in (c) larger deviations are visible while in (d) no shift of the midline occurs.

combined parameter $\mu^\star dt^{-1}$ of the underlying Stokes equation, we took the ratio determined in Section 4.6, namely the ratio $\mu^\star_{br} dt^{-1}/\mu^\star_{sk} dt^{-1} = 0.0001$ between rigid and soft materials, which have been modeled here as thick liquids and thin liquids, respectively.

According to the advantages of divergence-free finite elements compared to the Q_2-P_1 Crouzeix-Raviart finite elements, see Section 4.3.3, we use divergence-free finite elements. Although the concept of divergence-free finite elements is generally extendible to 3D [57, 25], we restrict our investigations here to 2D images only since the complexity of the approach increases significantly otherwise. For the construction of the underlying finite element mesh, a direct mapping between image pixels and finite elements is used since this allows a simple assignment of different material parameter values to the corresponding anatomical structures. Additionally, the segmentation of an inhomogeneous body is simplified such that the segmentation must not follow the finite element boundaries of the underlying finite element mesh exactly, see Appendix B for further details. This mapping results in $2(N+1)(2N+1)+(N+1)^2 = 5N^2+8N+3$ degrees-of-freedom for a 2D image with $N \times N$ pixels. In the concrete case of an image with 256×256 pixels, the final matrix system contains 329731 degrees-of-freedom. To furthermore prevent from an assignment of explicit values to the stream function $\tilde{\boldsymbol{\psi}}$, see Section 4.5 for details, all given correspondences are incorporated by assigning the given displacement vectors to the four corner nodes $\mathbf{x}_1, \ldots, \mathbf{x}_4$ of the appropriate divergence-free finite elements only. As a consequence, the resulting displacements of the image pixels will usually not preserve the given displacement vectors, instead the vectors calculated for the mid-node $\mathbf{x}_9$ of the divergence-free finite elements will result.

5.3.1 2D synthetic images

Our synthetic experiments with the fluid approach consists of different types of movements (translation) and affine transformations (scaling, shear) of a simulated rigid object, embedded into simulated soft material. As mentioned above, since all structures being physically simulated using the Stokes equation are treated as fluids, we model rigid structures by using thick liquids and soft structures by using thin liquids. The image size in all experiments is restricted to 151×151 pixels due to the significantly higher calculation times for larger image sizes, see Table 4.1 in Section 4.3.3.

Translation of a rigid structure

Again, we start our experiments with investigating the effect of a translation of a thick liquid structure of rectangular shape, originally centered at the middle of the image. For these experiments, we use a set of two identical prescribed displacements, each acting at one of the right corners of the rectangle. The calculated deformed images as well as the corresponding grid deformations for the prescribed displacements $\mathbf{u} = (10.0, 0.0)^T$ and $\mathbf{u} = (20.0, 0.0)^T$ are shown in the left and right columns of Figure 5.17, respectively. It is clearly visible from Figure 5.17, that the shape of the thick liquid structure is well preserved in both cases while the surrounding thin liquid deforms in a physical plausible way.

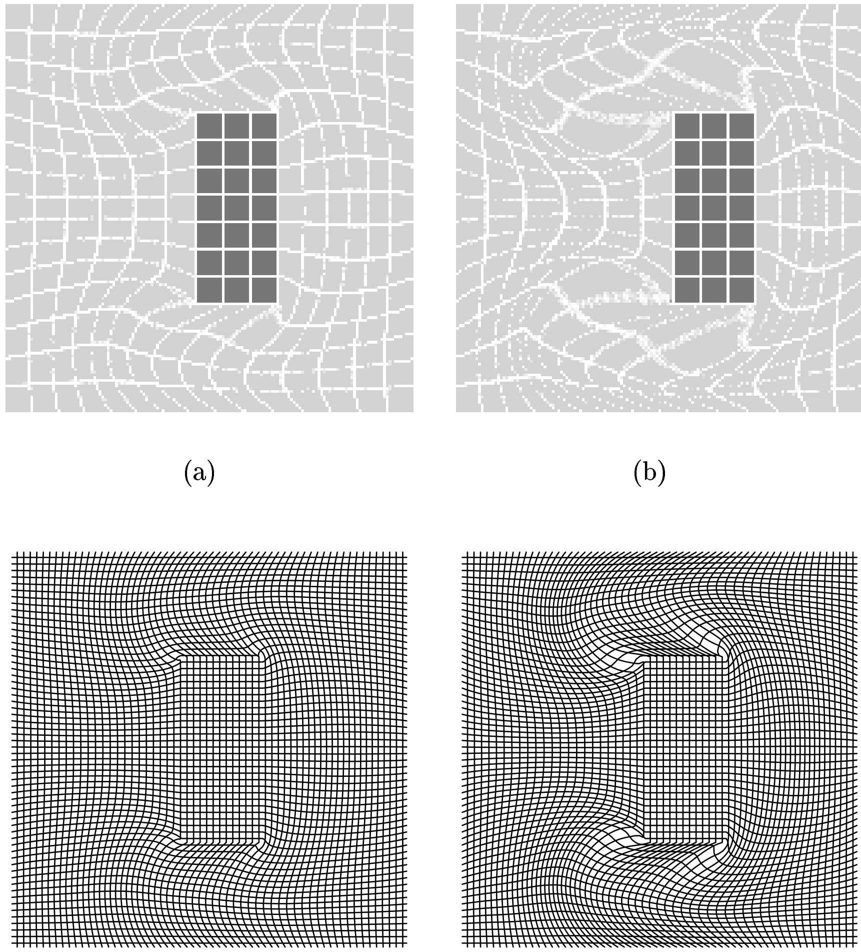

(a) (b)

(c) (d)

Figure 5.17: Resulting deformations (top row) and corresponding grid deformations (bottom row) for different magnitudes of translation using the prescribed displacement vectors $\mathbf{u} = (10.0, 0.0)^T$ (left column) and $\mathbf{u} = (20.0, 0.0)^T$ (right column), respectively.

Scaling of a Rigid Structure

In our second experiment, we analyze the effect of scaling a thick liquid structure of rectangular shape by applying a set of prescribed displacement vectors pointing outwards such that a magnification of the thick liquid structure results. The components of the prescribed displacements, each acting at

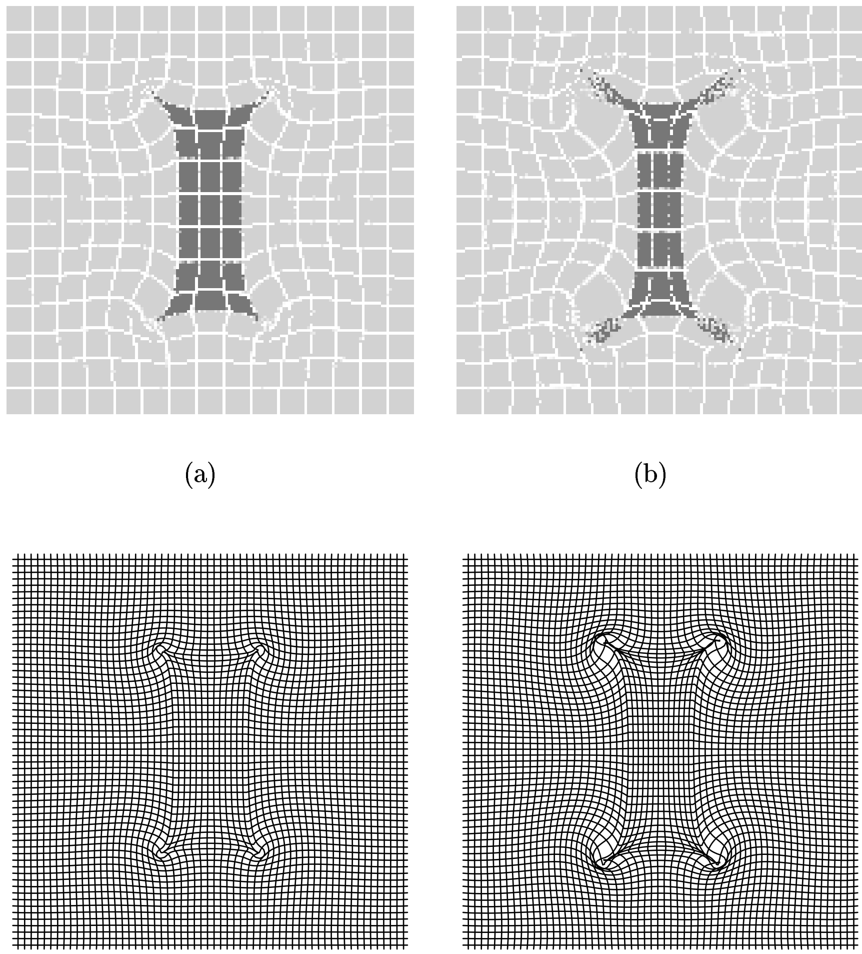

(a) (b) (c) (d)

Figure 5.18: Scaling of a thick liquid structure of rectangular shape with a sparse set of prescribed displacements. The vector components acting on each corner of the rectangle read $\mathbf{u} = (\pm 10.0, \pm 10.0)^T$ (left column) and $\mathbf{u} = (\pm 20.0, \pm 20.0)^T$ (right column).

a corner of the rectangle, read $\mathbf{u} = (\pm 10.0, \pm 10.0)^T$ or $\mathbf{u} = (\pm 20.0, \pm 20.0)^T$ where the signs of the components have to be adjusted to match the corresponding corner considered. The deformed images and corresponding grid deformations are shown in Figure 5.18. It turns out, that the deformation result is somewhat similar to the calculated deformation result using our elastic model (compare Figure 5.18 with the results shown in the left column of Figure 5.5). Interestingly, the deformation behavior of the surrounding thin liquid shows a more global behavior in this case for the fluid model than for the elastic model.

Shearing of a Rigid Structure

The last synthetic image experiments with our fluid model comprise different magnitudes of shearing of a thick liquid structure of rectangular shape. To enforce the shear, we applied two identical displacements at each upper corner of the rectangle while preventing a movement of both lower corners of the rectangle using the displacement vectors $\mathbf{u} = (0.0, 0.0)^T$. The left column of Figure 5.19 shows the deformation result and corresponding grid deformation, if the vector components of the upper prescribed displacements read $\mathbf{u} = (10.0, 0.0)^T$. For the results shown in the right column of Figure 5.19, prescribed displacements with components $\mathbf{u} = (20.0, 0.0)^T$ have been used instead.

In both cases, the calculated deformation shows that the used displacements lead to a roughly ideal shearing of the thick liquid structure since the resulting shape of the rectangle is rather similar to a parallelogram. A comparison of these results with those of our elastic model, which were depicted in Figure 5.6, reveals, that the fluid model leads to a significantly different deformation in the case of shearing. Using the fluid model, hardly any bending of the thick liquid structure is visible, neither at the boundary nor inside the rectangle. This is in contrast to the results of the elastic model where significant bendings are clearly visible (compare these results with those of the elastic model in Section 5.2.1 above). The physical reason for this deformation behavior of the fluid model can be found in the fact, that fluids cannot sustain a shear stress at rest or uniform flow [100, 47], i.e. the shape of a structure in the equilibrium is such that the Cauchy stress vector $\hat{\mathbf{t}}(\hat{\mathbf{x}}, \hat{\mathbf{n}})$ acts always normal to the boundary [100, 21] and consequently the shape is preserved.

5.3.2 2D MR images

Following our experimental strategy described in Section 5.1, we carried out registration experiments using the pre- and postoperative MR images of Figure 5.11 as well as the previously used set of 618 prescribed displacements, which were determined by applying a snake algorithm using the contours depicted in Figures 5.12(a) and (b). Again, our first registration experiment assumes a homogeneous fluid model only. The combined parameter of the underlying Stokes equation was set to $\mu^{\star} dt^{-1} = 1.0$ for all image regions.

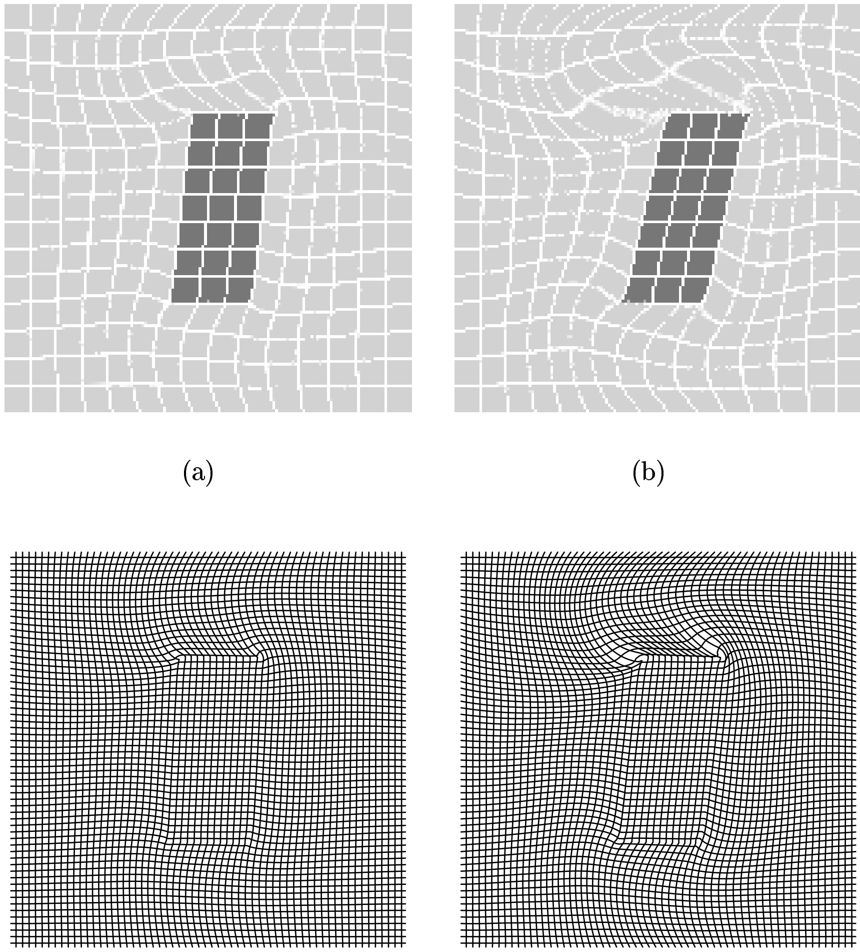

(a) (b)

(c) (d)

Figure 5.19: Resulting deformation (top row) and corresponding grid deformation (bottom row) for different amounts of shearing a rectangle (see text).

The second experiment assumes an inhomogeneous fluid model instead with spatially varying values of the viscosity parameter (applying the same ratios as in the synthetic experiments), based on the segmentation shown in Figure 5.12(c). For comparison purposes with the elastic model, we simulated the skull, the image background, and the ventricular system as rigid structures using a thick liquid, while the brain tissue was simulated as soft material using a thin liquid. Although it seems inappropriate, the simulation of the

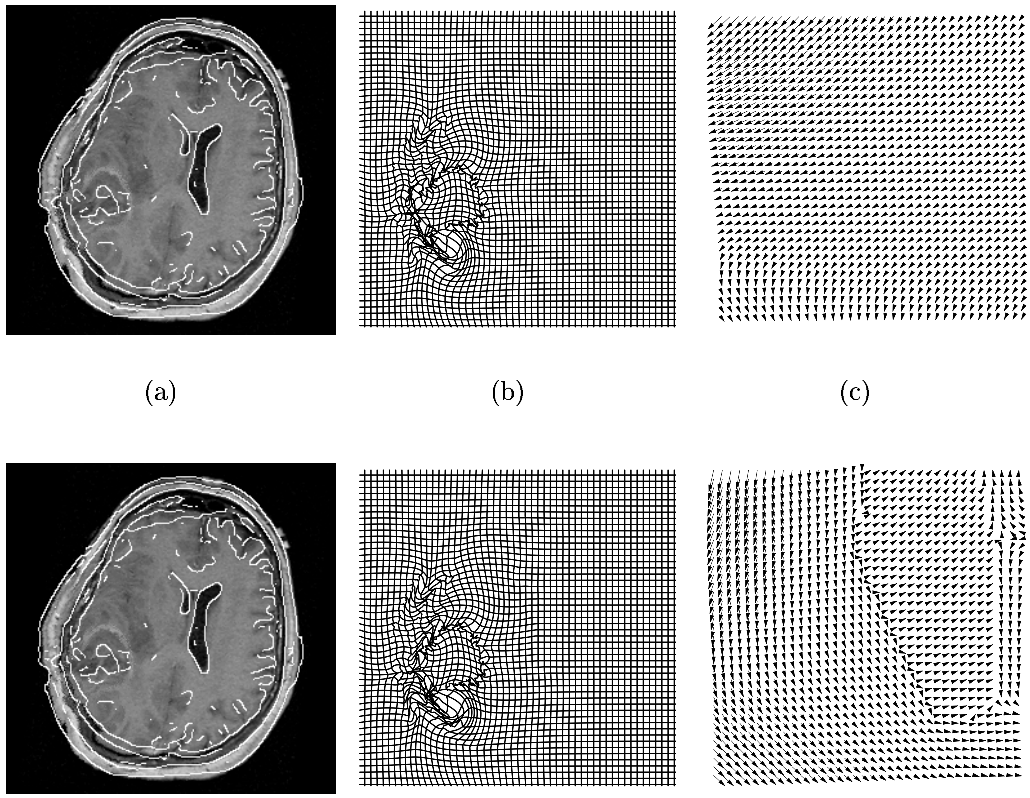

(a) (b) (c)

(d) (e) (f)

Figure 5.20: Registration result using a homogeneous fluid model (top row) and an inhomogeneous fluid model (bottom row): Transformed preoperative image with overlaid Canny edges of the original postoperative image (left column), corresponding grid deformation (middle column), and a section of the interpolated displacement vector field (right column).

ventricular system as a thick liquid structure allows a direct comparison of the deformation results with those obtained by the elastic model. However, we expect that the simulation of the ventricular system as a thin liquid structure instead will lead to results that are rather similar to those calculated by the homogeneous fluid model.

Figure 5.20 shows the registration results, the corresponding grid deformations, and a section of the displacement vector fields, taken from the vicinity of the ventricular system, for the homogeneous fluid model (top row) and the inhomogeneous fluid model (bottom row), respectively. Note, that both

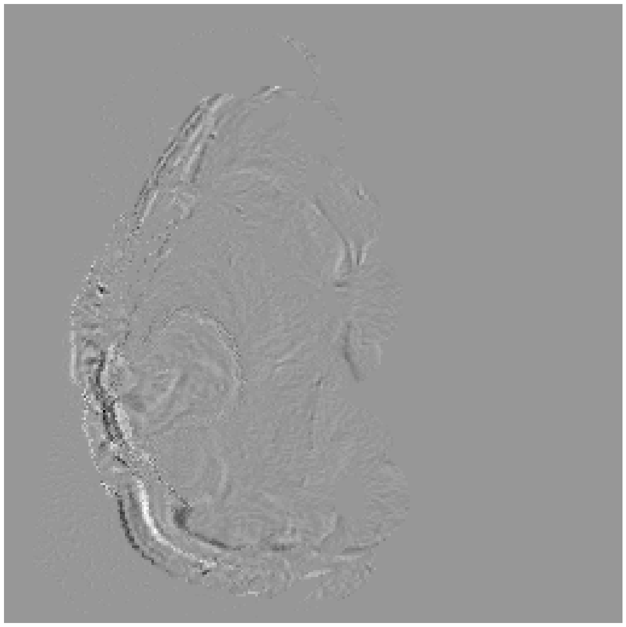

Figure 5.21: Difference image between Figures 5.20(a) and (d).

sections of the displacement vector fields shown in Figures 5.20(c) and (f) merely display the displacement vector fields used for transforming the image, i.e. only the vectors belonging to the mid-node $\mathbf{x}_9$ of the divergence-free finite elements are depicted. All vectors associated to the nodes $\mathbf{x}_1, \ldots, \mathbf{x}_8$ of the divergence-free finite elements have been dropped here since these vectors do not contribute to the final image deformation using the homogeneous and the inhomogeneous fluid models.

Surprisingly, both registration results are rather similar, although Figure 5.21, showing the difference image between Figures 5.20(a) and (d), reveals that slight differences at the combined skin/skull surfaces in the lower left part of the image occur. Compared to the results of the inhomogeneous elastic model, see Figures 5.13 and 5.14, equivalent registration results are obtained in the vicinity of the ventricular system for both fluid models. In contrast to the results of the elastic model, a shift of the posterior midline is always suppressed here without any additional correspondences, irrespectively whether homogeneous or inhomogeneous material properties are assumed for the fluid model. For better visualization purposes of this behavior, Figure 5.22 depicts enlarged sections of the posterior midline.

However, as shown in Figure 5.23, the lower left part of the combined skin/skull region of the preoperative image is mapped with a somewhat worse

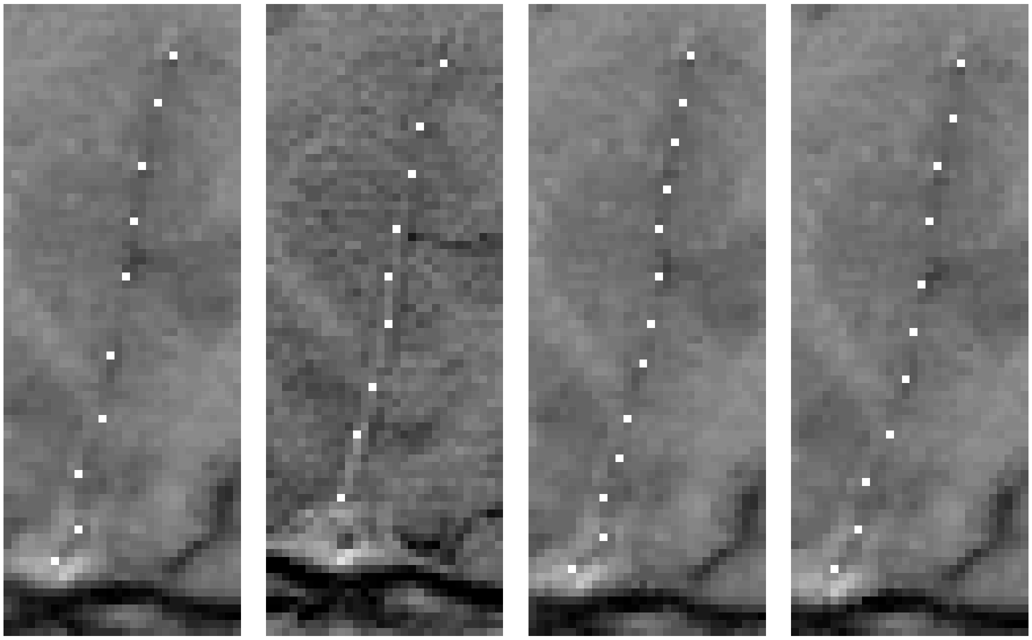

(a) (b) (c) (d)

Figure 5.22: Enlarged parts of the posterior midline for (a) the preoperative image, (b) the postoperative image, (c) the homogeneous fluid model and (d) the inhomogeneous fluid model. For better visualization purposes, we manually marked the posterior line with white squares.

accuracy onto the corresponding region of the postoperative image compared to the elastic model. Especially in the vicinity of the tumor region, the calculated deformation using both fluid models remain unsatisfactory since no significant compression of the tumor occurs. This can be best seen in the corresponding grid deformations depicted in Figures 5.20(b) and (e). In contrast, the elastic model leads to a significant compression of the tumor and hence, to a better registration result in this case (compare the deformation results of the fluid model with those obtained by the elastic model in Figures 5.13 and 5.14).

A closer look at some parts of the calculated displacement vector field of the inhomogeneous fluid model, which are shown on the right hand side of Figure 5.24, reveals that the displacement vectors indicate a significant material flow in the vicinity of the tumor region. As clearly visible in the displacement vector field shown in the upper right part of Figure 5.24, a large

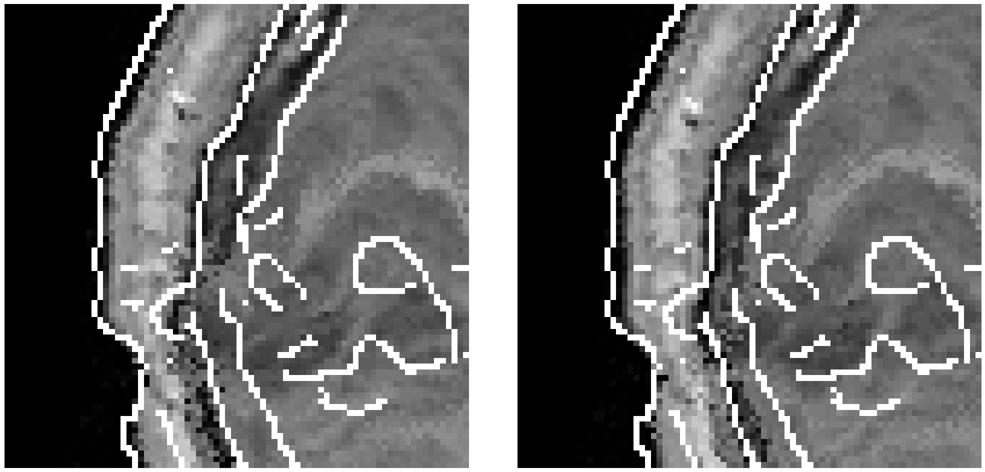

(a) (b)

Figure 5.23: Enlarged sections of the lower left part of the combined skin/skull regions of (a) the homogeneous fluid model and (b) the inhomogeneous fluid model. The desiderative accuracy of the mapping at the combined skin/skull surface is clearly visible.

mass transport to the upper right corner of the section, which is located between the skull and the tumor regions, occurs. Due to the physical properties of the underlying fluid model, this mass transport is a consequence of the material inflow enforced by the given correspondences at the location where skull and tumor are directly adjacent to each other. The corresponding section of the displacement vector field of this location is shown in the lower right part of Figure 5.24.

As pointed out above, the registration results of the fluid model in the vicinity of the tumor region are rather poor compared to the registration results of the elastic model since both fluid models yield no compression of the tumor and hence the white tumor outline remains nearly unchanged. To further investigate the rather sobering registration results of the fluid model at the tumor region, we consider an enlarged section of the complete displacement vector field of the inhomogeneous fluid model at the tumor boundary, as shown in Figure 5.25. The given correspondences, which are the set of large displacements pointing to the lower right corner of Figure 5.25, are clearly visible here. Looking at a single divergence-free finite element only, as marked by the black square, reveals a relatively small displacement of the

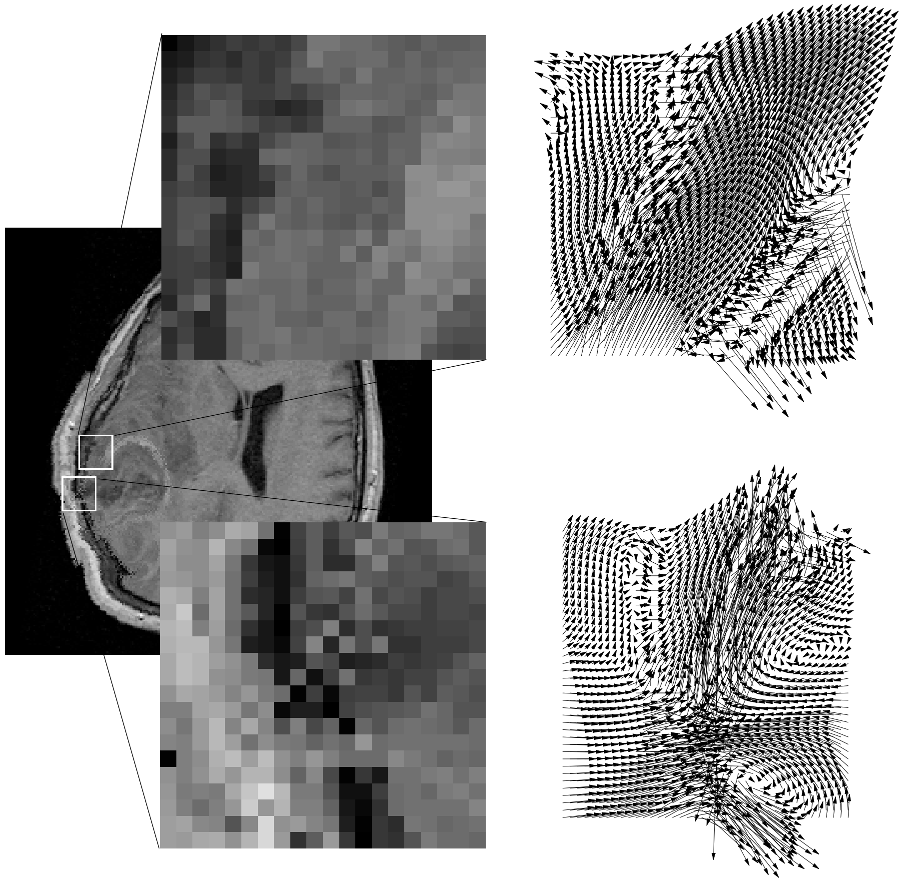

Figure 5.24: Different sections of the calculated displacement vector field of the inhomogeneous fluid model, taken from the marked parts of the image. The sections show the complete displacement vector field, i.e. the calculated displacement vectors from all nodes of the underlying divergence-free finite element mesh.

mid-node $\mathbf{x}_9$, which is indicated by the black arrow. This small displacement results from the necessary final multiplication $\tilde{\mathbf{u}} = \mathbf{R}_d\tilde{\mathbf{u}}_d$, as described in Section 4.3.2, to reconstruct the displacement of the mid-node $\mathbf{x}_9$ since this node determines the displacement of the associated pixel, see Appendix B for further details. As a consequence, the fluid-based approach leads to a locally bad result. Additionally, the displacement vectors located at the mid-side nodes $\mathbf{x}_5, \ldots, \mathbf{x}_8$, according to the notation in Figure 4.6, of the finite element boundary point in directions opposite to the given correspondences. This behavior is forced through the tumor compression as a result

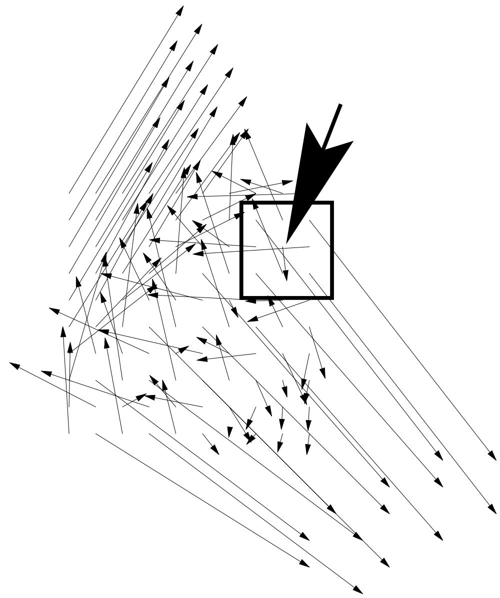

Figure 5.25: Enlarged section of the calculated displacement vector field depicted in the top row of Figure 5.24, showing some of the given correspondences at the tumor boundary. The black square indicates a single finite element while the black arrow points to the center node $\mathbf{x}_9$.

of the given correspondences since the incompressibility of the fluid demands a material outflow. However, a significant improvement of the registration result is expected, if the underlying mapping between image pixels and finite elements is changed. It seems most promising instead, to use a mapping that aligns each image pixel to those nodes of the underlying finite element mesh where four neighboring finite elements meet, or, in other words, a mapping that aligns the pixels to the appropriate nodes $\mathbf{x}_1, \ldots, \mathbf{x}_4$ of the underlying divergence-free finite elements, see also Appendix B.

5.4 The coupled rigid/elastic/fluid model

In this section, we describe experiments using our coupled rigid/elastic/fluid model which allows for a simulation of deformations of inhomogeneous materials under load using the appropriate physical models, namely the Navier equation for rigid and elastic materials coupled with the Stokes equation for fluid regions, see Section 4.4 for details. In order to investigate the influence of different physical models on the calculated deformations, we will directly compare the results of the coupled approach with those determined previously by a pure elastic model and a pure fluid model, respectively.

For the coupled rigid/elastic/fluid model, we use the common Q_2-P_1 Crouzeix-Raviart finite element for all fluid regions and the biquadratic finite element for all elastic and rigid regions, respectively. Both types of finite elements have been described in detail in Section 4.3.2. As mentioned in Section 4.4.3 above, we have to use these types of finite elements here since a direct coupling between divergence-free finite elements and bilinear finite elements is not possible. Therefore, the here used elements result in $2(2N+1)^2 + 3N^2 - 3M^2$ degrees-of-freedom for a 2D image with $N \times N$ pixels, where M denotes the number of biquadratic finite elements included in the finite element mesh. This limits the image sizes used in our experiments to 61×61 pixels since the large number of degrees-of-freedom leads to very long calculation times, see Table 4.1 for details. To further reduce the degrees-of-freedom (as well as the memory requirements of the approach) to manageable sizes, we directly map each image pixel onto a node of the underlying finite element mesh such that all regions of the inhomogeneous body must follow exactly the finite element boundaries, see Appendix B for detailed informations.

As material parameter values for the coupled rigid/elastic/fluid model, we took the ratios determined in Section 4.6 for the Lamé constants λ and μ in case of the skull bone and brain tissue (i.e. $\lambda_{br}/\mu_{br} = 135.111$, $\lambda_{sk}/\mu_{sk} = 0.718666$, and $\lambda_{sk}/\lambda_{br} = 1011.72$), respectively, and a value of 0.01 for the combined parameter $\mu^{\star}dt^{-1}$ of the fluid regions. For the elastic model and the fluid model, we applied material parameter ratios identical to those in Sections 5.2 and 5.3.

5.4.1 2D synthetic images

The synthetic images used in our experiments are depicted in Figures 5.26(a) and (b). Each image contains the following three different materials: rigid skull bone (black), soft brain tissue (dark grey), and cerebrospinal fluid (bright grey). Note, that the terms *rigid*, *soft*, and *fluid* are used here to describe the expected material behavior of the corresponding regions while the actual simulation of these structures depends on the applied physical model. In fact, the fluid model can simulate rigid and elastic regions by treating them as thick liquid and thin liquid structures, respectively.

As pointed out in Section 5.1, we directly compare the calculated results of our coupled rigid/elastic/fluid model with those determined by the pure elastic model and the pure fluid model. Using these models, we carried out experiments firstly assuming a homogeneous body only and secondly

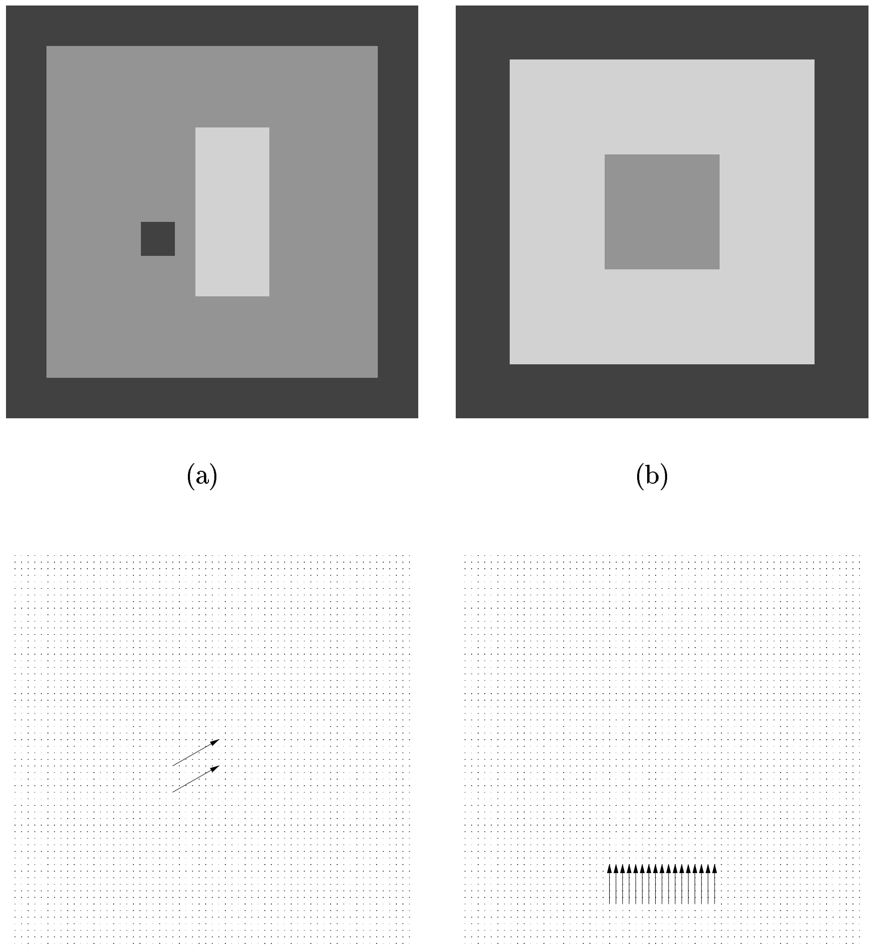

(a) (b)

(c) (d)

Figure 5.26: The synthetic images used in our experiments (top row) and the prescribed displacements (bottom row). Both images comprise three different materials: rigid skull bone (black), soft brain tissue (dark grey), and cerebrospinal fluid (bright grey).

assuming an inhomogeneous body comprising brain tissue, skull bone, and fluid treated as a rigid object. As mentioned above, this kind of simulation of fluid regions was motivated by the reported incompressibility of cerebrospinal fluid [135, 146]. In the following, we will refer to these five approaches as *homogeneous elastic model*, *inhomogeneous elastic model*, *homogeneous fluid model*, *inhomogeneous fluid model*, and *coupled rigid/elastic/fluid model*, respectively.

In the first experiment, we simulated the movement of a rigid object towards a nearby fluid region, using the synthetic image shown in Figure 5.26(a). The rigid object (represented by the small black square) may represent, e.g., a surgical instrument, a rigid foreign body, or a particle of skull bone. For simplicity, the movement is modeled as a pure translation of the squared object using two parallel displacements with components $\mathbf{u} = (7.0, -4.0)^T$ each, as shown in Figure 5.26(c). We expect that the resulting deformation leads to a pure translation of the rigid object in the direction of the fluid region which should deform accordingly.

As can be seen from the calculated results and the corresponding grid deformations depicted in Figure 5.27, the homogeneous elastic model as well as the homogeneous fluid model result in deformations where both, the object and the surrounding skull bone were deformed which is in contrast to the assumed rigid material behavior. With the inhomogeneous elastic model this is not the case, but the assumed rigidity of the fluid structure leads to physically incorrect violations of the grid topology as is clearly visible in Figures 5.28(a) and (b). Additionally, no deformations occur in the fluid region and the soft material between the object and the fluid region is no longer visible (note, that the rigid and elastic parts lie one above the other). Similar considerations hold for the inhomogeneous fluid model in Figure 5.28(c), but the corresponding grid deformation shown in Figure 5.28(d) indicates that the deformation is more local here as compared to the inhomogeneous elastic model. A complete different behavior shows the coupled rigid/elastic/fluid model. Here, the shape of the rigid object is still preserved while the complete deformation takes place in the fluid and soft tissue regions, see Figures 5.28(e) and (f).

In our second experiment we simulated the growth of a tumor located inside a simulated skull bone, by applying 17 parallel correspondences given by $\mathbf{u} = (0.0, -6.0)^T$ at the bottom part of the skull, as shown in Figure 5.26(d). We expect that, due to the incompressibility of the fluid and the rigidity of the surrounding bone, the soft brain tissue will be compressed. As can be seen from Figure 5.29, both, the homogeneous elastic model and the homogeneous fluid model, lead to incorrect results: no compression of the soft part can be observed and even at the rigid bone deformations occur. Additionally, large, topology-disturbing deformations occur in the rear of the given correspondences for the homogeneous elastic model due to the applied homogeneous Dirichlet boundary conditions, as indicated by the sizeable grid deformation at the bottom part of Figure 5.29(b).

Instead, the inhomogeneous elastic model leads mainly to a deformation of the enclosed brain tissue with a slight compression at the bottom part,

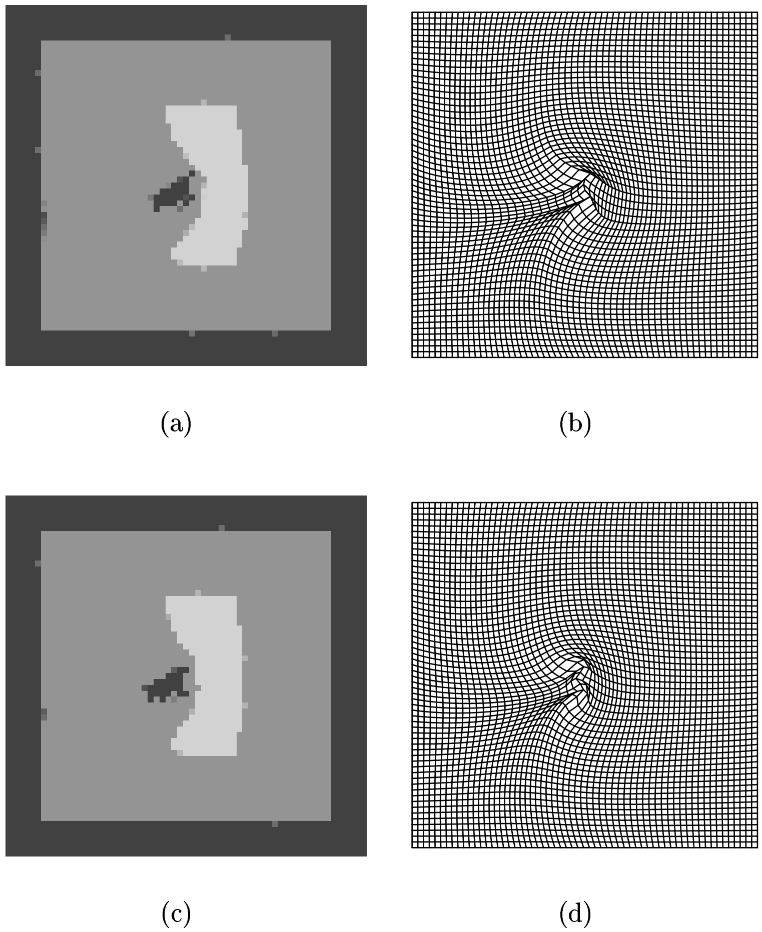

Figure 5.27: Calculated deformations (left column) for the synthetic image shown in Figure 5.26(a) and corresponding grid deformations (right column) using the homogeneous elastic model (top row) and the homogeneous fluid model (bottom row).

see Figures 5.30(a) and (b). Changing the Lamé constants λ and μ from soft to rigid material values, the violation of the grid topology is completely prevented. In contrast to these results, no compression of the soft region occurs while using the inhomogeneous fluid model because the physical properties of the underlying Stokes equation prevent from a compression of the soft material. Therefore, only a slight deformation of the soft material results. The deformation in the vicinity of the prescribed displacements is rather similar to the homogeneous fluid model here since the underlying incompressibility

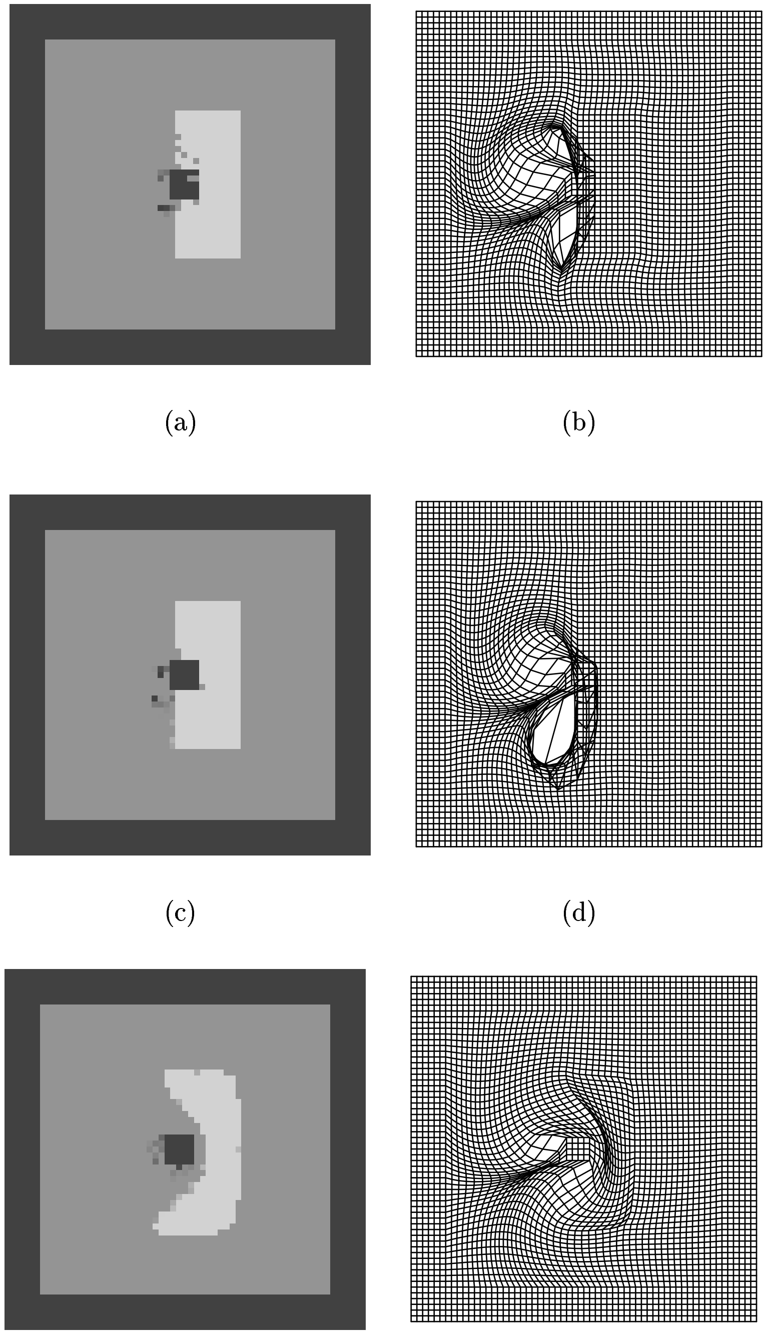

(a) (b)

(c) (d)

(e) (f)

Figure 5.28: Calculated deformations (left column) for the synthetic image shown in Figure 5.26(a) and corresponding grid deformations (right column) using the inhomogeneous elastic model (top row), the inhomogeneous fluid model (middle row), and the coupled rigid/elastic/fluid model (bottom row).

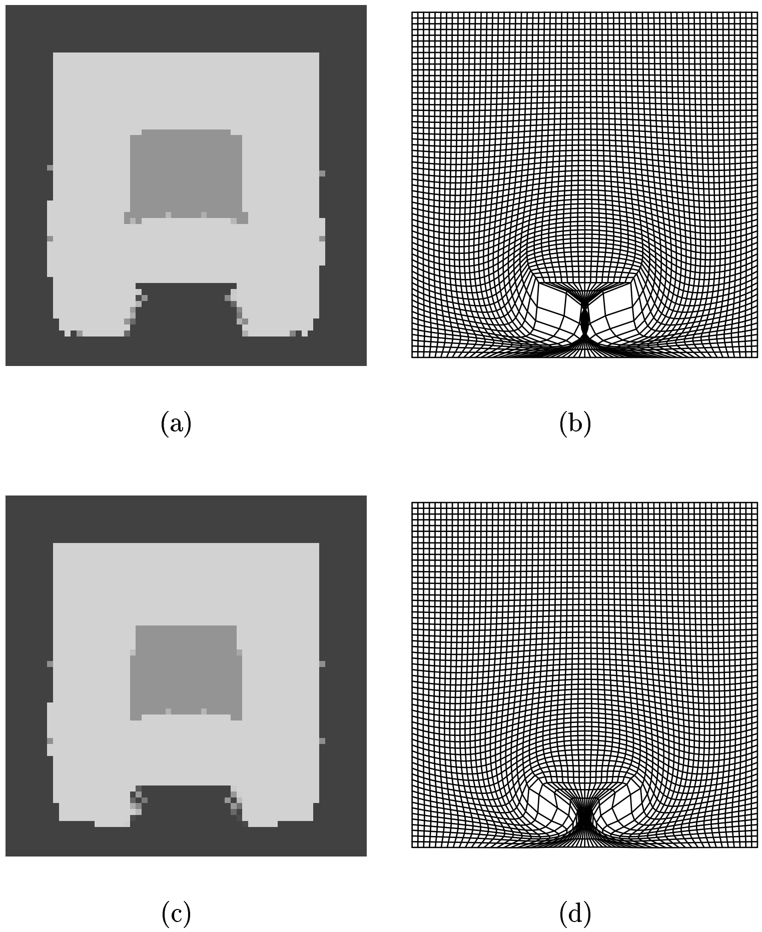

Figure 5.29: Calculated deformations (left column) for the synthetic image shown in Figure 5.26(b) and corresponding grid deformations (right column) using a homogeneous elastic model (top row) and a homogeneous fluid model (bottom row).

constraint demands that the rigid skull region has to shrink elsewhere.

Again, only the inhomogeneous coupled rigid/elastic/fluid model gives the expected result. In the simulation, the brain tissue has been significantly compressed, as can be clearly seen in the corresponding grid deformation shown in Figure 5.30(f). Also, after a detailed analysis of the pixels belonging to each region (not shown here), it turns out that the tumor enlargement is roughly equal to the shrinking of brain tissue which clearly demonstrates that the incompressibility of the fluid region holds here.

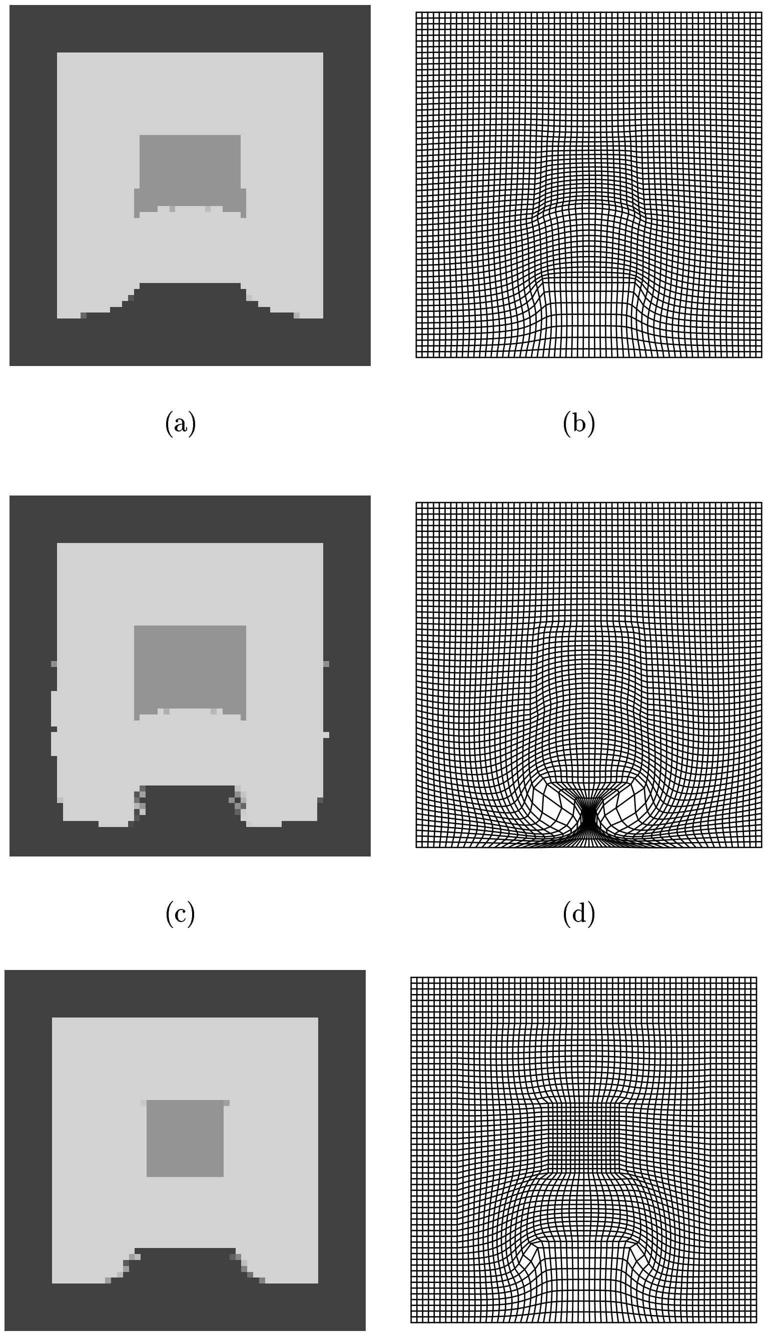

(a) (b)

(c) (d)

(e) (f)

Figure 5.30: Calculated deformations (left column) for the synthetic image shown in Figure 5.26(b) and corresponding grid deformations (right column) using an inhomogeneous elastic model (top row), an inhomogeneous fluid model (middle row), and a coupled rigid/elastic/fluid model (bottom row).

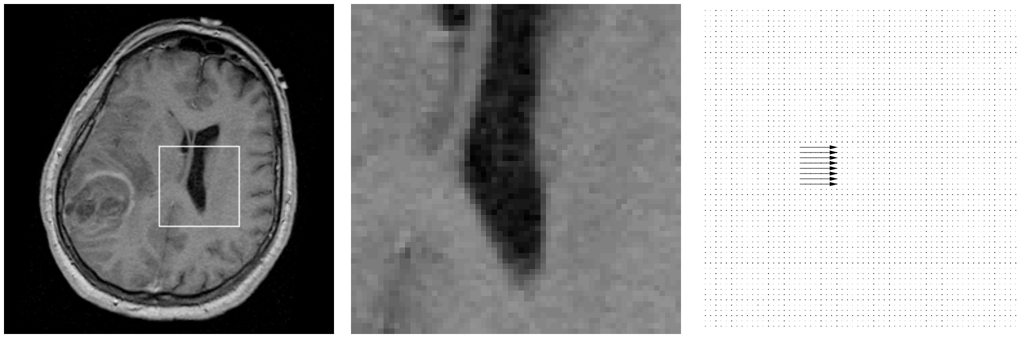

(a) (b) (c)

Figure 5.31: Enlarged part (b) of the ventricular system of the original preoperative image (a). The applied correspondences are depicted in (c).

5.4.2 2D MR images

For our experiment with a real tomographic image, we used the section of the preoperative MR image marked in Figure 5.31. The resulting image of size 61×61 pixels shows a part of the ventricular system surrounded by soft brain tissue. In order to segment both regions, we applied a Canny edge detector to the image. Thereafter, the resulting segmentation has been locally corrected such as to match the underlying finite element mesh. The final segmentation thus follows exactly the finite element boundaries.

Figures 5.32 and 5.33 show the results and corresponding grid deformations for 8 prescribed, parallel displacements $\mathbf{u} = (7.0, 0.0)^T$ given at the left side of the ventricular system, as indicated in Figure 5.31(c). Using the homogeneous elastic model and the homogeneous fluid model, rather similar deformations result, both leading to a remarkably bended shape of the ventricular system, see Figures 5.32(a) and (c). As indicated by the corresponding grid deformations in Figures 5.32(b) and (d) as well as by the displacement vector fields shown in Figures 5.34(a) and (b), this bending is symmetric with regard to the applied correspondences. Significant displacements occur in both cases in a rather local neighborhood, i.e. no material flows to remote parts of the image. In contrast, the inhomogeneous elastic model leads to a corrupted and physically incorrect result due to a violation of the underlying topology, which is clearly visible in the grid deformation shown in Figure 5.33(b). As observed in the first synthetic experiment shown in Figure 5.28, such foldings sometimes occur in the vicinity of rigid structures due to large

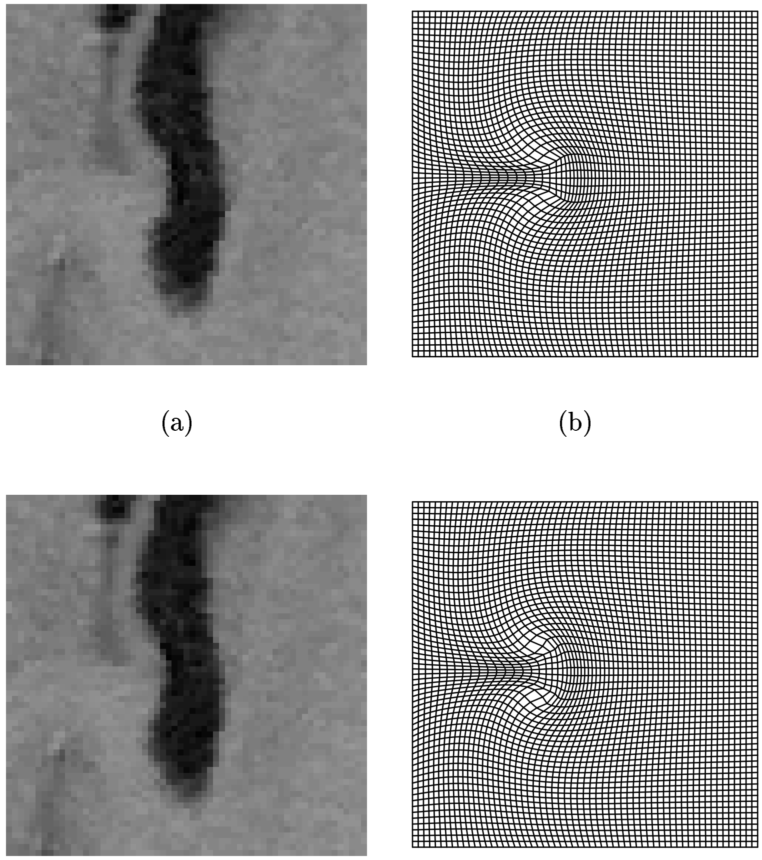

(a) (b)

(c) (d)

Figure 5.32: Resulting calculated deformations (left column) for the image in Figure 5.31(b) and corresponding grid deformations (right column) while using a homogeneous elastic model (top row) and a homogeneous fluid model (bottom row).

deformations at the boundary between a soft and a rigid region (see also the corresponding displacement vector field in Figure 5.34(c)). Additionally, the shape of the ventricular system is nearly preserved thus indicating that the inhomogeneous elastic model is insufficient in this case.

A similar deformation is obtained with the inhomogeneous fluid model. According to the underlying direct mapping between image pixels and finite elements, only slight deformations occur since the final multiplication $\tilde{\mathbf{u}} = \mathbf{R}_d \tilde{\mathbf{u}}_d$ suppresses large deformations at the boundary between brain tissue

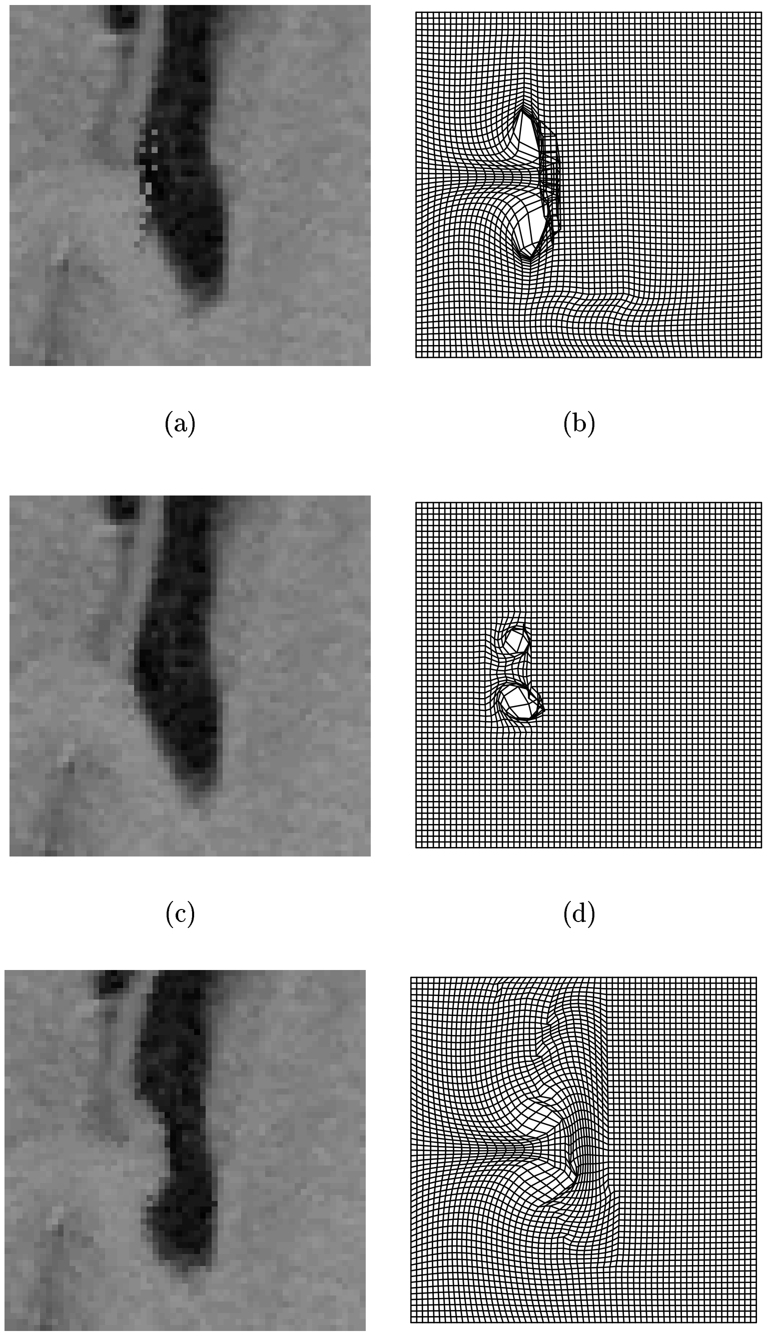

(a) (b)

(c) (d)

(e) (f)

Figure 5.33: Resulting calculated deformations (left column) for the image in Figure 5.31(b) and corresponding grid deformations (right column) while using an inhomogeneous elastic model (top row), an inhomogeneous fluid model (middle row), and the coupled rigid/elastic/fluid model (bottom row).

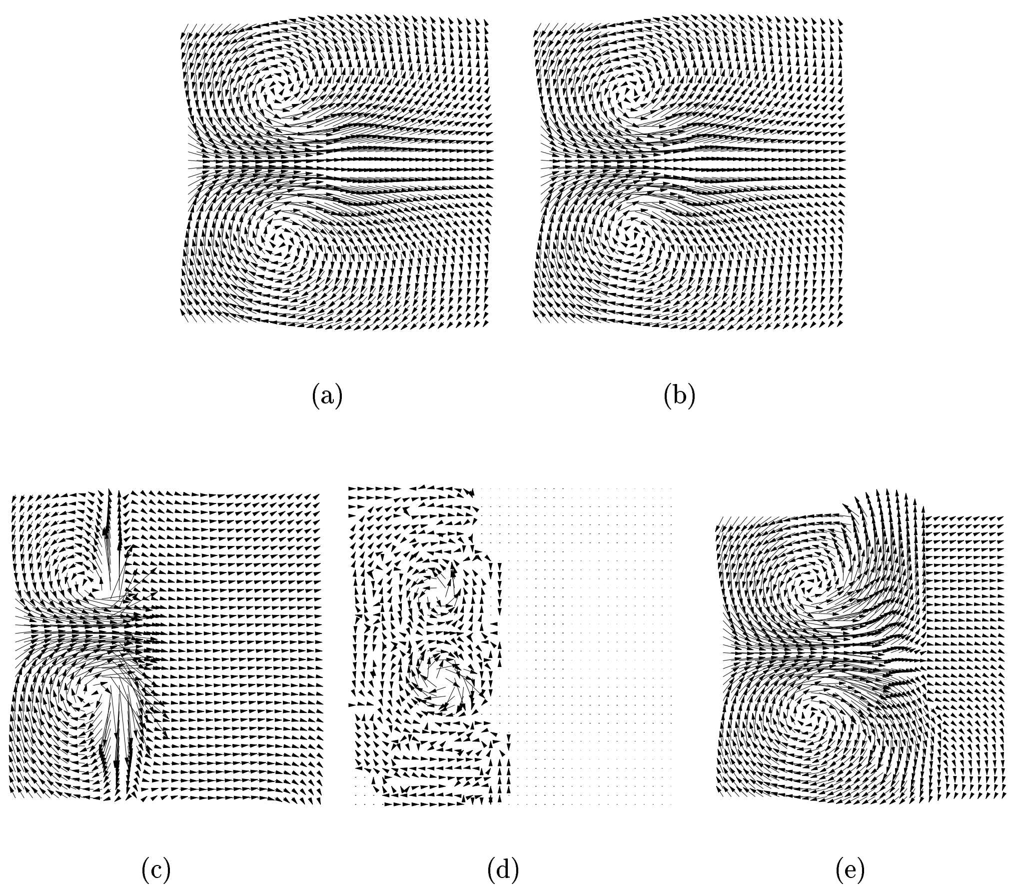

Figure 5.34: Parts of the calculated displacement vector fields for (a) the homogeneous elastic model, (b) the homogeneous fluid model, (c) the inhomogeneous elastic model, (d) the inhomogeneous fluid model, and (e) the coupled rigid/elastic/fluid model. Note, that the vector fields of the fluid models in subfigures (b) and (d) show only the relevant displacement vectors of the mid-node $\mathbf{x}_9$. The sections were taken from the middle of the image shown in Figure 5.31(b).

and ventricular system (see also Figure 5.34(d) as well as the discussion in Section 5.3). In contrast, the coupled rigid/elastic/fluid model results in a completely different behavior, see Figures 5.33(e) and (f). Due to the shape of the enclosed fluid region, the calculated deformation is non-symmetric with regard to the given correspondences. Also, a clearly visible flow of material inside the fluid region to the upper part of the image occurs. The result is a roughly straight right side of the ventricular system. Interestingly, the pressure of the fluid onto the brain tissue at the right side is nearly uniformly distributed as indicated by the resulting overall small displacements of the brain tissue there, see Figure 5.34(e).

5.5 Summary

In this chapter, we experimentally compared different biomechanical models to assess the physical plausibility of the computed deformations. In Sections 5.2 and 5.3 experiments were carried out using a pure elastic model and a pure fluid model only, i.e. all materials were simulated using either the Navier equation or the Stokes equation. Experiments with 2D (and 3D) synthetic images revealed, that both approaches lead to physically plausible deformations such that the shapes of simulated rigid structures have been preserved. Differences occur in case of experiments with real MR data, where the fluid model leads to insufficient registration results compared to the elastic model. But this can be traced back to the underlying mapping process between image pixels and finite elements. Consequently, a significant enhancement of the quality of the registration results can be expected if another mapping would be chosen.

In Section 5.4 we saw that problems arise for inhomogeneous elastic and fluid models when prescribed displacements act in the vicinity of anatomical structures whose physical behaviors differ significantly from the underlying physical model. In this case, both approaches, the inhomogeneous elastic model and the inhomogeneous fluid model, lead to insufficient deformation results that are physically incorrect. Instead, the coupled rigid/elastic/fluid model, which allows for an adequate physical simulation of rigid, elastic, and fluid structures through a coupling of the Navier equation and the Stokes equation, yields physically plausible deformation results. With this approach, both, the shape of rigid structures and the volume of fluid regions, i.e. the number of pixels representing each fluid structure, remain preserved in all experiments while the soft regions deform in a physically plausible way. Nevertheless, we expect that problems arise in case of large deformations, since our approach is valid for small deformations only. But these limitations should be overcome by using either a Lagrangian incremental method [21, 118] or an arbitrary Lagrangian-Eulerian (ALE) formulation [31, 73, 159]. However, our experiments show, that the coupled rigid/elastic/fluid approach results in a significant improvement of the computed deformation results compared to either a pure elastic model or a pure fluid model.

To further investigate both, the potential properties and limits of our coupled rigid/elastic/fluid model, a larger number of experiments (especially based on real image datasets) should be carried out. By using intra- or post-operative image datasets as ground truth for comparison purposes with the computed deformations, first steps in the direction of a more formal validation could be made. Additionally, such an experimental series, especially with varying material parameter values for the combined parameter $\mu^{\star}dt^{-1}$, would allow for a further judgement of the validity of the assumed material parameter values for the fluid regions, which have been determined heuristically only due to the lack of reported measurements. However, according to our current experience with biomechanical models, we do not expect a significant change of the physical plausibility of the computed deformation results once the combined parameter $\mu^{\star}dt^{-1}$ changes.

Chapter 6

Conclusion

In this thesis, we developed a new biomechanical model of the human head for intraoperative image correction purposes in order to increase the accuracy of image-guided neuronavigation systems. In contrast to the existing biomechanical models, our new approach copes with different anatomical structures consisting of *rigid*, *elastic*, and *fluid* materials while using the appropriate physical models, namely the *Navier equation* and the *Stokes equation*, respectively.

For the derivation of our model, we used the well-established physical theory of *continuum mechanics* to handle inhomogeneous materials. With our scheme, an *inhomogeneous* body is divided into a set of *homogeneous* regions, each representing a different material for which the appropriate physical model is utilized. For the discretization and solution of the problem, we apply the *finite element method* (FEM) to each region, leading to a corresponding set of sparse linear matrix systems. To merge these linear matrix systems into a single one, we apply appropriate boundary conditions, namely the *equilibrium boundary condition*, the *compatibility boundary condition*, and the *no-slip condition*, all of which establish a physical link between rigid, elastic, and fluid regions. Using these boundary conditions, a single linear matrix system results which completely describes the physical behavior of an inhomogeneous domain, comprising rigid, elastic, and fluid materials.

Instead of using forces, which are generally difficult to be determined from corresponding images, we used a set of prescribed landmark correspondences to drive the deformation. In our approach, it is ensured that these prescribed correspondences are exactly fulfilled by the computed deformation thus our approach can be regarded as a landmark-based registration scheme. Additionally, it turns out that the external forces are automatically adjusted by our approach such that the necessary material parameter values are decoupled from explicit physical units. As a result, only the ratios of all material parameter values with respect to each other determine the deformation behavior of an inhomogeneous domain. Based on a comprehensive literature study, we determined appropriate ratios between the material parameters λ and μ characterizing skull bone and brain tissue, respectively, by using the mean of all values found. Due to the lack of reported material parameter values for cerebrospinal fluid, we were forced to use heuristically determined ratios between cerebrospinal fluid and other materials instead. Note, that despite the visual appealing deformations resulting from the chosen value for the combined parameter $\mu^{\star}dt^{-1}$, the validity of this value remains unclear. So further research and measurements are necessary to determine a reliable value for $\mu^{\star}dt^{-1}$. Additionally, since the development of more precise biomechanical models demands the incorporation of further anatomical structures [91] like, e.g., the falx or the tentorium, further research is required to determine appropriate material values for those structures.

In the last part of this thesis, we reported on experiments carried out using different biomechanical models of the human head and compared the computed deformations to assess the influence of different physical models on the results. Besides the coupled rigid/elastic/fluid model, we developed two other biomechanical models, each of them based on a single physical model only. This leads to an elastic model based entirely on the Navier equation and a fluid model based entirely on the Stokes equation, respectively. In the latter case, problems arise with the solution due to the additional pressure function which demands the usage of *mixed finite elements*. The commonly applied Q_2-P_1 *Crouzeix-Raviart finite element* leads to a large number of degrees-of-freedom and thus to unacceptable computation times as well as memory requirements that usually prevent the application of such fluid models. To reduce the computation times and storage requirements, we introduced so-called *divergence-free finite elements* which reduce the number of degrees-of-freedom and simultaneously enhance the numerical properties, i.e. the condition number, of the final stiffness matrix. For the simulation of different material properties in the purely elastic model and the purely fluid model, we used a spatial variation of the underlaying material parameter values. The experimental comparison revealed, that the integrated treatment of rigid, elastic, and fluid materials significantly improved the physical plausibility of the calculated deformation results as compared to approaches based on a single physical model only.

However, a larger number of further experiments (especially with clinical relevant MR images) is necessary to fully investigate the properties and limits of our coupled rigid/elastic/fluid model. In particular, we expect that problems arise in case of large deformations since the approach is formally valid for small deformations only. But such limitations should be overwhelmed using either a Lagrangian incremental method [21, 118] or an arbitrary Lagrangian-Eulerian (ALE) formulation [31, 73, 159]. By comparing the results of the approach to real intra- or postoperative image datasets, a more precise estimation of the physical plausibility of the computed deformations should be obtained.

To further enhance the computational efficiency of the coupled rigid/elastic/fluid model, an integration of divergence-free finite elements seems desirable. But this requires a derivation of transition elements which remains an open problem. Alternatively, regions representing fluids could be simulated using the *boundary element method* (BEM) instead [8]. Again, a linear matrix system results which can be directly coupled with those linear matrix systems derived with the finite element method by using the same scheme as described in Section 4.4 [8, 77]. The advantage of using the boundary element method is also a significant reduction of the number of degrees-of-freedom, but the mandatory accuracy of the boundary representations in this case [53] requires the usage of a finite element mesher to generate the underlying finite element grid [65].

However, further investigations are necessary towards the development of biomechanical models of the human head with a maximal physical realism. As a first step in this direction, we propose the incorporation of further anatomical structures. Additionally, as a second step, an integration of anisotropic material behavior, where a preferred direction of the material exists [77, 21], arising from, e.g., arteries, veins, or variations of cell density between white matter and grey matter seems to be necessary [78]. But both extensions require the derivation of new *constitutive equations* which remains a challenging and complex task [46, 48, 32, 101]. All in all, the development of as-precise-as-possible biomechanical models of the human head with maximal physical realism remains an exciting and challenging problem.

Appendix A

Notation

$\mathbb{R}$	space of real numbers
$\mathbb{R}^+$	space of positive real numbers
$\mathbb{R}^n$	space of real vectors
$\mathbb{R}^{n\times n}$	space of real square matrices
Ω	bounded, open, connected subset of $\mathbb{R}^3$
$\bar{\Omega}$	closure of Ω
Γ	boundary of Ω
$\partial\Delta$	boundary of a region $\Delta \subset \bar{\Omega}$
$\emptyset$	empty set
α	scalar value
f	scalar function
$\mathbf{a}$	vector valued function in the Lagrangian configuration
$\mathbf{A}$	tensor valued function in the Lagrangian configuration
$\hat{\mathbf{a}}$	vector valued function in the Eulerian configuration

$\hat{\mathbf{A}}$	tensor valued function in the Eulerian configuration
$\mathbf{A}^T$	transpose of a tensor
δ_{ij}	Kronecker delta symbol
∂_i	partial derivative with respect to the ith component
∂^i	partial derivative of order i
∇	Nabla operator
$\mathbf{J}(\cdot)$	Jacobian matrix
$(\mathrm{tr}\,\cdot)$	trace operator
$(\det\cdot)$	determinant of a matrix
$\mathrm{div}[\cdot]$	divergence of a vector or tensor field
$\mathrm{curl}[\cdot]$	curl of a vector or tensor field
$\lvert\cdot\rvert$	absolute value
$(\cdot,\cdot)$	inner product of vectors or tensors
$\langle\cdot,\cdot\rangle$	inner product of a function space
$\lVert\cdot\rVert_V$	norm in the space V
$\subset$	a subspace
$\subseteq$	a subspace or equal space
$\cup$	unification of sets
$\cap$	intersection of sets
$\setminus$	set difference
$\mathrm{span}(\cdot,\ldots,\cdot)$	space spanned by some functions

$\oplus$	orthogonal decomposition of a vector space
$V^*(\Omega)$	dual space of $V(\Omega)$
$H^m(\Omega)$	Sobolev space of order m
$L_2(\Omega)$	space of quadratic integrable functions on Ω
$C^\infty(\Omega)$	space of functions whose derivatives of arbitrary order exist
$C^m(\Omega)$	space of functions whose derivatives up to order m exist
$P_m(\Omega)$	space of polynomials of order m
$Q_m(\Omega)$	space of polynomials of order m in each variable
$S(\Omega)$	space of all weakly solenoidal functions

Appendix B

Finite element mesh generation

Throughout this thesis, the finite element method is used for solving the Navier equation and the Stokes equation, respectively. As pointed out in Sections 2.3 and 4.3, the finite element method is based on a discretization of the body Ω into a set of disjunct areas Ω_k denoted as finite elements. The underlying discretization process is usually known as *finite element mesh generation process*, which is in general a computationally quite costly process [72, 65].

In our case, the discrete pixel (voxel) structure of a 2D (3D) image already provides the necessary discretization of the underlying body Ω, such that it suffices to define a mapping between the image pixels (voxels) and the nodal points $\mathbf{x}_j$ of each *bilinear* finite element Ω_k. A simple choice of a mapping function which has been used in this thesis, is depicted in Figure B.1, where each nodal point $\mathbf{x}_j \in \Omega_k$ is directly mapped onto a pixel (voxel) of the 2D (3D) image. The advantage of this simple mapping is a relatively small number of degrees-of-freedom and, moreover, that all calculated displacements $\mathbf{u}_i$ can be directly applied to their corresponding pixels (voxels) to transform the image. But problems arise if the underlying body Ω consists of different regions Ω_i, as indicated by the different grey values of the image pixels (voxels) in Figure B.1. Now, the nodal points $\mathbf{x}_j$ of some finite elements Ω_k may be assigned to different regions Ω_i of the inhomogeneous body such that an assignment of appropriate material parameter values is difficult. For a direct usage of this mapping in conjunction with inhomogeneous bodies Ω, the final segmentation of Ω into different regions Ω_i, according to the underlying anatomical structure, must ensure that the boundaries between all regions Ω_i must follow exactly the boundaries between different finite elements Ω_k of the finite element mesh.

To circumvent this problem, another mapping according to Figure B.2 can be used. In this case, each nodal point $\mathbf{x}_j$ is mapped in-between the

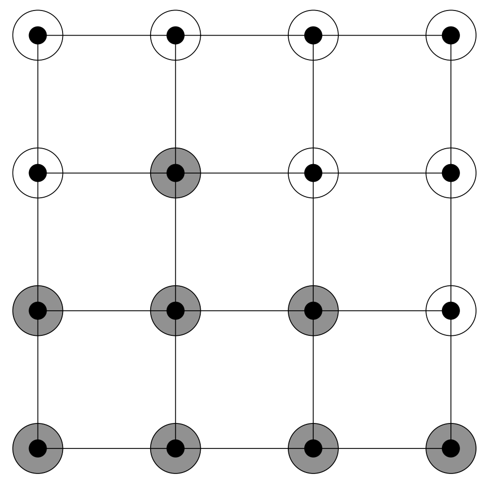

Figure B.1: A direct mapping between the image pixels ◯ and the nodal points • using bilinear finite elements Ω_k leads to a finite element mesh laying directly on the image pixels. Different grey values of the ◯ denote pixels belonging to different regions Ω_i of an inhomogeneous body Ω. Note, that the nodal points of the finite element Ω_k in the middle of the mesh have been assigned to different regions Ω_i, thus causing problems with respect to an assignment of appropriate material parameter values to the corresponding finite element Ω_k.

image pixels (voxels) such that the resulting finite element mesh is displaced with respect to the pixel (voxel) positions. All problems associated with inhomogeneous material properties vanish here, but now the displacements $\mathbf{u}_i$ are calculated for positions which do not match the pixel (voxel) positions. As a result, an interpolation of the displacement vector field $\mathbf{u}$ is mandatory to calculate the final pixel (voxel) displacements and thus the image deformation.

Similar considerations hold if *biquadratic* finite elements are used instead. Using a direct mapping as indicated in Figure B.1 requires again a segmentation of the inhomogeneous body that follows exactly the boundaries of the biquadratic finite elements. The usage of a mapping as indicated in Figure B.3 instead relaxes the necessity of interpolation since the center node $\mathbf{x}_9$ of each biquadratic finite element is directly mapped onto the image pixel (voxel) position while all other nodal points are mapped in-between the pixel (voxel) positions. But for a 2D image consisting of $N \times N$ pixels, this results in a large number of degrees-of-freedom where $3N^2 + 2N$ degrees-of-freedom are related to nodal points in-between the pixel positions which are therefore

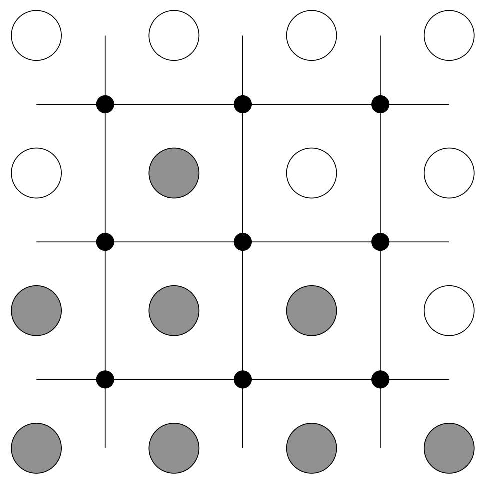

Figure B.2: A mapping between the image pixels ◯ and the nodal points • using bilinear finite elements, where each pixel is mapped into the center of the corresponding finite element thus leading to a displaced finite element mesh with respect to the pixel positions. The differences in grey values of ◯ denote pixels belonging to different regions Ω_i of an inhomogeneous body Ω.

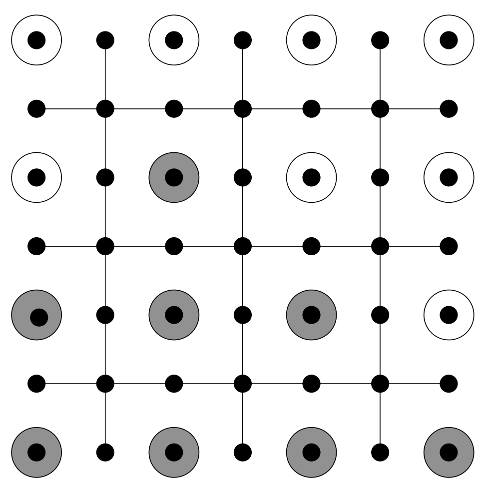

Figure B.3: A mapping between the image pixels ◯ and the nodal points • using biquadratic finite elements such that each pixel is mapped onto the center node $\mathbf{x}_9$ of the corresponding finite element, see also Figure 4.4(a) for the notation used for biquadratic finite elements. Again, different pixel grey values denote different regions Ω_i.

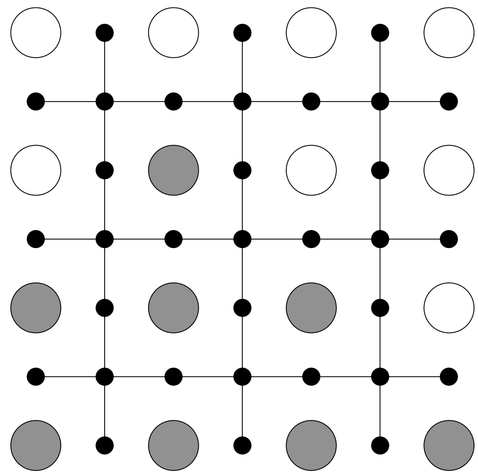

Figure B.4: A mapping between the image pixels ○ and the nodal points • using divergence-free finite elements such that each pixel is mapped into the center of the corresponding finite element mesh. Again, different pixel grey values denote different regions Ω_i.

unused for the final image transformation.

In order to use *divergence-free* finite elements instead, the transformation $\tilde{\mathbf{u}} = \mathbf{R}_d \tilde{\mathbf{u}}_d$ is applied to each biquadratic finite element leading to the finite element mesh shown in Figure B.4. Here, the nodal points $\mathbf{x}_9$ of all biquadratic finite elements, originally located at the pixel positions, have been eliminated such that a direct assignment of prescribed displacements to image pixels remains difficult, as pointed out in Section 4.5. To circumvent this, four adjacent image pixels should be mapped onto the corner nodes of a divergence-free finite element instead, see Figure B.5, but again, in this case, the segmentation of an inhomogeneous body Ω into homogeneous regions Ω_i has to follow exactly the boundaries of the finite elements. If this requirement with respect to accuracy cannot be fulfilled, local errors in the computed deformation will occur.

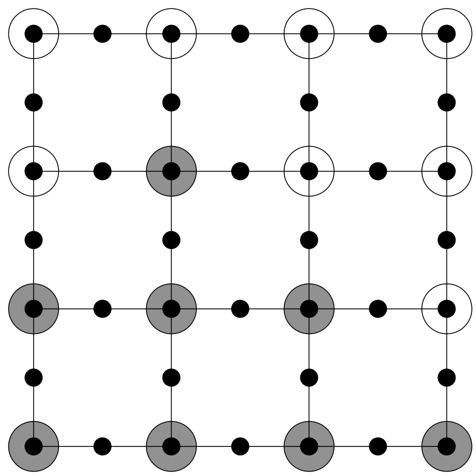

Figure B.5: A direct mapping between the image pixels ◯ and the nodal points • using divergence-free finite elements Ω_k leads to a finite element mesh laying directly on the image pixels. As usual, different grey values of the ◯ denote pixels belonging to different regions Ω_i of an inhomogeneous body Ω. Note, that the nodal points of the finite element Ω_k embedded in the middle of the mesh have been assigned to different regions Ω_i, thus causing problems with an assignment of appropriate material parameter values to the corresponding finite element Ω_k.

Bibliography

[1] S. H. Advani and R. P. Owings. Structural Modeling of Human Head. *Journal of the Engineering Mechanics Division*, pages 257–266, 1975.

[2] A. Anzelius. The Effect of an Impact on a Spherical Liquid Mass. *Acta Pathologica et Microbiologica Scandinavia (Supplementum XLVIII)*, 48:153–159, 1943.

[3] F. A. Bandak and R. H. Eppinger. A Three-Dimensional Finite Element Analysis of the Human Brain Under Combined Rotational and Translational Accelerations. In *Proceedings of the 38th Stapp Car Crash Conference*, pages 145–163. Society of Automotive Engineers, 1994.

[4] M. Bertero, T. A. Poggio, and V. Torre. Ill-Posed Problems in Early Vision. *Proceedings of the IEEE*, 76(8):869–889, August 1988.

[5] D. E. Beskos. *Boundary Element Methods in Mechanics.* North-Holland, 1987.

[6] F. Bookstein. Principal Warps: Thin-Plate Splines and the Decomposition of Deformations. *IEEE Transactions on Pattern Analysis and Machine Intelligence*, 11(6):567–585, June 1989.

[7] D. Braess. *Finite Elemente: Theorie, schnelle Löser und Anwendungen in der Elastizitätstheorie.* Springer Verlag, 1997.

[8] C. A. Brebbia, J. C. F. Telles, and L. C. Wrobel. *Boundary Element Techniques.* Springer Verlag, 1984.

[9] M. Bro-Nielsen. *Medical image registration and surgery simulation.* PhD thesis, Institute of Mathematical Modelling, Technical University of Denmark, 1996.

[10] M. Bro-Nielsen. Finite Element Modeling in Surgery Simulation. *Proceedings of the IEEE*, 86(3):490–503, March 1998.

[11] M. Bro-Nielsen and S. Cotin. Real-time Volumetric Deformable Models for Surgery Simulation using Finite Elements and Condensation. *Computer Graphics Forum (Eurographics'96)*, 15(3):57–66, 1996.

[12] I. N. Bronstein and K. A. Semendjajew. *Teubner-Taschenbuch der Mathematik*. Teubner Verlagsgesellschaft, 1996.

[13] R. D. Bucholz, D. D. Yeh, J. Trobaugh, L. L. McDurmont, C. D. Sturm, C. Baumann, J. M. Henderson, A. Levy, and P. Kessman. The Correction of Stereotactic Inaccuracy Caused by Brain Shift Using an Intraoperative Ultrasound Device. In J. Troccaz, E. Grimson, and R. Mösges, editors, *Computer Vision, Virtual Reality and Robotics in Medicine and Medicial Robotics and Computer-Assisted Surgery (CVRMed-MRCAS'97)*, volume 1205 of *Lecture Notes in Computer Science*, pages 459–466, Grenoble, France, 1997. Springer Verlag.

[14] D. T. Chen and D. Zeltzer. Pump It Up: Computer Animation of a Biomechanically Based Model of Muscle Using the Finite Element Method. *Computer Graphics*, 26(2):89–98, July 1992.

[15] G. E. Christensen. *Deformable Shape Models for Anatomy*. PhD thesis, Sever Institute of Technology, Washington University, August 1994.

[16] G. E. Christensen, S. C. Joshi, and M. I. Miller. Volumetric Transformation of Brain Anatomy. *IEEE Transactions on Medical Imaging*, 16(6):864–877, December 1997.

[17] G. E. Christensen, R. D. Rabbitt, and M. I. Miller. 3D Brain Mapping Using a Deformable Neuroanatomy. *Physics in Medicine and Biology*, 39:609–618, 1994.

[18] G. E. Christensen, R. D. Rabbitt, and M. I. Miller. Deformable Templates Using Large Deformation Kinematics. *IEEE Transactions on Image Processing*, 5(10):1435–1447, October 1996.

[19] C.-S. Chu, M.-S. Lin, H.-M. Huang, and Maw-Chang Lee. Finite element analysis of cerebral contusion. *Journal of Biomechanics*, 27(2):187–194, February 1994.

[20] P. G. Ciarlet. *The Finite Element Method for Elliptic Problems*, volume 4 of *Studies in Mathematics and its Applications*. North-Holland, 1978.

[21] P. G. Ciarlet. *Mathematical Elasticity. Volume 1: Three-Dimensional Elasticity*, volume 20 of *Studies in Mathematics and its Applications.* North-Holland, 1988.

[22] S. Cotin, H. Delingette, and N. Ayache. Real Time Volumetric Deformable Models for Surgery Simulation. In K. H. Höhne and R. Kikinis, editors, *Visualization in Biomedical Computing (VBC'96)*, volume 1131 of *Lecture Notes in Computer Science*, pages 535–540, Hamburg, Germany, September 1996. Springer Verlag.

[23] S. Cotin, H. Delingette, M. Bro-Nielsen, N. Ayache, J. M. Clément, and J. Marescaux. Geometric and Physical Representations for a Simulator of Hepatic Surgery. In *Medicine Meets Virtual Reality IV: Health Care in the Information Age - Future Tools for Transforming Medicine*, pages 17–20, San Diego, CA, USA, January 1996.

[24] S. Cotin, H. Delingette, J. M. Clément, V. Tassetti, J. Marescaux, and N. Ayache. Volumetric Deformable Models for Simulation of Laparoscopic Surgery. In H. U. Lemke, M. W. Vannier, K. Inamura, and A. G. Farman, editors, *Computer Assisted Radiology (CAR'96)*, volume 1124 of *International Congress Series*, pages 793–798, Paris, France, June 1996. Elsevier.

[25] C. Cuvelier, A. Segal, and A. A. van Steenhoven. *Finite Element Methods and Navier-Stokes Equations.* D. Reidel Publishing Company, 1986.

[26] C. Davatzikos. Nonlinear Registration of Brain Images Using Deformable Models. In M. E. Kavanaugh, editor, *Proceedings of the IEEE Workshop on Mathematical Methods in Biomedical Image Analysis*, pages 94–103, San Francisco, CA, USA, June 1996.

[27] C. Davatzikos. Spatial Transformation and Registration of Brain Images Using Elastically Deformable Models. *Computer Vision and Image Understanding, Special Issue on Medical Imaging*, 66(2):207–222, 1997.

[28] H. Delingette. Toward Realistic Soft-Tissue Modeling in Medical Simulation. *Proceedings of the IEEE*, 86(3):512–523, March 1998.

[29] F. P. DiMasi, R. H. Eppinger, and F. A. Bandak. Computational Analysis of Head Impact Response Under Car Crash Loadings. In *Proceedings of the 39th Stapp Car Crash Conference*, pages 425–438, San Francisco, CA, USA, 1995. Society of Automotive Engineers.

[30] F. P. DiMasi, J. Marcus, and R. H. Eppinger. 3-D Anatomic Brain Model for Relating Cortical Strains to Automobile Crash Loading. In *Proceedings of the 13th International Technical Conference on Experimental Safety Vehicles*, pages 916–924, November 1991.

[31] J. Donea. Arbitrary Lagrangian-Eulerian Finite Element Methods. In T. Belytschko and T. J. R. Hughes, editors, *Computational Methods for Transient Analysis*, volume 1 of *Computational methods in mechanics*, pages 473–516. Elsevier, 1983.

[32] A. D. Drozdov. *Mechanics of Viscoelastic Solids.* John Wiley & Sons, 1998.

[33] P. J. Edwards, D. L. G. Hill, J. A. Little, and D. J. Hawkes. Deformation for Image Guided Interventions Using a Three Component Tissue Model. In J. Duncan and G. Gindi, editors, *Information Processing in Medical Imaging (IPMI'97)*, volume 1230 of *Lecture Notes in Computer Science*, pages 218–231, Poultney, VT, USA, June 1997. Springer Verlag.

[34] P. J. Edwards, D. L. G. Hill, J. A. Little, and D. J. Hawkes. A three-component deformation model for image-guided surgery. *Medical Image Analysis*, 2(4):355–367, 1998.

[35] A. E. Engin. The Axisymmetric Response of a Fluid-filled Spherical Shell to a Local Radial Impulse - a Model for Head Injury. *Journal of Biomechanics*, 2:324–341, 1969.

[36] M. S. Estes and J. H. McElhaney. Response of Brain Tissue to Compressive Loading. *American Society of Mechanical Engineers*, 70-BHF-13:1–4, 1970.

[37] M. Ferrant, S. K. Warfield, C. R. G. Guttmann, R. V. Mulkern, F. A. Jolesz, and R. Kikinis. 3D Image Matching Using a Finite Element Based Elastic Deformation Model. In C. Taylor and A. Colchester, editors, *Medical Image Computing and Computer-Assisted Intervention (MICCAI'99)*, number 1679 in Lecture Notes in Computer Science, pages 202–209, Cambridge, UK, September 1999. Springer Verlag.

[38] G. Fischer. *Lineare Algebra.* Vieweg, 1997.

[39] J. D. Foley, A. van Dam, S. K. Feiner, and J. F. Hughes. *Computer Graphics: Principles and Practice.* The System Programming Series. Addison Wesley, 1992.

[40] M. Fornefett, K. Rohr, R. Sprengel, and H. S. Stiehl. Elastic Medical Image Registration using Orientation Attributes at Landmarks. In E. Berry, D. C. Hogg, K. V. Mardia, and M. A. Smith, editors, *Proceedings of the Medical Image Understanding and Analysis 98 (MIUA'98)*, pages 49–52, Leeds, UK, July 1998.

[41] M. Fornefett, K. Rohr, and H. S. Stiehl. Elastic Medical Image Registration Using Surface Landmarks With Automatic Finding of Correspondences. In A. Horsch and T. Lehmann, editors, *Bildverarbeitung für die Medizin (BVM'00)*, Informatik aktuell, pages 48–52, München, Germany, March 2000. Springer Verlag.

[42] M. Fornefett, K. Rohr, and H. S. Stiehl. Radial Basis Functions with Compact Support for Elastic Registration of Medical Images. *Image and Vision Computing*, 19(1 and 2):87–96, January 2001.

[43] O. Forster. *Analysis 2*. Vieweg, 1987.

[44] Y. C. Fung. *Foundations of Solid Mechanics*. Prentice-Hall, 1965.

[45] Y. C. Fung. *Biomechanics: Motion, Flow, Stress and Growth*. Springer-Verlag, 1990.

[46] Y. C. Fung. *Biomechanics: Mechanical Properties of Living Tissues*. Springer-Verlag, 1993.

[47] Y. C. Fung. *A First Course In Continuum Mechanics*. Prentice-Hall, 1994.

[48] Y. C. Fung. *Selected Works on Biomechanics and Aeroelasticity*, volume 1 of *Advanced Series in Biomechanics*. World Scientific, 1997.

[49] J. E. Galford and J. H. McElhaney. A viscoelastic study of scalp, brain, and dura. *Journal of Biomechanics*, 3:211–221, 1970.

[50] K. A. Ganser, H. Dickhaus, A. Staubert, M. M. Bonsanto, C. R. Wirtz, V. M. Tronnier, and S. Kunze. Quantifizierung von Brain-Shift durch Vergleich von prä- und intraoperativ erzeugten MR-Volumandaten. In T. Lehmann, V. Metzler, K. Spitzer, and T. Tolxdorff, editors, *Bildverarbeitung für die Medizin 1998 (BVM'98)*, Informatik aktuell, pages 422–426, Aachen, Germany, March 1998. Springer Verlag.

[51] S. Gibson, C. Fyock, E. Grimson, T. Kanade, R. Kikinis, H. Lauer, N. McKenzie, A. Mor, S. Nakajima, H. Ohkami, R. Osborne,

J. Samosky, and A. Sawada. Volumetric object modeling for surgical simulation. *Medical Image Analysis*, 2(2):121–132, 1998.

[52] S. Gibson, J. Samosky, A. Mor, C. Fyock, E. Grimson, T. Kanade, R. Kikinis, H. Lauer, N. McKenzie, S. Nakajima, H. Ohkami, R. Osborne, and A. Sawada. Simulating Arthroscopic Knee Surgery Using Volumetric Object Representations, Real-Time Volume Rendering and Haptic Feedback. In J. Troccaz, E. Grimson, and R. Mösges, editors, *Computer Vision, Virtual Reality and Robotics in Medicine and Medical Robotics and Computer-Assisted Surgery (CVRMed-MRCAS'97)*, volume 1205 of *Lecture Notes in Computer Science*, pages 369–378, Grenoble, France, 1997. Springer Verlag.

[53] E. Gladilin, W. Peckar, K. Rohr, and H. S. Stiehl. Vergleich der Randelemente- mit der Finite-Elemente-Methode zur elastischen Registrierung medizinischer Bilder. Technical Report FBI-HH-M-287/99, Universität Hamburg, Fachbereich Informatik, June 1999. Vogt-Kölln-Straße 30, 22527 Hamburg, Germany.

[54] W. Goldsmith. The Physical Processes Producing Head Injury. In W. F. Caveness and A. E. Walker, editors, *Head Injury Conference Proceedings*, pages 350–383, 1966.

[55] D. F. Griffiths. The construction of approximately divergence-free finite elements. In J. R. Whiteman, editor, *The mathematics of finite elements and applications III (MAFELAP'78)*, pages 237–245. Academic Press, April 1978.

[56] D. F. Griffiths. Finite Elements for Incompressible Flow. *Mathematical Methods in Applied Science*, 1:16–31, 1979.

[57] D. F. Griffiths. An approximately divergence-free 9-node velocity element (with variations) for incompressible flows. *International Journal for Numerical Methods in Fluids*, 1:323–346, 1981.

[58] W. Hackbusch. *Theorie und Numerik elliptischer Differentialgleichungen.* Teubner Verlag, 1996.

[59] A. Hagemann, K. Rohr, and H. S. Stiehl. Biomechanically based simulation of brain deformations for intraoperative image correction: coupling of elastic and fluid models. In K. M. Hanson, editor, *Medical Imaging 2000 – Image Processing (MI'00)*, Proceedings of SPIE Volume 3979, pages 658–667, San Diego, CA, USA, February 2000.

[60] A. Hagemann, K. Rohr, H. S. Stiehl, U. Spetzger, and J. M. Gilsbach. A Biomechanical Model of the Human Head for Elastic Registration of MR-Images. In H. Evers, G. Glombitza, T. Lehmann, and H.-P. Meinzer, editors, *Bildverarbeitung für die Medizin 1999 (BVM'99)*, Informatik aktuell, pages 44–48, Heidelberg, Germany, March 1999. Springer Verlag.

[61] A. Hagemann, K. Rohr, H. S. Stiehl, U. Spetzger, and J. M. Gilsbach. Biomechanical Modeling of the Human Head for Physically Based, Nonrigid Image Registration. *IEEE Transactions on Medical Imaging*, 18(10):875–884, October 1999.

[62] A. Hagemann, K. Rohr, H. S. Stiehl, U. Spetzger, and J. M. Gilsbach. Elastic Registration of MR-Images Based on a Biomechanical Model of the Human Head. In U. Spetzger, H. S. Stiehl, and J. M. Gilsbach, editors, *Navigated Brain Surgery*, pages 203–209. Wissenschaftsverlag Mainz, 1999.

[63] A. Hagemann, K. Rohr, H. S. Stiehl, U. Spetzger, and J. M. Gilsbach. Intraoperative Image Correction Using a Biomechanical Model of the Human Head with Different Material Properties. In W. Förstner, J. M. Buhmann, A. Faber, and P. Faber, editors, *Mustererkennung 1999 (DAGM'99)*, Informatik aktuell, pages 223–231, Bonn, Germany, September 1999. Springer Verlag.

[64] A. Hagemann, K. Rohr, H. S. Stiehl, U. Spetzger, and J. M. Gilsbach. Nonrigid matching of tomographic images based on a biomechanical model of the human head. In K. M. Hanson, editor, *Medical Imaging 1999 – Image Processing (MI'99)*, Proceedings of SPIE Volume 3661, pages 583–592, San Diego, CA, USA, February 1999.

[65] U. Hartmann. *Ein mechanisches Finite-Elemente-Modell des menschlichen Kopfes*. PhD thesis, Fakultät für Mathematik und Informatik, Universität Leipzig, 1999.

[66] U. Hartmann and F. Kruggel. Ein mechanisches dreidimensionales Finite-Elemente-Modell des menschlichen Gehirns. In B. Arnolds, H. Müller, D. Saupe, and T. Tolxdorff, editors, *Digitale Bildverarbeitung in der Medizin*, Tagungsband zum 5. Freiburger Workshop, pages 219–224, Freiburg, Germany, März 1997. Universität Freiburg.

[67] U. Hartmann and F. Kruggel. Erste klinische Untersuchungen mit einem mechanischen Finite-Elemente-Modell des menschlichen Kopfes.

In T. Lehmann, V. Metzler, K. Spitzer, and T. Tolxdorff, editors, *Bildverarbeitung für die Medizin 1998 (BVM'98)*, *Informatik aktuell*, pages 59–63, Aachen, Germany, March 1998. Springer Verlag.

[68] E. Hering, R. Martin, and M. Stohrer. *Physik für Ingenieure*. VDI Verlag, 1988.

[69] R. Hickling and M. L. Wenner. Mathematical Model of a Head Subjected to an Axisymmetric Impact. *Journal of Biomechanics*, 6:115–132, 1973.

[70] D. L. G. Hill, C. R. Maurer, R. J. Maciunas, J. A. Barwise, J. M. Fitzpatrick, and M. Y. Wang. Measurement of Intraoperative Brain Surface Deformation under a Craniotomy. *Neurosurgery*, 43(3):514–526, September 1998.

[71] R. R. Hosey and Y. K. Liu. A Homeomorphic Finite Element Model of the Human Head and Neck. In R. H. Gallagher, B. R. Simon, P. C. Johnson, and J. F. Gross, editors, *Finite Elements in Biomechanics*, pages 379–401. John Wiley & Sons, 1982.

[72] K. H. Huebner, E. A. Thornton, and T. G. Byrom. *The Finite Element Method for Engineers*. John Wiley & Sons, 1995.

[73] T. J. R. Hughes, W. K. Liu, and T. K. Zimmermann. Lagrangian-eulerian finite element formulation for incompressible viscous flows. *Computer methods in applied mechanics and engineering*, 29:329–349, 1981.

[74] M. K. Jain, A. Chernomorsky, F. H. Silver, and R. A. Berg. Material properties of living soft tissue composites. *Journal of Biomedical Material Research*, 22(3):311–326, 1988.

[75] D. Kallieris, A. Rizzetti, and R. Mattern. Verhalten der Kopf-Hals-Einheit bei der dynamischen Belastung — Vergleich zwischen Dummy und Leiche. *Zentralblatt Rechtsmedizin*, 42(6), 1994.

[76] H. Kanaya, H. Yukawa, Z. Itoh, T. Kanno, T. Kuwabara, M. Kagawa, and M. Mizukami. A neurological grading for patients with hypertensive intracerebral hemorrhage and a classification for hematoma location on computed tomography. In *Proceedings of 7th Japanese Conference on Surgery of Cerebral Stroke*, pages 265–270, 1978.

[77] H. Kardestuncer and D. H. Norrie. *Finite Element Handbook.* McGraw-Hill Company, 1987.

[78] Z. Karni, L. P. Ivan, and J. Bear. An Outline of Continuum Modeling of Brain Tissue Mechanics. *Journal of Child Neurology*, 1(2):119–125, April 1986.

[79] M. Kass, A. Witkin, and D. Terzopoulos. Snakes: Active contour models. *International Journal of Computer Vision*, 1(4):321–331, 1988.

[80] E. Keeve, S. Girod, and B. Girod. Craniofacial Surgery Simulation. In K. H. Höhne and R. Kikinis, editors, *Visualization in Biomedical Computing (VBC'96)*, volume 1131 of *Lecture Notes in Computer Science*, pages 541–546, Hamburg, Germany, September 1996. Springer Verlag.

[81] E. Keeve, S. Girod, P. Pfeifle, and B. Girod. Anatomy-Based Facial Tissue Modeling Using the Finite Element Method. In *Proceedings of IEEE Visualization '96*, pages 21–28, San Francisco, CA, USA, October 1996.

[82] T. B. Khalil and D. C. Viano. Critical Issues in Finite Element Modeling of Head Impact. In *Proceedings of the 26st Stapp Car Crash Conference*, pages 87–102. Society of Automotive Engineers, 1982.

[83] A. I. King, J. S. Ruan, C. Zhou, W. N. Hardy, and T. B. Khalil. Recent Advances in Biomechanics of Brain Injury Research: A Review. *Journal of Neurotrauma*, 12(4):651–658, 1995.

[84] R.M. Koch, M.H. Gross, F.R. Carls, D.F. von Büren, G. Fankhauser, and Y.I.H. Parish. Simulating Facial Surgery Using Finite Element Models. In *Computer Graphics Proceedings. Annual Conference Series. (SIGGRAPH'96)*, pages 421–428, New Orleans, LA, USA, August 1996.

[85] G. Krabbel and R. Müller. Development of a Finite Element Model of the Head Using the Visible Human Data. http://www.tu-berlin.de/fb10/ISS/FG7/broschuere/projekte/kopfschutz/vhp_tu.html, October 1996.

[86] G. Krabbel, S. Nitsche, and H. Appel. Development of an Anatomic 3-D Finite Element Model of the Human Head for Occupant Simulation. In *Beijing Automobile in Harmony with Human Society, Technical Papers*, pages 82–87, Beijing, China, October 1994. International Academic Publishers.

[87] G. Krabbel, S. Nitsche, and H. Appel. Methode zur Entwicklung biomechanischer Finite-Elemente-Modelle des Menschen. In *Berechnung im Automobilbau*, volume 1153, pages 503–516, Würzburg, Germany, September 1994. VDI-Gesellschaft Fahrzeug- und Verkehrstechnik, VDI Verlag.

[88] C. Kuhn. *Modellbildung und Echtzeitsimulation deformierbarer Objekte zur Entwicklung einer interaktiven Trainingsumgebung für die Minimal-Invasive Chirurgie.* PhD thesis, Fakultät für Informatik, Universität Karlsruhe, 1997.

[89] C. Kuhn, U. Kühnapfel, and O. Deussen. Echtzeitsimulation deformierbarer Objekte zur Ausbildungsunterstützung in der Minimal-Invasiven Chirurgie. In *Proceedings of the International GI Workshop: Modelling, Virtual Worlds, Distributed Graphics (MVD'95)*, Bad Honnef, Germany, November 1995. Infix Verlag.

[90] A. H. W. M. Kuijpers, M. H. A. Claessens, and A. A. H. J. Sauren. The Influence of Different Boundary Conditions on the Response of the Head to Impact: A Two-Dimensional Finite Element Study. *Journal of Neurotrauma*, 12(4):715–724, 1995.

[91] S. Kumaresan and S. Radhakrishnan. Importance of partitioning membranes of the brain and the influence of the neck in head injury modelling. *Medical and Biological Engineering and Computing*, 34:27–34, January 1996.

[92] S. Kumaresan, S. Radhakrishnan, and N. Ganesan. Generation of geometry of closed human head and discretisation for finite element analysis. *Medical and Biological Engineering and Computing*, 33:349–353, May 1995.

[93] S. K. Kyriacou and C. Davatzikos. A Biomechanical Model of Soft Tissue Deformation, with Applications to Non-rigid Registration of Brain Images with Tumor Pathology. In W. M. Wells, A. Colchester, and S. Delp, editors, *Medical Image Computing and Computer-Assisted Intervention (MICCAI'98)*, number 1496 in Lecture Notes in Computer Science, pages 531–538, Cambridge, MA, USA, October 1998. Springer Verlag.

[94] S. K. Kyriacou, C. Davatzikos, S. J. Zinreich, and R. N. Bryan. Nonlinear Elastic Registration of Brain Images with Tumor Pathology Using a Biomechanical Model. *IEEE Transactions on Medical Imaging*, 18(7):580–592, July 1999.

[95] H. P. Langtangen. *Computational Partial Differential Equations: Numerical Methods and Diffpack Programming.* Number 2 in Lecture Notes in Computational Science and Engineering. Springer Verlag, 1999.

[96] H. Lester and S. R. Arridge. A survey of hierarchical non-linear medical image registration. *Pattern Recognition*, 32(1):129–149, January 1999.

[97] H. Lester, S. R. Arridge, and K. M. Jansons. Local deformation metrics and nonlinear registration using a fluid model with variable viscosity. In E. Berry, D. C. Hogg, K. V. Mardia, and M. A. Smith, editors, *Proceedings of the Medical Image Understanding and Analysis 98 (MIUA'98)*, pages 44–48, Leeds, UK, July 1998. University of Leeds.

[98] H. Lester, S. R. Arridge, K. M. Jansons, L. Lemieux, J. V. Hajnal, and A. Oatridge. Non-linear Registration with the Variable Viscosity Fluid Algorithm. In A. Kuba, M. Šámal, and A. Todd-Pokropek, editors, *Information Processing in Medical Imaging (IPMI'99)*, number 1613 in Lecture Notes in Computer Science, pages 238–251, Visegrád, Hungary, June 1999. Springer Verlag.

[99] A. I. Lurie. *Nonlinear theory of elasticity.* North-Holland series in Applied mathematics and mechanics. North-Holland, 1990.

[100] L. E. Malvern. *Introduction to the Mechanics of a Continuous Medium.* Prentice-Hall, 1969.

[101] W. Maurel, Y. Wu, N. Magnenat Thalmann, and D. Thalmann. *Biomechanical Models for Soft Tissue Simulation.* Basic Research Series. Springer Verlag, 1998.

[102] C. R. Maurer, D. L. G. Hill, A. J. Martin, H. Liu, M. McCue, D. Rueckert, D. Lloret, W. A. Hall, R. E. Maxwell, D. J. Hawkes, and C. L. Truwit. Investigation of Intraoperative Brain Deformation Using a 1.5-T Interventional MR System: Preliminary Results. *IEEE Transactions on Medical Imaging*, 17(5):817–825, October 1998.

[103] J. H. McElhaney, R. L. Stalnaker, and V. L. Roberts. Biomechanical Aspects of Head Injury. In *Human Impact Response*, pages 85–112, New York, NY, USA., 1973. Plenum Press.

[104] T. McInerney and D. Terzopoulos. Deformable Models in Medical Image Analysis: A Survey. *Medical Image Analysis*, 1(2):91–108, 1996.

[105] K. K. Mendis, R. L. Stalnaker, and S. H Advani. A Constitutive Relationship for Large Deformation Finite Element Modeling of Brain Tissue. *Journal of Biomechanical Engineering*, 117:279–285, August 1995.

[106] H. Metz, J. H. McElhaney, and A. K. Ommaya. A comparsion of the elasticity of live, dead, and fixed brain tissue. *Journal of Biomechanics*, 3:453–458, 1970.

[107] M. I. Miga, K. D. Paulsen, J. M. Lemery, S. D. Eisner, A. Hartov, F. E. Kennedy, and D. W. Roberts. Model-Updated Image Guidance: Initial Clinical Experiences with Gravity-Induced Brain Deformation. *IEEE Transactions on Medical Imaging*, 18(10):866–874, October 1999.

[108] T. H. Milhorat and M. K Hammock. Cerebrospinal Fluid as Reflection of Internal Milieu of Brain. In J. Wood, editor, *Neurobiology of cerebrospinal fluids*, pages 1–23. Harold-New York, 1983.

[109] J. W. Millen and D. H. M. Woollam. *The anatomy of the cerebrospinal fluid.* Oxford University Press, 1962.

[110] K. Miller and K. Chinzei. Constitutive modelling of brain tissue: Experiment and theory. *Journal of Biomechanics*, 30:1115–1121, 1997.

[111] C. Monserrat, V. Hernández, M. Alcañiz, M. C. Juan, and V. Grau. Evaluation and study of a new deformable model based on boundary element methods. In H. U. Lemke, M. W. Vannier, K. Inamura, and A. G. Farman, editors, *Computer Assisted Radiology and Surgery (CARS'99)*, number 1191 in International Congress Series, pages 860–864, Paris, France, June 1999. Elsevier.

[112] C. Monserrat, U. Meier, F. Chinesta, M. Alcañiz, and V. Grau. A fast real time tissue deformation algorithm for surgery simulation. In H. U. Lemke, M. W. Vannier, and K. Inamura, editors, *Computer Assisted Radiology and Surgery (CAR'97)*, number 1134 in Excerpta Medica International Congress Series, pages 812–817, Berlin, Germany, June 1997. Elsevier.

[113] M. Mooney. A Theory of Large Elastic Deformation. *Journal of Applied Physics*, 11:582–592, September 1940.

[114] T. Nagashima, T. Shirakuni, and S. I. Rapoport. A two-dimensional finite element analysis of vasogenic brain edema. *Neurologica Medico-Chirurgica.*, 30:1–9, 1990.

[115] A. M. Nahum, R. Smith, and C. C. Ward. Intracranial Pressure Dynamics During Head Impact. In *Proceedings of the 21st Stapp Car Crash Conference*, pages 339–366. Society of Automotive Engineers, October 1977.

[116] M. R. Pamidi and S. H. Advani. Nonlinear Constitutive Relations for Human Brain Tissue. *Journal of Biomechanical Engineering*, 100:44–48, 1978.

[117] K. D. Paulsen, M. I. Miga, F. E. Kennedy, P. J. Hoopes, A. Hartov, and D. W. Roberts. A Computational Model for Tracking Subsurface Tissue Deformation During Stereotactic Neurosurgery. *IEEE Transactions on Biomedical Engineering*, 46(2):213–225, February 1999.

[118] W. Peckar. *Application of Variational Methods to Elastic Registration of Medical Images.* PhD thesis, Universität Hamburg, Fachbereich Informatik, AB KOGS, 1998.

[119] W. Peckar, C. Schnörr, K. Rohr, and H. S. Stiehl. Two-Step Parameter-Free Elastic Image Registration with Prescribed Point Displacements. In A. Del Bimbo, editor, *9th Int. Conf. on Image Analysis and Processing (ICIAP'97)*, volume 1310 of *Lecture Notes in Computer Science*, pages 527–534, Florence, Italy, September 1997. Springer Verlag.

[120] W. Peckar, C. Schnörr, K. Rohr, and H. S. Stiehl. Parameter-Free Elastic Deformation Approach for 2-D and 3-D Registration Using Prescribed Displacements. *Journal of Mathematical Imaging and Vision*, 10:143–162, 1999.

[121] W. Peckar, C. Schnörr, K. Rohr, H. S. Stiehl, and U. Spetzger. Linear and Incremental Estimation of Elastic Deformations in Medical Registration Using Prescribed Displacements. *Machine GRAPHICS & VISION*, 7(4):807–829, 1998.

[122] M. H. T. Reinges, H.-H. Nguyen, U. Spetzger, W. Küker, and J. M. Gilsbach. Beurteilung des präoperativen Brain shift mit Hilfe des Neuronavigationssystems EasyGuide Neuro. In T. Lehmann, V. Metzler, K. Spitzer, and T. Tolxdorff, editors, *Bildverarbeitung für die Medizin 1998 (BVM'98)*, Informatik aktuell, pages 124–128, Aachen, Germany, March 1998. Springer Verlag.

[123] K. Rohr. Elastic Registration of Multimodal Medical Images: A Survey. *KI – Künstliche Intelligenz*, 3:11–17, July 2000.

[124] K. Rohr, M. Fornefett, and H. S. Stiehl. Approximating Thin-Plate Splines for Elastic Registration: Integration of Landmark Errors and Orientation Attributes. In A. Kuba, M. Šámal, and A. Todd-Pokropek, editors, *Information Processing in Medical Imaging (IPMI'99)*, number 1613 in Lecture Notes in Computer Science, pages 252–265, Visegrád, Hungary, June 1999. Springer Verlag.

[125] K. Rohr, R. Sprengel, and H.S. Stiehl. Incorporation of Landmark Error Ellipsoids for Image Registration Based on Approximating Thin-Plate Splines. In H.U. Lemke, M.W. Vannier, and K. Inamura, editors, *Computer Assisted Radiology and Surgery (CAR'97)*, number 1134 in Excerpta Medica International Congress Series, pages 234–239, Berlin, Germany, 1997. Elsevier.

[126] K. Rohr and H. S. Stiehl. On the Definition and Characterization of 3D Brain Landmarks. Technical Report FBI-HH-M-268/96, Universität Hamburg, Fachbereich Informatik, December 1996. Vogt-Kölln-Straße 30, 22527 Hamburg, Germany.

[127] K. Rohr and H. S. Stiehl. Characterization and Localization of Anatomical Landmarks in Medical Images. In B. O. Hütter and J. M. Gilsbach, editors, *Proceedings of the 1st Aachen Conference on Neuropsychology in Neurosurgery, Psychiatry, and Neurology*, pages 9–12, Aachen, Germany, December 1997. Verlag der Augustinus Buchhandlung.

[128] K. Rohr, H. S. Stiehl, M. Fornefett, S. Frantz, and A. Hagemann. Landmark-Based Elastic Registration of Human Brain Images. In U. Spetzger, H. S. Stiehl, and J. M. Gilsbach, editors, *Navigated Brain Surgery*, pages 137–148. Wissenschaftsverlag Mainz, 1999.

[129] K. Rohr, H. S. Stiehl, M. Fornefett, S. Frantz, and A. Hagemann. Project IMAGINE: Landmark-Based Elastic Registration and Biomechanical Brain Modelling. *KI – Künstliche Intelligenz*, 3:37–39, July 2000.

[130] K. Rohr, H. S. Stiehl, R. Sprengel, W. Beil, T. M. Buzug, J. Weese, and M. H. Kuhn. Point-Based Elastic Registration of Medical Image Data Using Approximating Thin-Plate Splines. In K. H. Höhne and R. Kikinis, editors, *Visualization in Biomedical Computing (VBC'96)*, volume 1131 of *Lecture Notes in Computer Science*, pages 297–306, Hamburg, Germany, September 1996. Springer Verlag.

[131] J. S. Ruan, T. B. Khalil, and A. I. King. Human Head Dynamic Response to Side Impact by Finite Element Modeling. *Journal of Biomechanical Engineering*, 113:276–283, August 1991.

[132] J. S. Ruan, T. B. Khalil, and A. I. King. Finite element analysis of the human head to impact. In *Winter Annual Meeting of ASME, Bioengineering Division BED*, volume 22, pages 249–252, November 1992.

[133] J. S. Ruan, T. B. Khalil, and A. I. King. Brain injury in direct impact. In *Proceedings of the 4th Injury Prevention Through Biomechanics Symposium*, volume 28, pages 313–314. ASME, 1994.

[134] J. S. Ruan, T. B. Khalil, and A. I. King. Dynamic Response of the Human Head to Impact by Three-Dimensional Finite Element Analysis. *Journal of Biomechanical Engineering*, 116:44–50, February 1994.

[135] K. B. Sahay, R. Mehrotra, U. Sachdeva, and A. K. Banerji. Elastomechanical characterization of brain tissues. *Journal of Biomechanics*, 25(3):319–326, March 1992.

[136] A. A. H. J. Sauren and M. H. A. Claessens. Finite element modeling of head impact: The second decade. In *Proceedings of the International Conference on the Biomechanics of Impact (IRCOBI)*, pages 241–254, 1993.

[137] A. Schettini and E. K. Walsh. Brain tissue elastic behavior and experimental brain compression. *American Journal of Physiology*, 255(5):799–805, November 1988.

[138] T. Schiemann and K. H. Höhne. Definition of Volume Transformations for Volume Interaction. In J. Duncan and G. Gindi, editors, *Information Processing in Medical Imaging (IPMI'97)*, volume 1230 of *Lecture Notes in Computer Science*, pages 245–258, Poultney, VT, USA, June 1997. Springer Verlag.

[139] M. Schill, C. Reinhart, T. Günther, C. Paliwoda, J. Hesser, M. Schinkmann, H.-J. Bender, and R. Männer. Simulation of Brain Tissue and Realtime Volume Visualization: Integrating Biomechanical Simulations into the VIRIM System. In H. U. Lemke, M. W. Vannier, and K. Inamura, editors, *Proceedings of the Computer Assisted Radiology and Surgery (CAR'97)*, number 1134 in Excerpta Medica International Congress Series, pages 283–288, Berlin, Germany, June 1997. Elsevier.

[140] M. A. Schill, C. Wagner, R. Männer, and H.-J. Bender. Biomechanical Modeling Techniques and their Application to the Simulation of Brain Tissue. In U. Spetzger, H. S. Stiehl, and J. M. Gilsbach, editors, *Navigated Brain Surgery*, pages 193–202. Wissenschaftsverlag Mainz, 1999.

[141] H. R. Schwarz. *Methode der Finiten Elemente.* Teubner Verlag, 1984.

[142] T. H. Smit. *The Mechanical Significance of the Trabecular Bone Architecture in a Human Vertebra.* PhD thesis, Technische Universität Hamburg Harburg, 1996.

[143] U. Spetzger, H. S. Stiehl, K. Rohr, and J. M. Gilsbach. Navigated Brain Surgery: An Interdisciplinary Introduction. In U. Spetzger, H. S. Stiehl, and J. M. Gilsbach, editors, *Navigated Brain Surgery*, pages 5–9. Wissenschaftsverlag Mainz, 1999.

[144] J. Stoer. *Numerische Mathematik.* Springer Verlag, 1989.

[145] R. Sube and G. Eisenreich. *Dictionary of Physics.* Verlag Harry Deutsch, 1987.

[146] Y. Tada, T. Nagashima, and M. Takada. Biomechanics of Brain Tissue (Simulation of Cerebrospinal Fluid Flow). *JSME International Journal, Series A (Mechanics and Material Engineering)*, 37(2):188–194, April 1994.

[147] H. Takizawa, K. Sugiura, M. Baba, and J. D. Miller. Analysis of Intracerebral Hematoma Shapes by Numerical Computer Simulation Using the Finite Element Method. *Neurologica Medico-Chirurgica*, 34(2):65–69, February 1994.

[148] D. Terzopoulos and K. Waters. Techniques for Realistic Facial Modeling and Animation. In N. Magnenat Thalmann and D. Thalmann, editors, *Computer Animation '91*, pages 59–74. Springer Verlag, 1991.

[149] D. Terzopoulos and K. Waters. Analysis and Synthesis of Facial Image Sequences Using Physical and Anatomical Models. *IEEE Transactions on Pattern Analysis and Machine Intelligence*, 15(6):569–579, June 1993.

[150] S. Tieck, S. Gerloff, and H. S. Stiehl. Interactive graph-based editing of watershed-segmented 2D-images. In *Workshop on Interactive Segmentation of Medical Images (ISMI'98)*, University of Amsterdam, Dept. of

Computer Science, Intelligent Sensory Information systems Research Group, September 1998. http://carol.wins.ura.nl/silvia/workshop.

[151] P. A. Tipler. *Physik*. Spektrum Akademischer Verlag, 1994.

[152] S. Turek. Multigrid techniques for a divergence-free finite element discretization. *Journal of Numerical Mathematics*, 2(3):229–256, 1994.

[153] K. Ueno, J. W. Melvin, L. Li, and J. W. Lighthall. Development of Tissue Level Brain Injury Criteria by Finite Element Analysis. *Journal of Neurotrauma*, 12(4):695–706, August 1995.

[154] D. C. Viano. Biomechanics of Bone and Tissue: A Review of Material Properties and Failure Characterisics. In *Symposium on Biomechanics and Medical Aspects of Lower Limb Injuries*, pages 33–63, San Diego, CA, USA, October 1986.

[155] L. Voo, S. Kumaresan, F. A. Pintar, N. Yoganandan, and A. Sances Jr. Finite-element models of the human head. *Medical and Biological Engineering and Computing*, 34(5):375–381, September 1996.

[156] J. Vossoughi and F. A. Bandak. Mechanical Characteristics of Vascular Tissue and Their Role in Brain Injury Modeling: A Review. *Journal of Neurotrauma*, 12(4):755–763, August 1995.

[157] O. M. Škrinjar and J. S. Duncan. Real Time 3D Brain Shift Compensation. In A. Kuba, M. Šámal, and A. Todd-Pokropek, editors, *Information Processing in Medical Imaging (IPMI'99)*, number 1613 in Lecture Notes in Computer Science, pages 42–55, Visegrád, Hungary, June 1999. Springer Verlag.

[158] O. M. Škrinjar, D. Spencer, and J. S. Duncan. Brain Shift Modeling for Use in Neurosurgery. In W. M. Wells, A. Colchester, and S. Delp, editors, *Medical Image Computing and Computer-Assisted Intervention (MICCAI'98)*, number 1496 in Lecture Notes in Computer Science, pages 641–649, Cambridge, MA, USA, October 1998. Springer Verlag.

[159] A. Wall and E. Ramm. Fluid-Structure Interaction Based Upon A Stabilized (ALE) Finite Element Method. In S. R. Idelsohn, E. Oñate, and E. N. Dvorkin, editors, *Computational Mechanics - New Trends and Applications, Proceedings of the 4th World Congress on Computational Mechanics*, Buenos Aires, Argentina, June 1998.

[160] E. K. Walsh and A. Schettini. Calculation of brain elastic parameters in vivo. *American Journal of Physiology*, 274:693–700, 1984.

[161] E. K. Walsh and A. Schettini. Brain tissue elasticity and CSF elastance. *Neurological Research*, 12:123–127, June 1990.

[162] C. C. Ward. Finite Element Models of the Head and Their Use in Brain Injury Research. In *Proceedings of the 26th Stapp Car Crash Conference*, pages 71–85, Ann Arbor, MI, USA, 1982.

[163] C. C. Ward, P. E. Nikravesh, and R. B. Thompson. Biodynamic Finite Element Models Used in Brain Injury Research. *Aviation, Space, and Environment Medicine*, 49(1):136–142, January 1978.

[164] J. A. Weiss, B. N. Maker, and S. Govindjee. Finite element implementation of incompressible, transversely isotropic hyperelasticity. *Computer Methods in Applied Mechanics and Engineering*, 135:107–128, August 1996.

[165] T. A. Whitman, G. R. Wodicka, M. T. Morgan, and J. D. Bourland. Measurement and modeling of the vibrational response of the ovine head as it relates to intracranial pressure. In *Bridging Disciplines For Biomedicine*, 18th Annual International Conference of the IEEE Engineering in Medicine and Biology Society, Amsterdam, Netherlands, October 1996.

[166] R. Willinger, C. M. Kopp, and D. Césari. New concept of contrecoup lesion mechanism: Modal analysis of a finite element model of the head. *Proceedings of the International Conference on the Biomechanics of Impact (IRCOBI)*, pages 283–297, September 1992.

[167] R. Willinger, L. Taleb, and C.-M. Kopp. Modal and Temporal Analysis of Head Mathematical Models. *Journal of Neurotrauma*, 12(4):743–754, August 1995.

[168] C. Zhou, T. B. Khalil, and A. I. King. A New Model Comparing Impact Responses of Homogeneous and Inhomogeneous Human Brain. In *Proceedings of the 39th Stapp Car Crash Conference*, pages 121–137, San Francisco, CA, USA, 1995. Society of Automotive Engineers.

Index

abstract problem, 24, 49, 52, 63

Babuška-Brezzi condition, 53
bilinear form, 24, 49, 52
biomechanical model, 2, 28–33
biomechanics, 2, 7
body forces, 14
boundary condition, 16, 22, 28
  compatibility, 70
  Dirichlet, 16, 30, 31, 57
  equilibrium, 70
  essential, 23
  Neumann, 16
  no-penetration, 71
  no-slip, 30, 71
  Robbins, 16
boundary element method, 23
brain tissue, 43–47

Cauchy's formula, 15
cerebrospinal fluid, 9, 43
constitutive behavior, 8
constitutive equation, 17–19
constrained minimization problem, 50
continuity equation, 20
continuum mechanics, 9–21
coup-contrecoup phenomenon, 29

deformation, 10
  finite, 17
  infinitesimal, 17
deformation gradient, 11
density, 20
diffuse axonal injury, 28
displacement, 11
displacement gradient, 11
displacement problem, 75
dual space, 25

equation of motion, 15
equilibrium equation, 16
Eulerian configuration, 11, 17

finite element method, 21–26, 47
  conforming, 23, 49
  non-conforming, 24, 53
finite elements, 55–68, 74
  bilinear, 58, 141
  biquadratic, 60–61, 142
  Crouzeix-Raviart, 61–62
  divergence-free, 62–68, 144
  solenoidal, 62–68
  trilinear, 59
fluid
  compressible, 20
  incompressible, 20
  non-viscous, 18, 71
  viscous, 18, 71

Galerkin method, 23–24, 49
generalized coefficients, 56
geometric isotropy, 56
Green's formula, 48, 51

Hilbert structure, 22
Hooke's law, 17, 18, 44, 46
hysteresis, 8

image correction, 29

Lagrangian configuration, 10
Lamé constants, 17, 79
Lax-Migram lemma, 26
linear form, 24, 49, 52
load vector, 24, 73
load-deformation curve, 8

mapping, 141–144
material
  elastic, 8
  homogeneous, 17
  hyperelastic, 45
  inhomogeneous, 69–74
  isotropic, 17
  nonlinear viscoelastic, 45
  St. Venant-Kirchhoff, 17
  viscoelastic, 8, 43
material derivative, 12
material parameter values, 79–86
mesh generation, 141
method of weighted residuals, 22–23, 48, 51

Navier equation, 19–20, 47–50, 71
Navier-Poisson law, 19
Navier-Stokes equation, 20

Piola transform, 15
preconditioned tissue, 8
prescribed displacements, 75–77
pressure, 19, 52
pressure load, 52

rate-of-deformation, 14
rate-of-deformation tensor, 14
reference configuration, 10
reference element, 57
residual error, 23
response function, 17, 69

saddlepoint problem, 53
Simpson's rule, 64
skull bone, 43
Sobolev space, 22
spin tensor, 14
stiffness matrix, 24, 73
Stokes equation, 20–21, 50–55, 71
strain, 12–13
  natural, 46
strain tensor
  Almansi, 13
  Cauchy's infinitesimal, 18, 43
  Green-St. Venant, 13
  left Cauchy-Green, 13
  right Cauchy-Green, 13
stream function, 63, 76
stress, 14–15
stress relaxation, 8
stress tensor
  Cauchy, 15
  Eulerian, 18
  first Piola-Kirchhoff, 15
  second Piola-Kirchhoff, 15
surface forces, 14

tensorial relaxation function, 43
traction problem, 75

V-ellipticity, 26, 49, 53
velocity, 12, 71
viscosity parameters, 19, 84

weighting function, 23
well-posed problem, 25, 53